Analysis of Chemical Reaction on Adiabatic Potential Energy Surface from a Viewpoint of Anharmonicity and Orbital Mixing: Bifurcation of Anharmonic Downward Distortion Following Paths and Natural Reaction Orbitals

Shuichi Ebisawa

Graduate School of Chemical Sciences and Engineering
Hokkaido University

Contents

Chapter 1

General introduction

Ten years before the discovery of Schrödinger equation, [159] a fundamental law of chemistry was decoded by G. N. Lewis. [101] The idea of covalent bond, a pair of electrons shared between two nuclei, was proposed in the article entitled "The Atom and the Molecule" with the invention of a sophisticated notation for the description of molecular structures, which is today known as Lewis dot formulas. Despite its simplicity, Lewis dot formulas have been successfully applied to explanations of wide range of chemical phenomena. It is also surprising that the concepts of valence, of which origin was discovered by E. Frankland, [40] had already been recognized at that time. [100] It is very amazing that all these significant findings preceded the birth of quantum mechanics. Subsequent to the development of Lewis dot formulas, R. Robinson introduced a notation to describe electron movements, which is referred as arrow pushing. [88] After its first application to an explanation of conjugation of ethylene linkings, [88] mechanisms of various reactions were explained so concisely with arrow pushing [79, 80] that it became a standard notation for reaction mechanism analysis of today. The electronic theory of organic chemistry, mainly developed by R. Robinson and C. K. Ingold, explains reactivities based on some fundamental rules. The most important and strong regulation is that electron pairs need to move with preservation of atomic octets and the original arrangements of nuclei. [79] This regulation effectively excludes unreasonably unstable species from consideration. Within the rule, some dominant polar effects on the reactivity are considered, e.g., inductive effect, [81] iductomeric effect, [78] and resonance effect [80, 134]. These polarization effects of molecules and electrostatic interaction are regarded as the essential factors for chemical reactions throughout the theory. Despite its simplicity, electronic theory of organic chemistry is fairly useful to explain the mechanisms of a wide range of reactions. It still has been one of the most practical theories for reaction design even today. Nevertheless, mechanism of a class of reactions, pericyclic reactions, had remained uncovered until the 1960's. [30]

At the same time as the aformentioned remarkable development of chemistry, physics experienced a historic paradigm shift: the birth of quantum mechanics. After the decades of old quantum mechanics, matrix mechanics was founded by W. Heisenberg, M. Born and P. Jordan, [12, 66] followed by the formulation of Schrödinger equation. [159] The two formalisms proposed independently were eventually turned out to be equivalent. [174] It is natural that quantum mechanics had a great impact on chemistry because it is the theory to describe the behavior of microscopic particles like electron. Indeed, valence bond (VB) theory developed by Heitler and London gave a quantum mechanical explanation for chemical bonds: chemical bonds are formed by the overlap of valence atomic orbitals. [67] It is remarkable that the chemical bond, an imaginary concept formulated inductively, turned into a subject of physics. Almost simultaneously, molecular orbital (MO) theory, another theory for describing the molecular structure, was developed. [75, 123] MO theory describes the nature of electrons with molecular orbitals delocalized over the molecule whereas VB theory suppose each electron to be localized in each atomic orbital. The most fundamental MO theory is Hartree-Fock (HF) theory. [39, 63, 64, 163] HF theory approximates a n-electron wavefunction by a single determinant, Slater determinant, [163] composed of n-spin orbitals. The n-spin orbitals are determined to variationally minimize the electronic energy with the constraint of orthonormal conditions. This simple and clear formalism, however, has a distinct drawback. For example, single determinant electronic wavefunction of H_2 molecule gives much higher energy at the large internuclear distances than that of VB theory. [162] It is shown that the poor behavior of single determinant wavefunction is caused by the undesirable contribution of ionic state to the wavefunction. At a glance MO theory seems to be inferior to VB theory. However, that is not the case at all because this problem can be overcome by using wavefunction composed of multiple determinants. Actually, it is pointed out that the two theories are essentially equivalent with the use of configuration interaction approach. [58] The difference between VB theory and MO theory is, therefore, just the difference of viewpoint toward the same thing. Nevertheless, MO theory is more widely used in the field of computational chemistry because of its simplicity of the formulation. Nowadays, indeed, there are various MO theories more sophisticated than HF theory, e.g., complete active space self-consistent field (CASSCF) theory [146]. Even today, however, HF theory is regarded as a very important theory because it can be utilized as the zeroth-order approximation of more sophisticated theories.

Although spin orbitals and MOs were nothing more than a mathematical construct for the approximation of n-electron wavefunction, they came to be recognized as an essential concept for understanding chemical reactivities after the works of K. Fukui, R. B. Woodward and R. Hoffmann. [57, 72, 178, 179] In 1952, Fukui found that the regios-

electivity of electrophilic reactions of aromatic hydrocarbons can be clearly explained with only a few representative orbitals, frontier orbitals (FOs). FOs are composed of the highest occupied molecular orbitals (HOMO) and the lowest unoccupied molecular orbitals (LUMO) of the reactants. It came as a great surprise that such a complicated process as chemical reaction can be explained with only a few representative molecular orbitals. In the theory, chemical reaction is understood as a delocalization of electrons in the HOMO of each fragment to the LUMO of the other. The significance of frontier orbital theory is that implied the deep relationship between MOs and chemical reactions and motivated chemists to associate MOs with reactivity. Subsequent to the report of frontier orbital theory, R. B. Woodward and R. Hoffmann uncovered the mechanism of pericyclic reactions motivated by the concept of frontier orbitals. Woodward-Hoffmann rules provide a feasible way to predict the stereoselectivities of various types of pericyclic reactions base on the phase of frontier orbitals, particularly HOMO. It is notable that the phase of MOs clarified the underlying mechanism which was difficult to understand with other approaches, e.g., the electronic theory of organic chemistry. Hence, it is not surprising that MOs became an essential concept for reaction mechanism analysis.

According to Woodward and Hoffmann, reaction mechanism analysis from a viewpoint of molecular orbital theory is summarized as follows: "a reaction may still be analyzed by writing down the orbitals involved, allowing them to mix according to well-defined quantum mechanical principles and following the interacting orbitals through the reaction." [180] This implies that some representative pathway which appropriately characterizes the chemical reaction is required to perform reaction mechanism analysis. As well known, intrinsic reaction coordinates (IRCs), one of such representative pathways, were introduced by Fukui. [52] IRC is defined as the steepest descent paths from the first-order saddle point or transition state (TS) of potential energy surface. IRC is apparently different from the trajectory of Newton's equation of motion because inertia of a molecule is not taken into account at all. Nonetheless, IRC is widely adopted for the characterization of chemical reactions. As a matter of fact, it is hardly possible to reproduce the actual motion of molecules because chemical reaction usually occurs with affected by the surroundings, e.g., solvent. As such, it seems not so essential to determine the detail of molecular dynamics in condensed systems only for a qualitative explanation of the chemical reaction. Actually, IRC enables to discuss a characteristic change in the reaction process without considering too much detailed dynamics. Also, IRC is highly compatible with the reaction mechanism analysis with MOs because the geometric symmetry of the system is preserved along the IRC. Therefore, IRC can provide a feasible way to analyze the orbital mixing [77] along the reaction process. Indeed, Fukui noted "Once IRC was determined in this way, the driving force of a chemical reaction was analyzed on the basis of the orbital interaction argument." [54, 55] In this way,

the concept of molecular orbital and reaction pathway became fundamental concepts for the theoretical analysis of chemical reaction mechanism.

It was not an easy task to compute IRC because TS or the first-order saddle point of potential energy surface is need to be located prior to the IRC calculation, obvious from the definition of IRC. The first *ab intio* IRC calculation was realized by K. Ishida, K. Morokuma and A. Komornicki and applied to the isomerization of a hydrogen cyanide ($HCN \leftrightarrows NCH$) and the S_N2 reaction between a hydride and methane ($H^- + CH_4 \leftrightarrows CH_4 + H^-$). [82,94,114] In their work, TS was located with the minimization of gradient norm. [94,114] Even though the IRCs were computed successfully, it still had remained a challenging issue to locate TSs systematically. Over the past a few decades, so much effort has been devoted to this issue. [26, 83, 104, 105, 113, 118, 119, 143, 157] Among them, anharmonic downward distortion following (ADDF) [105, 130] method proposed by S. Maeda and K. Ohno was very important in that the method automated the TS search to a considerable extent. The concept of ADDF method is clear. It is known that harmonic potential around a potential minimum cannot describe any reaction because the harmonic potential has no stationary point other than its origin. In other words, second derivatives of potential is not essential for chemical reaction. Hence, ADDF method searches TSs by following the direction with large anaharmonic downward distortion (ADD), i.e., the difference between the real potential and the harmonic potential. Actually, anharmonicity has a deep relationship to electronic wavefunction. Based on perturbation theory, configuration mixing induced by nuclear displacements induces the ADD. [150]

Even though the concept of anharmonicity has been regarded essential for the chemical reaction, there is few analyses of its behavior on potential energy surface. This is contrast to the case of gradient extremals (GE). [10, 137, 166] GEs are defined as the curves at every point on which the gradient vector becomes an eigenvector of the Hessian matrix at the point. Actually, any given point on GEs is a stationary point (not necessarily minimum) of gradient norm on the contour of potential energy surface. [4, 5, 10, 71, 84, 133, 137, 149, 155, 161, 166] These analyses are not only important for the issue of systematic TS search but also for the understanding of the behavior of gradient norm on the potential energy surface. Since the negative gradient of potential energy is equivalent to the force on the nuclei, GE is also studied in the relation to dynamics on potential energy surface. [9] Considering the importance of ADD on chemical reaction, its behavior on potential energy surface seems also to be analyzed in detail. Especially, bifurcation of ADD around a potential minimum is important not only for the understanding of chemical reaction but also for the understanding of molecular vibration. It also has an importance on the issue of TS search because bifurcation can cause the overlooking of TSs. Accordingly, as the first topic of this thesis, the

bifurcation of ADD stationary paths around a potential minimum is studied in detail (Chapter 2).

The second topic is the automation of orbital analysis along IRC. As noted above, reaction pathway search has been automated to a considerable extent. [26,104,105,113] This automation drastically increased the amount of data provided by the reaction pathway search calculation. The manual analysis in a conventional manner is apparently unsuitable for such a great amount of data anymore. Thus, a new automated analysis method compatible with the automated reaction pathway search is needed. Among the various reaction mechanism analyses, molecular orbital analysis seems to be one of the most basic and essential analyses because it can clarify the driving force of the reaction. [54,55]. Automated extraction of important MO is not only convenient but also technically important for the application of data science to computational chemistry. [120, 173] Since data scientific approaches require a large amount of data, automation of data sampling is so essential. Combined with the aformentioned technique of automated reaction pathway search, [104] an automated method to extract essential MOs for the reactivity is expected to be a powerful tool for the realization of an automated data sampling system with computational chemistry.

Although there are various sophisticated orbital analysis methods, [35–37,44,48–51, 68, 103, 112, 117, 121, 124, 131, 144, 145] there seems to be no method designed for the automated extraction of MOs responsible for given reaction process. Accordingly, new orbital analysis method specialized to the automated extraction needs to be developed. For the design of such new orbital, the idea of ADD gives a big hint. As shown in [150], for example, ADD or relaxation of potential energy is induced by the configuration mixing induced by nuclear displacements. Actually, the configuration mixing induced by nuclear displacements can be represented with orbital basis. This is essentially because differential operators with respect to nuclear coordinates act as if they are one-electron operators. Even though some additional consideration is required for multiconfigurational theory, the configuration mixing in such cases can also be represented with MO basis. This implies that there exits a definition of MO which optimally characterizes the essential configuration mixing for the increase of ADD. Considering that the increase of ADD is necessary for a direction to be that of reaction, MO responsible for the increase of ADD seems to be essential for the reaction. That is, the driving force of a chemical reaction is expected to be extracted with such MO.

It should be referred that intrinsic soft molecular orbital (ISMO), a technique to extract MOs characterizing the response to partial charge fluctuation, was proposed by A. Morita and S. Kato. [121] ISMO is defined as the left and right singular vectors of the virtual-occupied block of the solution of coupled-perturbed self-consistent field (CP-SCF) equation [60, 136] with respect to the perturbation of external electrostatic

potential at each atomic site. CP-SCF equation is usually solved to obtain Hessian matrix with respect to some perturbation, e.g., nuclear displacements. In the course of Hessian calculation, the first-order response matrix of MOs with respect to the perturbation, conventionally denoted by **U**, is computed. Thus, CP-SCF equation provides the matrix **U** as the by-product. Even though it is not the main interest of CP-SCF calculation to obtain **U**, it is a very informative quantity. Indeed, **U** represents the orbital mixing induced by the perturbation applied to the system. Now it won't be difficult to understand how essential the quantity is for describing the change arising in the system. Another point of ISMO method is that it applies singular value decomposition (SVD) [89] or Autonne-Eckart-Young decomposition to characterization of the change. SVD is a matrix factorization method widely applied to dimensionality reduction. It had been applied to molecular orbital analysis even before the development of ISMO. [1, 44, 48, 56] In every case, SVD considerably simplifies the correlation between MOs in different orbital spaces, e.g., occupied orbital space and virtual orbital space, characterizing the correlation with only a small number of representative MO pairs. Hence, it seems reasonable to expect the representative MOs that are essential for the response to the external potential perturbation to be extracted by applying SVD to **U**. Subsequent to the report of ISMO, similar idea was applied to linear response theory to concisely characterize the single-electron excitation, which is referred as natural transition orbital (NTO). [112] Actually, natural reaction orbital (NRO) [33], which is introduced in the current thesis, also uses CP-SCF and SVD to automatically extract the representative MOs essential for reactivity. In the current thesis, a detailed analysis of the nature of NRO method and its applications to a series of typical reactions will be presented (Chapter 3) followed by its extension to multiconfigurational theory (Chapter 4). [34]

Chapter 2

Geometric Analysis of Anharmonic Downward Distortion Following Path

Abstract

A mathematical aspect of the anharmonic downward distortion (ADD) on potential energy surface is analyzed along ADD stationary paths. ADD is defined as the difference between harmonic potential around an equilibrium and the real potential. ADD stationary path is the curve connecting stationary points of ADD on isosurfaces of the harmonic potential. It was found that the maximum number of ADD stationary paths intersecting the potential minimum is given by $2^{f+1} - 2$, where f denotes the vibrational degrees of freedom. Also, bifurcation of ADD stationary paths was observed not only on model potentials but also on the *ab initio* potential energy surface of a H_2O molecule.

2.1 Introduction

Reaction path has been a fundamental concept for theoretical study of reaction mechanism. Intrinsic reaction coordinate (IRC) [52,53], which is defined as the steepest descent paths from the first-order saddle point or transition state (TS) geometry to the reactant and product minima on the potential energy surface (PES) in mass-weighted Cartesian coordinates. Although IRC is distinctly different from the trajectories of Newton's equation of motion, it provides a feasible way to characterize chemical reaction process without considering too detailed dynamics of molecules. [82] Apparent from the definition, IRC calculation requires to locate TS geometry beforehand. The computation of TS has been a challenging issue because no local criterion is known to locate TS. Indeed, a number of TS optimization methods have been proposed. [157] Double-ended

method, e.g., nudged elastic band (NEB) method [83], locates TSs and obtain the corresponding minimum energy path by an iterative relaxation of a trial pathway connecting a pair of potential minima. Double-ended method is very convenient when the geometries of reactant and product are known. Another class of TS optimization methods is single-ended method which does not require the geometries of the reactant and product. The most basic single-ended method is distinguished coordinate or coordinate driving method. [6, 15, 148, 154, 177] In coordinate driving methods, one coordinate is selected as the reaction coordinate with the remaining coordinates optimized at each point. The gradient extremals following (GEF) method locate TSs by following stationary points of gradient norm on iso-potential surface. [4, 5, 10, 71, 84, 133, 137, 149, 155, 161, 166] The reduced gradient following (RGF) method [70, 138, 141–143] and the Newton trajectories (NTs) [9, 69, 69, 139, 140] are related to the distinguished coordinate method. RGF and NTs, however, continuously trace the curve on which stationary (not necessarily minimum) condition of energy is satisfied, except for the selected direction. This procedure allows RGF and NTs to improve the problems [6, 15, 177] of the coordinate driving method. [143] Anharmonic downward distortion (ADDF) method [105, 130] is a constrained optimization method. In ADDF method, the normal coordinates are scaled by square root of their corresponding eigenvalues for a given equilibrium structure (EQ). ADDF basically steps in the radial direction of the hypersphere centered at the EQ and minimizes energy on the hypersphere; non-minimum points are additionally traced in practice. [105] Similar to the coordinate driving method, ADDF uses a predictor-corrector procedure, but it does not require selecting any direction beforehand because the step direction at every step is determined automatically as the radial direction of the hypersphere. ADDF method has been applied to many systems and a number of TSs have been located that are difficult to locate manually. [92, 104, 106, 108–110] Recently, ADDF method is also extended to the reaction path network calculation on a free energy surface. [118, 119]

In ADDF method, the concept of anharmonic downward distortion (ADD), defined as the difference between the harmonic potential around a minimum and the real PES, is utilized as a local criterion to locate TSs. Indeed, even a principle, named ADD principle, that "reaction channels can be found by following ADD maxima starting from an EQ structure on a PES" was suggested. [107] Nevertheless, there can be found only a few empirical discussion of the behavior of the ADDF path. [105, 130] This is in contrast to the cases of GEF [10, 137, 166] and RGF (or NTs) [70, 141], for which detailed mathematical analyses have been presented. At least, with the fundamental nature of ADD maxima even unclear, it is far from possible to verify the aforementioned ADD principle. While it seems reasonable to expect ADD to be maximum in the vicinity of TSs, the behavior elsewhere is hard to imagine. Accordingly, it is essential to analyze

the behavior of ADD stationary paths, the curve connecting stationary points of ADD on isosurfaces of the harmonic potential, to correctly understand the nature of ADD maxima around a potential minimum.

In this chapter, the geometrical feature of the ADD stationary path are analyzed. Firstly, ADDF method is briefly reviewed in Section 2.2.1. In Section 2.2.2, the maximum number of ADD stationary paths intersecting a potential minimum is discussed from a point of view of algebraic geometry. Subsequently, the bifurcation of ADD stationary paths is discussed in Section 2.2.3. Also, some representative examples of bifurcations of ADD stationary paths are demonstrated. In Section 2.2.4, ADD inflection paths, curves connecting ADD inflection points, are analyzed. Bifurcations of ADD stationary paths on *ab initio* potential energy surface of a H_2O molecule are discussed in Section 2.3. Finally, the possible effect of bifurcation of ADD stationary paths on reaction pathway search is discussed.

2.2 Theory

2.2.1 Anharmonic downward distortion following

The geometrical structure of a N^{nuc}-atomic molecule is specified with a $3N^{nuc}$-dimensional vector $\boldsymbol{X} \coloneqq (\boldsymbol{X}_1, \ldots, \boldsymbol{X}_{N^{nuc}})$ where $\boldsymbol{X}_I \quad (\in \mathbb{R}^3)$ denotes the I-th nuclear Cartesian coordinates. The mass-weighted coordinates are defined by $\boldsymbol{R}_I \coloneqq m_I^{1/2}\boldsymbol{X}_I \quad (I = 1, \ldots, N^{nuc})$ where m_I is the I-th nuclear mass. The differential operator in the mass-weighted operator is given by $\nabla_{\boldsymbol{R}} = \left(m_1^{-1/2}\partial/\partial\boldsymbol{X}_1, \ldots, m_I^{-1/2}\partial/\partial\boldsymbol{X}_{N^{nuc}}\right)$. Then, Hessian matrix of potential energy surface $V(\boldsymbol{R})$ is given by $\nabla_{\boldsymbol{R}}\nabla_{\boldsymbol{R}}V(\boldsymbol{R})$. The normalmode vectors $\{\boldsymbol{L}_I\}_{I=1,\ldots,f}$ are the orthonormal eigenvectors of the mass-weighted Hessian matrix with eigenvalues $\{k_I\}_{I=1,\ldots,f}$ whereas the translational and rotational modes are projected out before the diagonalization. The vibrational degrees of freedom f are given by $3N^{nuc} - 5$ and $3N^{nuc} - 6$ for linear molecules and non-linear molecules respectively.

The ADD function around the EQ, denoted by V_{ADD}, is defined as follows:

$$V_{\mathrm{ADD}}(\boldsymbol{Q}) \coloneqq \frac{1}{2}\sum_{I=1}^{f} k_I Q_I^2 - V(\boldsymbol{Q}), \tag{2.2.1}$$

where $\boldsymbol{Q} \coloneqq \sum_{I=1}^{f} Q_I \boldsymbol{L}_I$ are the normal coordinates and the potential energy at the EQ is set to be zero ($V(\boldsymbol{0}) = 0$). That is, V_{ADD} is the difference between the harmonic potential and real potential energy as shown in Fig. 2.1. For convenience, scaled normal

coordinates are introduced:

$$\bar{Q}_I \coloneqq k_I^{1/2} Q_I. \quad (I = 1, \ldots, f) \tag{2.2.2}$$

With the scaled normal coordinates, Eq. (2.2.1) is rewritten by

$$V_{\mathrm{ADD}}(\bar{\boldsymbol{Q}}) = \frac{\rho^2}{2} - V(\bar{\boldsymbol{Q}}), \tag{2.2.3}$$

where $\rho = \|\bar{\boldsymbol{Q}}\|$. In the following, a hypersphere of radius $\rho(> 0)$ centered at the EQ is denoted by $S^{f-1}(\rho)$. The local maxima of V_{ADD} on $S^{f-1}(\rho)$ are equivalent to the local minima of the real potential energy on $S^{f-1}(\rho)$.

Herein, the procedure of ADDF method is briefly reviewed.

STEP1 Index i is set to be 0. All the ADD maxima and *hidden* ADD maxima (explained later) on $S^{f-1}(\rho_i)$ are located. The j-th ADD maxima on $S^{f-1}(\rho_i)$ is denoted by $\bar{\boldsymbol{Q}}_j^{(i)}$.

STEP2 Index i is increased by one. $\bar{\boldsymbol{Q}}_j^{(i-1)}$ are projected onto a new hypersphere $S^{f-1}(\rho_i)$ where $\rho_i > \rho_{i-1}$. Local ADD maxima on $S^{f-1}(\rho_i)$, $\bar{\boldsymbol{Q}}_j^{(i)}$, are located started from the projected points.

STEP3 If the energy at $\bar{\boldsymbol{Q}}_j^{(i)}$ is higher than that at $\bar{\boldsymbol{Q}}_j^{(i-1)}$, return to STEP 2. Otherwise, go to STEP 4.

STEP4 TS geometry is located started from $\bar{\boldsymbol{Q}}_j^{(i-1)}$.

Following the above procedure, TS geometries are located. The initial radius ρ_0 is determined so that the displacement along the normal mode with the largest force constant becomes 0.03 Åwhereas the radius of the i-th hypersphere is given by $\rho_i = i\rho_1 (i \geq 1)$. ρ_1 is determined so that the displacement along the normal mode with the largest force constant becomes 0.1 Å. [109] In the ADDF method implemented in the GRRM14 program, [111] the search for the local minima on the initial hypersphere (in STEP 1) is carried out by the iterative optimization and elimination (IOE) method. [105] The IOE method on the initial hypersphere is as follows:

STEPA ADD maxima on the initial hypersphere $S^{f-1}(\rho_0)$ are located started from $2f$ intersections of $S^{f-1}(\rho_0)$ with the normal coordinate directions. The located maxima are denoted by $\bar{\boldsymbol{Q}}_1^{(0)}, \ldots, \bar{\boldsymbol{Q}}_m^{(0)}$.

STEPB The located ADD maxima are eliminated by adding shape functions [105] $G_1(\bar{\boldsymbol{Q}}_1^{(0)}), \ldots, G_m(\bar{\boldsymbol{Q}}_m^{(0)})$ to potential energy V. The potential energy after the elimination is denoted by $V_a \quad (a = m)$.

STEPC ADD maximum of V_a on $S^{f-1}(\rho^{(0)})$, referred as *hidden* ADD maximum, is located and the located maximum is denoted by $\bar{\boldsymbol{Q}}_{a+1}^{(0)}$.

STEPD The located *hidden* ADD maximum is eliminated by adding shape function $G_{a+1}(\bar{\boldsymbol{Q}}_{a+1}^{(0)})$ to V_a, and the potential energy after the elimination is denoted by V_{a+1}. Index a is increase by 1 and return to STEP C.

STEP C and STEP D are repeated until no new ADD maximum point with ADD larger than a given threshold is found anymore. IOE method attempts to detect directions in which new ADD maxima emerge at a distance from the potential minimum. [105] Except for the initial hypersphere, a computation of ADD maxima on a hypersphere is carried out by the predictor-corrector IOE (PC-IOE) method, [105] in which the ADD maxima on the last hypersphere are projected onto the current hypersphere, and then, STEP A is conducted started from the projected points. A computation of the ADD maximum point and elimination of the maximum are performed in a descending order of the magnitude of the ADD on the last hypersphere.

Hence, ADDF method follows not only the ADD maximum points but also some additional points. The paths followed by ADDF method, distinguished from ADD stationary path, are called ADDF paths in this chapter. The behavior of ADDF paths evidently depends on the form of the shape function used in IOE method. However, IOE method is to be considered as a heuristic algorithm designed to find TSs that cannot be found by only tracing ADD maxima of original potential. Considering that, in the first place, the behavior of ADD maxima of the original potential needs to be clarified before taking the heuristic into account. Actually, ADD stationary paths are more essential than ADDF paths to characterize the behavior of ADD maxima of the original PES. Therefore, the nature of ADD stationary paths are mainly discussed in the following part.

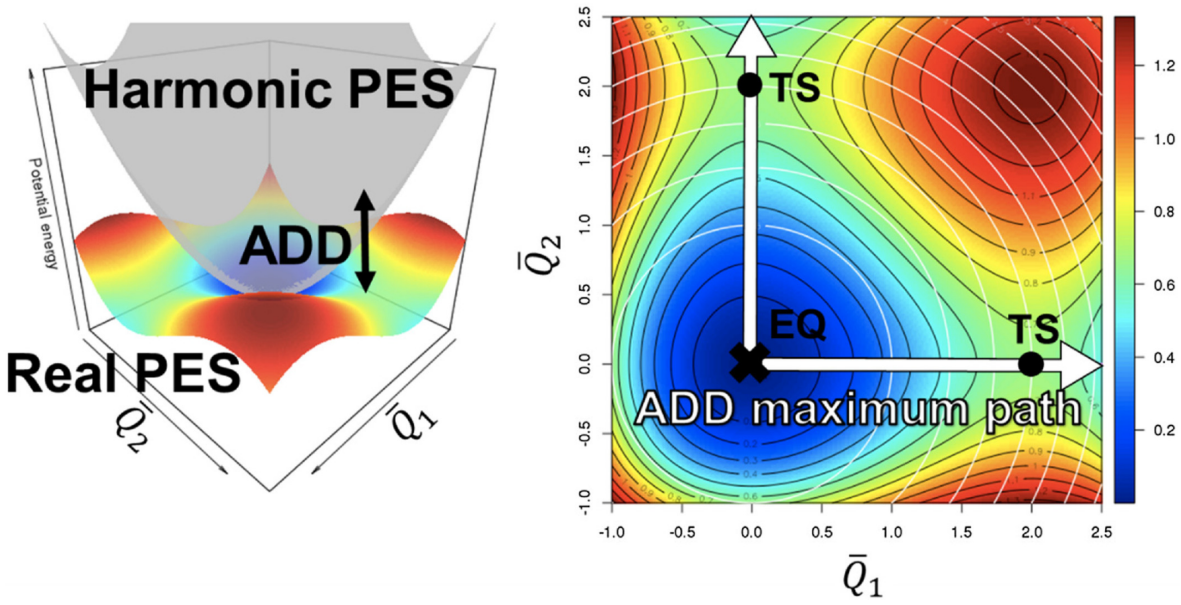

Fig. 2.1: Schematic of ADD and ADD maximum path. Left panel: Harmonic PES and real PES around the EQ are shown as the transparent surface and iridescent surface respectively. Right panel: Two-dimensional map of the real PES in the left panel. Black lines and white lines are contours of the real PES and the harmonic PES respectively. The ADD maximum path follows ADD maximum points or minimum energy points on the circles centered at the EQ, shown by white arrows from the EQ.

2.2.2 Maximum Number of ADD Stationary Paths Intersecting EQ

The ADD maximum path traces the ADD maximum point on $S^{f-1}(\rho)$ with expanding the radius of the hypersphere. The ADD maxima on $S^{f-1}(\rho)$ are located by the Lagrange multiplier method. The Lagrangian is given by

$$\mathcal{L}(\bar{\boldsymbol{Q}}, \mu) \coloneqq V_{\mathrm{ADD}} - \frac{\mu}{2}\left(\sum_{I=1}^{f} \bar{Q}_I^2 - \rho^2\right). \tag{2.2.4}$$

If $\bar{\boldsymbol{Q}}$ is a stationary point of V_{ADD} on $S^{f-1}(\rho)$, the following equations hold:

$$\begin{cases} \partial_I \mathcal{L}(\bar{\boldsymbol{Q}}, \mu) = & 0 \quad (I = 1, \ldots, f) \\ \frac{\partial}{\partial \mu}\mathcal{L}(\bar{\boldsymbol{Q}}, \mu) = & 0 \end{cases} \tag{2.2.5}$$

where $\partial_I \coloneqq \partial/\partial \bar{Q}_I$. The stationary points are classified into maximum, minimum, and saddle points based on the sign of the eigenvalues of Hessian matrix of potential energy on the hypersphere. The solutions of Eq. (2.2.5) are called the ADD stationary points in this chapter.

The behavior of ADD stationary paths in the vicinity of EQ is analyzed in order to clarify the law which determines the number of the ADD stationary paths that intersect the EQ. Since Eq. (2.2.5) are satisfied everywhere along the ADD stationary paths, the derivatives of the left-hand sides of Eq. (2.2.5) are also zero along the ADD stationary paths. In general, the following equations are satisfied along the ADD stationary paths:

$$\begin{cases} d^r \partial_I \mathcal{L}(\bar{\boldsymbol{Q}}, \mu) & = 0 \quad (I = 1, \ldots, f) \\ d^r \frac{\partial}{\partial \mu}\mathcal{L}(\bar{\boldsymbol{Q}}, \mu) & = 0 \end{cases}. \tag{2.2.6}$$

where r is a given non-negative integer. Eq. (2.2.6) can be also regarded as the r-th order perturbation equation, with the radius of hypersphere being the perturbation parameter. When $r = 1$, Eq. (2.2.6) is written as follows:

$$\begin{cases} \sum_{J=1}^{f} \partial_I \partial_J V_{\mathrm{ADD}}(\bar{\boldsymbol{Q}}) d\bar{Q}_J - \bar{Q}_I d\mu - \mu d\bar{Q}_I & = 0 \quad (I = 1, \ldots, f) \\ \sum_{I=1}^{f} \bar{Q}_I d\bar{Q}_I - \rho d\rho & = 0 \end{cases} \tag{2.2.7}$$

At the EQ, the latter of Eq. (2.2.7) is obvious. Since V_{ADD} does not include monomials of $\bar{\boldsymbol{Q}}$ with a total degree lower than 3 (see Eq. (2.2.1)),

$$\partial_I \partial_J V_{\mathrm{ADD}}(\boldsymbol{0}) = 0. \tag{2.2.8}$$

Thus, the following is satisfied:

$$\mu = 0. \tag{2.2.9}$$

If V_{ADD} included quadratic term, Eq. (2.2.7) gives a linear eigenvalue equation. However, there is no quadratic term in V_{ADD} and the problem becomes nonlinear as shown below. When $r = 2$, Eq. (2.2.6) is written as follows:

$$\begin{cases} \sum_{J,K=1}^{f} \partial_I \partial_J \partial_K V_{\mathrm{ADD}}(\bar{\boldsymbol{Q}}) d\bar{Q}_J d\bar{Q}_K - 2d\bar{Q}_I d\mu \\ + \sum_{J=1}^{f} \partial_I \partial_J V_{\mathrm{ADD}}(\bar{\boldsymbol{Q}}) d^2\bar{Q}_J - \bar{Q}_I d^2\mu - \mu d^2\bar{Q}_I = 0 \quad (I = 1, \ldots, f)\,. \\ \sum_{I=1}^{f} d\bar{Q}_I d\bar{Q}_I - (d\rho)^2 + \sum_{I=1}^{f} \bar{Q}_I d^2\bar{Q}_I - \rho d^2\rho = 0 \end{cases} \tag{2.2.10}$$

Using Eq. (2.2.8), Eq. (2.2.9) and the relation

$$\partial_I \partial_J \partial_K V_{\mathrm{ADD}}(\bar{\boldsymbol{Q}}) = -\partial_I \partial_J \partial_K V(\bar{\boldsymbol{Q}}), \tag{2.2.11}$$

Eq. (2.2.10) can be rewritten as follows:

$$\begin{cases} \sum_{J,K=1}^{f} \partial_I \partial_J \partial_K V_{\mathrm{ADD}}(\bar{\boldsymbol{Q}}) d\bar{Q}_J d\bar{Q}_K - 2d\bar{Q}_I d\mu = 0 \quad (I = 1, \ldots, f) \\ \sum_{I=1}^{f} d\bar{Q}_I d\bar{Q}_I - (d\rho)^2 = 0 \end{cases}. \tag{2.2.12}$$

Eq. (2.2.12) can be regarded as $f + 1$ homogeneous polynomial equations with variables $d\bar{Q}_1, \ldots, d\bar{Q}_f, d\mu$ and $d\rho$. Thus, the ratio of these variables is obtained by solving Eq. (2.2.12). ($cd\bar{Q}_1$,...,$cd\bar{Q}_f$,$cd\mu$,$cd\rho$) is identified with ($d\bar{Q}_1$,...,$d\bar{Q}_f$,$d\mu$,$d\rho$) for arbitrary nonzero complex value c and the ratio is regarded as the root of Eq. (2.2.12) because the absolute values of these infinitesimal variables are rather trivial. The independent real roots of Eq. (2.2.12) correspond to the directions of the ADD stationary paths intersecting the EQ. Hence, the problem to determine the number of the ADD stationary paths intersecting the EQ is reduced to the problem to determine the number of stationary points of the third-order Taylor polynomial of the ADD function around the EQ (denoted as $V_{\mathrm{ADD}}^{(3)}$) below) on a hypersphere with any radius other than zero. The three-dimensional version of this problem was solved by Kuznetsov and Kholshevnikov. [97] Ni, Qi, Wang, and Wang solved the problem in the case of an even degree. [126] Cartwright and Sturmfels generalized the result to the case of an odd degree. [17] According to the work of Cartwright and Sturmfels, the maximum number of stationary points of homogeneous polynomial of n variables with a degree of $m(\geq 3)$ on a hypersphere centered at the origin is given by $2\{(m-1)^n - 1\}/(m-2)$ when the number of the stationary point is finite. Thus, the possible maximum number of the ADD stationary paths intersecting the EQ or the maximum number of real roots of

Eq. (2.2.12) is given by

$$2^{f+1} - 2, \tag{2.2.13}$$

It should be remarked that this number is larger than the number of the gradient extremal paths, i.e., $2f$, except for the trivial case of $f = 1$. [10]

2.2.3 Bifurcation of ADD stationary paths

In the following part, Einstein notation is used unless otherwise noted. Greek indices, $\lambda, \mu, \nu, \ldots$, are used for the tangent space of $S^{f-1}(\rho)$, and uppercase Roman, $I, J, K, \ldots$, are used for the full f-dimensional space. Let $\{\boldsymbol{e}_\mu(\bar{\boldsymbol{Q}})\}_{\mu=1,\ldots,f-1}$ be the orthonormal tangent vectors of $S^{f-1}(\rho)$ at $\bar{\boldsymbol{Q}}$. The outward unit normal vector at $\bar{\boldsymbol{Q}}$ is given by

$$\boldsymbol{e}_f(\bar{\boldsymbol{Q}}) = \frac{\bar{\boldsymbol{Q}}}{|\bar{\boldsymbol{Q}}|} \tag{2.2.14}$$

The f-th basis is always assumed to be perpendicular to $S^{f-1}(\rho)$ throughout this subsection. The orthonormal tangent vectors and unit normal vector are regarded as vector functions of $\bar{\boldsymbol{Q}} \in S^{f-1}(\rho)$. The derivatives of the orthonormal tangent vectors are given by

$$\partial_\mu \boldsymbol{e}_\nu = \Gamma^\lambda_{\mu\nu} \boldsymbol{e}_\lambda + \Omega_{\mu\nu} \boldsymbol{e}_f, \tag{2.2.15}$$

where $\Gamma^\lambda_{\mu\nu}$ and $\Omega_{\mu\nu}$ are the Cristoffel symbols and Euler-Schouten curvature tensor, respectively. According to Riemannian geometry, the Cristoffel symbols vanish by choosing $\{\boldsymbol{e}_\mu(\bar{\boldsymbol{Q}})\}_{\mu=1,\ldots,f-1}$ as the basis of a geodesic coordinate system at $\bar{\boldsymbol{Q}}$: [176]

$$\Gamma^\lambda_{\mu\nu} = 0. \tag{2.2.16}$$

The Euler-Schouten curvature tensor of the hypersphere is given by

$$\begin{aligned}
\Omega_{\mu\nu} &= \langle \boldsymbol{e}_f, \partial_\mu \boldsymbol{e}_\nu \rangle \\
&= -\langle \partial_\mu \boldsymbol{e}_f, \boldsymbol{e}_\nu \rangle \quad (\because \partial_\mu \langle \boldsymbol{e}_f, \boldsymbol{e}_\nu \rangle = 0) \\
&= -\left\langle \partial_\mu (\bar{\boldsymbol{Q}}/|\bar{\boldsymbol{Q}}|), \boldsymbol{e}_\nu \right\rangle \quad (\because \text{Eq. (2.2.14)}) \\
&= -\left\langle \boldsymbol{e}_\mu/|\bar{\boldsymbol{Q}}| - (\bar{Q}_\mu/|\bar{\boldsymbol{Q}}|^2)\boldsymbol{e}_f, \boldsymbol{e}_\nu \right\rangle \\
&= -\rho^{-1}\delta_{\mu\nu}. \quad (\because \langle \boldsymbol{e}_f, \boldsymbol{e}_\nu \rangle = 0)
\end{aligned} \tag{2.2.17}$$

Then, the Hessian matrix of V_{ADD} on $S^{f-1}(\rho)$ is given by

$$\partial_\mu \partial_\nu V_{\mathrm{ADD}} - \frac{\delta_{\mu\nu}}{\rho} \partial_f V_{\mathrm{ADD}}. \tag{2.2.18}$$

The first term is the Hessian matrix of V_{ADD} on the hyperplane tangent to $S^{f-1}(\rho)$. The second term originates from the curvature of $S^{f-1}(\rho)$. Thus, the Hessian matrix of the ADD function on $S^{f-1}(\rho)$ is not equivalent to that on the hyperplane normal to the ADD stationary path.

In the following part, the necessary conditions for the ADD stationary path to bifurcate is discussed. It will be shown that bifurcation of the ADD stationary path take places where its tangent vector is either tangent to the hypersphere or is not unique. Let $\bar{\boldsymbol{Q}}$ be an ADD stationary point so that $\partial_\mu V_{\mathrm{ADD}} = 0 \ \ (\mu = 1, \ldots, f-1)$ at $\bar{\boldsymbol{Q}}$. Since these stationary conditions are satisfied at every point on the ADD stationary path, the directional derivatives of $\partial_\mu V_{\mathrm{ADD}}$ along the ADD stationary path are also zero. The first-order directional derivative along the ADD stationary path is given by

$$d\partial_\mu V_{\mathrm{ADD}} = d\bar{Q}^\nu \left(\partial_\nu \partial_\mu - \rho^{-1}\delta_{\nu\mu}\partial_f\right) V_{\mathrm{ADD}} + d\bar{Q}^f \partial_f \partial_\mu V_{\mathrm{ADD}} = 0. \tag{2.2.19}$$

For convenience, $H_{\mu\nu}$, b_μ and $A_{\mu\nu}$ are introduced as follows:

$$H_{\mu\nu} \coloneqq \partial_\nu \partial_\mu V_{\mathrm{ADD}} - \rho^{-1}\delta_{\nu\mu}\partial_f V_{\mathrm{ADD}}, \quad (\mu, \nu = 1, \ldots, f-1) \tag{2.2.20}$$

$$b_\mu \coloneqq \partial_f \partial_\mu V_{\mathrm{ADD}}, \quad (\mu = 1, \ldots, f-1) \tag{2.2.21}$$

$$A_{\mu\nu} = \begin{cases} H_{\mu\nu} & (\nu = 1, \ldots, f-1) \\ b_\mu & (\nu = f) \end{cases}. \quad (\mu = 1, \ldots, f-1) \tag{2.2.22}$$

Then, Eq. (2.2.19) can be rewritten by

$$\mathbf{A} d\bar{\boldsymbol{Q}} = \mathbf{0} \Leftrightarrow H_{\mu\nu} d\bar{Q}^\nu + d\bar{Q}^f b_\mu = 0 \quad (\mu = 1, \ldots, f-1) \tag{2.2.23}$$

By choosing the orthonormalized eigenvectors of $H_{\mu\nu}$, $\{\boldsymbol{l}_1(\bar{\boldsymbol{Q}}), \ldots, \boldsymbol{l}_{f-1}(\bar{\boldsymbol{Q}})\}$, as the basis, Eqs. (2.2.20) and (2.2.22) can be rewritten by

$$H_{\mu\nu} = h_\mu \delta_{\mu\nu}, \quad (\mu, \nu = 1, \ldots, f-1) \tag{2.2.24}$$

$$A_{\mu\nu} = \begin{cases} h_\mu \delta_{\mu\nu} & (\nu = 1, \ldots, f-1) \\ b_\mu & (\nu = f) \end{cases}, \quad (\mu = 1, \ldots, f-1) \tag{2.2.25}$$

and Eq. (2.2.23) is simplified as follows:

$$h_\mu \delta_{\mu\nu} d\bar{Q}^\nu = -b_\mu d\bar{Q}^f. \quad (\mu = 1, \ldots, f-1) \tag{2.2.26}$$

Eq. (2.2.26) is a set of $f-1$ linear equations with f variables, $d\bar{Q}^1, \ldots, d\bar{Q}^{f-1}, d\bar{Q}^f$. The non-trivial solution of Eq. (2.2.26) corresponds to the tangent vector of the ADD

stationary path. The solution of Eq. (2.2.26) is classified into four cases in terms of bifurcation. In the first case, the solution of Eq. (2.2.26) is unique and there is no bifurcation. In the second case, the solution is unique and the tangent vector of the ADD stationary path is also tangent to the hypersphere. There is a possibility of bifurcation in this case despite the uniqueness of the solution. In the third case, there are some solutions. If there are more than one real solution, ADD stationary paths intersect at the ADD stationary point. In the fourth case, there are some solutions and all the tangent vector of the ADD stationary paths are also tangent to the hypersphere. These four cases are discussed in detail in the followings.

(CASE1) No bifurcation: $h_\mu \neq 0 \ \ (\mu = 1, \ldots, f-1)$.

In this case, the solution of Eq. (2.2.26) is unique:

$$\begin{cases} d\bar{Q}^\mu & = -c\frac{b_\mu}{h_\mu} \quad (\mu = 1, \ldots, f-1) \\ d\bar{Q}^f & = c \end{cases} \tag{2.2.27}$$

where c is an arbitrary constant. Hence, there is only one ADD stationary path crossing the point $\bar{\boldsymbol{Q}}$.

(CASE2) Bifurcations without crossing of paths: $h_1 = 0, \quad h_\mu \neq 0 \quad (\mu = 2, \ldots, f-1)$ and $b_1 \neq 0$.

In this case, the solution of Eq. (2.2.26) is unique:

$$\begin{cases} d\bar{Q}^\mu & = c\delta_1^\mu \quad (\mu = 1, \ldots, f-1) \\ d\bar{Q}^f & = 0 \end{cases} \tag{2.2.28}$$

where c is an arbitray constant. Although the solution is determined uniquely, there is a possibility of bifurcation in this case. The tangent vector of the ADD stationary path at $\bar{\boldsymbol{Q}}$ given by Eq. (2.2.28), $d\bar{\boldsymbol{Q}}$, is also tangent to the hypersphere $S^{f-1}(\rho)$. If $d^k\bar{Q}^f = 0 \ \ (1 \leq k < 2l)$ and $d^{2l}\bar{Q}^f \neq 0$ for some positive integer l, the ADD stationary path does not intersect $S^{f-1}(\rho)$, i.e., the ADD stationary path is not transverse to $S^{f-1}(\rho)$. In this case, along the radial direction, a pair of ADD stationary paths emerge or disappear at $\bar{\boldsymbol{Q}}$. Saddle-node bifurcation [165] is one such bifurcation (see Fig. 2.5). It should be remarked that there is no ADD stationary path connecting the saddle-node bifurcation point and the EQ (the origin). Therefore, if only ADD stationary paths intersecting the EQ are followed, the TS located at $(x, y) = (-3.035, -10.776)$ will be overlooked. Saddle-node bifurcation in gradient extremals, which is also unfavorable for reaction path search, was reported. [122, 156]

(CASE3) Crossing point of paths: $h_\mu, b_\mu \neq 0, \ \ (\mu = 1, \ldots, r)$ and $h_\mu, b_\mu = 0 \ \ (\mu = r+1, \ldots, f-1)$.

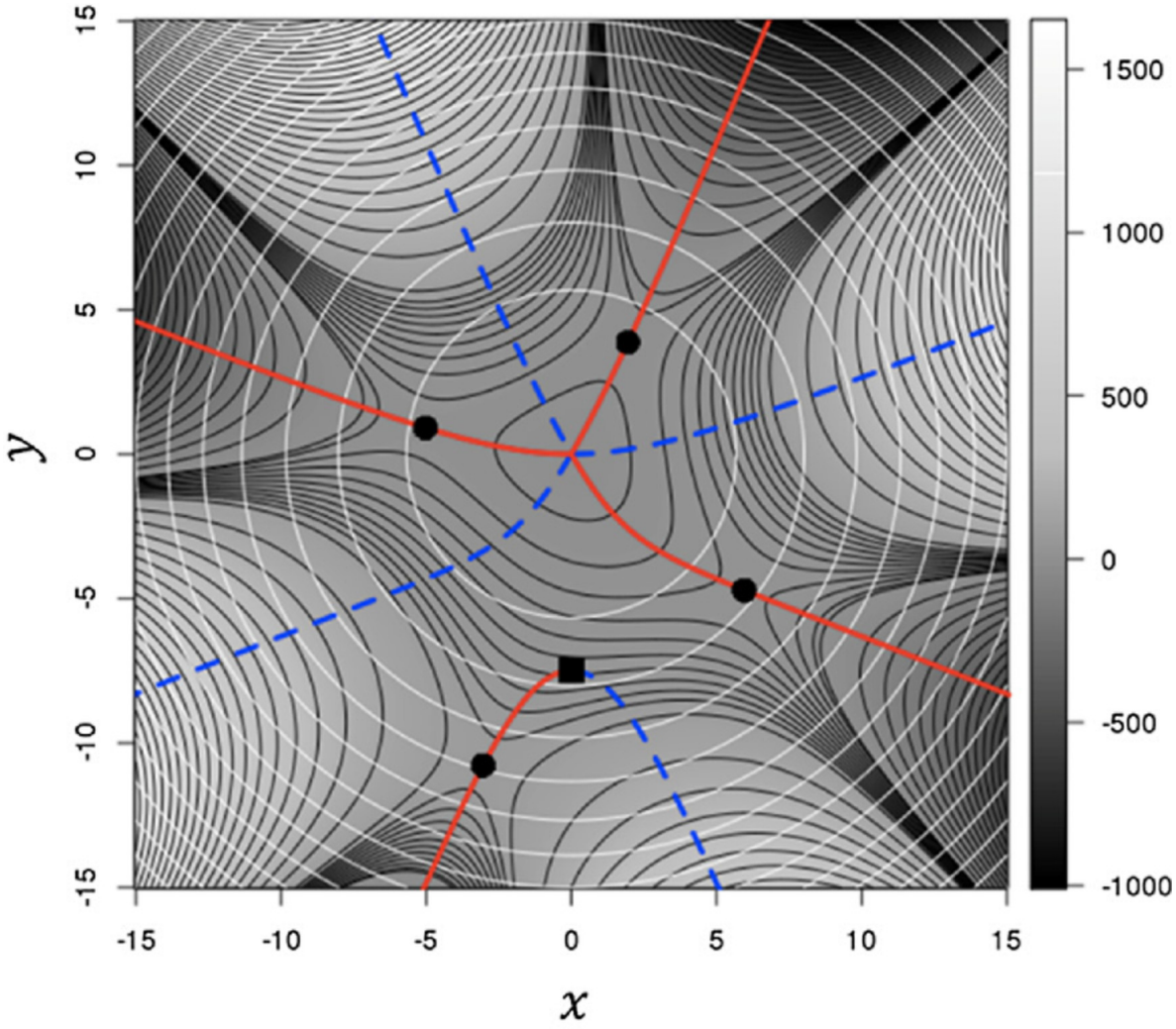

Fig. 2.2: Saddle-node bifurcation: Model potential is given by $f(x, y) = x^2 + y^2 + 0.1(x^3 - 3xy^2) + 0.04(x^3y - xy^3)$. The origin is the minimum (EQ). The black solid curves and white circles represent the contours of $f(x, y)$ and those of the harmonic potential. TSs are shown by black circles, located at $(x, y) = (5.960, -4.715), (1.951, 3.870), (-3.035, -10.776), (-5.022, 0.911)$. The ADD maximum and minimum paths are shown by red and blue dashed curves, respectively. A pair of ADD stationary paths emerge at the saddle-node bifurcation point, shown by a black square located at $(x, y) = (0, -7.5)$.

In this case, there are fewer equations than unknowns. Hence, higher-order derivatives need to be considered in order to determine the tangent vectors of ADD stationary paths. Provided $\mathrm{rank}(\mathbf{A}) = r(< f-1)$, Eq. (2.2.24) can be rewritten as follows by applying Gaussian elimination:

$$\begin{bmatrix} \mathbf{D}_r \\ \mathbf{O}_{f-1-r} \end{bmatrix} d\bar{\boldsymbol{Q}} = \mathbf{0}, \tag{2.2.29}$$

where $\mathbf{D}_r$ is a $r \times f$ matrix with $\mathrm{rank}(\mathbf{D}_r) = r$. $\mathbf{O}_{f-1-r}$ is the $(f-1-r) \times f$ zero matrix. The general solution of Eq. (2.2.29) is given by

$$d\bar{\boldsymbol{Q}} = \sum_{\mu=1}^{f-r} c^\mu \boldsymbol{v}_\mu, \tag{2.2.30}$$

where $\boldsymbol{v}_\mu$ $(\mu = 1, \ldots, f-r)$ are orthonormal vectors that satisfy $\mathbf{D}_r \boldsymbol{v}_\mu = \mathbf{0}$. c^μ $(\mu = 1, \ldots, f-r)$ are the coefficients. The second-order derivative of Eq. (2.2.19), i.e., the first-order derivative of Eq. (2.2.26), is given by

$$d(\mathbf{A} d\bar{\boldsymbol{Q}}) = \mathbf{A} d^2\bar{\boldsymbol{Q}} + d\bar{Q}^I \partial_I \mathbf{A} d\bar{\boldsymbol{Q}} = \mathbf{0}. \tag{2.2.31}$$

By Gaussian elimination of $\mathbf{A}$ in Eq. (2.2.31), Eq. (2.2.31) can be rewritten by

$$\begin{bmatrix} \mathbf{D}_r \\ \mathbf{O}_{f-1-r} \end{bmatrix} d^2\bar{\boldsymbol{Q}} + \begin{bmatrix} \mathbf{E}_r(d\bar{\boldsymbol{Q}}) \\ \mathbf{F}_{f-1-r}(d\bar{\boldsymbol{Q}}) \end{bmatrix} d\bar{\boldsymbol{Q}} = \mathbf{0}, \tag{2.2.32}$$

where $\boldsymbol{e}_r(d\bar{\boldsymbol{Q}})$ and $\mathbf{F}_{f-1-r}(d\bar{\boldsymbol{Q}})$ are $r \times f$ matrix and $(f-1-r) \times f$ matrix, the elements of which are linear in $d\bar{\boldsymbol{Q}}$. The tangent vector $d\bar{\boldsymbol{Q}}$ might be determined by

$$\begin{bmatrix} \mathbf{D}_r \\ \mathbf{F}_{f-1-r}(d\bar{\boldsymbol{Q}}) \end{bmatrix} d\bar{\boldsymbol{Q}} = \mathbf{0}. \tag{2.2.33}$$

However, it should be remarked that there can be a case in which even higher-order derivatives of Eq. (2.2.26) are required to determine the tangent vector $d\bar{\boldsymbol{Q}}$. Since Eq. (2.2.33) are nonlinear equations, there can be more than a single solution. Each real solution corresponds to a tangent vector of the ADD stationary path crossing $\bar{\boldsymbol{Q}}$. Thus, when there are multiple real solutions, $\bar{\boldsymbol{Q}}$ is a bifurcation point and some ADD stationary paths intersect at the point. Pitchfork bifurcation is an example of such bifurcation (see Fig. 2.3). Pitchfork bifurcation points can be found by following the ADD saddle paths crossing the EQ. The ADD maximum path generated by pitchfork bifurcation might be overlooked if only ADD maximum paths are traced from the EQ.

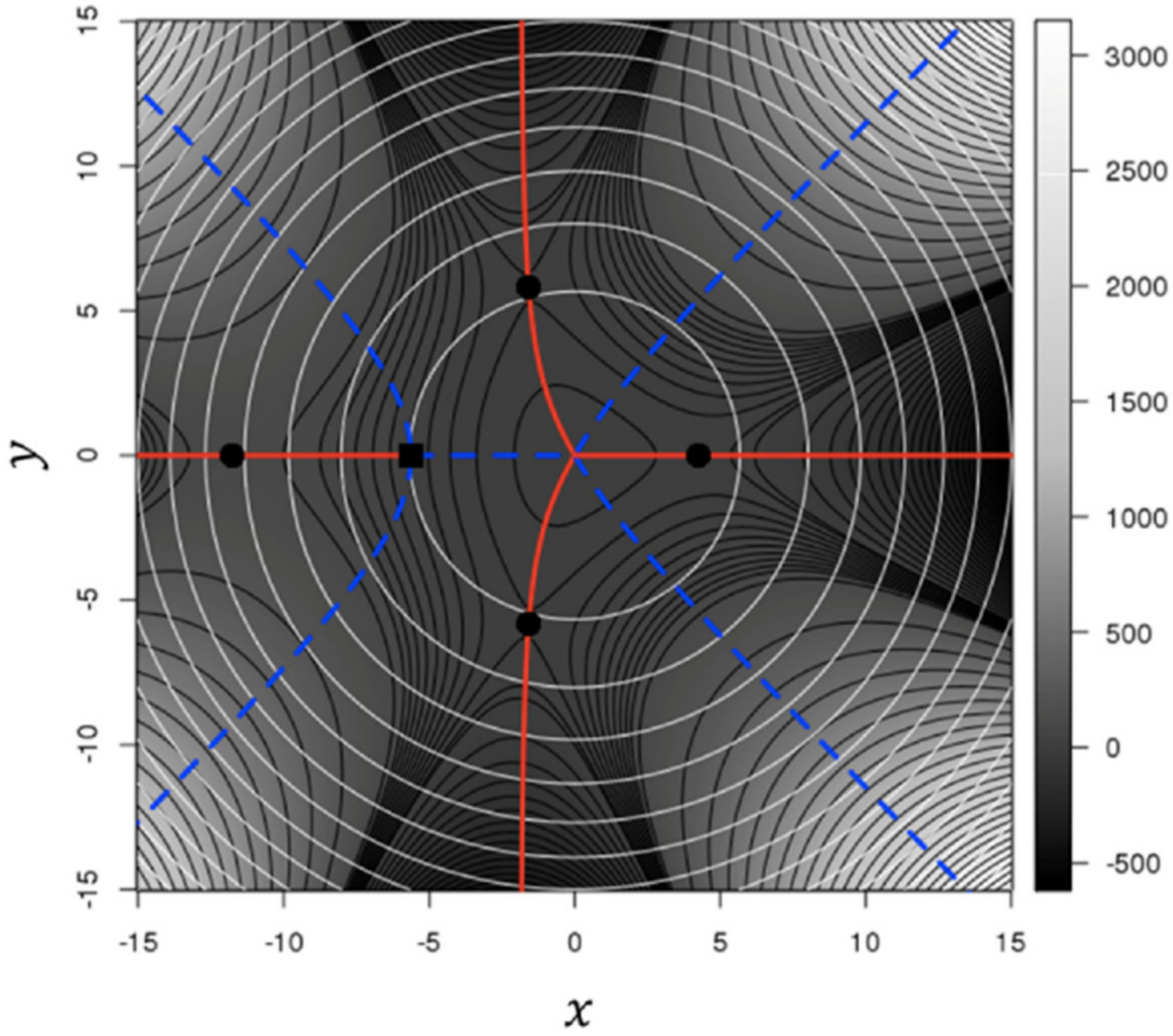

Fig. 2.3: Pitchfork bifurcation: Model potentials are given by $f(x, y) = x^2 + y^2 - 0.1(x^3 - 3xy^2) - 0.01(x^4 - 6x^2y^2 + y^4)$. The origin is the minimum (EQ). The black curves represent the contours of $f(x, y)$. TSs are shown by black circles, located at $(x, y) = (4.254, 0), (-1.577, \pm 5.814), (-11.754, 0)$. At the pitchfork bifurcation point, shown by a black square located at $(x, y) = (-5.625, 0)$, the ADD maximum path bifurcates, resulting in one minimum path and two maximum paths.

(CASE 4) Crossing of paths tangent to the hypersphere: $\mathrm{rank}(\mathbf{H}) < \mathrm{rank}(\mathbf{A})$, $\mathrm{rank}(\mathbf{H}) \leq f-3$.
In this case, $d\bar{Q}^f = 0$ and some ADD stationary paths intersect at $\bar{\boldsymbol{Q}}$.

Eventually, the necessary condition for $\bar{\boldsymbol{Q}}$ to be a bifurcation point of the ADD stationary path is given by

$$\det \mathbf{H} = 0. \tag{2.2.34}$$

Otherwise, the tangent vector is uniquely determined (see Eq. (2.2.28)). This condition shows the singularity of the Hessian matrix defined by Eq. (2.2.20). It is obvious that CASE 2-CASE 4 satisfy Eq. (2.2.34).

It should be referred that bifurcation of ADD stationary paths and that of gradient extremals are essentially the same phenomenon. The gradient extremals are the curves connecting the stationary points of the gradient norm on the potential energy isosurfaces. Similarly, the ADD stationary paths are the curves connecting the stationary points of ADD on the harmonic potential isosurfaces. As shown above, bifurcation of the ADD stationary path occurs only at the non-regular point of the Hessian matrix of the ADD function on the harmonic potential isosurfaces. In fact, the bifurcation of the gradient extremals takes place at the non-regular point of the Hessian matrix of the gradient norm on the potential energy isosurfaces. [10, 137]

2.2.4 ADD Inflection Paths

Considering that ADD stationary paths bifurcate at the non-regular point of the Hessian matrix on hyperspheres, some of bifurcation points may be found by tracing the ADD inflection points. In this section, it is confirmed that the saddle-node bifurcation point shown in Fig. 2.2 can be located by following ADD inflection paths, that are the curves connecting the ADD inflection points.

Firstly, ADD inflection path is introduced. Let $\bar{\boldsymbol{Q}}$ be an ADD non-stationary inflection point on a hypersphere. Then, there exists at least one zero eigenvalue of the Hessian matrix of ADD on the hypersphere:

$$\mathbf{H}(\bar{\boldsymbol{Q}})\boldsymbol{l}_1 = \mathbf{0}. \tag{2.2.35}$$

Also, the ADD gradient on the hypersphere is parallel to the eigenmode with zero eigenvalue:

$$\sum_{\mu=1}^{f-1} (\boldsymbol{l}_\mu \otimes \boldsymbol{l}_\mu) \frac{\partial V_{\mathrm{ADD}}}{\partial \bar{\boldsymbol{Q}}}(\bar{\boldsymbol{Q}}) = \left\langle \boldsymbol{l}_1, \partial V_{\mathrm{ADD}}/\partial \bar{\boldsymbol{Q}} \right\rangle \boldsymbol{l}_1. \tag{2.2.36}$$

If $\bar{\boldsymbol{Q}}$ is an ADD stationary inflection point, Eq. (2.2.36) becomes obvious because $\left\langle \boldsymbol{l}_\mu, \partial V_{\mathrm{ADD}}/\partial \bar{\boldsymbol{Q}} \right\rangle = 0$ $(\mu = 1, \ldots, f-1)$ are satisfied. ADD inflection paths are defined

as the curves on which Eq. (2.2.35) and Eq. (2.2.36) are satisfied. Fig. 2.4 shows the ADD inflection paths of the potential shown in Fig. 2.2. If the ADD inflection path given by $x = 0$ is traced from the EQ, the ADD maximum path appearing at the saddle-node bifurcation point can be found. Although it seems to be not feasible to trace all the ADD inflection paths, ADD inflection points on a hypersphere can be located as the stationary points of ADD gradient norm on the hypersphere. Similar to the discussion of the maximum number of ADD stationary paths, the maximum number of ADD inflection paths and ADD stationary paths crossing the EQ is given by $(5^f - 1)/2$. This can be confirmed as follows. The squared norm of ADD gradient on a hypersphere is given by $g^2 = \left\langle \partial V_{\mathrm{ADD}}/\partial \bar{\boldsymbol{Q}}, \mathbf{P}\partial V_{\mathrm{ADD}}/\partial \bar{\boldsymbol{Q}} \right\rangle$, where $\mathbf{P} = \mathbf{1} - \bar{\boldsymbol{Q}} \otimes \bar{\boldsymbol{Q}} / \left\langle \bar{\boldsymbol{Q}}, \bar{\boldsymbol{Q}} \right\rangle$. Considering that $\left\langle \bar{\boldsymbol{Q}}, \bar{\boldsymbol{Q}} \right\rangle$ is constant on the hypersphere, the stationary point of g^2 is identical to that of $\left\langle \bar{\boldsymbol{Q}}, \bar{\boldsymbol{Q}} \right\rangle g^2$. The lowest degree of the Taylor series of $\left\langle \bar{\boldsymbol{Q}}, \bar{\boldsymbol{Q}} \right\rangle g^2$ is six. Using the theorem shown by Sturmfels and Cartwright, the maximum number of stationary points of homogeneous polynomial of n variables with a degree of $m(\geq 3)$ on a hypersphere centered at the origin is given by $2\{(m-1)^n - 1\}/((m-2)$ provided that the number of stationary points is finite. [17] Thus, the maximum number of ADD inflection paths and stationary paths shown above is obtained.

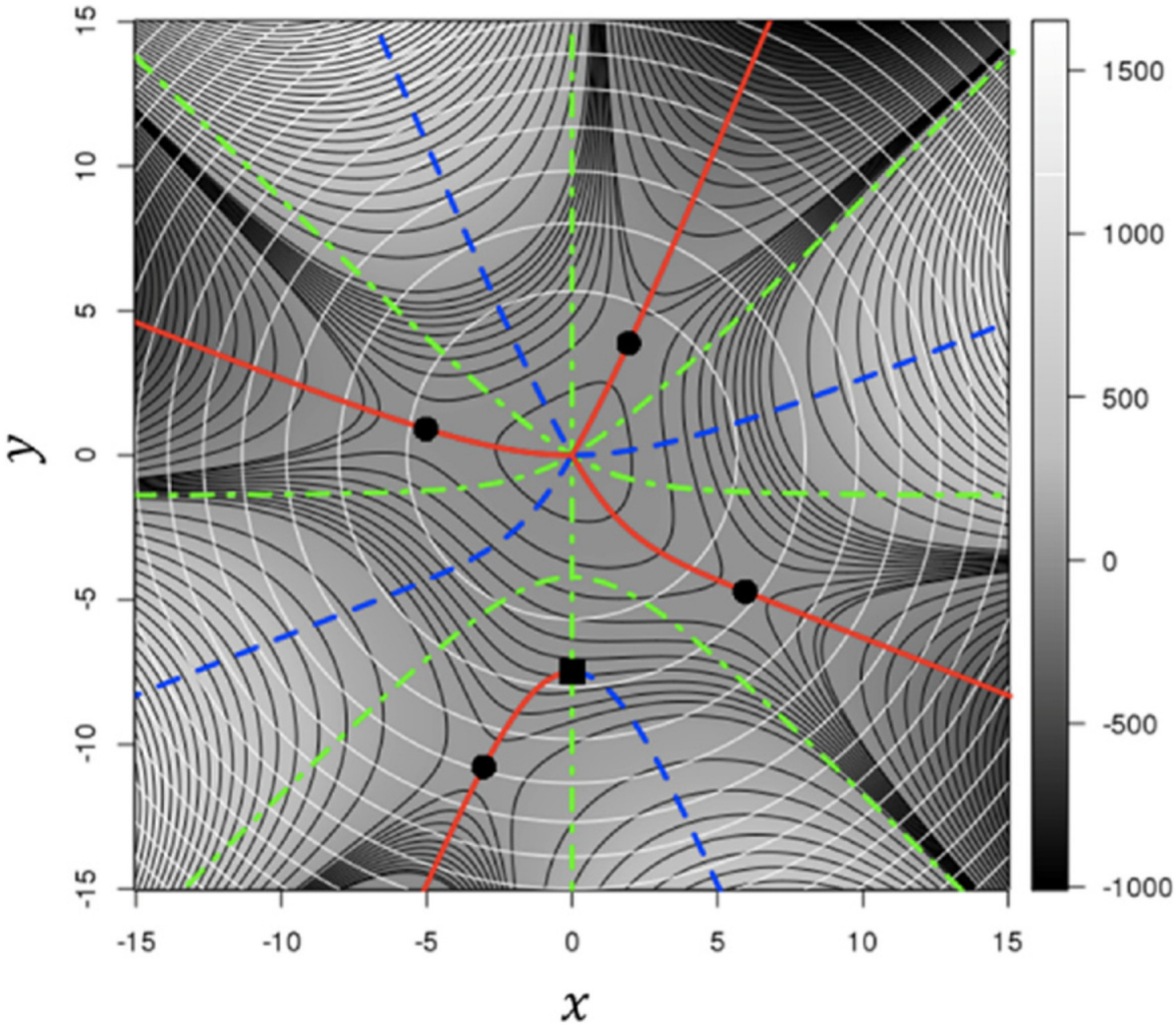

Fig. 2.4: ADD inflection paths (green dot-dash curves) determined on the model potential (the same as in Fig. 2.2). The saddle-node bifurcation point and the origin (EQ) are connected by the ADD inflection path given by $x = 0$.

2.3 Numerical results

In this section, the maximum number of ADD stationary paths crossing an EQ and bifurcation of ADD stationary paths are analyzed on the *ab initio* PES of a H_2O molecule.

As aformentioned, the maximum number of ADD stationary paths crossing an EQ is determined by only the third-order Taylor polynomial of the PES provided that the number of stationary points is finite. However, the PES was approximated by fourth-order Taylor polynomial because the higher-order terms are necessary to describe bifurcation at a distance from the EQ. The electronic structure calculation at the EQ was carried out by the spin-restricted Hartree-Fock (RHF) method with a 6-31G(d,p) basis set using Gaussian09. [42] The second-, third-, and fourth-order derivatives were computed using an option of anharmonic frequency calculations that are also implemented in Gaussian09. In order to ensure that all the ADD stationary paths crossing the EQ to be obtained, An algebraic geometric method that is a partial modification of Auzinger ' s algorithm [2] was adopted to compute common roots of multivariate polynomials of Eq. (2.2.12). It must be emphasized that this algebraic geometric approach is able to ensure all the common roots of given multivariate polynomials to be obtained provided that the number of roots is finite whereas other iterative optimization methods are not. This is the reason to adopt the algebraic geometric method.

By using the scaled normal coordinates defined by Eq. (2.2.2), an isosurface of the harmonic potential becomes the sphere centered at the EQ. Fig. 2.5 shows the ADD contour of the H_2O molecule on a sphere of radius 0.3 hartree$^{1/2}$ viewed from six directions where red indicates a large ADD or low-potential-energy region and blue indicates a small ADD or high-potential-energy region. There are 14 ADD stationary points, comprising four maxima (Max1-Max4), six saddle points (S1-S6) and four minima (Min1-Min4)). This number 14 is equal to the upper limit calculated with using Eq. (2.2.13).

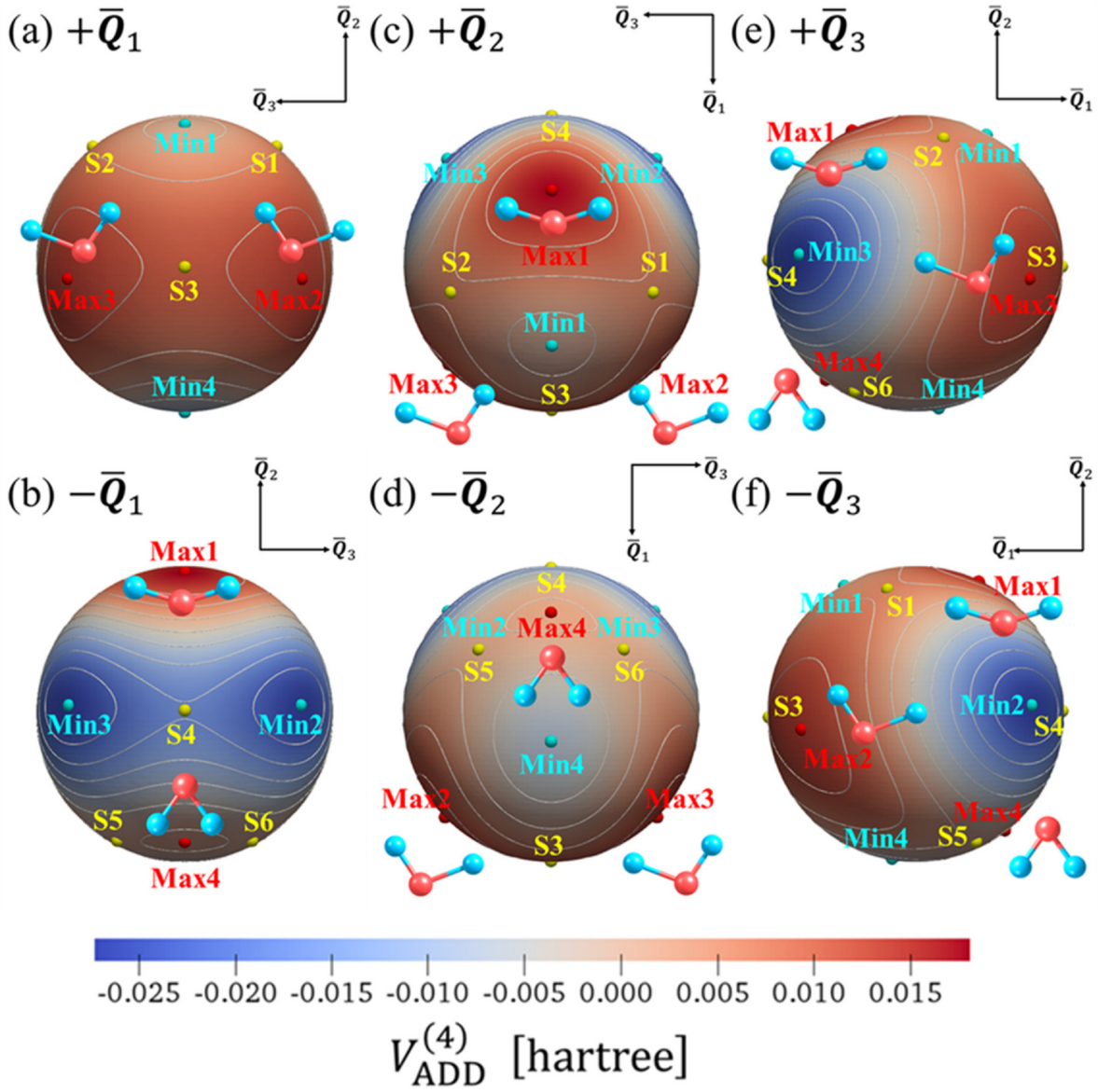

Fig. 2.5: ADD contour of the H_2O molecule on a sphere of radius 0.3 hartree$^{1/2}$ centered at the EQ. Each panel shows a view from the direction of (a) $+\bar{Q}_1$, (b) $-\bar{Q}_1$, (c) $+\bar{Q}_2$, (d) $-\bar{Q}_2$, (e) $+\bar{Q}_3$, and (f) $-\bar{Q}_3$, where $\bar{Q}_1$, $\bar{Q}_2$, and $\bar{Q}_3$ are scaled normal coordinates for OH symmetric stretching (A1), H-O-H bending (A1), and OH antisymmetric stretching (B2) vibrational modes, respectively. The ADD function is approximated by the fourth-order Taylor polynomial (denoted as $V_{\mathrm{ADD}}^{(4)}$), where white lines are the contours of $V_{\mathrm{ADD}}^{(4)}$. The value of $V_{\mathrm{ADD}}^{(4)}$ is shown by color (blue-red), and the red points (Max1-Max4), yellow points (S1-S6) and cyan points (Min1-Min4) denote ADD maxima, ADD saddle points and ADD minima, respectively. Ball-stick models beside the ADD maxima show the corresponding H_2O geometries.

Fig. 2.6 shows the ADD stationary paths determined by tracing the ADD stationary points with increasing the sphere radius as (a) $\rho = 0$ to 1.0 hartree$^{1/2}$ and (b) $\rho = 0$ to 0.3 hartree$^{1/2}$. ADD stationary points on each sphere was computed with the algebraic geometric method. The number of ADD stationary points on each sphere varies with the radius of sphere, as shown in Fig. 2.6 a. It should be remarked that one ADD saddle path (= a curve connecting ADD saddle points) turns into an ADD maximum path (path 5) and two new ADD saddle paths at a radius of 0.66 hartree$^{1/2}$ (referred as pitchfork bifurcation [141,165]). Because of bifurcation, the number of ADD stationary paths increases to 20 on a sphere of radius 1.0 hartree$^{1/2}$. In the vicinity of the EQ, the opposite direction of each ADD maximum path corresponds to the ADD minimum path, and the opposite direction of each ADD saddle path corresponds to another ADD saddle path. This correspondence is understood by the parity of $V^{(3)}_{\mathrm{ADD}}$. Since $V^{(3)}_{\mathrm{ADD}}$ is the third-order homogeneous polynomial, $V^{(3)}_{\mathrm{ADD}}(-d\bar{\boldsymbol{Q}}) = -V^{(3)}_{\mathrm{ADD}}(d\bar{\boldsymbol{Q}})$ holds and the antipodal point of an ADD stationary point is also an ADD stationary point. Moreover, the antipodal point of the l-th order ADD saddle point ($0 \leq l \leq f-1$) corresponds to the $(f-1-l)$-th order ADD saddle point because the Hessian matrix of $V^{(3)}_{\mathrm{ADD}}$ on a sphere (see Eq. (2.2.18)) is also antisymmetric with respect to the spatial inversion. There are some other characteristic bifurcations in Fig. 2.6 (c), transcritical bifurcation and hysteresis loop. [165] At the transcritical bifurcation point, the ADD saddle path and ADD minimum path intersect and the nature of the path is swapped. In the hysteresis loop, an ADD saddle path turns into an ADD maximum path and then turns into the ADD saddle path again.

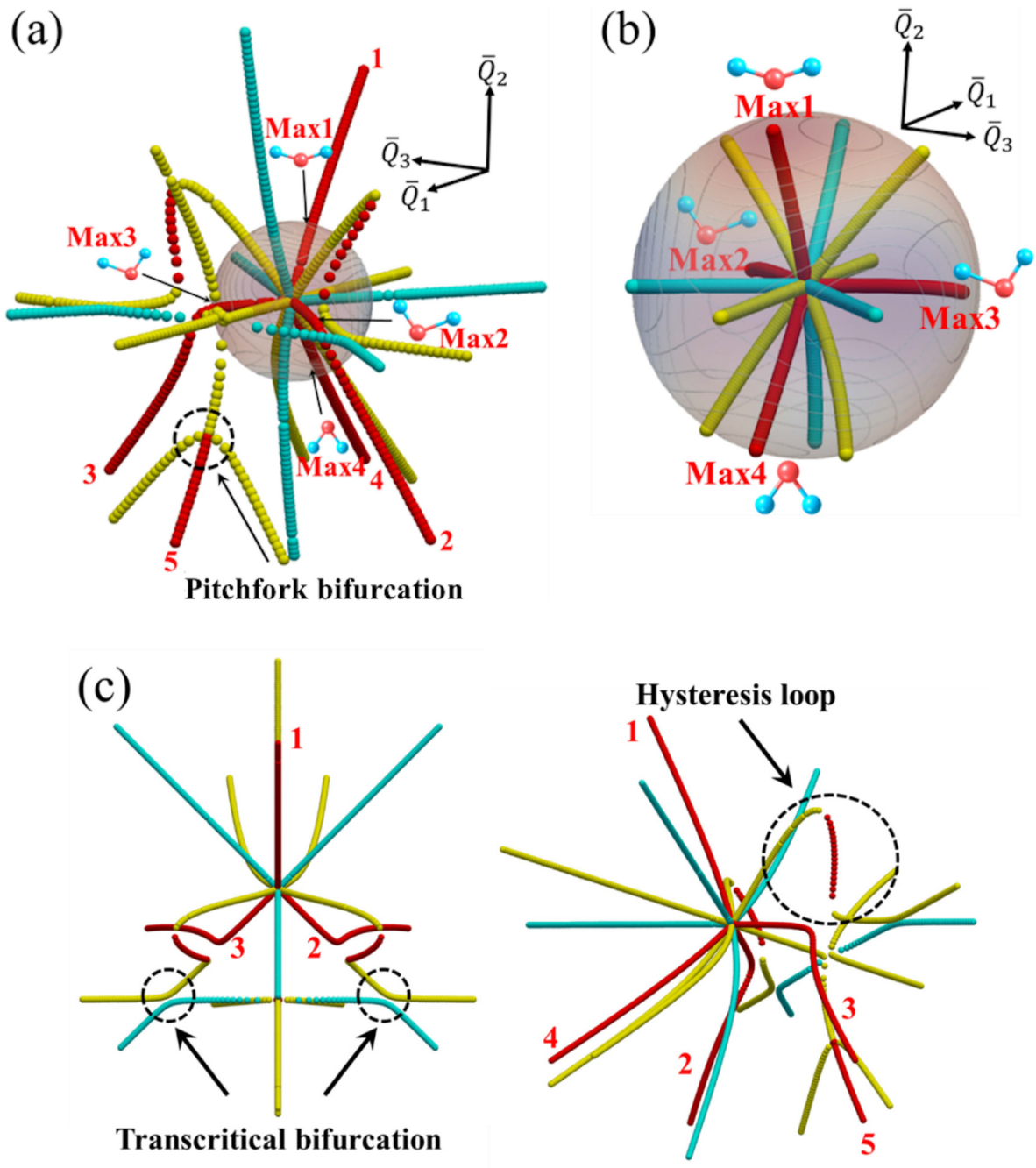

Fig. 2.6: ADD stationary paths of H_2O determined by tracing the stationary points of $V_{\mathrm{ADD}}^{(4)}$ with increasing the sphere radius as (a) $\rho = 0$ to 1.0 hartree$^{1/2}$ and (b) $\rho = 0$ to 0.3 hartree$^{1/2}$. Red, yellow and cyan points correspond to the ADD maxima, ADD saddle points and ADD minima respectively. The transparent sphere is the same as that shown in Fig. 2.5. In (a), a pitchfork bifurcation of an ADD saddle path takes place at $\rho = 0.66$ hartree$^{1/2}$, resulting in one ADD maximum and two ADD saddle paths. Other characteristic bifurcations are shown in (c).

As shown in the case of H_2O molecule, the number of ADD maxima on hypersphere may change due to the bifurcation of the ADD stationary paths. ADD maximum path 5 shown in Fig. 2.6 (a) appears at the pitchfork bifurcation point. This pitchfork bifurcation point is not an artifact caused by the approximation of the PES. Indeed, Fig. 2.7 shows that a pitchfork bifurcation point appears on a sphere of radius $\rho = 0.78$ hartree$^{1/2}$ on the real PES computed by the spin-unrestricted Hartree-Fock (UHF) method with 6-31G(d,p) basis sets. The UHF method was employed with the option Stable=Opt in Gaussian09 to describe the dissociation pathway into two fragments of doublet spin multiplicity. ADD maximum points were located by Newton-Raphson method, i.e., iterative energy minimization on each sphere. It should be noted that the ADD maximum path appearing at the pitchfork bifurcation point leads to TS of the dissociation to O + H_2. This result indicates that bifurcation of ADD stationary paths need to be taken into account to search chemical reaction pathways around an EQ.

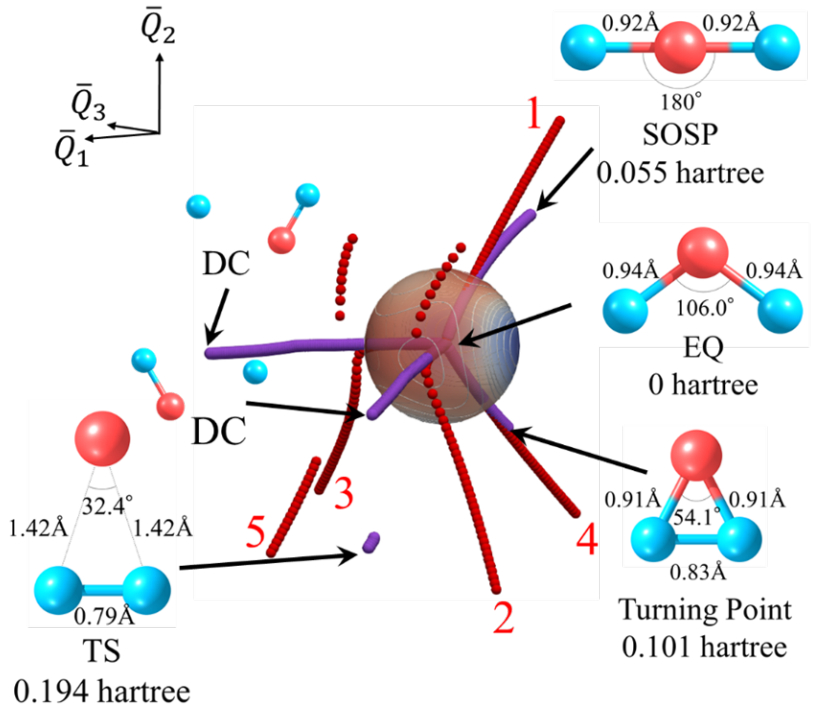

Fig. 2.7: The ADD maximum paths on the fourth-order Taylor polynomial of the PES (red points) and the ADD maximum paths on the real PES (purple points), computed within a radius of 1.0 hartree$^{1/2}$ from the EQ. The sphere with a radius of 0.3 hartree$^{1/2}$ is also shown. SOSP denotes a second-order saddle point with a linear geometry of H-O-H, which is the terminal of the real ADD maximum path along path 1. DC denotes a structure leading to the dissociation into OH and H along paths 2 and 3. The real ADD maximum path corresponding to path 4 turns into an ADD saddle path on the way (at the turning point). The real ADD maximum path corresponding to path 5 appears suddenly. Except for DC, the bond lengths and angles of H_2O at the terminal point of each path is shown. The total energies relative to the EQ are also shown.

ADDF was also carried out for H_2O on the real PES using the GRRM14 program [111] with the options MO GUESS, Opt=Tight, and Stable=Opt. In the GRRM program, aforementioned IOE procedure is implemented to detect the direction of the *hidden* ADD maxima on the initial hypersphere. [105,130] However, IOE method failed to detect the direction of the pitchfork bifurcation in this system. Fig. 2.8 shows the ADDF paths (shown by orange dots) computed by GRRM14. [111] Dots on the floor are projected points of the ADDF paths. With ADDF of GRRM14, five ADDF paths were obtained whereas one of them was discarded in the very early step of the ADDF procedure. Hence, four ADDF paths are shown in Fig. 2.8. Compared withFig. 2.7, it can be seen that ADDF paths almost coincide with the ADD maximum paths in the vicinity of the EQ. This result indicates that IOE method located the ADD maxima of the original PES, and the direction of the pitchfork bifurcation on the initial sphere (*hidden* ADD maximum) could not be detected in this case. One ADDF path leads to the linear geometry (H-O-H) of the second-order saddle point (SOSP) whereas two ADDF paths lead to the dissociation channels (DC) to OH + H. The remaining leads to X‴ via geometries X, X′, and X″. Around X, the ADD maximum turns into an ADD saddle. Then, the ADDF path leads to X″ and falls in the basin of the ADD maximum around X‴. At X‴, the potential energy starts decreasing along the ADDF path. Hence, the ADDF is stopped and TS(guess) is located as the energy-top point along the ADDF path. The TS optimization from TS(guess) led to TS1 (linear $HH\cdots O$), which connects O + H_2 and OH + H. In fact, the step size of expanding the sphere radius affects which TS is found. When ε is determined so that the displacement becomes 0.02 Å(the default is 0.1 Å), not TS1 but TS2 was obtained that connects the EQ and O + H_2 keeping the C_{2v} symmetry. When the displacement was given by 0.09 Å, both TSs were not found. Ohno and Maeda discussed the overlooking of TSs in ADDF method from an empirical viewpoint. [105] According to their consideration, such overlooking is attributed to the fitting error of shape functions used in IOE method to detect the *hidden* ADDs covered by large ADD maxima. [105] In the case of H_2O, the ADD in the direction of H_2 dissociation channel (via TS2) is regarded to be small and hidden by the large ADDs of H atom dissociation channels. This explanation is not wrong, however, it seems somehow indirect and ambiguous. The direct and root cause of the overlooking is obviously bifurcation of ADD stationary paths. IOE method should be regarded as nothing but a heuristic algorithm to detect the direction of ADD maxima that appear at bifurcation points at a distance from potential minima. The quality of shape functions is not the essence of this problem.

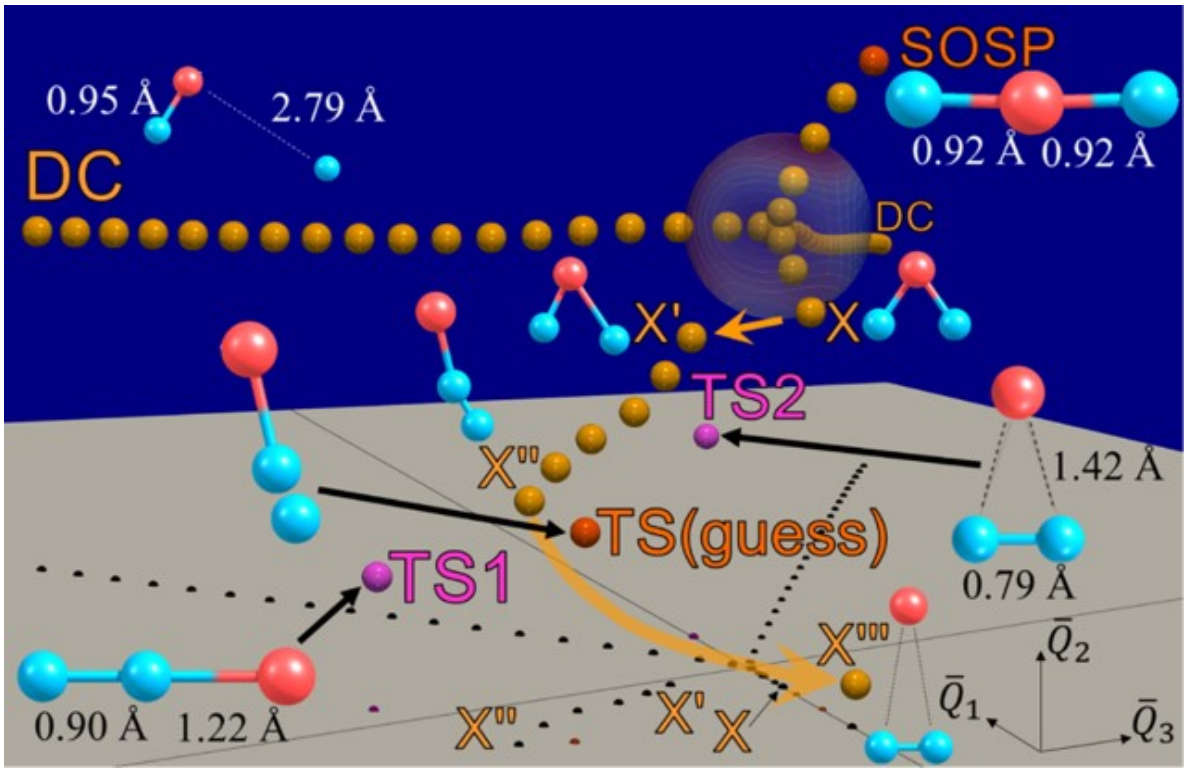

Fig. 2.8: ADDF paths (orange dots) of the H_2O molecule computed by GRRM14. Dots on the floor are the projected points of ADDF paths and TS geometries, and the two orthogonal lines on the floor denote the $\bar{Q}_1$ and $\bar{Q}_3$ axes. The transparent sphere is the same as that shown in Fig. 2.5. Four ADDF paths were obtained: one leads to SOSP, two lead to DC to OH + H, and the remaining leads to X‴ via geometries X, X′, and X″. Starting from the TS(guess), the top of the ADDF path, the TS with the linear structure (TS1) was obtained, but the TS with the C_{2v} symmetry (TS2) was overlooked.

2.4 Discussion

Fig. 2.9 shows the schematic of typical bifurcations of ADD stationary paths. All the TSs shown in the four panels will be successfully located by tracing not only ADD maximum paths but also ADD stationary and inflection paths whereas the maximum number of ADD stationary and inflection paths is so large as $(5^f - 1)/2$. The point is that trace of only ADD maxima is not satisfactory to locate TSs like shown in Fig. 2.9 (c) and (d). Indeed, the TS of a H_2O molecule with C_{2v} symmetry was not necessarily found by ADDF method while it follows some points other than ADD maxima with using IOE technique. The nature of ADD seems quite different from what imagined from the ADD principle due to the existence of bifurcation of ADD stationary paths. Whether ADD is large or not in the vicinity of an EQ is not an essential factor for knowing the direction of chemical reaction.

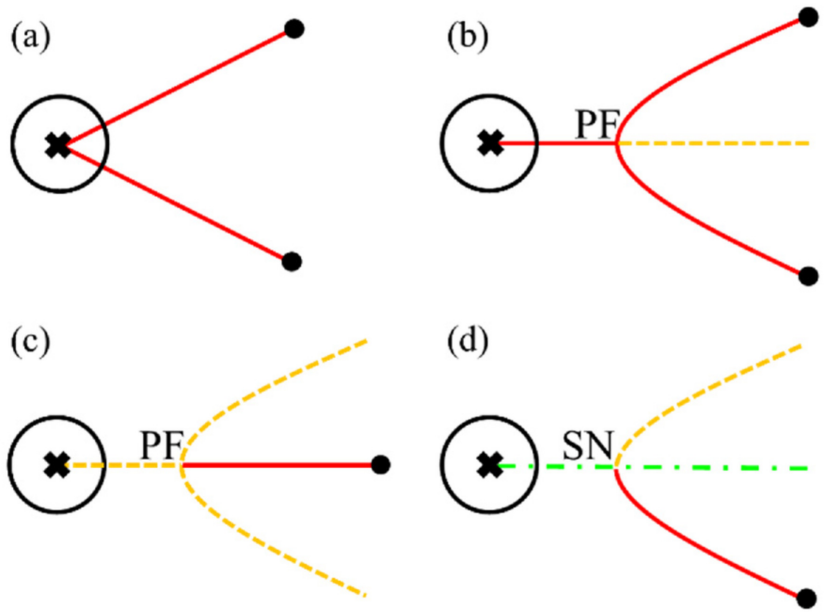

Fig. 2.9: Schematic of typical bifurcations of ADD stationary paths. The red curves and the yellow dashed curves denote the ADD maximum paths and ADD saddle paths, respectively, while the green dot-dash line denotes the ADD inflection path. Black crosses and circles indicate EQs and TSs, and the circles around the EQs show the initial hyperspheres of the ADDF method. (a) Both of the two ADD maximum paths intersect with the initial hypersphere; (b) the ADD maximum path intersecting with the initial hypersphere bifurcates at the pitchfork (PF) bifurcation point; (c) the ADD maximum path appears at the PF bifurcation point; and (d) the ADD maximum path appears at the saddle-node (SN) bifurcation point.

2.5 Conclusion

In this chapter, a detailed investigation of the mathematical aspect of the ADD stationary path was presented. Firstly, it was confirmed that the maximum number of the ADD stationary paths crossing the EQ is given by $2^{f+1} - 2$, where f is the vibrational degrees of freedom of the system. Next, the bifurcation of the ADD stationary path was analyzed. It was confirmed that bifurcation of ADD stationary paths takes place at non-regular point of ADD Hessian on an isosurface of harmonic potential. As a demonstration, typical bifurcations like saddle-node bifurcation and pitchfork bifurcation of ADD stationary paths were presented. Similar to the case of gradient extremals, bifurcation of ADD stationary paths was found to be unfavorable for reaction path search. In order for preventing overlooking of TSs essentially caused by such bifurcation, trace of some ADD saddle and inflection paths from every equilibrium point seems to be effective whereas it is not feasible to trace all of them. Although IOE method also traces some points other than ADD maxima, there is a case where TS is overlooked as shown in the case of a H_2O molecule. In conclusion, whether ADD is large or not in the vicinity of an EQ is not an essential factor for knowing the direction of chemical reaction even though ADD tends to be maximum in the vicinity of TS. This study is expected to provide a detailed understanding of the behavior of anharmonicity around an equilibrium geometry.

Chapter 3

Natural Reaction Orbital

Abstract

Natural reaction orbital (NRO) is a new orbital analysis method which automatically extracts representative molecular orbitals essential for the chemical reaction. NRO is generated by singular value decomposition (SVD) or Autonne-Eckart-Young decomposition of the virtual-occupied block of the first-order response matrix of molecular orbitals with respect to nuclear displacements, $\mathbf{U}_{\mathrm{VO}}^{(1)}$, the solution of coupled-perturbed self-consistent field (CP-SCF) equation. $\mathbf{U}_{\mathrm{VO}}^{(1)}$ represents the first-order transition amplitudes from the occupied orbital space to the virtual orbital space or orbital mixing induced by infinitesimal nuclear displacements. The SVD basis of $\mathbf{U}_{\mathrm{VO}}^{(1)}$, NRO, can be regarded as a basis to characterize the orbital mixing. As the nature of SVD, NRO forms pairs of occupied and virtual orbitals and singular value of each pair represents the orbital mixing rate of the pair. Accordingly, NRO pairs with large singular values can be extracted as the representative orbitals essential for the chemical reaction, In the NRO representation, the orbital mixing is maximally simplified because mixing occurs only within each NRO pair. Also, NRO basis becomes symmetry-adapted when a system has some symmetry and the direction of nuclear displacements belongs to a irreducible representation of the system, Conveniently, NRO shows semi-localized character and relatively low basis set dependence. For all these favorable features, NRO seems to be a very promising method to analyze reaction mechanisms from a viewpoint of electronic structure. Actually, application of NRO method to a dozen of typical reactions demonstrated its universality and robustness in consistency with conventional understanding or chemical intuition. A non-trivial difference between paired interacting orbital (PIO) and NRO is also discussed.

3.1 Introduction

As quoted everywhere, P. A. M. Dirac claimed "the underlying physical laws necessary for the mathematical theory of a large part of physics and the whole of chemistry are thus completely known, and the difficulty is only that the exact application of

these laws leads to equations much too complicated to be soluble". [29] The fundamental equations ruling chemistry are Dirac equation [28] and its approximations, e.g., Schrödinger equation, [159] non-relativistic limit of Dirac equation. Except for the case where the relativistic effect is essential, Schrödinger equation is the equation to solve. Unfortunately, as Dirac claimed, generally it is hardly possible to solve Schrödinger equation. Consequently, enormous methods have been proposed to obtain better approximation of the exact solution or wavefunction of Schrödinger equation. Among the enormous approximations, the Born-Oppenherimer (BO) approximation [13] will be one of the most fundamental approximation for chemistry. In the BO approximation, the motion of nuclei and electrons are separated. Since the mass of nuclei is at least 1800 times of the mass of electron, the motion of nuclei will be very slow compared to that of electrons. Accordingly, the electronic motion is approximated by the motion for stationary nuclei. In the BO approximation, electronic wavefuntion for given fixed nuclear coordinates and potential function for nuclei are provided. It implies that the electronic wavefunction parametrically depends on the nuclear coordinates. The BO approximation is not only important for reducing computational cost but also very convenient for studying chemical phenomena. In chemistry, molecular geometry, the shape of molecule, is extremely important to explain chemical stability and reactivity. To analyze the electronic properties of a molecule with specific nuclear coordinates, the electronic wavefunction for stationary nuclei seems to be much more convenient than that for the nuclear wavefunction distributed to various molecular geometries. Thus, the BO approximation is highly compatible with chemistry.

Another fundamental approximation will be Hartree-Fock (HF) approximation. [39, 63, 64, 163] In HF approximation, the electronic wavefunction is approximated by single Slater determinant. Slater determinant of n-electron system is given by the determinant of n functions $(\psi_1, \ldots, \psi_n)$, ψ_i is the function of a single electron. With the orthonormal condition of the the n functions, the electronic energy of the system is variationally optimized. The variationally optimal functions are called occupied spin orbitals and the space spanned by them are called Hartree-Fock manifold. In this context, the spin orbitals are nothing more than mathematical constructs for the approximation. Interestingly, however, the mathematical constructs have been playing a significant role of theoretical and computational chemistry.

One great success of the concept of molecular orbital is its application to the understanding of chemical reactivity. Frontier orbital theory proposed by Fukui [57] and Woodward-Hoffmann rules [72, 178, 179] uncovered a close relationship between MOs and chemical reactivity. Frontier orbital theory showed regioselectivity of chemical reactions of aromatic hydrocarbons can be clearly explained with only a few representative orbitals, frontier molecular orbitals (FMOs). FMOs are constituted of the highest occu-

pied molecular orbitals (HOMOs) and lowest unoccupied molecular orbitals (LUMOs) of isolated reagent and reactant molecules. Based on the perturbation theory, the interaction between the HOMO (LUMO) of reagent molecule and the LUMO (HOMO) of the reactant molecule is assumed to be dominant in the reaction. Since orbitals need to overlap to establish effective interaction, the atomic sites with the largest FMO amplitudes are expected to be favorable sites for the interaction between the reagent and reactant molecules. In addition to the overlap, the phases of HOMO and LUMO is a key of the reactivity. The HOMO and LUMO need to realize in-phase overlap for new bond formation (phase-matching). Accordingly, chemical bonds are expected to be formed between the atoms with the largest FMO amplitudes, with the phases of FMOs matched. Although the idea seems to be too simplified, frontier orbital theory has been widely adopted with a series of successful applications to various type of reactions. Frontier orbital theory profoundly affected the subsequent studies of chemistry and strongly motivated chemists to pay attention to molecular orbitals to understand chemical reactivity. Woodward-Hoffmann rules are known as a series of outstanding works among such studies that revealed the generalized selection rule of pericyclic reactions in terms of orbital symmetry. [180] Nowadays, molecular orbital is no longer a mathematical construct only for the approximation of Schrödinger equation but a basic concept to extract the essence of chemical phenomena.

However, some limitations and failures of FMO theory came to be recognized. [25] In FMO theory, the transition state (first-order saddle point) geometry is assumed to resemble the reactants. This assumption is essential because it allows FMO theory to explain the reactivity based on the MOs of reactants instead of those of the transition state. Also, the orbital interaction between MOs other than frontier orbitals are assumed to be negligible. This anzats significantly simplifies the perturbation expansion. However, it is pointed out that the former assumption cannot be justified for late transition states. The latter is also criticized as unjustifiable because the order of denominators of perturbation expansion are usually comparable and the variations in the numerators are commonly greater than that of denominators. Failures in predicting regioselectivities are also known. Indeed, mis-prediction is reported for isoquinoline although even resonance theory can lead to the correct prediction. The meta-selectivity of nitrobenzene is also unclear in the viewpoint of FMO theory because there is only a subtle difference between the ortho and meta coefficients of HOMO. Although FMO theory does not loose its historical importance in that it revealed the relevance between molecular orbitals and regioselectivity and leaded to the finding of Woodward-Hoffmann rules, its applicability to selectivity prediction should be recognized as a limited one. [23]

As another issue of FMO theory, canonical molecular orbital (CMO), [38] the diagonal basis of Fock operator, is known to essentially show a highly delocalized nature. [37]

The gap between the delocalized picture shown by CMO and the locality in chemical interaction came to be recognized as a kind of problem. [49] As pointed out by Edmiston and Ruedenberg, [37] for example, another orbital basis than CMO can be more effective for analyses of properties of a particular state while CMO may be convenient for spectral transitions and ionization potentials. Indeed, a variety of MOs other than CMO convenient for various analyses have been proposed. Some demonstrative MOs will be introduced here. Natural orbital (NO) proposed by Löwdin [103] is one of the most well-known orbitals. Natural orbital is defined as the diagonal basis of the first-order reduced density matrix (RDM). Since the first-order RDM can be defined even for the exact wavefunction, the concept of NO is general. The significance of NO is that NO provides a general way to analyze and understand the many-electron wavefunction. From the definition, NO is the optimal basis to characterize the first-order RDM or electron density. Thus, the spatial distribution of electrons can be analyzed through NO. Subsequently, various types of orbitals for various objectives have been proposed: localized orbital (LO), [37] pair natural orbital (PNO), [35, 36, 117] paired interacting orbital (PIO), [44, 48, 49] natural bond orbital (NBO), [144, 145] natural localized molecular orbital (NLMO), [145] projected reactive orbital (PRO), [49–51] intrinsic soft molecular orbital (ISMO), [121] natural transition orbital (NTO), [112] reactive hybrid orbital (RHO), [68, 124, 131] excited state paired interacting orbital (EPIO), [86] intrinsic bond orbital (IBO), [90, 91] valence virtual orbital (VVO), [158] Dyson orbital (DO), [116] principal interacting orbital (PIO') [182] and energy natural orbital (ENO). [170] Such innumerable definitions of MOs seems to reflect that a single definition of the best molecular orbitals does not exist. [96] As such, it is very important to adequately choose a definition of MO suited for the objective of analysis. This is also the case for the analysis of chemical reactivity. It should not be forgotten that no single definition of MO is the best any more than no single definition of coordinate is always the best.

Among many definitions of MOs other than CMO, which definitions are suited for reaction mechanism analysis? Reaction mechanism analysis is one of the most fundamental and essential analyses in chemistry. Reaction mechanism analysis from a viewpoint of molecular orbital theory may be concisely summarized by the words of Woodward and Hoffmann: "a reaction may still be analyzed by writing down the orbitals involved, allowing them to mix according to well-defined quantum mechanical principles and following the interacting orbitals through the reaction." [180] Based on the words, molecular orbitals characterizing the orbital mixing along some reaction coordinates, e.g., intrinsic reaction coordinates (IRC), [52] will be the orbitals suited for reaction mechanism analysis. There will be some possible choices of definition of MOs for characterization of orbital interaction. However, interaction frontier orbitals

(IFOs) [56] and paired interacting orbitals (PIOs) [44, 48, 169] seem to be especially important. In IFO, the interaction between occupied orbitals of donor fragment and virtual orbitals of acceptor fragments is evaluated by the delocalization energy matrix $\mathbf{D}$ which is rectangular in general. IFO basis is defined as the diagonal basis of $\mathbf{D}^\dagger\mathbf{D}$ like singular value decomposition (SVD) or Autonne-Eckart-Young decomposition. [89] Because of the non-linearity of Fock operator, $\mathbf{D}^\dagger\mathbf{D}$ is diagonalized in an iterative manner. Just like SVD basis, occupied IFOs of donor and virtual IFOs of acceptor form pairs. Each IFO pair has a singular value (square root of the corresponding eigenvalue of $\mathbf{D}^\dagger\mathbf{D}$) which represents the strength of interaction of the pair. Usually, only a few IFO pairs have large singular values. Therefore, IFO can provide a succinct expression of interaction. IFO can take account of the contribution of MOs other than frontier orbitals in addition to that of frontier orbitals. Thus, IFO can be considered as a generalization of frontier orbitals. Additionally, IFO shows semi-localized feature with clearly characterizing the interaction between the donor and acceptor. Subsequently, more practical version of paired fragment orbitals, paired interacting orbital (PIO), was proposed. The occupied MOs of interacting system is represented as linear combinations of MOs of non-interacting fragments. The occupied MOs of interacting system can contain the contribution of virtual fragment MOs because electron transfer between the fragments takes place:

$$\psi_f = \sum_{i=1}^{m} c_{if}^{\mathrm{A}}\psi_i^{\mathrm{A}} + \sum_{i=1}^{M-m} c_{(m+i)f}^{\mathrm{A}}\psi_{m+i}^{\mathrm{A}} + \sum_{i=1}^{n} c_{if}^{\mathrm{B}}\psi_i^{\mathrm{B}} + \sum_{i=1}^{N-n} c_{(n+i)f}^{\mathrm{B}}\psi_{n+i}^{\mathrm{B}}, \quad (f = 1, \ldots, m+n)$$

where ψ_f, ψ_i^{A} and ψ_i^{B} denote the MOs of the interacting system, the fragment A and the fragment B respectively. The number of electrons of the fragment A and B are denoted by m and n. M and N denote the number of basis functions of the fragment A and B. This division of interacting system into fragments is referred as fragment molecular orbital (FMO) scheme [46]. A matrix defined by

$$P_{ij} \coloneqq 2\sum_{f=1}^{m+n} c_{if}^{\mathrm{A}*} c_{(n+j)f}^{\mathrm{B}} \quad (i = 1, \ldots, m,\ j = 1, \ldots, N-n)$$

is used to measure the interaction between the fragments A and B. The SVD basis of $\mathbf{P}$, i.e., PIO, succinctly characterizes the electron delocalization from A to B. PIO is also useful for the analysis of physical properties. The potential for electron donation and acceptance of PIOs of substituted benzenes shows a good correlation with the Hammett σ constants. As Fujimoto mentioned, different from CMO, PIO enables comparison of different substituent groups and of their effect at different positions in a unified

manner. Accordingly, PIO will be one definition applicable to reaction mechanism analysis for all the nice features reviewed above. Indeed, PIO has been applied to various systems. [19, 45, 47, 61, 65, 129, 132, 153, 167]

As noted above, some reaction coordinates and MOs characterizing orbital mixing along the coordinates are required to analyze chemical reaction mechanisms. Nowadays, computation of reaction pathways are automated to a considerable extent. [26, 104, 105, 113] Orbital mixing is also suitably characterized with PIO. Thus, sufficient tools for performing reaction mechanism analysis are already available. Even though, still we need another molecular orbital analysis method to automate reaction mechanism analysis. What makes it difficult to apply PIO to automation of reaction mechanism analysis is the concept of fragment. The way of division of a system into fragments is not necessarily obvious nor unique. Nevertheless, the way of division affects the resulting orbitals. Therefore, a system must be divided in a reasonable manner in order to provide a chemically meaningful result. There are two possible approaches to realize automated orbital analysis: (1) automation of division of a system; (2) development of another orbital analysis method. The first approach, however, seems to be difficult since some universal criteria for division need to be established. On the other hand, the second plan appears to be feasible because there exist some orbital analysis methods free from the concept of fragment. Actually, the idea of ISMO and NTO seems to be really helpful. Both ISMO and NTO extract some chemical essence by performing SVD of the first-order or linear response of molecular orbitals to some perturbation. [112,121] ISMO and NTO utilize the entanglement between occupied orbitals and virtual orbitals induced by the perturbation applied to the system while PIO use the entanglement or interaction between fragments. Consequently, ISMO and NTO can automatically extract essential orbitals without requiring any division of the system. The success of ISMO and NTO implies that the essence of chemical reaction may be automatically extracted by SVD of the first-order response of molecular orbitals to some perturbation which appropriately characterizes the chemical reaction. The simplest and most important one of such perturbation will be the nuclear displacements during the chemical reaction. Actually, electron density change induced by nuclear displacements [21] is applied to an investigation of the conformation dependence of fundamental and overtone intensity. [172] Ref. [172] vividly demonstrates the significance of electron density change to vibrational absorption intensities and highlighted the central importance of electron density migrations caused by molecular structure changes for physical nature of molecules. Then, it also seems very natural to focus on the electron density change in reaction analysis. From the quantum-mechanical point of view, the change of given observable may be represented as the change of basis just as Schrödinger picture does. Hence, the density change can be analyzed as the change of molecular orbitals or orbital

mixing. Even though the concept of orbital is not essential for density functional theory (DFT) [74, 93], it can still be introduced as the basis to represent the electron density with no trouble. It should be noted that the introduction of orbital basis is by no means trivial. The information of phase provides a qualitative way to explain the possibility of given electron density change in terms of interference between occupied and virtual orbitals. Hence, SVD basis of the first-order response matrix of molecular orbitals to nuclear coordinate perturbation, natural reaction orbital (NRO) [33] presented in this study, is expected to be the optimal basis for chemical reaction analysis. The aim of this study is to establish an orbital analysis method specialized in reaction mechanism analysis which enables an automated extraction of molecular orbitals essential for the reactivity.

The current chapter is composed as follows. In the section 2, the theory of NRO is shown. Also, theories used in NRO, e.g., coupled perturbed SCF (CP-SCF) theory, [60, 136] are shortly reviewed. In the section 3, numerical applications to typical reactions will be presented. In the section 4, the numerical results in the section 3 are discussed.

3.2 Theory

In this section, Dirac notation is used for convenience.

3.2.1 Schrödinger equation for moleculer system

The Lagrangian of time-independent Schrödinger equation is given by

$$\mathcal{L} = \langle\Psi|\,\hat{H}\,|\Psi\rangle - E\left(\langle\Psi|\Psi\rangle - 1\right), \tag{3.2.1}$$

where $\langle\Psi|$ and $|\Psi\rangle$ are the state bra and ket vectors respectively. The operator $\hat{H}$ is referred as Hamiltonian, which determines the nature of the system. [159] Hamiltonian is usually Hermitian to the boundary condition imposed. E is the Lagrange multiplier. The state ket of n-particle system can be linearly expanded with tensor products of n ope-particle kets:

$$\big|\mathbf{x}_1\big\rangle \otimes \cdots \otimes \big|\mathbf{x}_n\big\rangle, \tag{3.2.2}$$

where each one-electron ket may be decomposed into the spatial part and spin part:

$$\big|\mathbf{x}_i\big\rangle = \big|\mathbf{r}_i\big\rangle \otimes \big|\omega_i\big\rangle. \tag{3.2.3}$$

In the following part, the symbol "$\otimes$" is omitted for simplicity. The spatial part, position basis, is an eigenket of the position operator $\hat{\mathbf{r}}_i$:

$$\hat{\mathbf{r}}_i\big|\mathbf{r}_i\big\rangle = \mathbf{r}_i\big|\mathbf{r}_i\big\rangle \quad (\mathbf{r}_i \in \mathbb{R}^3). \tag{3.2.4}$$

The eigenvalues are the spatial coordinates of the i-th particle in the usual sense. The inner product of position basis is given by

$$\langle \mathbf{r}' | \mathbf{r} \rangle = \delta(\mathbf{r}' - \mathbf{r}), \tag{3.2.5}$$

where $\delta(\mathbf{r} - \mathbf{r}')$ is Dirac delta distribution:

$$\delta(\mathbf{r}' - \mathbf{r}) = \frac{1}{(2\pi)^3} \int_{\mathbb{R}^3} d\mathbf{k} \exp\left(i \left\langle \mathbf{k}, \mathbf{r}' - \mathbf{r} \right\rangle\right). \tag{3.2.6}$$

In the case of fermion, the spin part is in a two dimensional Hilbert space. If z-axis is chosen as the quantization axis, spin eigenkets are the diagonal basis of the spin operator $\hat{S}_z$:

$$\hat{S}_z \big| \omega_i \big\rangle = \begin{cases} +\frac{1}{2} \big| \omega_i \big\rangle & (\omega_i = \alpha_i) \\ -\frac{1}{2} \big| \omega_i \big\rangle & (\omega_i = \beta_i) \end{cases} . \tag{3.2.7}$$

The spin eigenkets satisfy the orthonormal condition:

$$\langle \omega_i' | \omega_i \rangle = \delta_{\omega_i' \omega_i}, \tag{3.2.8}$$

where $\delta_{\omega_i' \omega_i}$ is Kronecker delta:

$$\delta_{\omega_i' \omega_i} = \begin{cases} 1 & (\omega_i' = \omega_i) \\ 0 & (\omega_i' \neq \omega_i) \end{cases} \tag{3.2.9}$$

As shown by Eq. (3.2.7), Fermion has half-integer spin angular momentum along the quantization axis. It is known that the fundamental components of molecules - electrons, protons and neutrons - are fermions.

If the system is composed of only one type of particles, e.g., electrons, the Hamiltonian of Schrödinger equation has a symmetry with respect to any permutation of the identical n particles.

$$|\Psi\rangle \equiv \frac{1}{n!} \int d\mathbf{x}_1 \cdots d\mathbf{x}_n \Big(\sum_{\sigma_1, \ldots, \sigma_n} \varepsilon^{\sigma_1 \ldots \sigma_n} \big| \mathbf{x}_{\sigma_1} \big\rangle \cdots \big| \mathbf{x}_{\sigma_n} \big\rangle \Big) \Big(\sum_{\sigma_1', \ldots, \sigma_n'} \varepsilon^{\sigma_1' \ldots \sigma_n'} \big\langle \mathbf{x}_{\sigma_1'} \big| \cdots \big\langle \mathbf{x}_{\sigma_n'} \big| \Big) \big| \Psi \big\rangle, \tag{3.2.10}$$

where

$$\int d\mathbf{x}_1 \cdots d\mathbf{x}_n = \prod_{i=1}^{n} \sum_{\omega_i \in \{\alpha_i, \beta_i\}} \int_{\mathbb{R}^3} d\mathbf{r}_i \tag{3.2.11}$$

and

$$\varepsilon^{\sigma_1 \cdots \sigma_n} = \begin{cases} +1 & (\text{if } (\sigma_1, \ldots, \sigma_n) \text{ is an even permutation of } (1, \ldots, n)) \\ -1 & (\text{if } (\sigma_1, \ldots, \sigma_n) \text{ is an odd permutation of } (1, \ldots, n)) \\ 0 & (\text{otherwise}) \end{cases} . \quad (3.2.12)$$

With the anti-symmetrized basis, the coefficients

$$\frac{1}{\sqrt{n!}} \left(\sum_{\sigma_1, \ldots, \sigma_n} \varepsilon^{\sigma_1 \cdots \sigma_n} \left\langle \mathbf{x}_{\sigma_1} \right| \cdots \left\langle \mathbf{x}_{\sigma_n} \right| \right) \left| \Psi \right\rangle \quad (3.2.13)$$

become symmetric. It is, in principle, also possible to represent the Hamiltonian with the anti-symmetrized basis. Conventionally, however, anti-symmetrized basis is not preferred and the state ket is usually expanded with the simple tensor products shown in Eq. (3.2.2):

$$\left| \Psi \right\rangle \equiv \int d\mathbf{x}_1 \cdots d\mathbf{x}_n \Big(\left| \mathbf{x}_1 \right\rangle \cdots \left| \mathbf{x}_n \right\rangle \left\langle \mathbf{x}_1 \right| \cdots \left\langle \mathbf{x}_n \right| \Big) \left| \Psi \right\rangle. \quad (3.2.14)$$

In this representation, the anti-symmetry of the state ket is not obvious. The anti-symmetry is imposed on the coefficient defined by

$$\Psi \left(\mathbf{x}_1, \ldots, \mathbf{x}_n \right) \coloneqq \left(\left\langle \mathbf{x}_1 \right| \cdots \left\langle \mathbf{x}_n \right| \right) \left| \Psi \right\rangle. \quad (3.2.15)$$

The complex conjugate of $\Psi \left(\mathbf{x}_1, \ldots, \mathbf{x}_n \right)$ is given by

$$\Psi^* \left(\mathbf{x}_1, \ldots, \mathbf{x}_n \right) = \left\langle \Psi \right| \left(\left| \mathbf{x}_1 \right\rangle \cdots \left| \mathbf{x}_n \right\rangle \right) \quad (3.2.16)$$

as the state bra is the conjugate transpose of the state ket. The anti-symmetric function of n-particle coordinates is referred as the fermionic wavefunction. Although protons and neutrons are fermions like electrons, it is usually less important to study the state of each proton or neutron in chemistry. Rather, the behavior of nuclei, particles consisting of protons and neutrons, is essential for typical chemical processes such as chemical reactions. Nuclei may have half-integer spins or integer spins because nuclei are composite systems composed of multiple fermions, protons and neutrons. A system of identical nuclei with half-integer spins are described by anti-symmetric wavefunction as mentioned above. In contrast, a system of identical nuclei with integer spins are described by symmetric wavefunction which is invariant to exchange of identical nuclei. However, nuclear spin is not important for the current work and not taken into account.

A molecular system composed of n electrons and N^{nuc} nuclei is generally described

as follows:

$$|\Psi\rangle \equiv \int d\mathbf{x} d\mathbf{X} |\mathbf{x}\rangle |\mathbf{X}\rangle \langle \mathbf{x}| \langle \mathbf{X}| |\Psi\rangle, \tag{3.2.17}$$

where $\mathbf{x}$ and $\mathbf{X}$ are the coordinates of n electrons and N^{nuc} nuclei: $\mathbf{x} = (\mathbf{x}_1, \ldots, \mathbf{x}_n)$ and $\mathbf{X} = (\mathbf{X}_1, \ldots, \mathbf{X}_{N^{nuc}})$. For convenience, however, mass-weighted coordinates are used for nuclei. The wavefunction of the moleculer system is given by

$$\Psi(\mathbf{x}, \mathbf{X}) \coloneqq (\langle \mathbf{x}| \langle \mathbf{X}|) |\Psi\rangle. \tag{3.2.18}$$

The wavefunction is antisymmetric under exchange of electrons. If the molecule includes identical nuclei, the wavefunction is also anti-symmetric or symmetric under exchange of identical nuclei. The molecular Hamiltonian operator is a sum of five operators:

$$\hat{H} = \hat{T}_e + \hat{T}_N + \hat{V}_{ee} + \hat{V}_{eN} + \hat{V}_{NN}. \tag{3.2.19}$$

T_e and T_N are the kinetic energy operators for electrons and nuclei respectively. $\hat{V}_{ee}$, $\hat{V}_{eN}$ and $\hat{V}_{NN}$ are the electron-electron, electron-nucleus and nucleus-nucleus Coulomb potentials respectively. Matrix elements of each operator are given by followings:

$$\begin{aligned} \hat{T}_e &\equiv \left(\langle \mathbf{x}'| \langle \mathbf{X}'|\right) \hat{T}_e \left(|\mathbf{x}\rangle |\mathbf{X}\rangle\right) \\ &= \prod_{i=1}^{n} \delta(\mathbf{x}_i' - \mathbf{x}_i) \prod_{I=1}^{N^{nuc}} \delta(\mathbf{X}_I' - \mathbf{X}_I) \sum_{i=1}^{n} -\frac{1}{2}\Delta_i, \end{aligned} \tag{3.2.20}$$

$$\begin{aligned} \hat{T}_N &\equiv \left(\langle \mathbf{x}'| \langle \mathbf{X}'|\right) \hat{T}_N \left(|\mathbf{x}\rangle |\mathbf{X}\rangle\right) \\ &= \prod_{i=1}^{n} \delta(\mathbf{x}_i' - \mathbf{x}_i) \prod_{I=1}^{N^{nuc}} \delta(\mathbf{X}_I' - \mathbf{X}_I) \sum_{I=1}^{N^{nuc}} -\frac{1}{2}\Delta_I, \end{aligned} \tag{3.2.21}$$

$$\begin{aligned} \hat{V}_{ee} &\equiv \left(\langle \mathbf{x}'| \langle \mathbf{X}'|\right) \hat{V}_{ee} \left(|\mathbf{x}\rangle |\mathbf{X}\rangle\right) \\ &= \prod_{i=1}^{n} \delta(\mathbf{x}_i' - \mathbf{x}_i) \prod_{I=1}^{N^{nuc}} \delta(\mathbf{X}_I' - \mathbf{X}_I) \sum_{j>i}^{n} \frac{1}{r_{ij}}, \end{aligned} \tag{3.2.22}$$

$$\begin{aligned} \hat{V}_{eN} &\equiv \left(\langle \mathbf{x}'| \langle \mathbf{X}'|\right) \hat{V}_{eN} \left(|\mathbf{x}\rangle |\mathbf{X}\rangle\right) \\ &= \prod_{i=1}^{n} \delta(\mathbf{x}_i' - \mathbf{x}_i) \prod_{I=1}^{N^{nuc}} \delta(\mathbf{X}_I' - \mathbf{X}_I) \sum_{i}^{n} \sum_{I} -\frac{Z_I}{r_{iI}}, \end{aligned} \tag{3.2.23}$$

$$\begin{aligned} \hat{V}_{NN} &\equiv \left(\langle \mathbf{x}'| \langle \mathbf{X}'|\right) \hat{V}_{NN} \left(|\mathbf{x}\rangle |\mathbf{X}\rangle\right) \\ &= \prod_{i=1}^{n} \delta(\mathbf{x}_i' - \mathbf{x}_i) \prod_{I=1}^{N^{nuc}} \delta(\mathbf{X}_I' - \mathbf{X}_I) \sum_{J>I} \frac{Z_I Z_J}{r_{IJ}}, \end{aligned} \tag{3.2.24}$$

where $\delta(\mathbf{x}_i'-\mathbf{x}_i) = \delta(\mathbf{r}_i'-\mathbf{r}_i)\delta_{\omega_i'\omega_i}$. $\Delta_i = \partial^2/\partial x_i^2+\partial^2/\partial y_i^2+\partial^2/\partial z_i^2$ is Laplacian. Z_I is the mass and atomic number of the I-th nucleus respectively. r_{ij} is the distance between the i-th and j-th electrons. r_{iI} denotes the distance between the i-th electron and I-th nucleus. r_{IJ} is the distance between the I-th and J-th nuclei. Then, the Hamiltonian for a molecular system is given by

$$\begin{aligned}
\langle\Psi|\,\hat{H}\,|\Psi\rangle \equiv & \int d\mathbf{x}d\mathbf{X}' \int d\mathbf{x}d\mathbf{X}\Psi^*(\mathbf{x}',\mathbf{X}) \\
& \prod_{i=1}^{n}\delta(\mathbf{x}_i'-\mathbf{x}_i)\prod_{I=1}^{N^{nuc}}\delta(\mathbf{X}_I'-\mathbf{X}_I)\Big(-\sum_{i=1}^{n}\frac{1}{2}\Delta_i-\sum_{I=1}^{N^{nuc}}\frac{1}{2}\Delta_I \\
& +\sum_{j>i}^{n}\frac{1}{r_{ij}}-\sum_{i=1}^{n}\sum_{I=1}^{N^{nuc}}\frac{Z_I}{r_{iI}}+\sum_{J>I}\frac{Z_IZ_J}{r_{IJ}}\Big)\Psi(\mathbf{x},\mathbf{X}) \\
= & \int d\mathbf{x}d\mathbf{X}\Psi^*(\mathbf{x}',\mathbf{X})\Big(-\sum_{i=1}^{n}\frac{1}{2}\Delta_i-\sum_{I=1}^{N^{nuc}}\frac{1}{2}\Delta_I \\
& +\sum_{j>i}^{n}\frac{1}{r_{ij}}-\sum_{i=1}^{n}\sum_{I=1}^{N^{nuc}}\frac{Z_I}{r_{iI}}+\sum_{J>I}\frac{Z_IZ_J}{r_{IJ}}\Big)\Psi(\mathbf{x},\mathbf{X})
\end{aligned} \tag{3.2.25}$$

The Hamiltonian is variationally optimized with respect to the wavefunction Ψ and Ψ^* under the constraint of $\left\langle\Psi \;\middle|\; \Psi\right\rangle = 1$. The variational optimization is achieved by finding a set of Ψ, Ψ^* and E that stationarize the Lagrangian:

$$\begin{aligned}
\delta\mathcal{L} &= \delta\langle\Psi|\,\hat{H}\,|\Psi\rangle - E\delta\langle\Psi|\Psi\rangle - \delta E(\langle\Psi|\Psi\rangle - 1) \\
&= \Big(\langle\Psi|\,\hat{H}\,|\delta\Psi\rangle - E\langle\Psi|\delta\Psi\rangle\Big) + h.c. - \delta E(\langle\Psi|\Psi\rangle - 1) \\
&= 0,
\end{aligned} \tag{3.2.26}$$

where $h.c.$ denotes Hermitian conjugate. In order for the stationary condition to be satisfied for any $\delta\Psi, \delta\Psi^*$ and δE, the followings need to hold:

$$\left(-\sum_{i=1}^{n}\frac{1}{2}\Delta_i-\sum_{I=1}^{N^{nuc}}\frac{1}{2}\Delta_I+\sum_{j>i}^{n}\frac{1}{r_{ij}}+\sum_{i=1}^{n}\sum_{I=1}^{N^{nuc}}-\frac{Z_I}{r_{iI}}+\sum_{J>I}\frac{Z_IZ_J}{r_{IJ}}\right)\Psi = E\Psi, \tag{3.2.27}$$

$$\left(-\sum_{i=1}^{n}\frac{1}{2}\Delta_i-\sum_{I=1}^{N^{nuc}}\frac{1}{2}\Delta_I+\sum_{j>i}^{n}\frac{1}{r_{ij}}-\sum_{i=1}^{n}\sum_{I=1}^{N^{nuc}}\frac{Z_I}{r_{iI}}+\sum_{J>I}\frac{Z_IZ_J}{r_{IJ}}\right)\Psi^* = E\Psi^*, \tag{3.2.28}$$

$$\int d\mathbf{x}d\mathbf{X}\Psi^*\Psi = 1. \tag{3.2.29}$$

The eigenvalue equation, Eq. (3.2.27), is referred as Schrödinger equation for a molecular system. Eq. (3.2.28) is the Hermitian conjugate of Eq. (3.2.27). The eigenvalue of Eq. (3.2.27) is the energy of the molecule. The nature of the eigenfunction Ψ, i.e., wavefunction of the molecule, will be explained in the lats part of this subsection. The last equation, Eq. (3.2.29), is the normalization condition for the wavefunction. Generally, Schrödinger equation is solved with some boundary condition. In the case of molecular system, Schrödinger equation is usually solved with a boundary condition at infinity:

$$\Psi \to 0 \ \text{ as} \begin{cases} |\mathbf{r}_i| & \to \infty \quad (i = 1, \ldots, n) \\ |\mathbf{R}_I| & \to \infty \quad (I = 1, \ldots, N^{nuc}) \end{cases}. \tag{3.2.30}$$

Additionally, wavefunction is required to be finite, single-valued and continuous everywhere. The derivatives of wavefunction must be continuous except at singular points of potential.

Finally, the nature of wavefunction is briefly explained. Based on the standard Copenhagen interpretation, wavefunction is not a real physical entity. [22] The statistical interpretation of Born tells that the absolute square of wavefunction,

$$\Psi^*(\mathbf{x}, \mathbf{X})\Psi(\mathbf{x}, \mathbf{X}) \tag{3.2.31}$$

gives the probability density of finding the particles at $(\mathbf{x}_1, \ldots, \mathbf{x}_n, \mathbf{X}_1, \ldots, \mathbf{X}_{N^{nuc}})$. [11, 22] Also, expectation value of given observable can be computed with using the wavefunction. Provided that the Hermitian operator corresponding to an observable $\mathcal{O}$ is given by $\hat{O}$, the expectation value of $\mathcal{O}$ for the eigenstate is given by

$$\langle \mathcal{O} \rangle = \int d\mathbf{x} d\mathbf{X} \Psi^* \hat{O} \Psi. \tag{3.2.32}$$

3.2.2 Born-Oppenheimer approximation

Generally, the state ket vector of a molecular system can be written as a linear combination of tensor products of ket vectors of electrons and nuclei:

$$\big|\Psi\big\rangle = \sum_i \sum_I C_{iI} \big|\Psi_i^{elec}\big\rangle \big|\Psi_I^{nuc}\big\rangle, \tag{3.2.33}$$

where C_{iI} is the coefficient of complex value. Throughout the current work, the spin of nuclei will be neglected. With the position eigenkets of nuclei dneoted by $|\mathbf{R}\rangle$, the

energy of a molecule can written by

$$\begin{aligned}\left\langle \Psi \middle| \hat{H} \middle| \Psi \right\rangle &= \sum_{i,j} \sum_{I,J} C_{iI}^* C_{jJ} \left(\left\langle \Psi_I^{nuc} \middle| \left\langle \Psi_i^{elec} \right| \right) \hat{H} \left(\left| \Psi_j^{elec} \right\rangle \middle| \Psi_J^{nuc} \right\rangle \right) \\ &= \int_{\mathbb{R}^{3N^{nuc}}} d\mathbf{R} \sum_{i,j} \sum_{I,J} C_{iI}^* C_{jJ} \Psi_I^{nuc*}(\mathbf{R}) \left\langle \Psi_i^{elec} \middle| \left\langle \mathbf{R} \middle| \hat{H} \middle| \mathbf{R} \right\rangle \middle| \Psi_j^{elec} \right\rangle \Psi_J^{nuc}(\mathbf{R})\end{aligned} \tag{3.2.34}$$

where the Hamiltonian is defined by Eq. (3.2.19). Herein, electronic Hamiltonian $\hat{H}^{elec}(\mathbf{R})$ is introduced:

$$\hat{H}^{elec}(\mathbf{R}) \coloneqq \hat{T}_e + \left\langle \mathbf{R} \middle| \hat{V}_{eN} \middle| \mathbf{R} \right\rangle + \hat{V}_{ee}. \tag{3.2.35}$$

$\hat{T}_e$, $\left\langle \mathbf{R} \middle| \hat{V}_{eN} \middle| \mathbf{R} \right\rangle$ and $\hat{V}_{ee}$ are the kinetic energy operator of electrons, the Coulomb potential between nuclei and electrons and Coulomb potential between electrons respectively. Adiabatic basis is defined as the eigenkets of electronic Hamiltonian:

$$\hat{H}^{elec}(\mathbf{R}) \left| \Psi_i{}^{adia}(\mathbf{R}) \right\rangle = E_i^{elec}(\mathbf{R}) \left| \Psi_i^{adia}(\mathbf{R}) \right\rangle. \tag{3.2.36}$$

Since the eigenkets form a complete set, rhs of Eq. (3.2.34) can be rewritten with adiabatic basis:

$$\int_{\mathbb{R}^{3N^{nuc}}} d\mathbf{R} \sum_{i,j} \sum_{I,J} C_{iI}^*(\mathbf{R}) C_{jJ}(\mathbf{R}) \Psi_I^{nuc*}(\mathbf{R}) \left\langle \Psi_i^{adia}(\mathbf{R}) \middle| \left\langle \mathbf{R} \middle| \hat{H} \middle| \mathbf{R} \right\rangle \middle| \Psi_j^{adia}(\mathbf{R}) \right\rangle \Psi_J^{nuc}(\mathbf{R}). \tag{3.2.37}$$

Then, the matrix elements of $\left\langle \mathbf{R} \middle| \hat{H} \middle| \mathbf{R} \right\rangle$ can be given by

$$\begin{aligned}\left\langle \Psi_i^{adia}(\mathbf{R}) \middle| \left\langle \mathbf{R} \middle| \hat{H} \middle| \mathbf{R} \right\rangle \middle| \Psi_j^{adia}(\mathbf{R}) \right\rangle =& \left\langle \Psi_i^{adia}(\mathbf{R}) \middle| \left\langle \mathbf{R} \middle| \hat{H}^{elec}(\mathbf{R}) + \hat{V}_{NN} + \hat{T}_N \middle| \mathbf{R} \right\rangle \middle| \Psi_j^{adia}(\mathbf{R}) \right\rangle \\ =& \delta_{ij} \left(E_j^{elec}(\mathbf{R}) + V_{NN}(\mathbf{R}) - \frac{1}{2} \Delta_{\mathbf{R}} \right) \\ & - \frac{1}{2} \left\langle \Psi_i^{adia}(\mathbf{R}) \middle| \Delta_{\mathbf{R}} \Psi_j^{adia}(\mathbf{R}) \right\rangle \\ & - \left\langle \Psi_i^{adia}(\mathbf{R}) \middle| \nabla_{\mathbf{R}} \Psi_j^{adia}(\mathbf{R}) \right\rangle \cdot \nabla_{\mathbf{R}},\end{aligned} \tag{3.2.38}$$

where $\nabla_{\mathbf{R}}$ is the usual derivative operator with respect to nuclear coordinates:

$$\nabla_{\mathbf{R}} = \sum_{\mathfrak{I}=1}^{3N^{nuc}} \boldsymbol{e}_{\mathfrak{I}} \partial_{\mathfrak{I}}, \tag{3.2.39}$$

where $\boldsymbol{e}_{\mathfrak{I}}$ $(\mathfrak{I} = 1, \ldots, 3N^{nuc})$ are orthonormal vectors. The quantity

$$\tau_{\mathfrak{I}}^{ij} \coloneqq \left\langle \Psi_i^{adia}(\mathbf{R}) \middle| \partial_{\mathfrak{I}} \Psi_j^{adia}(\mathbf{R}) \right\rangle \tag{3.2.40}$$

appeared in Eq. (3.2.38) is referred as the first-order non-adabatic coupling (NAC). [3] From the orthonormal condition of adiabatic basis:

$$\partial_{\mathfrak{I}} \left\langle \Psi_i^{adia}(\mathbf{R}) \middle| \Psi_j^{adia}(\mathbf{R}) \right\rangle = 0 = \tau_{\mathfrak{I}}^{ij} + \tau_{\mathfrak{I}}^{ji*} \tag{3.2.41}$$

is derived. Thus, the first-order NAC is anti-Hermitian with respect to the indices of adiabatic basis:

$$\tau_{\mathfrak{I}}^{ij} = -\tau_{\mathfrak{I}}^{ji*}. \quad (\forall i, j, \mathfrak{I}) \tag{3.2.42}$$

Also, an equation

$$\partial_{\mathfrak{H}} \tau_{\mathfrak{I}} - \partial_{\mathfrak{I}} \tau_{\mathfrak{H}} + \left[\tau_{\mathfrak{H}}, \tau_{\mathfrak{I}} \right] = \mathbf{0} \quad (\forall \mathfrak{H}, \mathfrak{I}) \tag{3.2.43}$$

can be derived from

$$\begin{aligned} \partial_{\mathfrak{H}} \tau_{\mathfrak{I}}^{ij} - \partial_{\mathfrak{I}} \tau_{\mathfrak{H}}^{ij} =& \partial_{\mathfrak{H}} \left\langle \Psi_i^{adia}(\mathbf{R}) \middle| \partial_{\mathfrak{I}} \Psi_j^{adia}(\mathbf{R}) \right\rangle - \partial_{\mathfrak{I}} \left\langle \Psi_i^{adia}(\mathbf{R}) \middle| \partial_{\mathfrak{H}} \Psi_j^{adia}(\mathbf{R}) \right\rangle \\ =& \sum_k \Big(\left\langle \partial_{\mathfrak{H}} \Psi_i^{adia}(\mathbf{R}) \middle| \Psi_k^{adia}(\mathbf{R}) \right\rangle \left\langle \Psi_k^{adia}(\mathbf{R}) \middle| \partial_{\mathfrak{I}} \Psi_j^{adia}(\mathbf{R}) \right\rangle \\ & - \left\langle \partial_{\mathfrak{I}} \Psi_i^{adia}(\mathbf{R}) \middle| \Psi_k^{adia}(\mathbf{R}) \right\rangle \left\langle \Psi_k^{adia}(\mathbf{R}) \middle| \partial_{\mathfrak{H}} \Psi_j^{adia}(\mathbf{R}) \right\rangle \Big) \\ =& - \sum_k \left(\tau_{\mathfrak{H}}^{ik} \tau_{\mathfrak{I}}^{kj} - \tau_{\mathfrak{I}}^{ik} \tau_{\mathfrak{H}}^{kj} \right). \end{aligned} \tag{3.2.44}$$

Eq. (3.2.43) is the integrability condition for

$$\partial_{\mathfrak{I}} \left| \Psi_i^{adia}(\mathbf{R}) \right\rangle = \sum_j \left| \Psi_j^{adia}(\mathbf{R}) \right\rangle \tau_{\mathfrak{I}}^{ji}(\mathbf{R}). \tag{3.2.45}$$

With the first-order NAC, Eq. (3.2.38) can be rewritten by

$$\begin{aligned} \left\langle \Psi_i^{adia}(\mathbf{R}) \middle| \left\langle \mathbf{R} \middle| \hat{H} \middle| \mathbf{R} \right\rangle \middle| \Psi_j^{adia}(\mathbf{R}) \right\rangle =& \delta_{ij} \left(E_j^{elec}(\mathbf{R}) + V_{NN}(\mathbf{R}) \right) \\ & - \frac{1}{2} \sum_{\mathfrak{I}=1}^{3N^{nuc}} \sum_k \left(\delta_{ik} \partial_{\mathfrak{I}} + \tau_{\mathfrak{I}}^{ik} \right) \left(\delta_{kj} \partial_{\mathfrak{I}} + \tau_{\mathfrak{I}}^{kj} \right). \end{aligned} \tag{3.2.46}$$

So far, the Hamiltonian is apparently gauge-covariant. [181] In the adiabatic approximation, the coupling terms between adiabatic states are ignored:

$$\left\langle \Psi_i^{adia}(\mathbf{R}) \middle| \left\langle \mathbf{R} \middle| \hat{H} \middle| \mathbf{R} \right\rangle \middle| \Psi_j^{adia}(\mathbf{R}) \right\rangle \approx \delta_{ij} \Bigg(E_j^{elec}(\mathbf{R}) + V_{NN}(\mathbf{R}) - \frac{1}{2} \sum_{\mathfrak{I}=1}^{3N^{nuc}} \sum_k \left(\delta_{ik}\partial_{\mathfrak{I}} + \tau_{\mathfrak{I}}^{ik}\right)\left(\delta_{kj}\partial_{\mathfrak{I}} + \tau_{\mathfrak{I}}^{kj}\right) \Bigg). \tag{3.2.47}$$

A local gauge transformation

$$\Psi_i^{adia}(\mathbf{R}) = \exp\left(-i\theta_i(\mathbf{R})\right) \tilde{\Psi}_i^{adia}(\mathbf{R}), \tag{3.2.48}$$

where θ_i satisfies

$$-i\partial_{\mathfrak{I}}\theta_i = \tau_{\mathfrak{I}}^{ii} \tag{3.2.49}$$

at $\mathbf{R}$, can locally eliminate the first-order terms of NAC in Eq. (3.2.46):

$$\left\langle \tilde{\Psi}_i^{adia}(\mathbf{R}) \middle| \left\langle \mathbf{R} \middle| \hat{H} \middle| \mathbf{R} \right\rangle \middle| \tilde{\Psi}_j^{adia}(\mathbf{R}) \right\rangle \approx \delta_{ij} \left(E_j^{elec}(\mathbf{R}) + V_{NN}(\mathbf{R}) - \frac{1}{2}\Delta_{\mathbf{R}} - \frac{1}{2} \sum_{\mathfrak{I}=1}^{3N^{nuc}} \sum_{k\neq i} \tau_{\mathfrak{I}}^{ik}\tau_{\mathfrak{I}}^{kj} \right). \tag{3.2.50}$$

If a conical intersection exists, however, there does not exist a function $\theta_i(\mathbf{R})$ which can globally eliminate the first-order terms of NAC. [8, 181]In the Born-Oppenheimer approximation, [13] the second-order terms of $\tau_{\mathfrak{I}}^{ij}$ are also ignored:

$$\left\langle \Psi_i^{adia}(\mathbf{R}) \middle| \left\langle \mathbf{R} \middle| \hat{H} \middle| \mathbf{R} \right\rangle \middle| \Psi_j^{adia}(\mathbf{R}) \right\rangle \approx \delta_{ij} \left(E_j^{elec}(\mathbf{R}) + V_{NN}(\mathbf{R}) - \frac{1}{2}\Delta_{\mathbf{R}} \right). \tag{3.2.51}$$

Then, sum of the electronic energy and nuclear repulsion,

$$E_i^{\mathrm{BO}}(\mathbf{R}) \coloneqq E_i^{elec}(\mathbf{R}) + V_{NN}(\mathbf{R}), \tag{3.2.52}$$

may be considered as the potential function for nuclei. This potential function is called Born-Oppenheimer potential energy surface (PES). Basically, Born-Oppenheimer approximation can provide reliable description in the vicinity of equilibrium geometries or minima of Born-Oppenheimer PES.

3.2.3 Hartree-Fock theory

Notation

$\langle\Psi|, |\Psi\rangle$	bra and ket vectors of many electrons (capital Greek letter)
$\langle\mu|, |p\rangle$	bra and ket vectors of one electron (Non-capital Greek or alphabet)
$a, b, c \ldots$	subscripts for virtual spin orbitals
$i, j, k, \ldots$	subscripts for occupied spin orbitals
$p, q, r, \ldots$	subscripts for occupied and virtual spin orbitals
$\kappa, \lambda, \mu, \ldots$	subscripts for atomic orbital basis
$\mathfrak{I}, \mathfrak{J}, \mathfrak{K}, \ldots$	subscripts for mass-weighted nuclear coordinates

For convenience, n-electron Slater determinants are introduced: [163]

$$\big|\Phi_I\big\rangle \coloneqq (n!)^{-1/2} \sum_{\sigma_1,\ldots,\sigma_n \in I} \varepsilon^{\sigma_1 \ldots \sigma_n} \big|\sigma_1\big\rangle \otimes \cdots \otimes \big|\sigma_n\big\rangle, \tag{3.2.53}$$

where I is a set of n positive integers. The set of one-electron kets is assumed to be complete. In general, the n-electron wavefunction can be represented by a linear combination of the n-electron Slater determinants:

$$|\Psi\rangle \equiv \sum_I \big|\Phi_I\big\rangle\big\langle\Phi_I\big|\Psi\big\rangle, \tag{3.2.54}$$

the summation is taken for all the sets of n positive integers.

Each one-electron ket is a tensor product of the spatial part and the spin part:

$$\big|i\big\rangle = \big|\varphi_i\big\rangle \otimes \big|\omega_i\big\rangle. \tag{3.2.55}$$

The spatial part can be projected onto the position basis:

$$\big|\varphi_i\big\rangle \equiv \left(\int_{\mathbb{R}^3} d\mathbf{r} \big|\mathbf{r}\big\rangle\big\langle\mathbf{r}\big|\right) \big|\varphi_i\big\rangle. \tag{3.2.56}$$

Functions defined by

$$\varphi_i(\mathbf{r}) \coloneqq \big\langle\mathbf{r}\big|\varphi_i\big\rangle \quad (i = 1, \ldots, n) \tag{3.2.57}$$

are called molecular orbitals (MOs). Spin orbital (SO) is defined as the product of MO and spin function:

$$\psi_i(\mathbf{r}, \omega) \coloneqq \big\langle\mathbf{r}\big|\varphi_i\big\rangle\big\langle\omega\big|\omega_i\big\rangle. \quad (i = 1, \ldots, n) \tag{3.2.58}$$

All MOs and SOs are assumed to be single-valued and continuous everywhere.

In Hartree-Fock (HF) theory, [39, 163] n-electron wavefunction is approximated by

a single Slater determinant Φ. The constituent SOs are variationally optimized so as to minimize the electronic energy with the orthonormality conditions of SOs. The Lagrangian of HF theory is given by

$$\mathcal{L}^{\mathrm{HF}} = \langle\Phi|\,\hat{H}\,|\Phi\rangle - \sum_{i,j=1}^{n} \varepsilon_{ji}\left(\langle i|j\rangle - \delta_{ij}\right), \tag{3.2.59}$$

where ε_{ji} are the Lagrange multipliers. [39] Using SOs, the energy can be written by

$$\langle\Phi|\,\hat{H}\,|\Phi\rangle = \sum_{i=1}^{n}\left(\langle i|\,\hat{T}_e\,|i\rangle + \langle i|\,\hat{V}_{eN}\,|i\rangle + \sum_{j=1}^{n}\langle ij\,||\,ij\rangle\right). \tag{3.2.60}$$

The first term is the kinetic energy of the n-electron given by

$$\left\langle i\middle|\hat{T}_e\middle|i\right\rangle = -\frac{1}{2}\int_{\mathbb{R}^3} d\mathbf{r}_1 \varphi_i^*(\mathbf{r}_1)\Delta\varphi_i(\mathbf{r}_1). \tag{3.2.61}$$

The second term is the Coulomb interaction between electrons and nuclei:

$$\left\langle i\middle|\hat{V}_{eN}\middle|i\right\rangle = -\sum_{I=1}^{N^{nuc}}\int_{\mathbb{R}^3} d\mathbf{r}_1 \frac{Z_I}{r_{1I}}\varphi_i^*(\mathbf{r}_1)\varphi_i(\mathbf{r}_1), \tag{3.2.62}$$

where r_I denotes the distance between the electron and the I-th nucleus. The third term is referred as two-electron integral defined by

$$\langle ij\,||\,ij\rangle \coloneqq \iint_{\mathbb{R}^3\times\mathbb{R}^3} d\mathbf{r}_1 d\mathbf{r}_2 \left(\frac{\varphi_i^*(\mathbf{r}_1)\varphi_j^*(\mathbf{r}_2)\varphi_i(\mathbf{r}_1)\varphi_j(\mathbf{r}_2)}{r_{12}} - \delta_{\omega_i\omega_j}\frac{\varphi_i^*(\mathbf{r}_1)\varphi_j^*(\mathbf{r}_2)\varphi_i(\mathbf{r}_2)\varphi_j(\mathbf{r}_1)}{r_{12}}\right), \tag{3.2.63}$$

where the first and second terms are called Coulomb and exchange terms. [27] Exchange term is derived from the anti-symmetry of the Slater determinant. Due to the orthonormality of spin functions, there is no exchange interaction between SOs with different spin. It should be noted that exchange term serves to cancel self-interaction. In the following, integral regions are omitted for simplicity.

In HF theory, the variational parameters are the n SOs, the constituents of the

Slater determinant. The first-order variation of HF Lagrangian is given by

$$\begin{aligned}\delta\mathcal{L}^{\mathrm{HF}} = \int d\mathbf{r}_1 \sum_{i=1}^{n} \delta\varphi_i^*(\mathbf{r}_1) \Bigg\{ & -\frac{1}{2}\Delta\varphi_i(\mathbf{r}_1) - \sum_{I=1}^{N^{nuc}} \frac{Z_I}{r_{1I}}\varphi_i(\mathbf{r}_1) + \sum_{j=1}^{n} \int d\mathbf{r}_2 \frac{\varphi_j^*(\mathbf{r}_2)\varphi_j(\mathbf{r}_2)}{r_{12}}\varphi_i(\mathbf{r}_1) \\ & - \sum_{j=1}^{n} \delta_{\omega_j\omega_i} \int d\mathbf{r}_2 \frac{\varphi_j^*(\mathbf{r}_2)\varphi_i(\mathbf{r}_2)}{r_{12}}\varphi_j(\mathbf{r}_1) - \sum_{j=1}^{n} \varepsilon_{ji}\varphi_j(\mathbf{r}_1) \Bigg\} + h.c. \\ & + \sum_{j=1}^{n} \delta\varepsilon_{ji} \left(\int d\mathbf{r}_1 \varphi_i^*(\mathbf{r}_1)\varphi_j(\mathbf{r}_1) - \delta_{ij} \right),\end{aligned} \tag{3.2.64}$$

where boundary conditions at infinity

$$\varphi_i(\mathbf{r}) \to 0 \ \text{ as } \ |\mathbf{r}| \to \infty \quad (i = 1, \ldots, n) \tag{3.2.65}$$

are imposed. The stationary condition of $\mathcal{L}^{\mathrm{HF}}$ is given by

$$\begin{cases} \left(-\frac{1}{2}\Delta - \sum_{I=1}^{N^{nuc}} \frac{Z_I}{r_{1I}}\right)\varphi_i(\mathbf{r}_1) + \sum_{j=1}^{n} \int d\mathbf{r}_2 \varphi_j^*(\mathbf{r}_2) \frac{\varphi_j(\mathbf{r}_2)\varphi_i(\mathbf{r}_1) - \delta_{\omega_j\omega_i}\varphi_i(\mathbf{r}_2)\varphi_j(\mathbf{r}_1)}{r_{12}} = \sum_{j=1}^{n} \varepsilon_{ji}\varphi_j(\mathbf{r}_1) \\ \int d\mathbf{r}_1 \varphi_i^*(\mathbf{r}_1)\varphi_j(\mathbf{r}_1) = \delta_{ij} \end{cases} . \tag{3.2.66}$$

For convenience, an operator, referred as Fock operator, is introduced:

$$\left\langle \mathbf{r}_1 \middle| \hat{F} \middle| \mathbf{r}_1 \right\rangle \coloneqq -\frac{1}{2}\Delta - \sum_{I=1}^{N^{nuc}} \frac{Z_I}{r_{1I}} + \sum_{j=1}^{n} \int d\mathbf{r}_2 \frac{\varphi_j^*(\mathbf{r}_2)\left(1 - \delta_{\omega_i\omega_j}\hat{P}\right)\varphi_j(\mathbf{r}_2)}{r_{12}}, \tag{3.2.67}$$

where $\hat{P}$ is the permutation operator defined by

$$\begin{cases} \hat{P}\varphi_j(\mathbf{r}_2)\varphi_i(\mathbf{r}_1) & = \varphi_j(\mathbf{r}_1)\varphi_i(\mathbf{r}_2) \\ \varphi_j^*(\mathbf{r}_2)\varphi_i^*(\mathbf{r}_1)\hat{P}^\dagger & = \varphi_j^*(\mathbf{r}_1)\varphi_i^*(\mathbf{r}_2) \end{cases} . \quad (\forall i, j) \tag{3.2.68}$$

Fock operator is Hermitian in the boundary condition Eq. (3.2.65):

$$\left\langle i \middle| \hat{F} \middle| j \right\rangle = \left\langle j \middle| \hat{F} \middle| i \right\rangle^*. \tag{3.2.69}$$

This and Eq. (3.2.66) require the matrix of Lagrangian multipliers also to be Hermitian:

$$\varepsilon_{ij} = \varepsilon_{ji}^*. \tag{3.2.70}$$

Therefore, there exists a set of MOs which diagonalizes $\boldsymbol{\varepsilon}$ [147] and the diagonal basis is referred as canonical molecular orbital (CMO). [38] With CMO basis used, Eq. (3.2.66) can be rewritten by

$$\begin{cases} \langle \mathbf{r}_1 | \hat{F} | \mathbf{r}_1 \rangle \varphi_i(\mathbf{r}_1) = \varepsilon_i \varphi_i(\mathbf{r}_1) \quad (i = 1, \ldots, n) \\ \int d\mathbf{r}_1 \varphi_i^*(\mathbf{r}_1) \varphi_j(\mathbf{r}_1) = \delta_{ij} \quad (i, j = 1, \ldots, n). \end{cases} \tag{3.2.71}$$

The non-linear eigenvalue equations are called canonical Hartree-Fock equation. The eigenvalues ε_i and eigenfunctions φ_i are referred as HF molecular orbital energies and occupied (canonical) MOs. [147] Once the occupied MOs are obtained, Hartree-Fock energy is given by

$$E^{\mathrm{HF}} = \sum_{i=1}^{n} \varepsilon_i - \frac{1}{2} \sum_{i,j=1}^{n} \langle ij \| ij \rangle \,. \tag{3.2.72}$$

HF theory provides a feasible procedure to obtain approximated solution of Schrödinger equation by reducing the problem of a $3n$-dimensional partial differential equation to that of n 3-dimensional partial differential equations. However, it is not so easy to solve HF equation because of its non-linearity. While SOs are determined as the eigenfunctions of Fock operator, Fock operator itself depends on SOs. Therefore, SOs must be determined in a consistent manner. That is, SOs must be the eigenfunctions of Fock operator composed of the SOs themselves. So, HF theory is also referred as self-consistent field (SCF) theory.

The orbital invariance of HF theory [39] is important for orbital analysis. If the occpied SOs are transformed by a unitary matrix $\mathbf{u}$:

$$|i\rangle \to |i'\rangle = \sum_{i'=1}^{n} |i\rangle u_{ii'}, \tag{3.2.73}$$

the HF wavefinction is transformed by

$$|\Phi\rangle \to |\Phi'\rangle = \sum_{\sigma_1, \ldots, \sigma_n} \left(\sum_{\sigma'_1, \ldots, \sigma'_n} \varepsilon^{\sigma'_1 \ldots \sigma'_n} u_{\sigma_1 \sigma'_1} \cdots u_{\sigma_n \sigma'_n} \right) |\sigma_1\rangle \otimes \cdots \otimes |\sigma_n\rangle. \tag{3.2.74}$$

Using the relation

$$\sum_{\sigma'_1, \ldots, \sigma'_n} \varepsilon^{\sigma'_1 \ldots \sigma'_n} u_{\sigma_1 \sigma'_1} \cdots u_{\sigma_n \sigma'_n} = (\det \mathbf{u}) \, \varepsilon_{\sigma_1 \ldots \sigma_n}, \tag{3.2.75}$$

the transformation rule of HF wavefunction can be simplified as follows:

$$\left|\Phi\right\rangle \rightarrow \left|\Phi'\right\rangle = (\det\mathbf{u}) \left|\Phi\right\rangle. \tag{3.2.76}$$

From the definition of unitary matrix, $\mathbf{u}^{\dagger}\mathbf{u} = \mathbf{1}$,

$$\det\mathbf{u} = e^{i\theta} \quad (\theta \in \mathbb{R}) \tag{3.2.77}$$

is obtained. Therefore, the energy of the system is invariant to the global unitary transformation of SOs:

$$\begin{aligned} \left\langle\Phi\right|\hat{H}\left|\Phi\right\rangle \rightarrow & \left\langle\Phi'\right|\hat{H}\left|\Phi'\right\rangle \\ & = e^{-i\theta}e^{i\theta}\left\langle\Phi\right|\hat{H}\left|\Phi\right\rangle \\ & = \left\langle\Phi\right|\hat{H}\left|\Phi\right\rangle. \end{aligned} \tag{3.2.78}$$

The constraint part of HF Lagrangian is also invariant:

$$\begin{aligned} \sum_{i,j=1}^{n} \varepsilon_{ji} \left(\langle i|j\rangle - \delta_{ij}\right) \rightarrow & \sum_{i',j'=1}^{n} \varepsilon_{j'i'} \left(\langle i'|j'\rangle - \delta_{i'j'}\right) \\ & = \sum_{i',j'=1}^{n} \sum_{i,j=1}^{n} \varepsilon_{ji} u^{*}_{jj'} u_{ii'} \sum_{k,l=1}^{n} \left(\langle k|l\rangle - \delta_{kl}\right) u^{*}_{kj'} u_{li'} \\ & = \sum_{i,j=1}^{n} \varepsilon_{ji} \sum_{k,l=1}^{n} \left(\langle k|l\rangle - \delta_{kl}\right) \delta_{kj}\delta_{li} \\ & = \sum_{i,j=1}^{n} \varepsilon_{ji} \left(\langle i|j\rangle - \delta_{ij}\right). \end{aligned} \tag{3.2.79}$$

Consequently, HF Lagrangian is confirmed to be invariant to arbitrary global unitary transformation of SOs:

$$\mathcal{L} \rightarrow \mathcal{L}' = \mathcal{L}. \tag{3.2.80}$$

This indicate that any global unitary transformation of occupied SOs dose not affect the nature of the system. Therefore, occupied SOs may be rotated for the convenience of analysis. It should be re-emphasized that there is no specific set of SOs which is physically more significant than the others. [168] The concept of SOs is just like that of coordinates and there is no absolute standard.

3.2.4 Hartree-Fock-Roothaan equation

Hartree-Fock-Roothaan (HFR) equation is obtained by introducing basis function to Hartree-Fock theory. [147] The unknown spin-orbitals (SOs) are represented as linear combinations of spin-orbital basis functions $\{\chi_\mu\}_{\mu=1,\ldots,2N_{basis}}$ [136]:

$$\psi_i(\mathbf{x}) \approx \sum_{\mu=1}^{2N_{basis}} c_{\mu i}\chi_\mu(\mathbf{x}) \tag{3.2.81}$$

where $c_{\mu i}$ is called spin-orbital (SO) coefficient. $2N_{basis}$ is the number of the spin-orbital basis functions. Generally, the basis set is not necessarily orthonormal and overlap matrix defined by

$$S_{\mu\nu} \coloneqq \langle \mu | \nu \rangle \tag{3.2.82}$$

gives the metric for the SO coefficient space. Overlap matrix is positive-semidefinite. Thus, the dimension of SO space, given by $\mathrm{rank}(\mathbf{S})$, is $2N_{basis}$ or less. Using basis functions, HF energy is given by

$$\begin{aligned}\langle \Phi | \hat{H} | \Phi \rangle \approx & \sum_{i=1}^{n}\sum_{\mu,\nu=1}^{2N_{basis}} \left(\langle \mu | \hat{T}_e | \nu \rangle + \langle \mu | \hat{V}_{eN} | \nu \rangle \right) c_{\mu i}^* c_{\nu i} \\ & + \frac{1}{2}\sum_{i,j=1}^{n}\sum_{\lambda,\kappa,\mu,\nu=1}^{2N_{basis}} \langle \mu\lambda \| \nu\kappa \rangle \, c_{\mu i}^* c_{\lambda j}^* c_{\nu i} c_{\kappa j}.\end{aligned} \tag{3.2.83}$$

Note that spin-orbital basis functions, that are the functions of not only space coordinates but also of spin coordinates, are used here. The stationary condition of HF Lagrangian is given by a set of matrix equations:

$$\begin{cases} \sum_{\nu=1}^{2N_{basis}} F_{\mu\nu} c_{\nu i} = \sum_{\nu=1}^{2N_{basis}} S_{\mu\nu} c_{\nu i} \varepsilon_i \\ \sum_{\mu,\nu=1}^{2N_{basis}} S_{\mu\nu} c_{\mu i}^* c_{\nu j} = \delta_{ij} \end{cases} . \quad (i,j = 1,\ldots,n) \tag{3.2.84}$$

The former is referred as HFR equation and the latter is the orthonormal condition of SOs. The solution of HFR equation is n SO coefficient vectors. These n SO coefficient vectors give a set of approximated occupied SOs by Eq. (3.2.81). As the by-product of HFR equation, $(\mathrm{rank}(\mathbf{S}) - n)$ SO coefficient vectors orthogonal to all the occupied ones are obtained. The excess are called virtual orbitals or unoccupied orbitals. [147] Apparently, the energy given by HFR equation is invariant to any unitary transformation within the virtual orbital space because HF Lagrangian does not include any contribution of virtual SOs. Also, arbitrary unitary transformation within occupied SO space leaves the energy invariant. Therefore, same as the case of HF equation, arbitrary

rotation within occupied or virtual SO space is allowed. However, any rotation between occupied and virtual orbitals alters the nature of the system. Therefore, any rotation between the occupied and virtual SO spaces should be avoided with no special reason.

3.2.5 Coupled perturbed self-consistent field theory

Coupled perturbed self-consistent field (CP-SCF) theory [60,136] is an application of perturbation theory to SCF theory. The type of perturbation is not limited to external field like electric field. Actually, CP-SCF calculation with respect to the perturbation of nuclear coordinates is utilized to compute Hessian matrix of potential energy which is especially important for vibrational analysis. [136] Also, CP-SCF calculation is required to confirm the stability of stationary point of potential energy surface. Thus, CP-SCF calculation is frequently performed in the course of minimum or saddle optimization. The derivation of CP-SCF mainly based on Ref. [136] is reviewed in the following.

Hartree-Fock-Roothaan (HFR) equation is given by

$$\mathbf{FC} - \mathbf{SC}\boldsymbol{\varepsilon} = \mathbf{0} \tag{3.2.85}$$

where $\mathbf{F}, \mathbf{C}, \mathbf{S}$ and $\boldsymbol{\varepsilon}$ are Fock matrix, spin orbital (SO) coefficient matrix, overlap matrix and diagonal SO energy matrix, respectively. With finite basis set, all of these matrices depend on molecular geometry. Since HFR equation holds at any geometry except for that located on conical intersection, derivatives of the lhs of equation Eq. (3.2.85)) with respective to nuclear coordinates must be zero:

$$\partial_{\mathfrak{I}}\mathbf{FC} + \mathbf{F}\partial_{\mathfrak{I}}\mathbf{C} - \partial_{\mathfrak{I}}\mathbf{SC}\boldsymbol{\varepsilon} - \mathbf{S}\partial_{\mathfrak{I}}\mathbf{C}\boldsymbol{\varepsilon} - \mathbf{SC}\partial_{\mathfrak{I}}\boldsymbol{\varepsilon} = \mathbf{0}. \quad (\mathfrak{I} = 1, \ldots, 3N^{nuc}) \tag{3.2.86}$$

By multiplying $\mathbf{C}^\dagger$, Hermititian conjugate of $\mathbf{C}$, from the left,

$$\mathbf{C}^\dagger\partial_{\mathfrak{I}}\mathbf{FC} + \boldsymbol{\varepsilon}\mathbf{C}^\dagger\mathbf{S}\partial_{\mathfrak{I}}\mathbf{C} - \mathbf{C}^\dagger\partial_{\mathfrak{I}}\mathbf{SC}\boldsymbol{\varepsilon} - \mathbf{C}^\dagger\mathbf{S}\partial_{\mathfrak{I}}\mathbf{C}\boldsymbol{\varepsilon} - \partial_{\mathfrak{I}}\boldsymbol{\varepsilon} = \mathbf{0} \tag{3.2.87}$$

is obtained, where equation Eq. (3.2.85) and the orthonormal condition of MOs:

$$\mathbf{C}^\dagger\mathbf{SC} = \mathbf{1} \tag{3.2.88}$$

are used. $\mathbf{1}$ is the unit matrix. By introducing the matrices

$$\begin{cases} \mathbf{F}^{(1)}_{\mathfrak{I}} & \coloneqq \mathbf{C}^\dagger\partial_{\mathfrak{I}}\mathbf{FC} \\ \mathbf{U}^{(1)}_{\mathfrak{I}} & \coloneqq \mathbf{C}^\dagger\mathbf{S}\partial_{\mathfrak{I}}\mathbf{C} \\ \mathbf{S}^{(1)}_{\mathfrak{I}} & \coloneqq \mathbf{C}^\dagger\partial_{\mathfrak{I}}\mathbf{SC} \end{cases}, \tag{3.2.89}$$

equation Eq. (3.2.87) can be rewritten by

$$\mathbf{F}_{\mathfrak{J}}^{(1)} + \boldsymbol{\varepsilon}\mathbf{U}_{\mathfrak{J}}^{(1)} - \mathbf{S}_{\mathfrak{J}}^{(1)}\boldsymbol{\varepsilon} - \mathbf{U}_{\mathfrak{J}}^{(1)}\boldsymbol{\varepsilon} - \partial_{\mathfrak{J}}\boldsymbol{\varepsilon} = \mathbf{0}. \tag{3.2.90}$$

Similarly, the derivatives of equation Eq. (3.2.88) with respect to nuclear coordinates give

$$\mathbf{U}_{\mathfrak{J}}^{(1)\dagger} + \mathbf{S}_{\mathfrak{J}}^{(1)} + \mathbf{U}_{\mathfrak{J}}^{(1)} = \mathbf{0}. \tag{3.2.91}$$

Equations Eq. (3.2.90) and Eq. (3.2.91) are solved for $\mathbf{U}_{\mathfrak{J}}^{(1)}$ and $\partial_{\mathfrak{J}}\boldsymbol{\varepsilon}$.

It should be noted that $\mathbf{F}_{\mathfrak{J}}^{(1)}$ depends on the virtual-occupied block of $\mathbf{U}_{\mathfrak{J}}^{(1)}$. $\mathbf{F}_{\mathfrak{J}}^{(1)}$ is divided into one-electron part $\mathbf{h}_{\mathfrak{J}}^{(1)}$ and two-electron part $\mathbf{G}_{\mathfrak{J}}^{(1)}$:

$$\mathbf{F}_{\mathfrak{J}}^{(1)} = \mathbf{h}_{\mathfrak{J}}^{(1)} + \mathbf{G}_{\mathfrak{J}}^{(1)}. \tag{3.2.92}$$

The one-electron part doesn't include derivative of SO coefficient while the two-electron part does.

$$\begin{aligned}\partial_{\mathfrak{J}} \sum_{\kappa,\lambda} \sum_{i\in occ.} c_{\lambda i}^* c_{\kappa i} \langle \mu\lambda \| \nu\kappa \rangle = &\sum_{\kappa,\lambda} \sum_{i\in occ.} \sum_{p} \left(U_{\mathfrak{J}pi}^{(1)*} c_{\lambda p}^* c_{\kappa i} + U_{\mathfrak{J}pi}^{(1)} c_{\lambda i}^* c_{\kappa p} \right) \langle \mu\lambda \| \nu\kappa \rangle \\ &+ \sum_{\kappa,\lambda} \sum_{i\in occ.} c_{\lambda i}^* c_{\kappa i} \partial_{\mathfrak{J}} \langle \mu\lambda \| \nu\kappa \rangle\end{aligned} \tag{3.2.93}$$

where

$$\begin{aligned}\partial_{\mathfrak{J}} c_{\mu p} &= \sum_{\kappa,\lambda} \sum_{q} c_{\mu q} c_{\kappa q}^* S_{\kappa\lambda} \partial_{\mathfrak{J}} c_{\lambda p} \\ &= \sum_{q} c_{\mu q} U_{\mathfrak{J}qp}^{(1)}\end{aligned} \tag{3.2.94}$$

is used. In uncoupled-perturbed SCF theory, the response of two-electron part is ignored. [18] The first term of Eq. (3.2.93) can be divided into the occupied part and the virtual part:

$$\sum_{\kappa,\lambda} \left(\sum_{i,j\in occ.} \left(U_{\mathfrak{J}ij}^{(1)*} c_{\lambda i}^* c_{\kappa j} + U_{\mathfrak{J}ij}^{(1)} c_{\lambda j}^* c_{\kappa i} \right) \langle \mu\lambda \| \nu\kappa \rangle + \sum_{a\in vir.} \sum_{j\in occ.} \left(U_{\mathfrak{J}aj}^{(1)*} c_{\lambda a}^* c_{\kappa j} + U_{\mathfrak{J}aj}^{(1)} c_{\lambda j}^* c_{\kappa a} \right) \langle \mu\lambda \| \nu\kappa \rangle \right) \tag{3.2.95}$$

The occupied part can be rewritten by

$$\begin{aligned}\sum_{\kappa,\lambda}\sum_{i,j\in occ.}\left(U^{(1)*}_{\mathfrak{J}ji}c^*_{\lambda j}c_{\kappa i}+U^{(1)}_{\mathfrak{J}ji}c^*_{\lambda i}c_{\kappa j}\right)\langle\mu\lambda\|\nu\kappa\rangle &= \sum_{\kappa,\lambda}\sum_{i,j\in occ.}\left(U^{(1)*}_{\mathfrak{J}ij}c^*_{\lambda i}c_{\kappa j}+U^{(1)}_{\mathfrak{J}ji}c^*_{\lambda i}c_{\kappa j}\right)\langle\mu\lambda\|\nu\kappa\rangle \\ &= -\sum_{\kappa,\lambda}\sum_{i,j\in occ.}S^{(1)}_{\mathfrak{J}ji}c^*_{\lambda i}c_{\kappa j}\langle\mu\lambda\|\nu\kappa\rangle\,. \quad (\because (3.2.91))\end{aligned} \tag{3.2.96}$$

Thus, matrix elements of $\mathbf{F}^{(1)}_{\mathfrak{J}}$ is given by

$$\begin{aligned}F^{(1)}_{\mathfrak{J}pq} =& \sum_{\mu,\nu}\partial_{\mathfrak{J}}h_{\mu\nu}c^*_{\mu p}c_{\nu q} \\ &+\sum_{i,j\in occ.}S^{(1)}_{\mathfrak{J}ji}\langle pi\|qj\rangle+\sum_{a\in vir.}\sum_{i\in occ.}\left(U^{(1)*}_{\mathfrak{J}ai}\langle pa\|qi\rangle+U^{(1)}_{\mathfrak{J}ai}\langle pi\|qa\rangle\right) \\ &+\sum_{\kappa,\lambda,\mu,\nu}\sum_{i\in occ.}c^*_{\mu p}c^*_{\lambda i}c_{\nu q}c_{\kappa i}\partial_{\mathfrak{J}}\langle\mu\lambda\|\nu\kappa\rangle\,.\end{aligned} \tag{3.2.97}$$

where

$$h_{\mu\nu}=\left\langle\mu\middle|\hat{T}_e+\hat{V}_{eN}\middle|\nu\right\rangle. \tag{3.2.98}$$

In CP-SCF calculation, the off-diagonal part of equation Eq. (3.2.90):

$$(\varepsilon_p-\varepsilon_q)U^{(1)}_{\mathfrak{J}pq}+F^{(1)}_{\mathfrak{J}pq}-S^{(1)}_{\mathfrak{J}pq}\varepsilon_q=0 \quad (p\neq q) \tag{3.2.99}$$

is solved for virtual-occupied block and $U^{(1)}_{\mathfrak{J}ai}(a\in vir.\ \ i\in occ.)$ are obtained. As shown in equation Eq. (3.2.97), $\mathbf{F}^{(1)}_{\mathfrak{J}}$ doesn't include the occupied-occupied and virtual-virtual blocks of $\mathbf{U}^{(1)}_{\mathfrak{J}}$. Thus, all the elements of $\mathbf{F}^{(1)}_{\mathfrak{J}}$ can be computed once the virtual-occupied block of $\mathbf{U}^{(1)}_{\mathfrak{J}}$ is obtained. Then, the diagonal part of equation Eq. (3.2.90):

$$\partial_{\mathfrak{J}}\varepsilon_p=F^{(1)}_{\mathfrak{J}pp}-S^{(1)}_{\mathfrak{J}pp}\varepsilon_p \tag{3.2.100}$$

gives all the elements of $\partial_{\mathfrak{J}}\boldsymbol{\varepsilon}$. It should be noted that $\partial_{\mathfrak{J}}\boldsymbol{\varepsilon}$ is diagonal matrix because $\boldsymbol{\varepsilon}$ is diagonal at any geometries. Usually, the virtual-virtual and occupied-occupied blocks of $\mathbf{U}^{(1)}_{\mathfrak{J}}$ are not computed since they are not necessary for Hessian matrix calculation. [136]

The Hessian matrix of Hartree-Fock energy is given by

$$\begin{aligned}\partial_{\mathfrak{H}}\partial_{\mathfrak{I}}E^{\mathrm{HF}} =& \sum_{i\in occ}\sum_{\mu,\nu} c^*_{\mu i}c_{\nu i}\partial_{\mathfrak{H}}\partial_{\mathfrak{I}}h_{\mu\nu} + \frac{1}{2}\sum_{i,j\in occ}\sum_{\kappa,\lambda,\mu,\nu} c^*_{\lambda i}c^*_{\mu j}c_{\kappa i}c_{\nu j}\partial_{\mathfrak{H}}\partial_{\mathfrak{I}}\left\langle\mu\lambda\|\nu\kappa\right\rangle + \partial_{\mathfrak{H}}\partial_{\mathfrak{I}}V_{NN} \\ &+ \sum_{i\in occ}\sum_{\mu,\nu}\partial_{\mathfrak{I}}\left(c^*_{\mu i}c_{\nu i}\right)\left(\partial_{\mathfrak{H}}h_{\mu\nu} + \sum_{j\in occ}\sum_{\kappa,\lambda} c^*_{\lambda j}c_{\kappa j}\partial_{\mathfrak{H}}\left\langle\mu\lambda\|\nu\kappa\right\rangle\right) \\ &- \sum_{i\in occ}\sum_{\mu,\nu}\partial_{\mathfrak{I}}\left(c^*_{\mu i}c_{\nu i}\varepsilon_i\partial_{\mathfrak{H}}S_{\mu\nu}\right).\end{aligned} \tag{3.2.101}$$

The three terms in the first line are the derivatives of operators and do not include the SO derivative. This Hessian matrix can be rewritten by

$$\begin{aligned}\partial_{\mathfrak{H}}\partial_{\mathfrak{I}}E^{\mathrm{HF}} =& \sum_{i\in occ}\sum_{\mu,\nu} c^*_{\mu i}c_{\nu i}\partial_{\mathfrak{H}}\partial_{\mathfrak{I}}h_{\mu\nu} + \frac{1}{2}\sum_{i,j\in occ}\sum_{\kappa,\lambda,\mu,\nu} c^*_{\lambda i}c^*_{\mu j}c_{\kappa i}c_{\nu j}\partial_{\mathfrak{H}}\partial_{\mathfrak{I}}\left\langle\mu\lambda\|\nu\kappa\right\rangle + \partial_{\mathfrak{H}}\partial_{\mathfrak{I}}V_{NN} \\ &+ \sum_{i\in occ}\sum_{\mu,\nu}\partial_{\mathfrak{I}}\left(c^*_{\mu i}c_{\nu i}\right)\left(F^{(1)}_{\mathfrak{H}\mu\nu} - S^{(1)}_{\mathfrak{H}\mu\nu}\varepsilon_i\right) \\ &- \sum_{i,j\in occ}\sum_{\kappa,\lambda,\mu,\nu}\partial_{\mathfrak{I}}\left(c^*_{\mu i}c_{\nu i}\right)\partial_{\mathfrak{H}}\left(c^*_{\lambda j}c_{\kappa j}\right)\left\langle\mu\lambda\|\nu\kappa\right\rangle \\ &- \sum_{i\in occ}\sum_{\mu,\nu} c^*_{\mu i}c_{\nu i}\partial_{\mathfrak{I}}\left(\varepsilon_i\partial_{\mathfrak{H}}S_{\mu\nu}\right)\end{aligned} \tag{3.2.102}$$

or

$$
\begin{aligned}
\partial_{\mathfrak{H}}\partial_{\mathfrak{I}}E^{\mathrm{HF}} = &\sum_{i\in occ}\sum_{\mu,\nu} c^*_{\mu i}c_{\nu i}\partial_{\mathfrak{H}}\partial_{\mathfrak{I}}h_{\mu\nu} + \frac{1}{2}\sum_{ij\in occ}\sum_{\kappa,\lambda,\mu,\nu} c^*_{\lambda i}c^*_{\mu j}c_{\kappa i}c_{\nu j}\partial_{\mathfrak{H}}\partial_{\mathfrak{I}}\left\langle \mu\lambda\|\nu\kappa\right\rangle + \partial_{\mathfrak{H}}\partial_{\mathfrak{I}}V_{NN} \\
&- \sum_{a\in vir}\sum_{i\in occ}\left(\varepsilon_a-\varepsilon_i\right)\left(U^{(1)*}_{\mathfrak{I}ai}U^{(1)}_{\mathfrak{H}ai} + U^{(1)*}_{\mathfrak{H}ai}U^{(1)}_{\mathfrak{I}ai}\right) \\
&- \sum_{i,j\in occ}\sum_{a,b\in vir} U^{(1)*}_{\mathfrak{I}ai}U^{(1)*}_{\mathfrak{H}bj}\left\langle ab\|ij\right\rangle + U^{(1)}_{\mathfrak{I}ai}U^{(1)}_{\mathfrak{H}bj}\left\langle ij\|ab\right\rangle \\
&- \sum_{i,j\in occ}\sum_{a,b\in vir}\left(U^{(1)*}_{\mathfrak{I}ai}U^{(1)}_{\mathfrak{H}bj} + U^{(1)*}_{\mathfrak{H}ai}U^{(1)}_{\mathfrak{I}bj}\right)\left\langle aj\|ib\right\rangle \\
&+ \sum_{i,j,k\in occ}\sum_{a\in vir} S^{(1)}_{\mathfrak{H}kj}\left(U^{(1)*}_{\mathfrak{I}ai}\left\langle ak\|ij\right\rangle + U^{(1)}_{\mathfrak{I}ai}\left\langle ik\|aj\right\rangle\right) \\
&+ \sum_{i,j,k\in occ}\sum_{a\in vir} S^{(1)}_{\mathfrak{I}kj}\left(U^{(1)*}_{\mathfrak{H}aj}\left\langle ak\|ij\right\rangle + U^{(1)}_{\mathfrak{H}ai}\left\langle ik\|aj\right\rangle\right) \\
&- \sum_{i,j,k,l\in occ} S^{(1)}_{\mathfrak{I}ki}S^{(1)}_{\mathfrak{H}lj}\left\langle kl\|ij\right\rangle \\
&- \sum_{i\in occ} S^{(1)}_{\mathfrak{I}ii}\partial_{\mathfrak{H}}\varepsilon_i + S^{(1)}_{\mathfrak{H}ii}\partial_{\mathfrak{I}}\varepsilon_i - \sum_{i\in occ}\sum_{\mu,\nu} c^*_{\mu i}c^*_{\nu i}\partial_{\mathfrak{I}}\partial_{\mathfrak{H}}S_{\mu\nu}\varepsilon_i.
\end{aligned}
\tag{3.2.103}
$$

The three terms in the first line are derivatives of operators and do not include SO derivatives. The second term, the derivative of two-electron integrals, is trivial at HF limit. The terms in the second to fourth lines include the contribution of orbital mixing between occupied and virtual SOs. All the remains include the derivatives of overlap matrix which disappear at HF limit with infinite basis set used. It should be remarked that Eq. (3.2.103) is analogous to Herzberg-Teller expansion. [150] The first and third terms in the first line are analogous to the non-vibronic term of Herzberg-Teller expansion and positive definite. [59] Hence, the cause of negative force constant is attributed to terms in the second to fourth lines at HF limit. This indicates that orbital mixing between occupied and virtual orbitals is essential for the relaxation of potential energy surface given by HF theory. Considering that the potential relaxation along a reaction pathway is essential for the reaction to proceed, [150] orbital mixing seems to be very important for understanding reaction mechanisms.

3.2.6 Singular value decomposition

Singular value decomposition (SVD) or Autonne-Eckart-Young decomposition is one of matrix decomposition methods. [89] There are many applications of SVD to MO analysis [1, 48, 56, 112, 121, 158, 182] because it is a very powerful tool for projection and

characterization of interaction or entanglement between different subspaces.

Given complex rectangular matrix $\mathbf{A}$ of oder $m \times n$ can be written by

$$\mathbf{A} = \sum_{i=1}^{m} \sum_{j=1}^{n} A_{ij} \boldsymbol{e}'_i \otimes \boldsymbol{e}_j, \tag{3.2.104}$$

where $\boldsymbol{e}'_i$, $\boldsymbol{e}_j$ and A_{ij} are some orthonormal basis for the i-th row and column and the elements respectively. SVD gives a pair of orthonormal basis sets $\{\boldsymbol{u}_i\}_{i\in\{1,\ldots,\min(m,n)\}}$ and $\{\boldsymbol{v}_i\}_{i\in\{1,\ldots,\min(m,n)\}}$ with which $\mathbf{A}$ is simplified as

$$\mathbf{A} = \sum_{i=1}^{\min(m,n)} \lambda_i \boldsymbol{u}_i \otimes \boldsymbol{v}_i. \tag{3.2.105}$$

The vectors $\boldsymbol{u}_i$ and $\boldsymbol{v}_i$ are called left- and right-singular vectors. Non-negative real values λ_i are called singular values. The right-singular vectors satisfy the following eigenvalue equation:

$$\left(\mathbf{A}^\dagger \mathbf{A}\right) \boldsymbol{v}_i = \lambda_i^2 \boldsymbol{v}_i. \quad (i = 1, \ldots, \min(m,n)) \tag{3.2.106}$$

Since $\mathbf{A}^\dagger\mathbf{A}$ is apparently Hermitian and positive semi-definite, it is always diagonalizable for any $\mathbf{A}$ and has non-negative real eigenvalues. Thus, there always exist an orthonormal basis which satisfies Eq. (3.2.106). Usually, the positive square roots of λ_i^2 are chosen as singular values. Multiplied $\mathbf{A}$ from the left of Eq. (3.2.106),

$$\left(\mathbf{A}\mathbf{A}^\dagger\right) \mathbf{A}\boldsymbol{v}_i = \lambda_i^2 \mathbf{A}\boldsymbol{v}_i. \quad (i = 1, \ldots, \min(m,n)) \tag{3.2.107}$$

is obtained. Eq. (3.2.107) shows that $\mathbf{A}\boldsymbol{v}_i$ is an eigenvector of the Hermitian matrix $\mathbf{A}\mathbf{A}^\dagger$ with the eigenvalue of λ_i^2. The norm of $\mathbf{A}\boldsymbol{v}_i$ is given by λ_i from Eq. (3.2.106). Then, orthonormal basis set $\{\boldsymbol{u}_i\}_{i\in\{1,\ldots,\min(m,n)\}}$ can be defined by

$$\mathbf{A}\boldsymbol{v}_i = \lambda_i \boldsymbol{u}_i \quad (i = 1, \ldots, \min(m,n)). \tag{3.2.108}$$

Then, the following equation is obtained

$$\langle \boldsymbol{u}_i, \mathbf{A}\boldsymbol{v}_j \rangle = \lambda_j \delta_{ij} \quad (i, j = 1, \ldots, \min(m,n)) \tag{3.2.109}$$

from the orthonormality of $\{\boldsymbol{u}_i\}_{i\in\{1,\ldots,\min(m,n)\}}$. This shows that $\mathbf{A}$ can be written in the form of Eq. (3.2.105).

Matrix representation of Eq. (3.2.105) is given by

$$\mathbf{A} = \mathbf{U}\mathbf{\Lambda}\mathbf{V}^{\dagger}, \tag{3.2.110}$$

where the columns of $\mathbf{U}$ and rows of $\mathbf{V}^{\dagger}$ the left- and right-singular vectors and the vectors respectively. For convenience, the basis in the orthocomplements of $\{\boldsymbol{u}_i\}_{i\in\{1,\ldots,\min(m,n)\}}$ and $\{\boldsymbol{v}_i\}_{i\in\{1,\ldots,\min(m,n)\}}$ are also included in $\mathbf{U}$ and $\mathbf{V}^{\dagger}$ respectively. Thus, $\mathbf{U}$ and $\mathbf{V}$ are square unitary matrices of order $m \times m$ and $n \times n$. The rectangular diagonal matrix $\mathbf{\Lambda}$ of order $m \times n$ contains the singular values as its diagonal elements.

SVD is known to preserve Frobenius norm of $\mathbf{A}$ defined by

$$\|\mathbf{A}\|_F \coloneqq \left(\mathrm{Tr}\left(\mathbf{A}^{\dagger}\mathbf{A}\right)\right)^{1/2} = \left(\mathrm{Tr}\left(\mathbf{A}\mathbf{A}^{\dagger}\right)\right)^{1/2}. \tag{3.2.111}$$

This is confirmed as following

$$\begin{aligned} \mathrm{Tr}\left(\mathbf{A}^{\dagger}\mathbf{A}\right) &= \mathrm{Tr}\left(\mathbf{V}\mathbf{\Lambda}^{\dagger}\mathbf{U}^{\dagger}\mathbf{U}\mathbf{\Lambda}\mathbf{V}^{\dagger}\right) \\ &= \mathrm{Tr}\left(\mathbf{\Lambda}^{\dagger}\mathbf{\Lambda}\right) \\ &= \sum_{i=1}^{\min(m,n)} \lambda_i^2. \end{aligned} \tag{3.2.112}$$

The quantity defined by

$$\frac{\lambda_i^2}{\sum_{i=1}^{\min(m,n)} \lambda_i^2} \tag{3.2.113}$$

is contribution ratio of the i-th singular vectors.

3.2.7 Natural reaction orbital (NRO)

Natural reaction orbital (NRO) is defined as the SVD basis of the virtual-occupied block of first-order response matrix of molecular orbital with respect to nuclear coordinate displacement in mass-weighted coordinates. [33]. Let $\boldsymbol{v}$ be a unit direction vector. The first-order orbital response matrix to the nuclear displacement in the direction of $\boldsymbol{v}$ is given by

$$\mathbf{U}^{(1)} \coloneqq \sum_{\mathfrak{I}=1}^{3N} v_{\mathfrak{I}} \mathbf{U}_{\mathfrak{I}}^{(1)}. \tag{3.2.114}$$

The virtual-occupied block of Eq. (3.2.114) is decomposed by SVD:

$$\mathbf{U}_{\mathrm{VO}}^{(1)} = \mathbf{L}\mathbf{\Lambda}\mathbf{R}^{\dagger}. \tag{3.2.115}$$

The left and right singular vectors $\mathbf{L}$ and $\mathbf{R}$ are $N_{vir} \times N_{vir}$ and $N_{occ} \times N_{occ}$ unitary matrices, N_{occ} and N_{vir} are number of occupied orbitals and number of virtual orbitals respectively. The occupied and virtual spin orbital coefficient matrix $\mathbf{C}_{\mathrm{O}}$ and $\mathbf{C}_{\mathrm{V}}$ are transformed separately with $\mathbf{L}$ and $\mathbf{R}$ respectively:

$$\begin{cases} \boldsymbol{n}_{\mathrm{O}} & \coloneqq \mathbf{C}_{\mathrm{O}}\mathbf{R} \\ \boldsymbol{n}_{\mathrm{V}} & \coloneqq \mathbf{C}_{\mathrm{V}}\mathbf{L} \end{cases}. \tag{3.2.116}$$

The generated orbital coefficient matrices $\boldsymbol{n}_{\mathrm{O}}$ and $\boldsymbol{n}_{\mathrm{V}}$ are the occupied and virtual natural reaction orbital (NRO) coefficient matrices respectively. It should be emphasized that the Hartree-Fock wavefunction is not altered through this transformation because HF wavefunction is invariant to given unitary transformation within the occupied orbital space and within the virtual orbital space.

As the nature of SVD, the occupied and virtual NROs form pairs sharing common singular values.

$$\sum_{a=N_{occ}+1}^{N_{occ}+N_{vir}} \sum_{i=1}^{N_{occ}} U_{ai}^{(1)} c_{\mu a} c_{\nu i}^{*} = \sum_{i=1}^{\min(N_{occ},N_{vir})} \lambda_i n_{\mu i}^{vir} n_{\nu i}^{occ*} \tag{3.2.117}$$

The virtual-occupied block of the first-order orbital response matrix can be simplified with NRO basis:

$$\sum_{a=N_{occ}+1}^{N_{occ}+N_{vir}} \sum_{i=1}^{N_{occ}} U_{ai}^{(1)} c_{\mu a} c_{\nu i}^{*} = \sum_{i=1}^{\min(N_{occ},N_{vir})} \lambda_i n_{\mu i}^{vir} n_{\nu i}^{occ*}. \tag{3.2.118}$$

Actually, the virtual-occupied block of the first-order orbital response matrix can be regarded as that of the first-order spin-orbital density response caused by the orbital mixing between occupied and virtual orbitals. The first-order spin-orbital density matrix of HF theory is defined by

$$\gamma_{\mu\nu} = \sum_{i \in occ} c_{\mu i} c_{\nu i}^{*}. \tag{3.2.119}$$

Directional derivative of the spin-orbital density matrix with respect to $\boldsymbol{v}$ is given by

$$\partial_{\boldsymbol{v}} \gamma_{\mu\nu} = \sum_{i \in occ} \sum_{p} \left(U_{pi}^{(1)} c_{\mu p} c_{\nu i}^{*} + U_{pi}^{(1)*} c_{\mu i} c_{\nu p}^{*} \right). \quad (\because (3.2.94)) \tag{3.2.120}$$

By separating occupied and virtual parts, the following is obtained,

$$\begin{aligned}\partial_{\boldsymbol{v}}\gamma_{\mu\nu} = &\sum_{i\in occ}\sum_{a\in vir}\left(U_{ai}^{(1)}c_{\mu a}c_{\nu i}^{*} + U_{ai}^{(1)*}c_{\mu i}c_{\nu a}^{*}\right) \\ &- \sum_{ij\in occ} S_{ji}^{(1)}c_{\mu j}c_{\nu i}^{*}. \quad (\because (3.2.91))\end{aligned} \tag{3.2.121}$$

The second term in the rhs is rather trivial term because it appears only to ensure the orthonormal condition of occupied orbitals to hold at any geometries. It appears just because the basis set is finite. Furthermore, orbital mixing within occupied orbitals gives no change to the system. Accordingly, the first-order response of the first-order spin-orbital density matrix caused by the orbital mixing between the occupied and virtual orbitals is given by [136]

$$\partial_{\boldsymbol{v}}(\gamma_{\mathrm{VO}})_{\mu\nu} = \sum_{i=1}^{\min(N_{occ},N_{vir})} \lambda_i \left(n_{\mu i}^{vir}n_{\nu i}^{occ*} + n_{\mu i}^{occ}n_{\nu i}^{vir*}\right). \tag{3.2.122}$$

Eq. (3.2.122) shows that NRO basis can be considered as an optimal basis to characterize spin-orbital density change induced by nuclear displacements. [172] Some demonstrative applications of the relationship between NRO and first-order response of spin-orbital density are presented in the next section.

Herein, the symmetry of NRO basis is discussed. If a system has some symmetry and the direction of the nuclear displacements belong to some irreducible representation of the symmetry, given *non-degenerated* NRO with non-zero singular value must belong to some appropriate irreducible representation. Assume a system with some symmetry higher than C_1 symmetry and the direction of nuclear displacements belong to some irreducible representation of the symmetry. Pairs of left and right singular vectors satisfy the following equation,

$$\begin{cases}\mathbf{U}_{\mathrm{VO}}^{(1)}\boldsymbol{r}_i &= \lambda_i\boldsymbol{l}_i \\ \mathbf{U}_{\mathrm{VO}}^{(1)\dagger}\boldsymbol{l}_i &= \lambda_i\boldsymbol{r}_i\end{cases}. \quad (i = 1,\ldots,\min(N_{occ},N_{vir})) \tag{3.2.123}$$

With symmetry-adapted basis, $\boldsymbol{l}_i$, $\boldsymbol{r}_i$ and $\mathbf{U}_{\mathrm{VO}}^{(1)}$ can be decomposed into the components of the irreducible representation. Accordingly, equation Eq. (3.2.123) can be rewritten by

$$\begin{cases}\sum_{\Gamma'\Gamma}\mathbf{U}_{\mathrm{VO}}^{(1)\Gamma\Gamma'}\boldsymbol{r}_i^{\Gamma'} &= \lambda_i\sum_{\Gamma}\boldsymbol{l}_i^{\Gamma} \\ \sum_{\Gamma'\Gamma}\mathbf{U}_{\mathrm{VO}}^{(1)\dagger\Gamma\Gamma'}\boldsymbol{l}_i^{\Gamma'} &= \lambda_i\sum_{\Gamma}\boldsymbol{r}_i^{\Gamma}\end{cases}, \quad (i = 1,\ldots,\min(N_{occ},N_{vir})) \tag{3.2.124}$$

where Γ and Γ' denote some irreducible representations. The summation is taken

over all the irreducible representations of the symmetry. Since any vectors in different irreducible representation are orthogonal to each other, the following equations must hold:

$$\begin{cases} \sum_{\Gamma'} \mathbf{U}_{\mathrm{VO}}^{(1)\Gamma\Gamma'} \boldsymbol{r}_i^{\Gamma'} & = \lambda_i \boldsymbol{l}_i^{\Gamma} \\ \sum_{\Gamma'} \mathbf{U}_{\mathrm{VO}}^{(1)\dagger\Gamma\Gamma'} \boldsymbol{l}_i^{\Gamma'} & = \lambda_i \boldsymbol{r}_i^{\Gamma} \end{cases} . \quad (\forall \Gamma) \tag{3.2.125}$$

If $\boldsymbol{r}_i^{\Gamma}$ and $\boldsymbol{l}_i^{\Gamma}$ are non-zero for more than one Γ, it contradicts the assumption that there is no degenerated singular value. Thus, if a singular value is not degenerated, the corresponding NROs belong to some irreducible representations. If a singular value has degeneracy, the corresponding NROs do not necessarily belong to irreducible representations. However, even in the presence of degeneracy, the corresponding NROs can always be made belong to some irreducible representations by solving Eq. (3.2.125) instead of Eq. (3.2.124).

3.2.8 NRO from a viewpoint of geometry

As aformentioned, NRO is the SVD basis of the virtual-occupied block of first-order response matrix of molecular orbitals. This will be enough to define NRO. However, this might be still unsatisfactory to grasp the image of NRO. Thus, some geometric image of NRO is provided in this section. For simplicity, the basis set is assumed to be complete only in this section.

Let canonical molecular orbitals be orthonormalized at every molecular geometry $\mathbf{R}$. Then, the transformation between CMOs at two different geometries are described by unitary transformation. Therefore, CMOs at a geometry infinitesimally displaced from $\mathbf{R}$ is given by

$$\psi_p \left(\mathbf{R} + d\mathbf{R} \right) = \sum_q \psi_q \left(\mathbf{R} \right) T_{qp} \left(\mathbf{R}, d\mathbf{R} \right) , \tag{3.2.126}$$

where T_{qp} is a unitary matrix. Let T_{qp} be expanded as the power series of $d\mathbf{R}$:

$$T_{qp} \left(\mathbf{R}, d\mathbf{R} \right) = \delta_{qp} + \sum_{\mathfrak{I}=1}^{3N^{nuc}} dR_{\mathfrak{I}} U_{\mathfrak{I}qp}^{(1)} \left(\mathbf{R} \right) + O\left(d\mathbf{R}^2 \right) , \tag{3.2.127}$$

where $U_{\mathfrak{I}qp}^{(1)}(\mathbf{R})$ is what defined in Eq. (3.2.89). Provided that the basis set is complete, the following holds:

$$U_{\mathfrak{I}pq}^{(1)*}(\mathbf{R}) = -U_{\mathfrak{I}qp}^{(1)} \left(\mathbf{R} \right) . \quad (\mathfrak{I} = 1, \ldots, 3N^{nuc}) \tag{3.2.128}$$

Thus, the first-order response matrices of MOs are anti-Hermitian. Analogous to Hamiltonian, the generator of infinitesimal time evolution, $-i\mathbf{U}_{\mathfrak{I}}^{(1)}$ can be regarded as the generator of infinitesimal nuclear displacements.

In order to grasp the image of SVD basis of the virtual-occupied block of $\mathbf{U}_{\mathfrak{I}}^{(1)}$, a 3-dimensional vector model is discussed: one virtual MO and two occupied MOs (Fig. 3.1(a)). In this model, the occupied orbital space or HF manifold is the circle spanned by the two occupied orbitals. The virtual orbital space is the poles of the unit sphere (Fig. 3.1(b)). From the orbital invariance of HF theory, orbital rotation between the two occupied orbitals does not affect the nature of the system (Fig. 3.1(c)). Nuclear displacements induce orbital mixing as shown in Fig. 3.1(d). With CMO basis, all the MOs participate in the orbital mixing. On the other hand, with NRO basis shown in Fig. 3.1(e), only two orbitals are mixed (Fig. 3.1(f)). One occupied NRO and the virtual NRO are rotated on the plane spanned by them. This clearly shows that there is no mixing between different NRO pairs. While the mixing shown in Fig. 3.1(f) does not include orbital rotation between the occupied, orbital rotation within occupied orbital space is trivial for the orbital invariance of HF theory. Thus, mixing shown in Fig. 3.1(f) is essentially equivalent to that of Fig. 3.1(d). The degree of orbital mixing between the NRO pair is measured by its singular value. Although there is only one NRO pair in this 3D model, orbital mixing takes place only within each NRO pair even in higher dimension with multiple NRO pairs. Therefore, NRO basis significantly simplifies the view of orbital mixing induced by nuclear displacements.

3.2.9 Straightforward generalization of NRO to mult-configurational theories

The formulation of NRO given above is only applicable to single-configurational theories, e.g., Hartree-Fock theory and Kohn-Sham theory. [74, 93] Theoretically, however, generalization of NRO to multiconfigurational theories [41, 99] is straightforward. Generally, state ket in multiconfigurational theory is given by a linear combination of configuration state functions (CSFs):

$$|\Psi\rangle = \sum_I C_I \, |\Phi_I\rangle \, . \tag{3.2.129}$$

For convenience, all the CSFs are assumed to be orthonormalized. The first-order reduced density (1RDM) operator is given by

$$\hat{\gamma}\left(\mathbf{x}', \mathbf{x}\right) = n|\mathbf{x}'\rangle\langle\,\mathbf{x}| \tag{3.2.130}$$

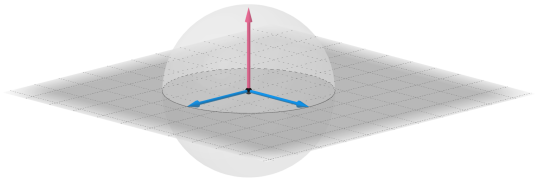

(a) Canonical molecular orbitals (CMOs). Blue / pink vectors represent the occupied / virtual CMOs.

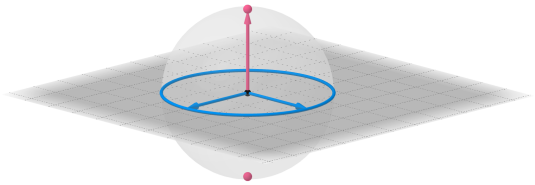

(b) Occupied and virtual orbital spaces. Blue circle represent occupied orbital space or Hartree-Fock manifold. Pink points represents virtual orbital space.

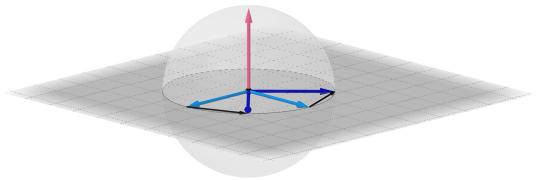

(c) Orbital rotation within occupied orbital space. Hartree-Fock wavefunction is invariant to orbital rotation within occupied / virtual orbital spaces.

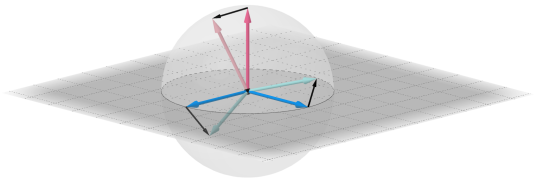

(d) Orbital mixing of CMOs. Light-colored vectors represent the CMOs of perturbed molecular geometry. Black vector represent the displacements of CMOs.

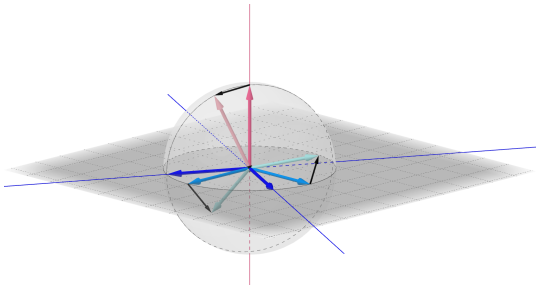

(e) Natural reaction orbitals (NROs). Deep blue vectors represent the occupied NROs. The virtual NRO is identical to the virtual CMO in this 3D model.

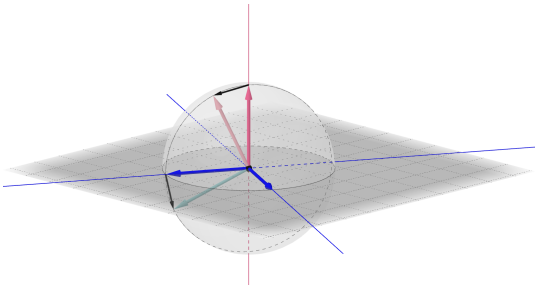

(f) Orbital mixing of NROs. Only one occupied NRO mixes with the virtual NRO. The other occupied NRO does not participate in the orbital mixing.

Fig. 3.1: 3-dimensional model of orbital mixing.

where n is the number of electrons. The 1RDM of multiconfigurational state is given by

$$\begin{aligned}\gamma(\mathbf{x}', \mathbf{x}) &= \sum_{I,J} C_I^* C_J \langle \Phi_I | \hat{\gamma}(\mathbf{x}', \mathbf{x}) | \Phi_J \rangle \\ &= \sum_{I,J} \sum_{p,q} \gamma_{pq}^{IJ} C_I^* C_J c_{\mu p}^* c_{\nu q} \chi_\mu^*(\mathbf{x}') \chi_\nu(\mathbf{x}),\end{aligned} \tag{3.2.131}$$

where $\chi_\mu(\mathbf{x})$ is atomic spin-orbital (SO) basis. Then, the 1RDM is given by

$$\gamma_{\mu\nu} = \sum_{I,J} \sum_{p,q} \gamma_{pq}^{IJ} C_I^* C_J c_{\mu p}^* c_{\nu q}. \tag{3.2.132}$$

The first-order response of state ket the 1RDM is the sum of

$$X_{\mu\nu}^{(1)} \coloneqq \sum_{I,J} \sum_{p,q} \gamma_{pq}^{IJ} C_I^* c_{\mu p}^* \left(C_J^{(1)} c_{\nu q} + C_J c_{\nu q}^{(1)} \right) \tag{3.2.133}$$

and its Hermitian conjugate. Herein, the first-order response matrices of CI coefficients and MO coefficients are introduced:

$$C_I^{(1)} = \sum_J C_J V_{JI}^{(1)}, \quad c_{\mu i}^{(1)} = \sum_j c_{\mu j} U_{ji}^{(1)}. \tag{3.2.134}$$

With the response matrices, Eq. (3.2.133) is rewritten by

$$X_{\mu\nu}^{(1)} = \sum_{I,J,K} \sum_{p,q,r} \gamma_{pq}^{IJ} C_I^* C_K c_{\mu p}^* c_{\nu r} \left(V_{KJ}^{(1)} \delta_{rq} + \delta_{KJ} U_{rq}^{(1)} \right). \tag{3.2.135}$$

The MO representation is given by

$$X_{pq}^{(1)} = \sum_{\kappa,\lambda,\mu,\nu} S_{\kappa\mu} X_{\mu\nu}^{(1)} S_{\nu\lambda} c_{\kappa p}^* c_{\lambda q}, \quad (p \in S, \;\; q \in S') \tag{3.2.136}$$

where S and S' denote some orbital spaces and the state ket is assumed to be invariant to any orbital rotation within each orbital space. If the atomic SO basis set is complete, SVD basis of the matrix $\mathbf{X}^{(1)}$ is the NRO basis for multiconfigurational theories. It should be emphasized that $\mathbf{X}^{(1)}$ also contains the contribution of CI coefficient change. Therefore, NRO basis provides a way to analyze CI coefficient change with MO basis.

Unfortunately, the generalization shown above is not very practical because computation of CI coefficients is sometimes computationally demanding. Also, some additional consideration is required for finite basis set as discussed in the next chapter. However,

it should be emphasized that the concept of NRO can be generalized to multiconfigurational theories.

3.2.10 Relevance between NRO and non-adiabatic coupling

NRO is proposed as a method to analyze the evolution of electron density on a single adiabatic potential energy surface. Therefore, there seems to be no relevance between NRO and non-adiabatic coupling (NAC) in principle. However, there is a kind of connection between the two different concepts as discussed below.

Although NAC is already defined by Eq. (3.2.40), the definition is given here again. The NAC matrix element between the M-th and N-th adiabatic electronic states are defined by

$$\tau_{\mathfrak{J}}^{MN}(\mathbf{R}) \coloneqq \left\langle \Psi_M^{adia}(\mathbf{R}) \middle| \partial_{\mathfrak{J}} \Psi_N^{adia}(\mathbf{R}) \right\rangle. \quad (\mathfrak{J} = 1, \ldots, 3N^{nuc}) \tag{3.2.137}$$

NAC matrix is anti-Hermitian

$$\tau_{\mathfrak{J}}^{MN} = -\tau_{\mathfrak{J}}^{NM*}. \quad (\forall i, j, \mathfrak{J}) \tag{3.2.138}$$

Therefore, the diagonal elements of NAC matrix is purely imaginary:

$$\Re\left(\tau_{\mathfrak{J}}^{MM}\right) = 0. \quad (\forall M) \tag{3.2.139}$$

The diagonal element of the ground state is given by

$$\tau_{\boldsymbol{v}}^{00} = \sum_{I,J} C_I^* C_J V_{JI}^{(1)} + \sum_{I,J} \sum_{p,q} C_I^* C_J \gamma_{pq}^{IJ} \left(U_{pq}^{(1)} + \sum_{\mu,\nu} \left\langle \mu \middle| \nu^{(1)} \right\rangle c_{\mu p}^* c_{\nu q} \right) = \Im\left(\tau_{\boldsymbol{v}}^{00}\right), \tag{3.2.140}$$

where $\boldsymbol{v}$ is some unit direction vector. $\left|\nu^{(1)}\right\rangle$ denotes the directional derivative of ν-th

atomic SO. The trace of $\mathbf{X}^{(1)}$ defined by Eq. (3.2.135) is given by

$$\begin{aligned}
\sum_{\mu,\nu} X^{(1)}_{\mu\nu} S_{\mu\nu} &= \sum_{I,J,K} \sum_{p,q,r} \gamma^{IK}_{pq} C^*_I C_K \sum_{\mu,\nu} S_{\mu\nu} c^*_{\mu p} c_{\nu r} \left(V^{(1)}_{KJ} \delta_{rq} + \delta_{KJ} U^{(1)}_{rq} \right) \\
&= \sum_{I,J,K} \sum_{p,q,r} \gamma^{I,J}_{p,q} C^*_I C_K \delta_{pr} \left(V^{(1)}_{KJ} \delta_{rq} + \delta_{KJ} U^{(1)}_{rq} \right) \\
&= \sum_{I,J,K} \sum_{p,q} \gamma^{IJ}_{pq} C^*_I C_K \left(V^{(1)}_{KJ} \delta_{pq} + \delta_{KJ} U^{(1)}_{pq} \right) \\
&= \sum_{I,J,K} \sum_{p} \gamma^{IJ}_{pp} C^*_I C_K V^{(1)}_{KJ} + \sum_{I,J} \sum_{p,q} \gamma^{IJ}_{pq} C^*_I C_J U^{(1)}_{pq} \\
&= \sum_{I,J} C^*_I C_J V^{(1)}_{JI} + \sum_{I,J} \sum_{p,q} \gamma^{IJ}_{pq} C^*_I C_J U^{(1)}_{pq} \quad (\because \gamma^{IK}_{pp} = \delta^{IK}) \\
&= \tau^{00}_{\boldsymbol{v}} - \sum_{I,J} \sum_{p,q} \sum_{\mu,\nu} C^*_I C_J \gamma^{IJ}_{pq} \left\langle \mu \middle| \nu^{(1)} \right\rangle c^*_{\mu p} c_{\nu q} \\
&= \Im\left(\tau^{00}_{\boldsymbol{v}}\right) - \sum_{I,J} \sum_{p,q} \sum_{\mu,\nu} C^*_I C_J \gamma^{IJ}_{pq} \left\langle \mu \middle| \nu^{(1)} \right\rangle c^*_{\mu p} c_{\nu q}
\end{aligned} \tag{3.2.141}$$

Thus, $\mathrm{Tr}(\mathbf{X}^{(1)})$ can be regarded as a diagonal element of the first-order NAC matrix with the difference of atomic SO basis derivatives ignored. This relation implies that SVD basis of the MO representation of $\tau^{MN}_{\mathfrak{J}}$ may be useful to characterize non-adiabatic transition.

3.3 Numerical results

Natural reaction orbital (NRO) analyses of typical reactions will be presented in this section. All the electronic structure calculation including CP-SCF calculation, geometry optimization and IRC calculation were performed with Gaussian16 Rev.C.01. [43] NRO calclation was performed with our own code written in Fortran90.

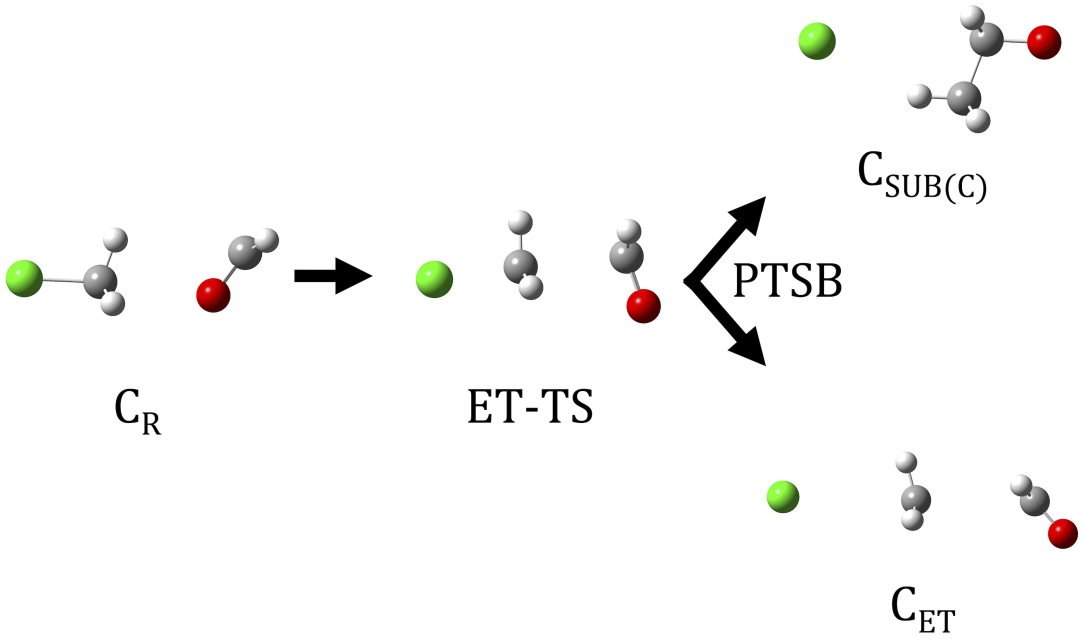

Fig. 3.2: S_N2-like reaction between H_2CO^- and H_3CCl.

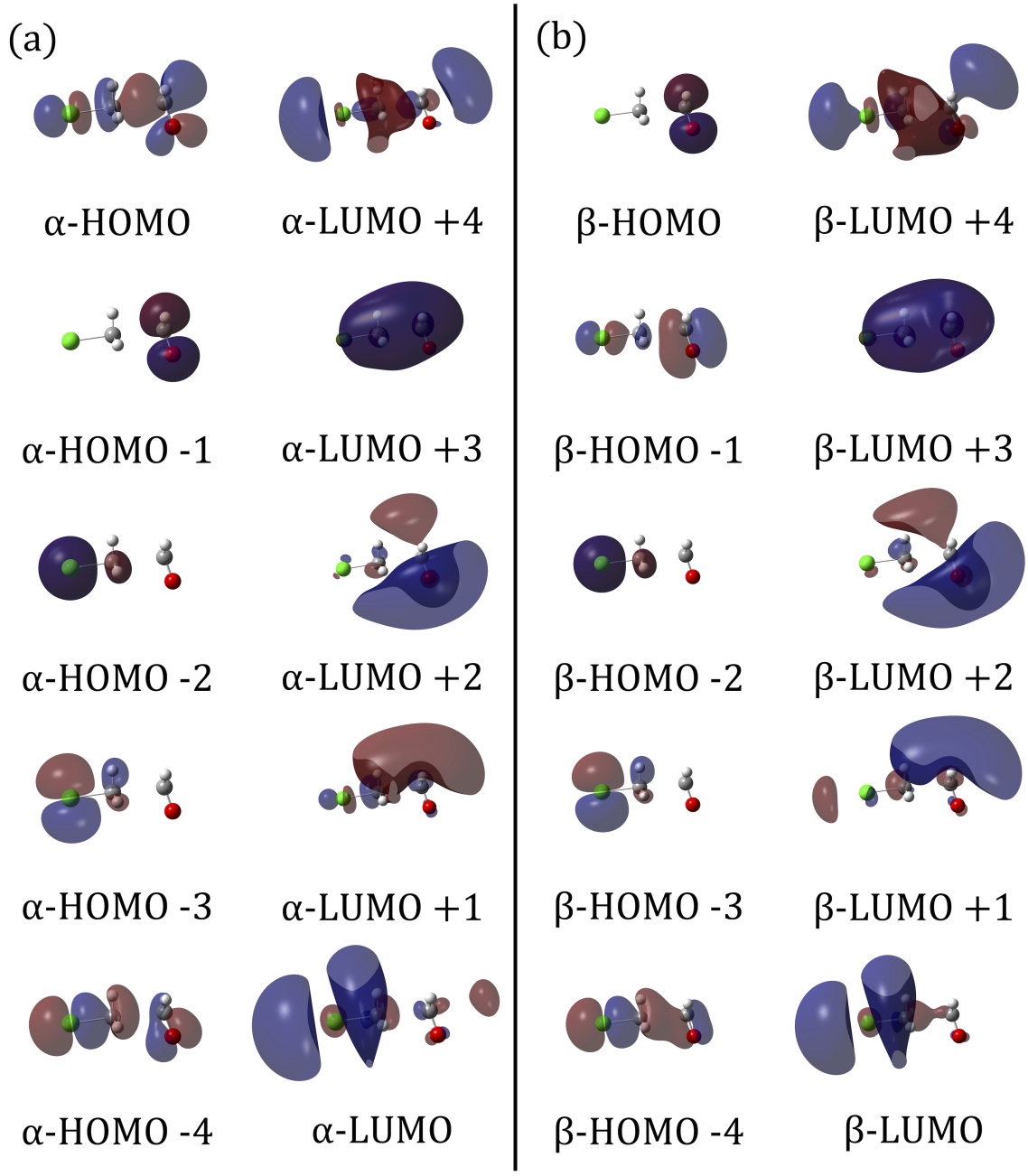

Fig. 3.3: Alpha and beta CMOs at the 1st-order saddle point of S_N2-like reaction between H_2CO^- and H_3CCl. The 1st-order saddle point was optimized in UHF/6-31+(d,p) level.

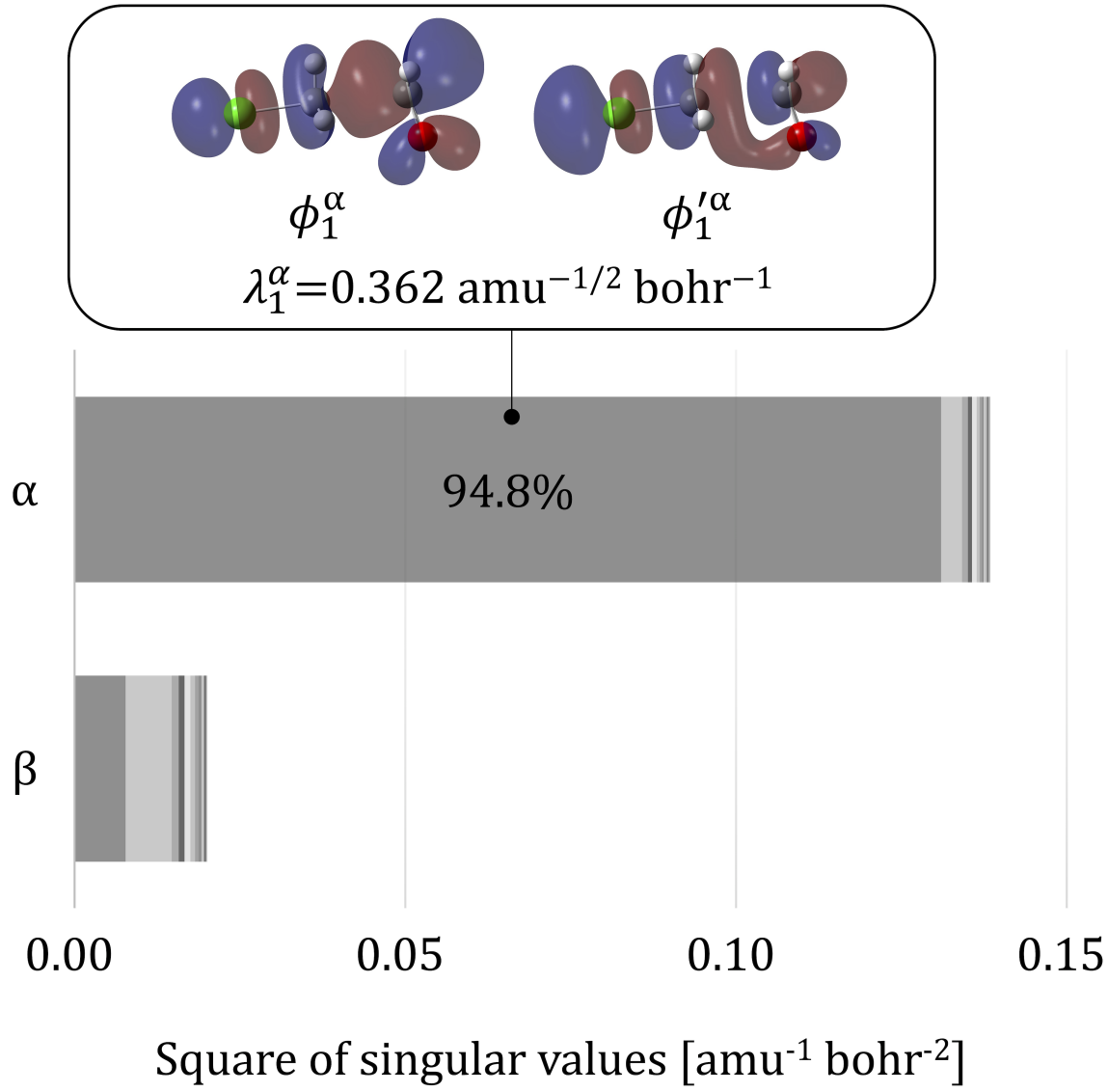

Fig. 3.4: NROs at the 1st-order saddle point of S_N2-like reaction between H_2CO^- and H_3CCl.

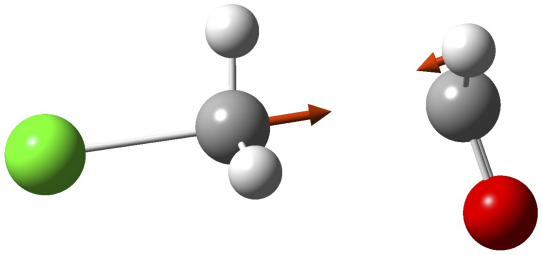

Fig. 3.5: Imaginary frequency mode at the 1st-order saddle point of S_N2-like reaction between H_2CO^- and H_3CCl.

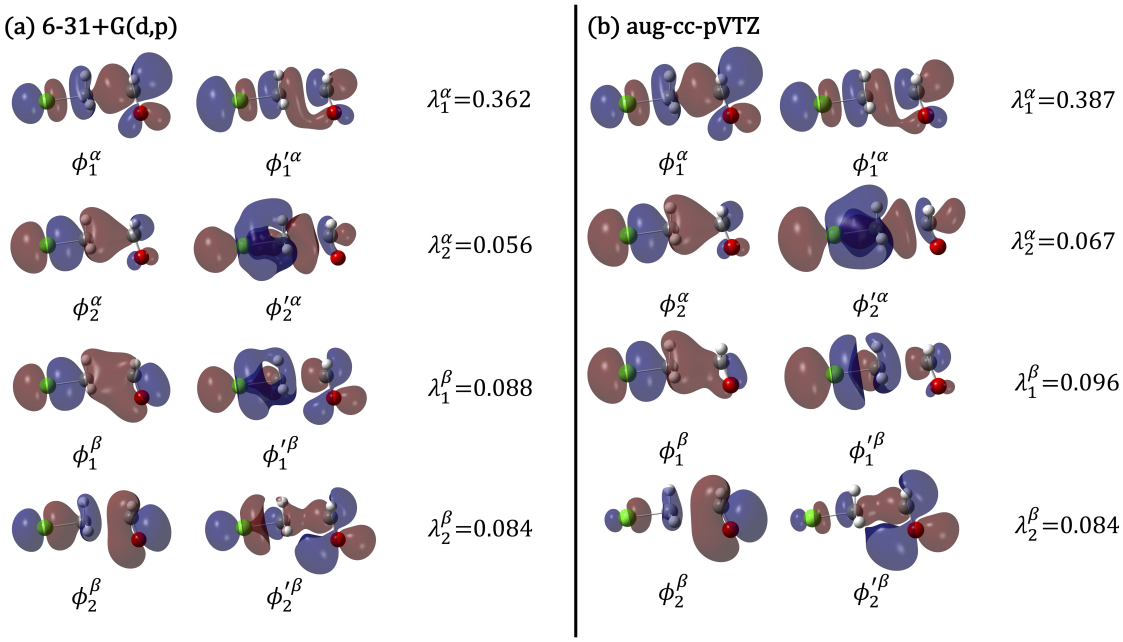

Fig. 3.6: Comparison of dominant NROs computed with 6-31+G(d,p) basis and aug-cc-pVTZ basis. The 1st-order saddle points were optimized individually.

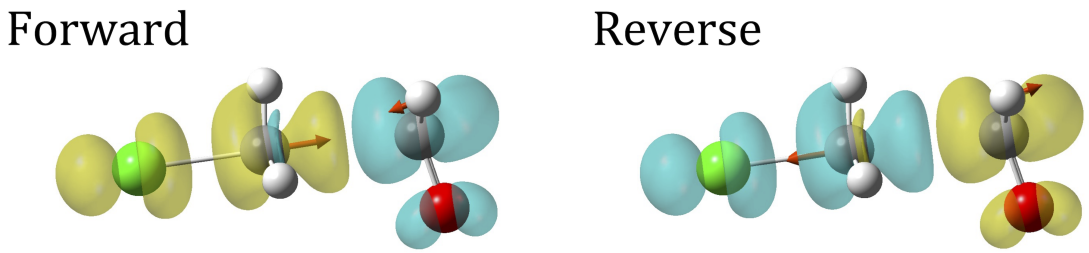

Fig. 3.7: Products of the 1st NRO pair at the 1st-order saddle point of S_N2-like reaction between H_2CO^- and H_3CCl.

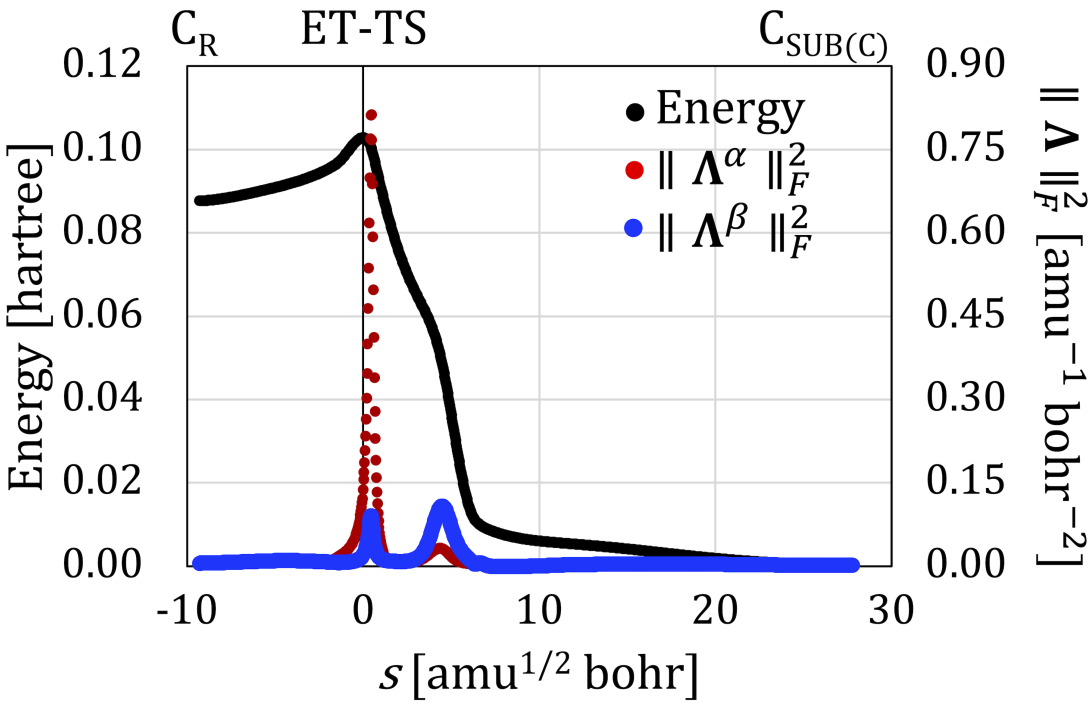

Fig. 3.8: Change of energy and Frobenius norm along the IRC of S_N2-like reaction between H_2CO^- and H_3CCl. IRC was calculated in UHF/6-31+(d,p) level.

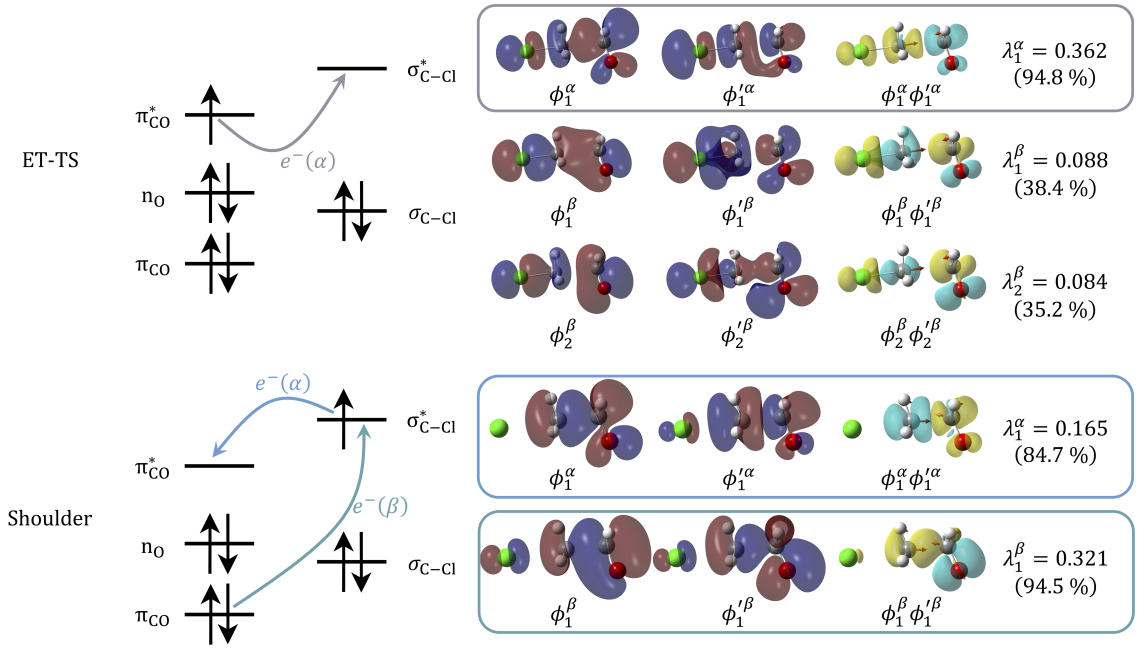

Fig. 3.9: Comparison with valence bond configuration mixing analysis of S_N2-like reaction [152] between H_2CO^- and H_3CCl.

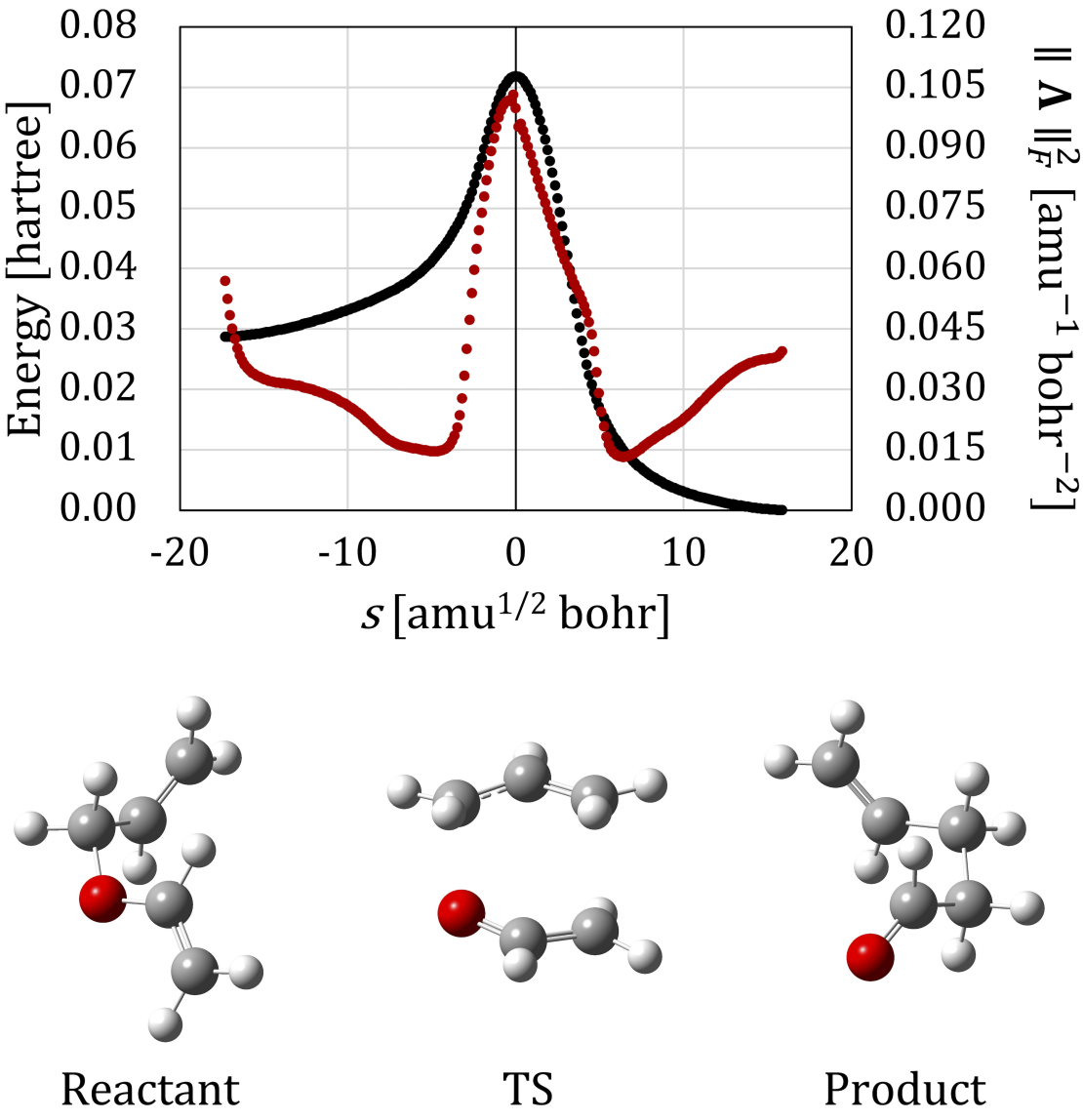

Fig. 3.10: Change of energy and Frobenius norm along the IRC of Claisen rearrangement of allyl vinyl ether. IRC was calculated in B3LYP/6-311+G(d,p) level.

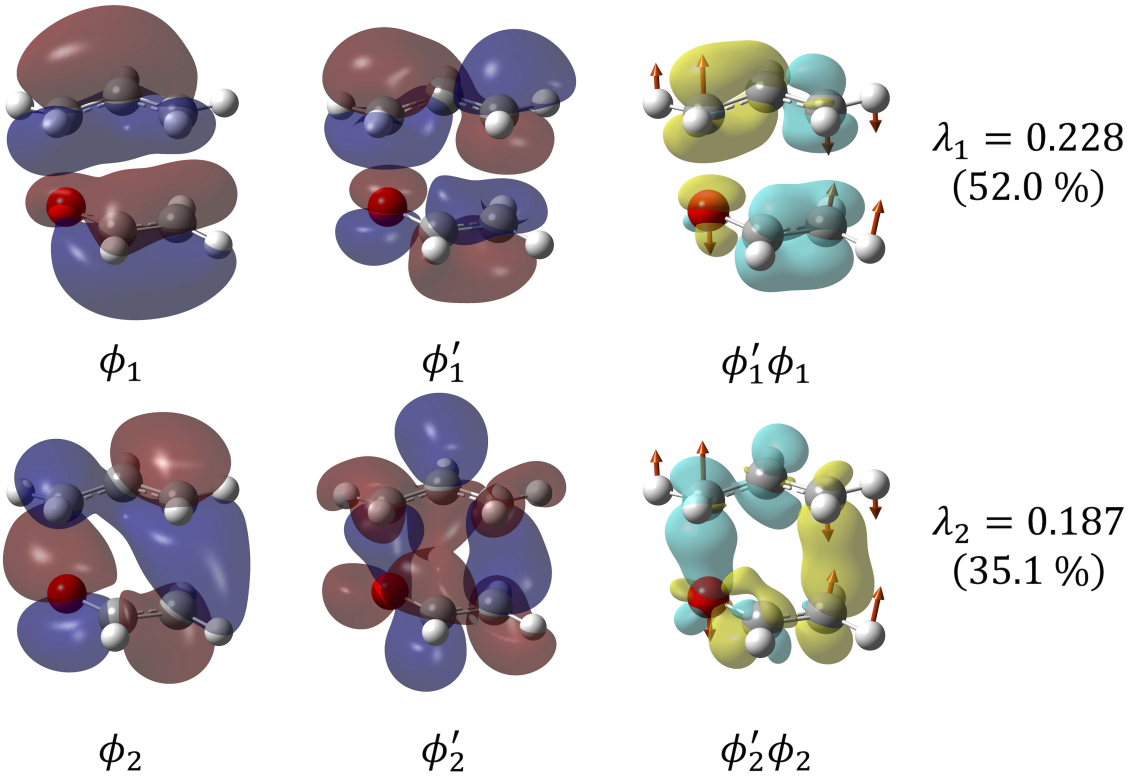

Fig. 3.11: The 1st and 2nd NRO pairs and their products at the 1st-order saddle point of Claisen rearrangement of allyl vinyl ether.

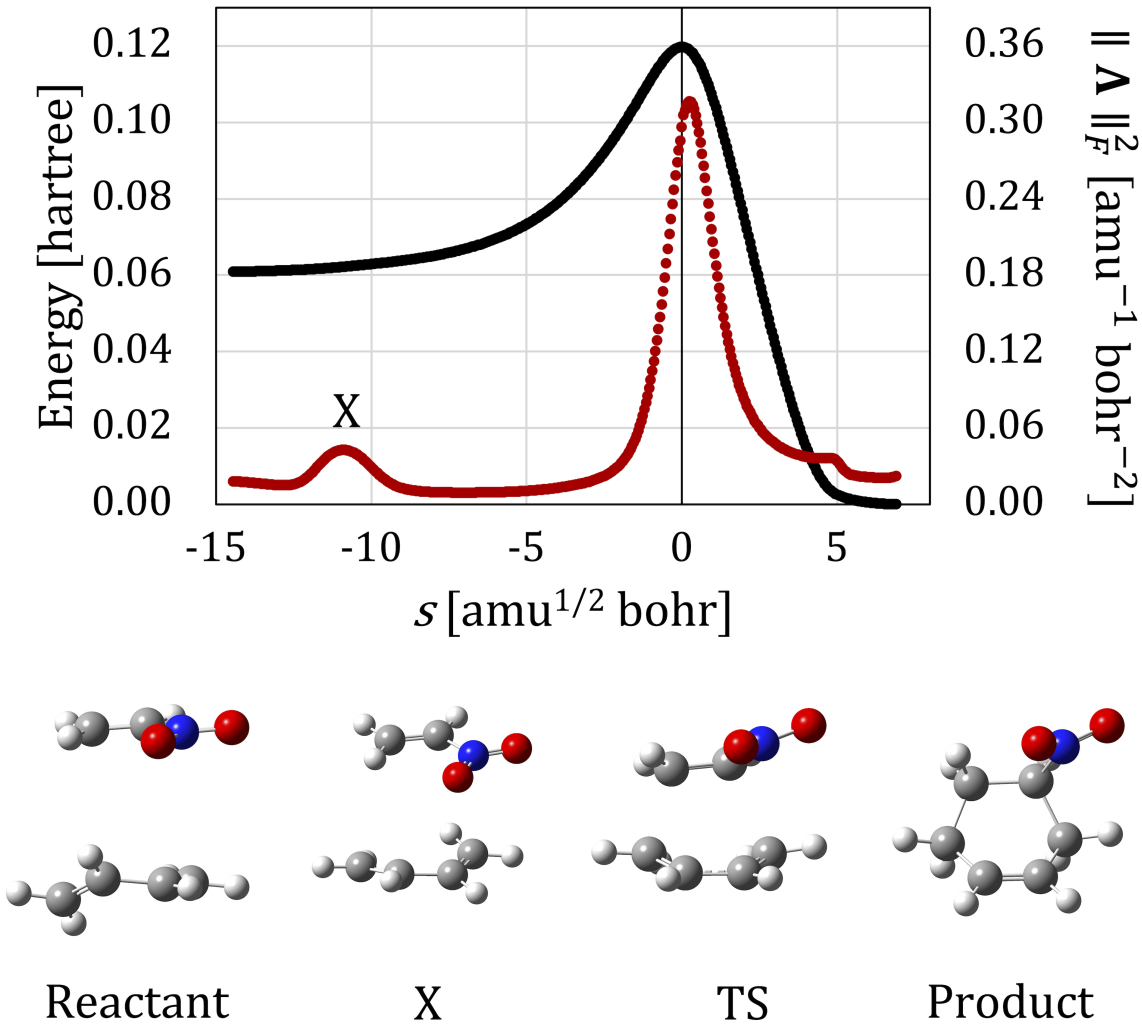

Fig. 3.12: Change of energy and Frobenius norm along the IRC of Diels-Alder reaction between nitroethylene and 1,3-butadiene. IRC was calculated in RHF/6-31G(d,p)

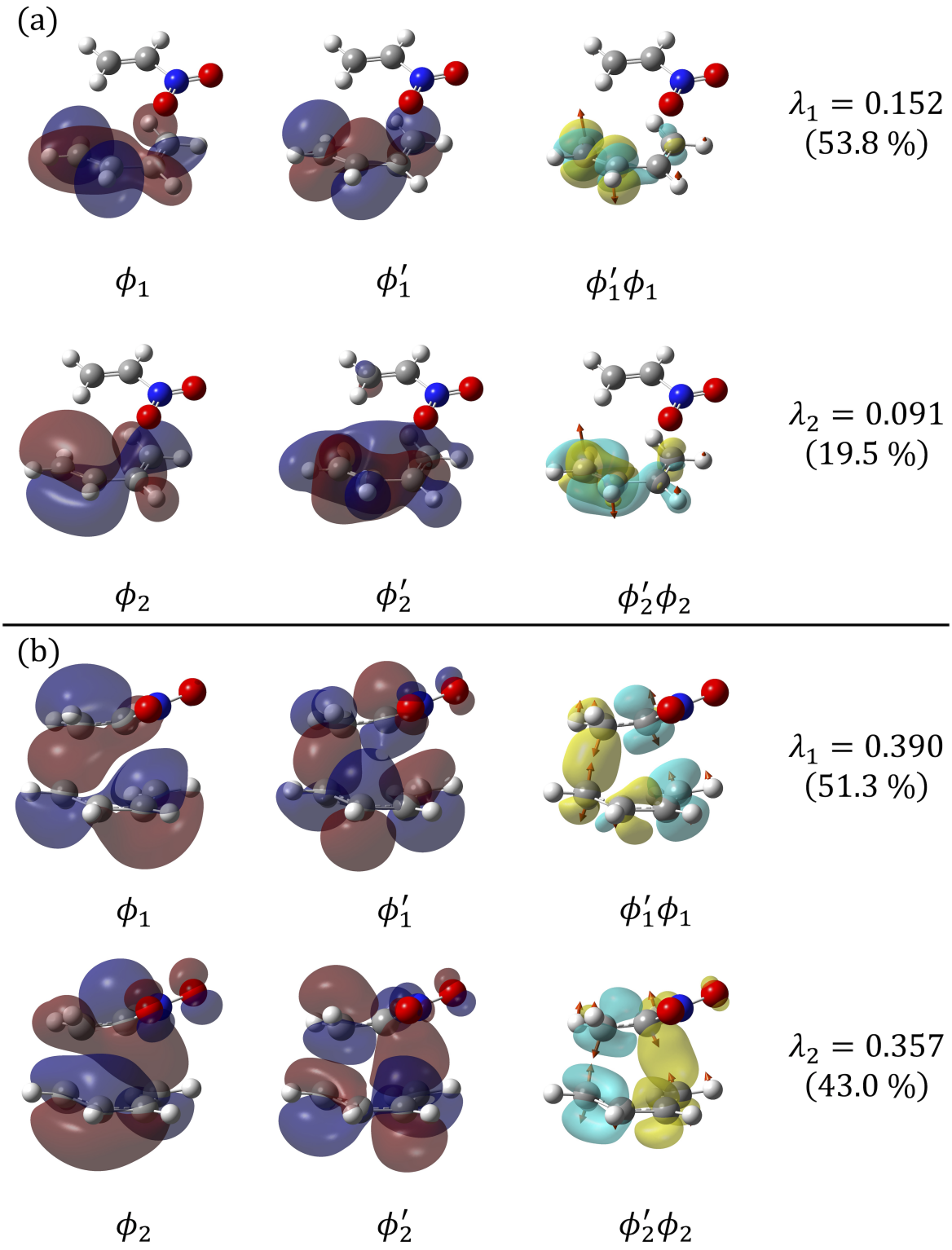

Fig. 3.13: The 1st and 2nd NRO pairs and their products at the 1st-order saddle point of Diels-Alder reaction between nitroethylene and 1,3-butadiene.

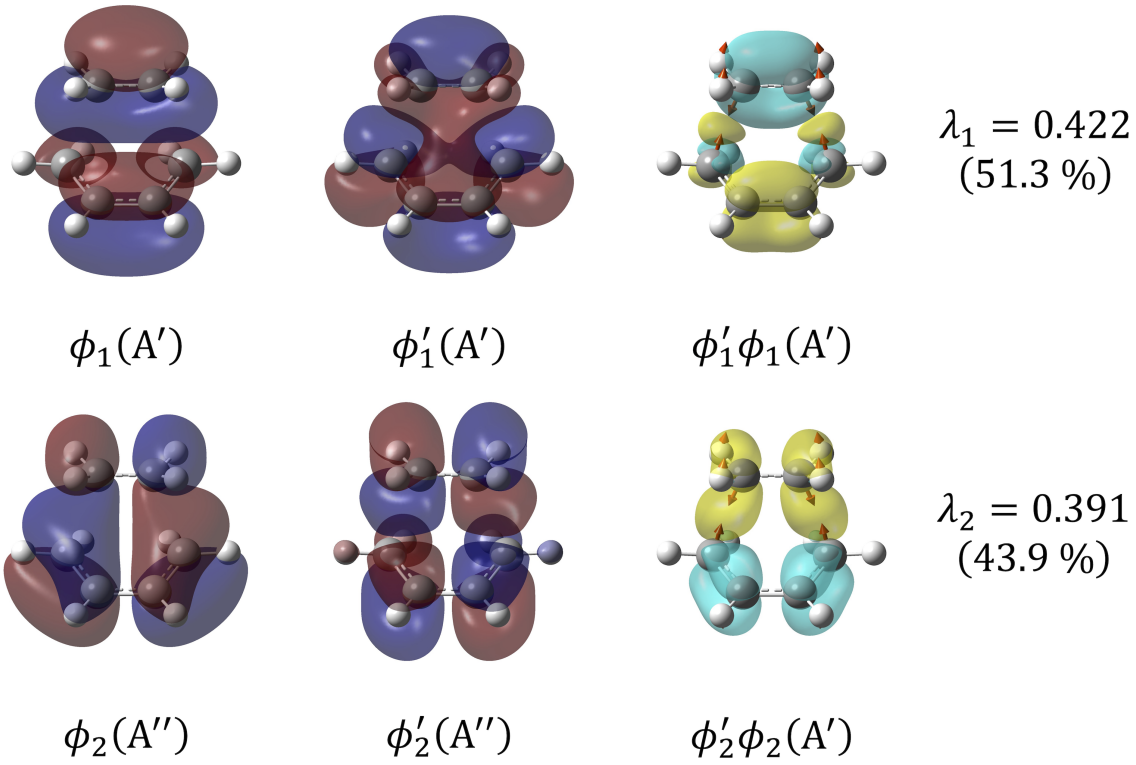

Fig. 3.14: The 1st and 2nd NRO pairs and their products at the 1st-order saddle point of Diels-Alder reaction between ethylene and 1,3-butadiene. The 1st-order saddle point was optimzed in RHF/6-31G(d,p)

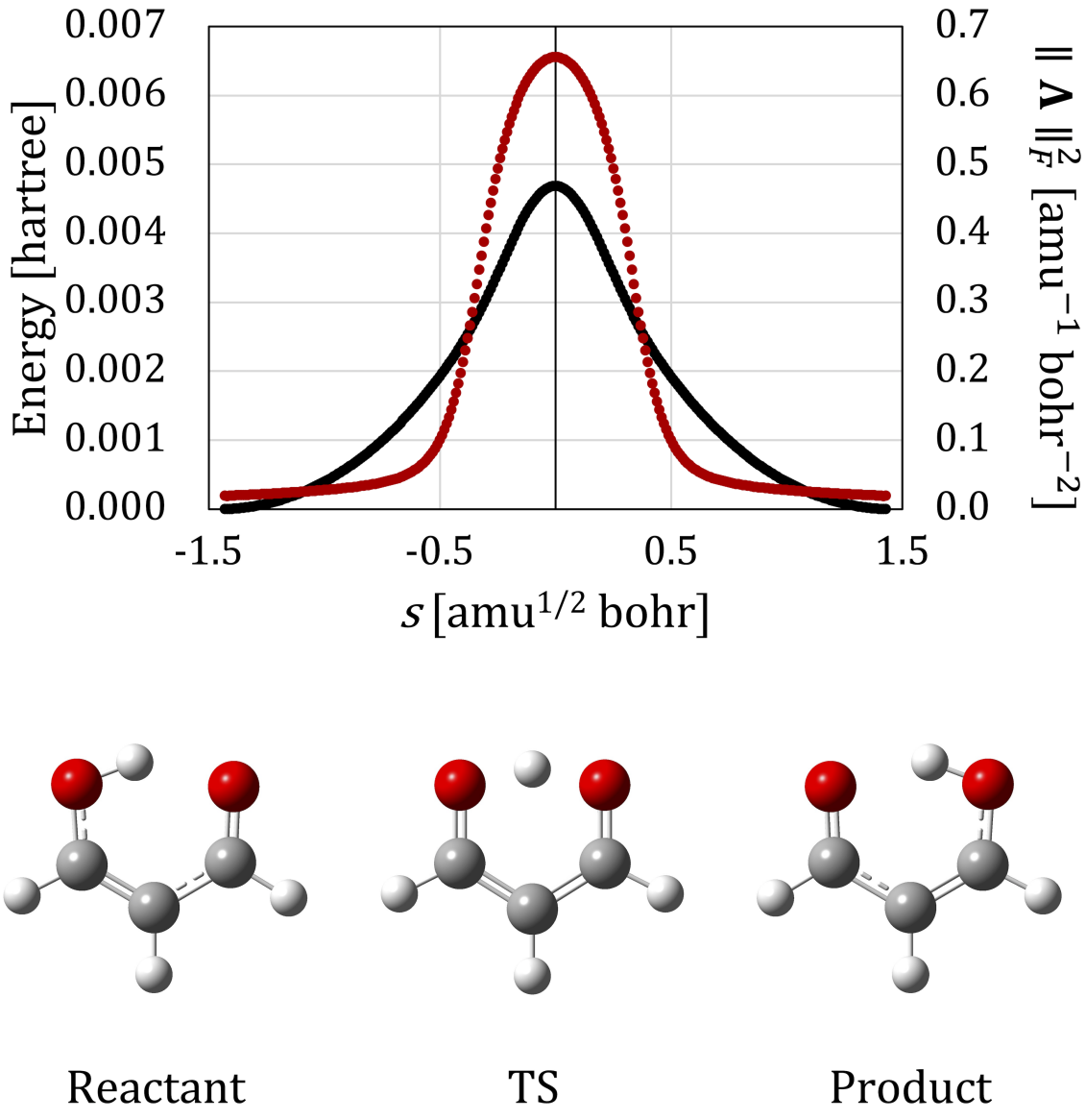

Fig. 3.15: Change of energy and Frobenius norm along the IRC of proton transfer of malonaldehyde. IRC was calculated in LC-BLYP/6-311+G(d,p) level. [76]

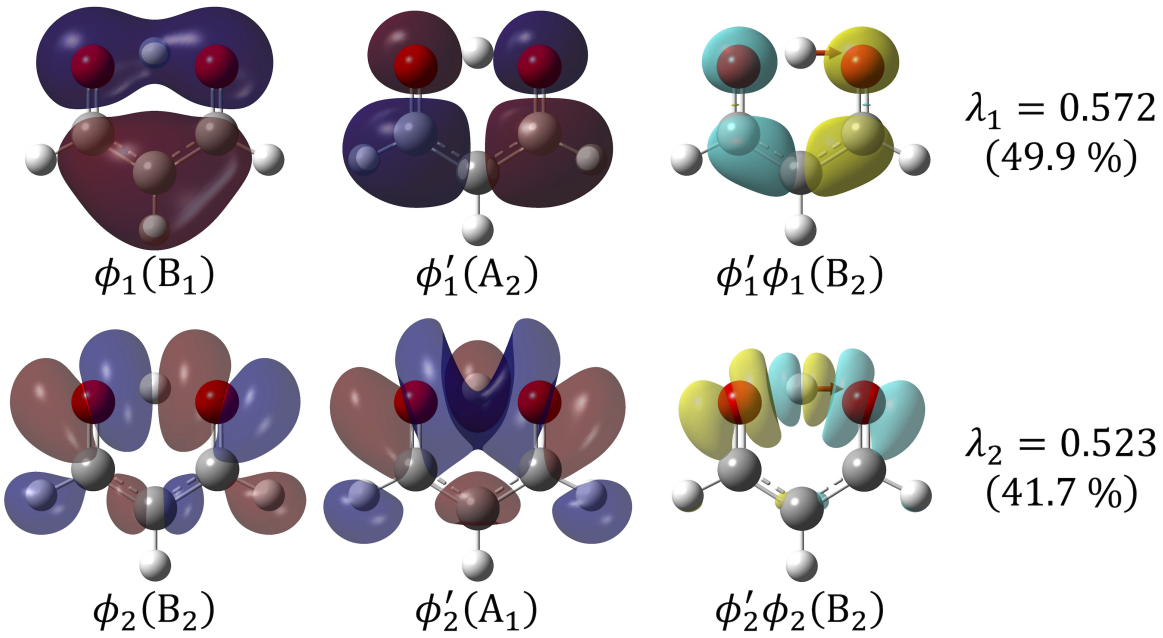

Fig. 3.16: The 1st and 2nd NRO pairs and their products at the 1st-order saddle point of proton transfer of malonaldehyde.

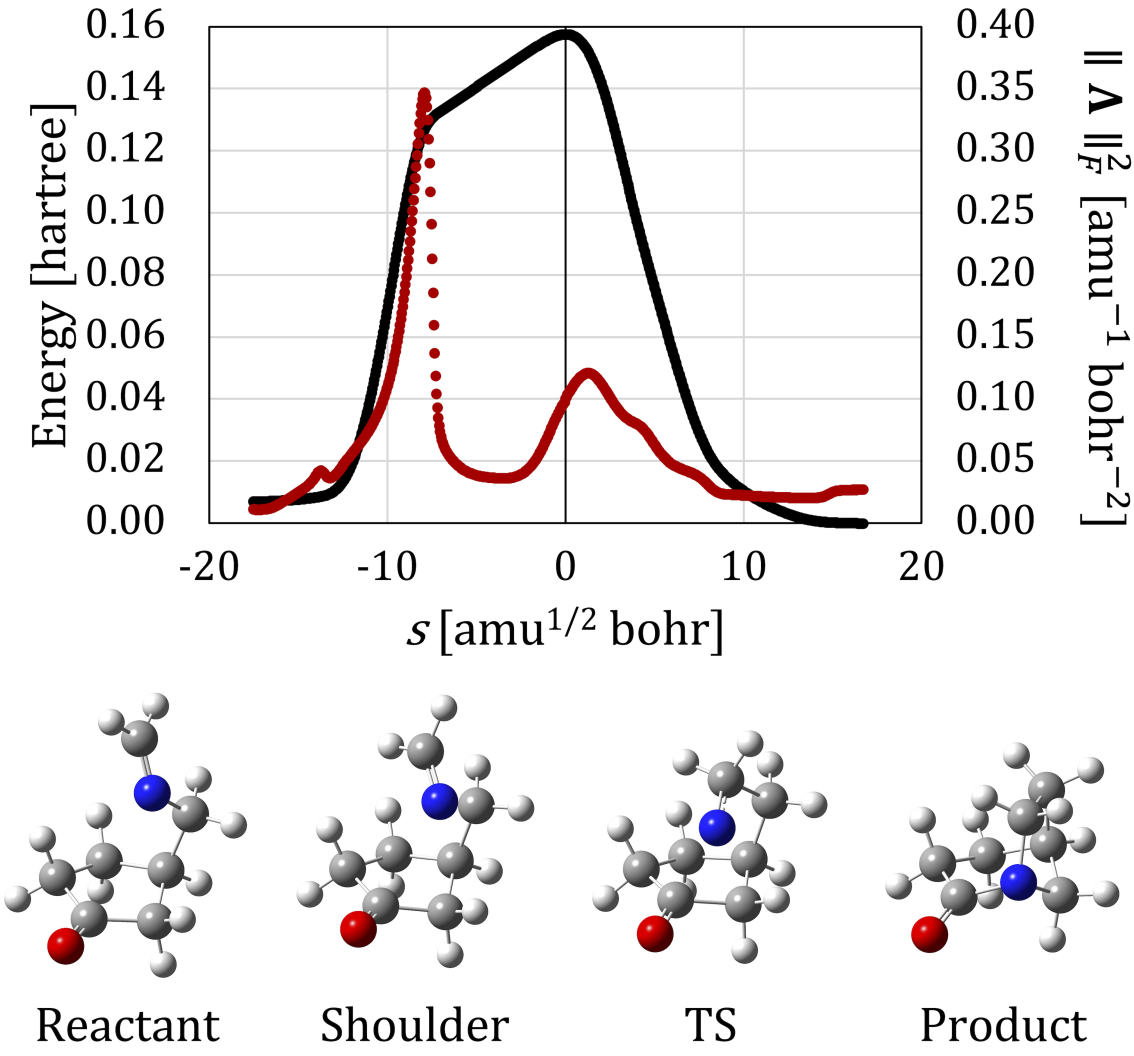

Fig. 3.17: Change of energy and Frobenius norm along the IRC of 1,2-alkyl shift/nitrene addition. [16] IRC was calculated in B3LYP/6-311++G(d,p) level.

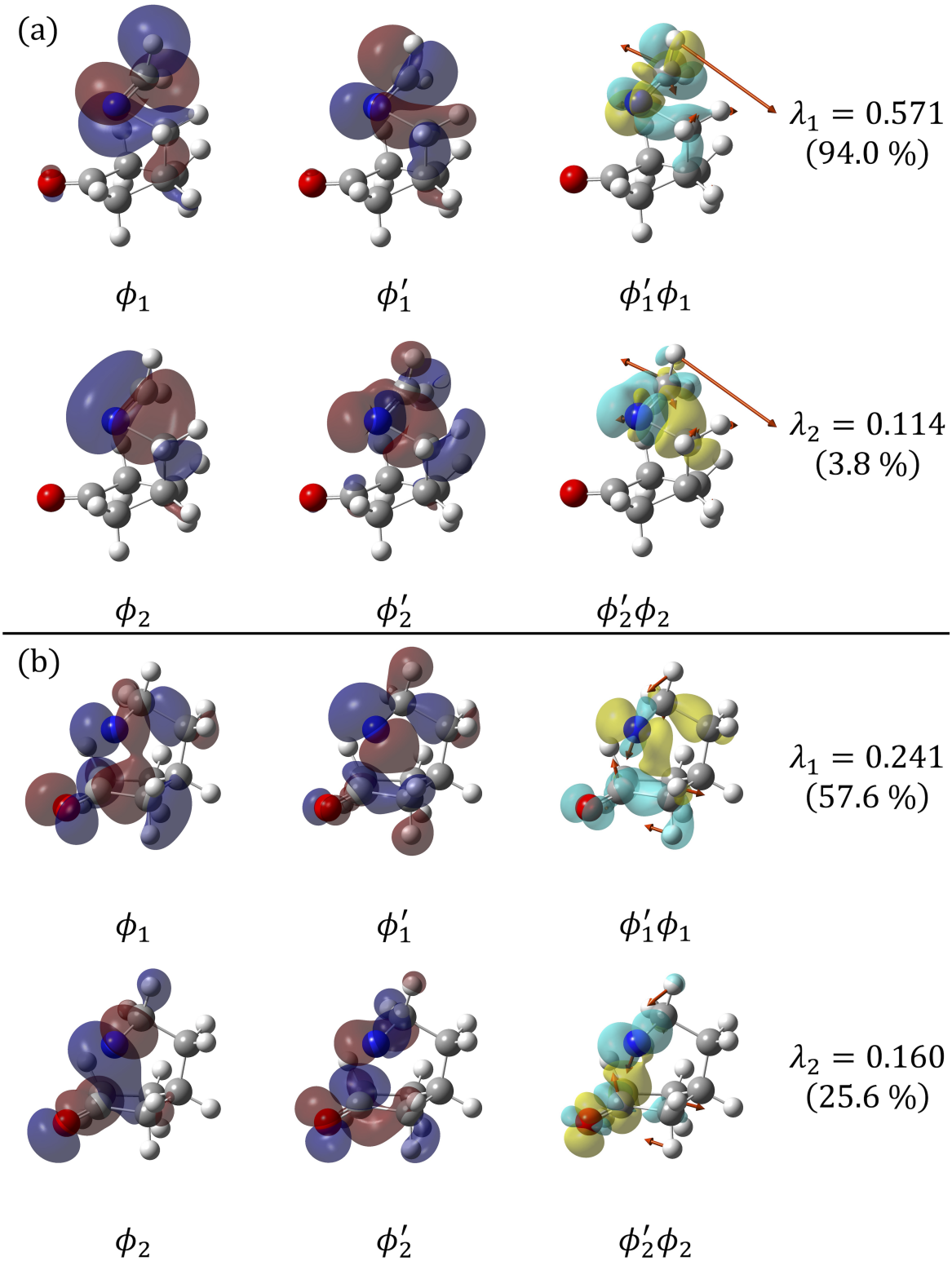

Fig. 3.18: The 1st and 2nd NRO pairs and their products at the shoulder of IRC and the 1st-order saddle point of 1,2-alkyl shift/nitrene addition.

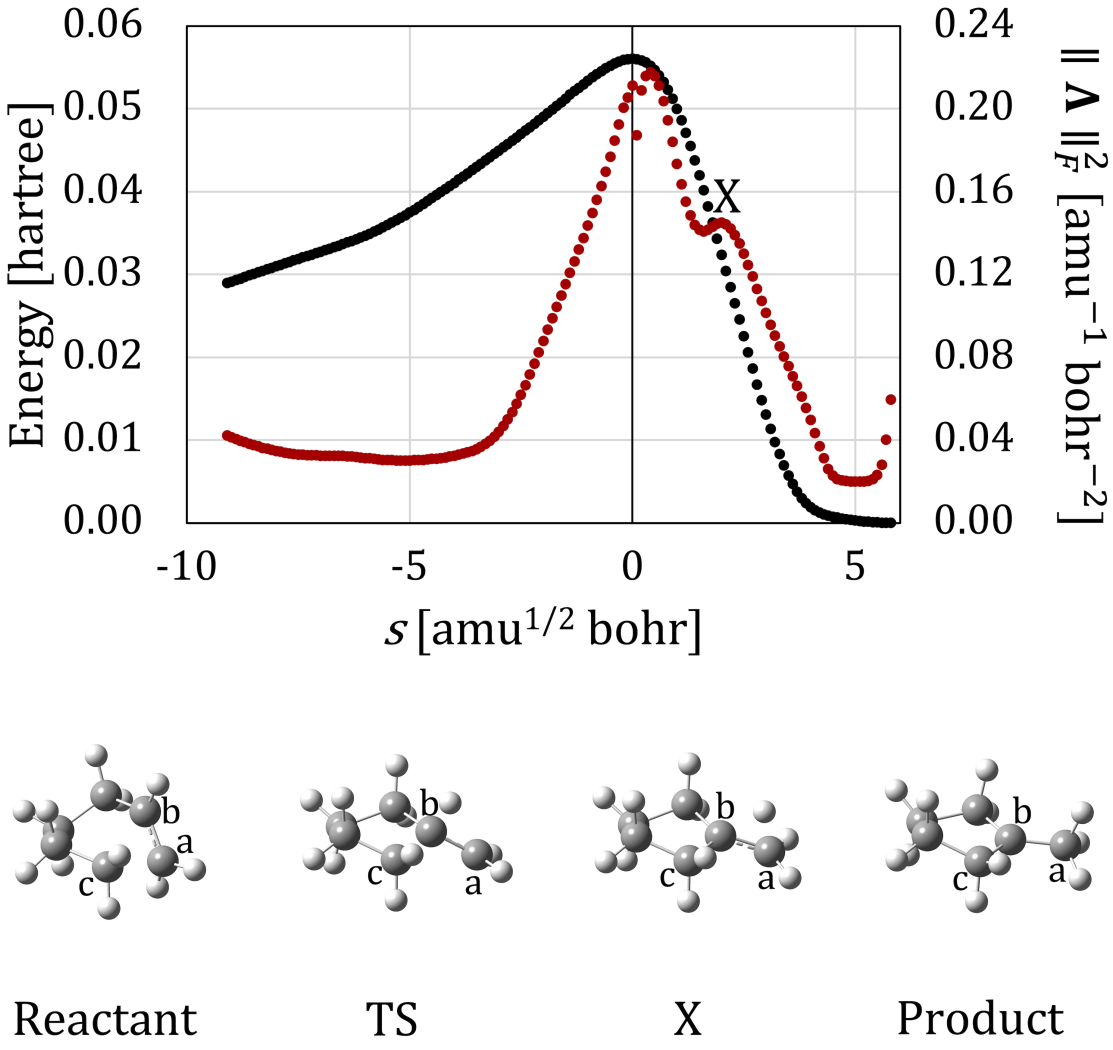

Fig. 3.19: Change of energy and Frobenius norm along the IRC of carbocation rearrangement reaction of cyclohexyl cation to methylcyclopentyl cation. [128, 171] IRC was calculated in B3LYP/6-311G(d,p) level.

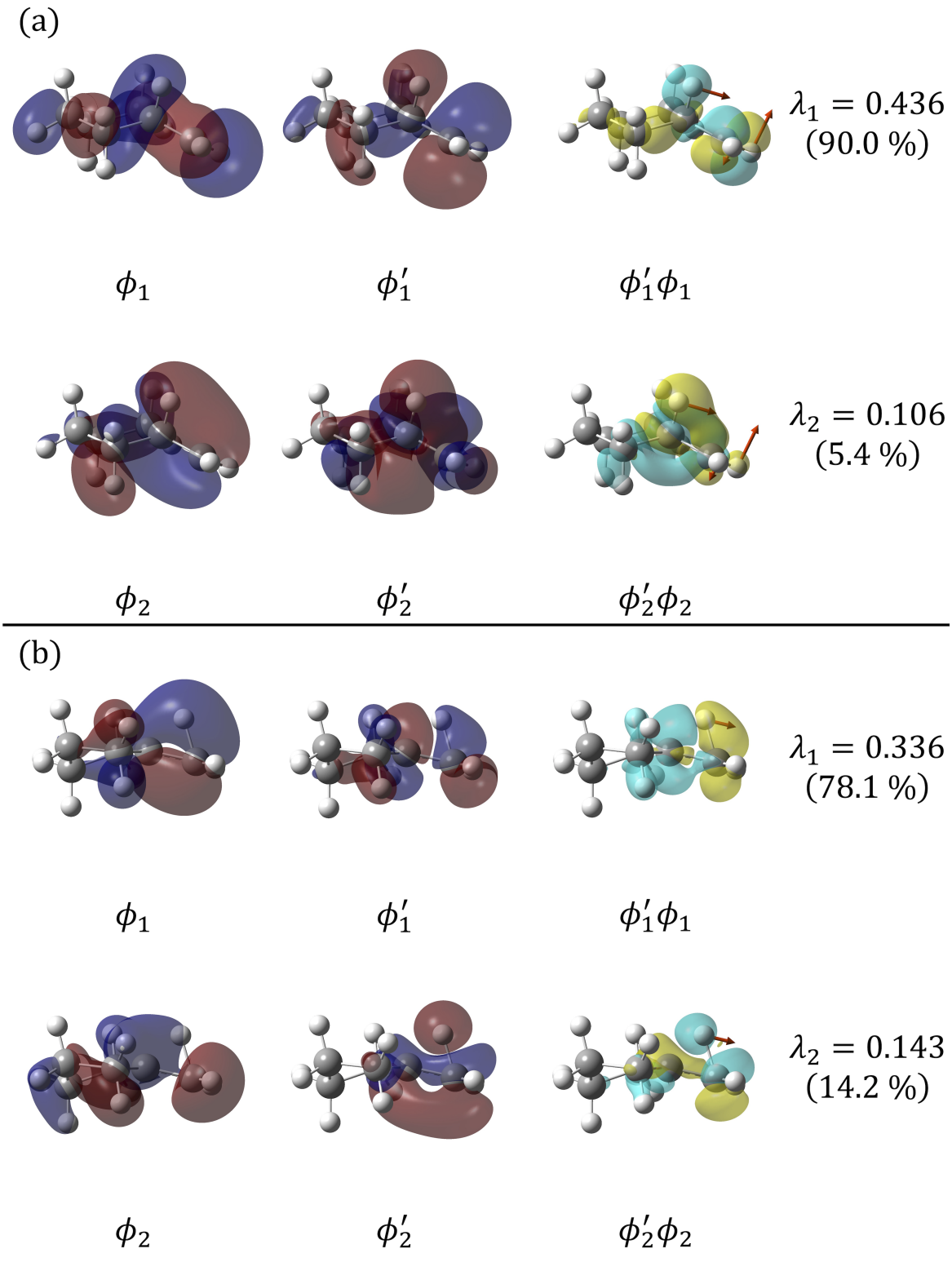

Fig. 3.20: The 1st and 2nd NRO pairs and their products at the 1st-order saddle point and the point X of carbocation rearrangement reaction of cyclohexyl cation to methylcyclopentyl cation.

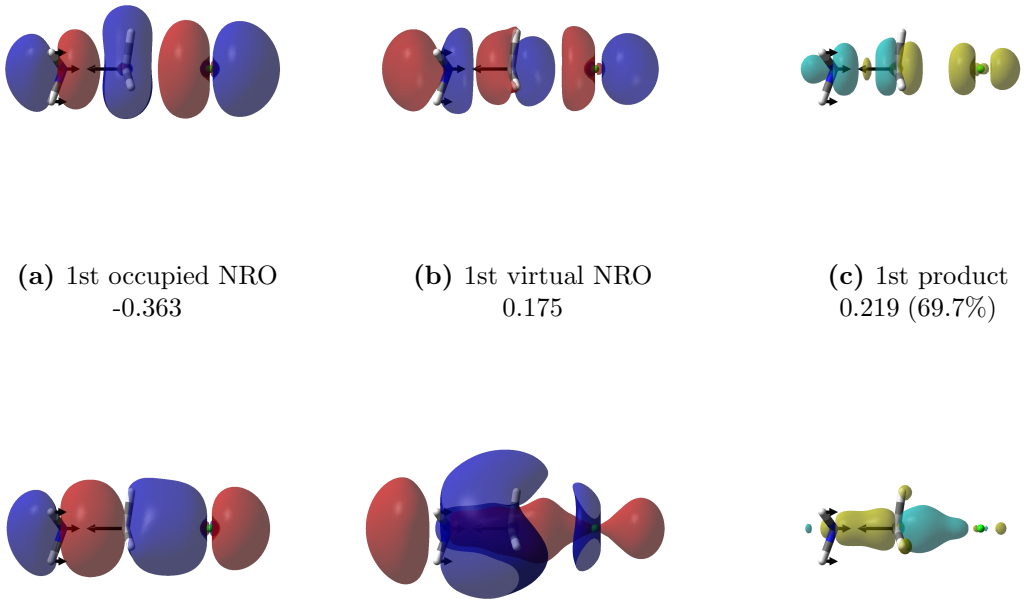

(a) 1st occupied NRO
-0.363

(b) 1st virtual NRO
0.175

(c) 1st product
0.219 (69.7%)

(d) 2nd occupied NRO
-0.519

(e) 2nd virtual NRO
0.407

(f) 2nd product
0.099 (14.3%)

Fig. 3.21: NRO pairs and their products at the 1st-order saddle point of S_N2 reaction between NH_3 and CH_3Cl. The 1st-order saddle point was optimized in ωB97XD/Def2QZVPP level. The number shown below is the one-electron energy of NRO (hartree). Singular value of each NRO pair is shown below its product with the cumulative contribution percentage (amu$^{-1/2}$ bohr^{-1}). Product of each NRO pair indicates that electron density increases/decreases in the region colored by yellow/cyan when the nuclei displaced in the direction shown by black arrows, the normalmode with imaginary frequency.

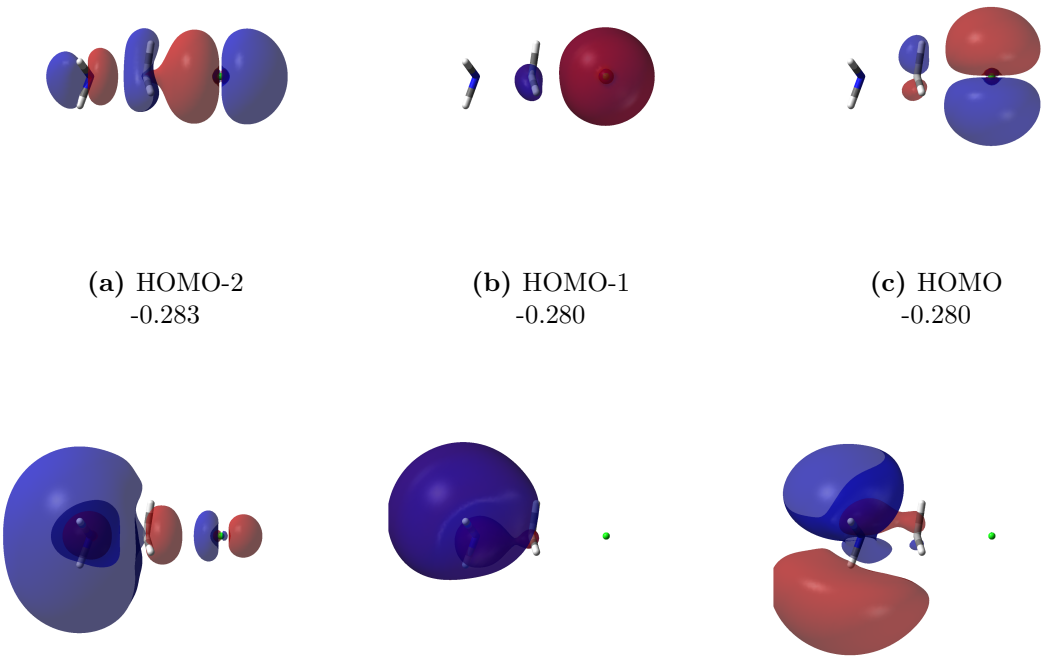

(a) HOMO-2
-0.283

(b) HOMO-1
-0.280

(c) HOMO
-0.280

(d) LUMO
0.019

(e) LUMO+1
0.087

(f) LUMO+2
0.087

Fig. 3.22: CMOs and their products at the 1st-order saddle point of S_N2 reaction between NH_3 and CH_3Cl. The 1st-order saddle point was optimized in ωB97XD/Def2QZVPP level. The number shown below each CMO is the one-electron energy of CMO (hartree).

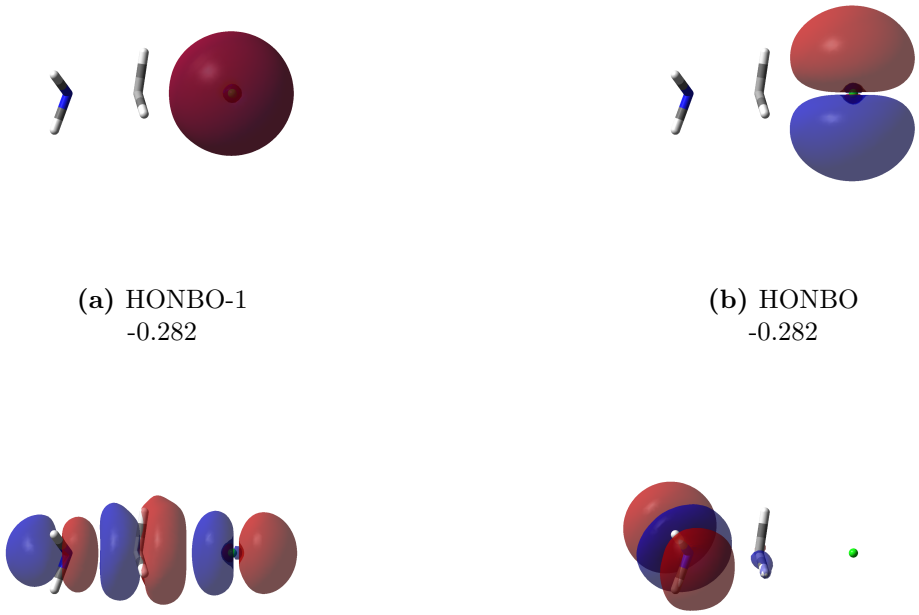

(a) HONBO-1
-0.282

(b) HONBO
-0.282

(c) LUNLMO
0.070

(d) LUNLMO+1
0.399

Fig. 3.23: NBOs and their products at the 1st-order saddle point of S_N2 reaction between NH_3 and CH_3Cl. The 1st-order saddle point was optimized in ωB97XD/Def2QZVPP level. The number shown below each NBO is the one-electron energy of NBO (hartree).

LG	1st occupied NRO	1st virtual NRO	1st product
Cl	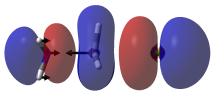	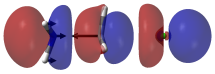	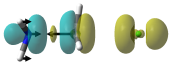
Br	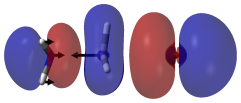	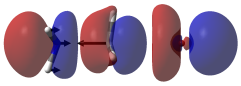	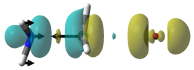
I	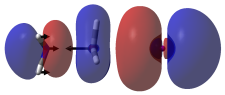	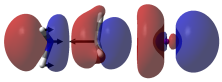	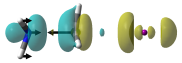
MsO	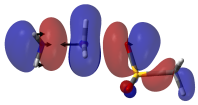	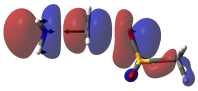	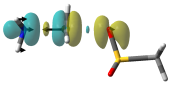
CN	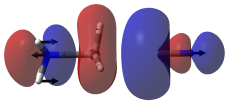	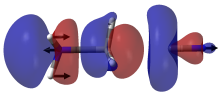	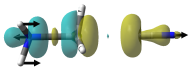

Fig. 3.24: 1st NRO pairs and their products at the 1st-order saddle point of S_N2 reaction between NH_3 and CH_3LG (LG $=$ Cl, Br, I, MsO, CN). The 1st-order saddle point was optimized in ωB97XD/Def2QZVPP level. Product of each NRO pair indicates that electron density increases/decreases in the region colored by yellow/cyan when the nuclei displaced in the direction shown by black arrows, the normalmode with imaginary frequency.

LG	2nd occupied NRO	2nd virtual NRO	2nd product
Cl	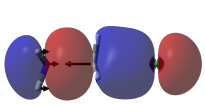	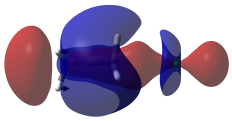	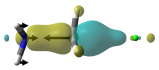
Br	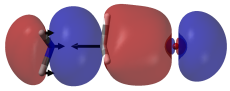	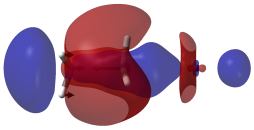	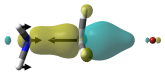
I	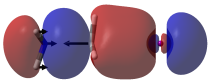	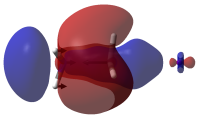	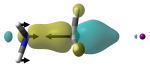
MsO	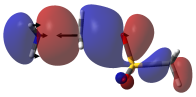	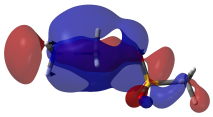	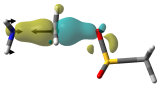
CN	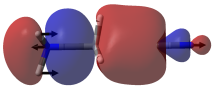	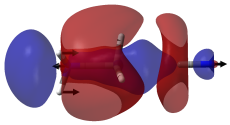	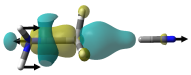

Fig. 3.25: 2nd NRO pairs and their products at the 1st-order saddle point of S_N2 reaction between NH_3 and CH_3LG (LG = Cl, Br, I, MsO, CN). The 1st-order saddle point was optimized in ωB97XD/Def2QZVPP level. Product of each NRO pair indicates that electron density increases/decreases in the region colored by yellow/cyan when the nuclei displaced in the direction shown by black arrows, the normalmode with imaginary frequency.

Table 3.1: Singular values and expectation values of orbital energies of 1st NROs of S_N2 reactions.

Leaving	Singular value	Contribution rate	Orbital enegry[hartree]		Energy gap
group	[amu$^{-1/2}$bohr^{-1}]	[%]	Occupied	Virtual	[hartree]
Cl	0.219	69.7	-0.363	0.175	0.538
Br	0.226	71.3	-0.350	0.143	0.492
I	0.232	72.7	-0.328	0.122	0.450
MsO	0.218	72.0	-0.424	0.158	0.582
CN	0.220	73.3	-0.369	0.188	0.557

Table 3.2: Singular values and expectation values of orbital energies of 2nd NROs of S_N2 reactions.

Leaving	Singular value	Contribution rate	Orbital enegry[hartree]		Energy gap
group	[amu$^{-1/2}$bohr^{-1}]	[%]	Occupied	Virtual	[hartree]
Cl	0.099	14.3	-0.518	0.407	0.925
Br	0.101	14.1	-0.517	0.401	0.918
I	0.103	14.4	-0.518	0.384	0.902
MsO	0.094	13.5	-0.517	0.405	0.922
CN	0.095	13.8	-0.569	0.432	1.001

Table 3.3: Frontier orbital energies and barrier heights of S_N2 reactions.

Leaving	Orbital enegry[hartree]		Energy gap	Energy [hartree]		Barrier
group	HOMO	LUMO	[hartree]	Reactant	TS	[kcal mol^{-1}]
Cl	-0.280	0.019	0.298	-556.7176	-556.6573	37.9
Br	-0.271	0.016	0.287	-2670.7619	-2670.7074	34.2
I	-0.257	0.011	0.269	-394.2801	-394.2281	32.6
MsO	-0.311	0.028	0.340	-760.3276	-760.2768	31.9
CN	-0.290	0.076	0.365	-189.3410	-189.2203	75.7

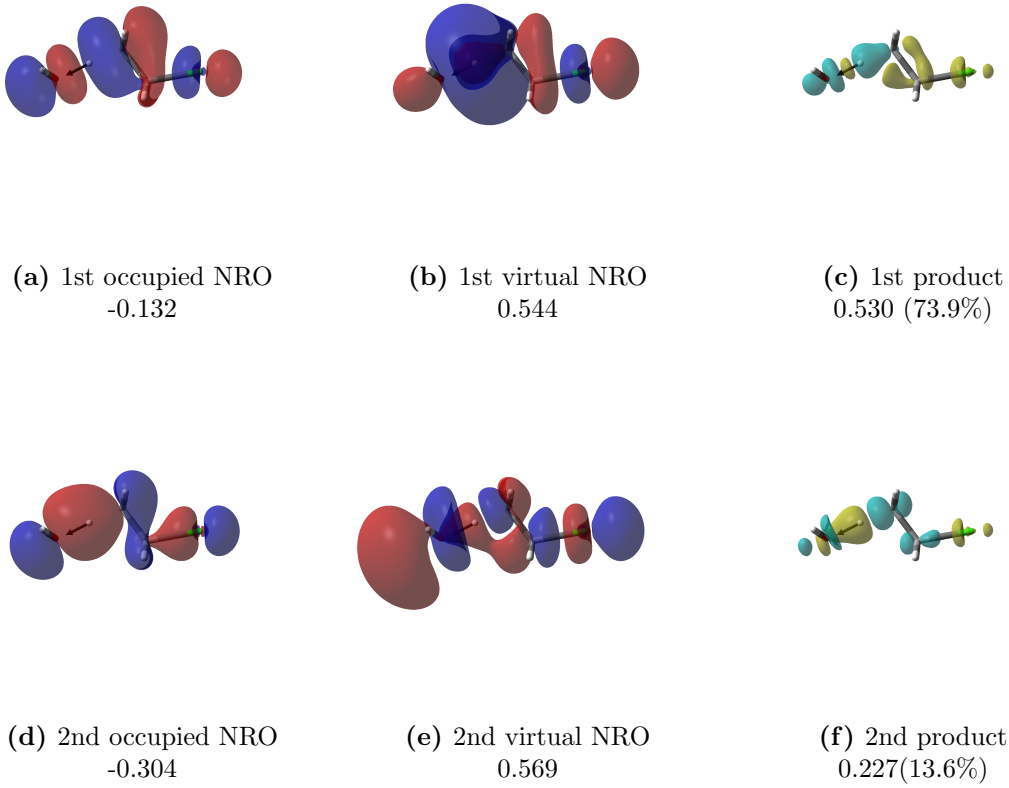

(a) 1st occupied NRO
-0.132

(b) 1st virtual NRO
0.544

(c) 1st product
0.530 (73.9%)

(d) 2nd occupied NRO
-0.304

(e) 2nd virtual NRO
0.569

(f) 2nd product
0.227(13.6%)

Fig. 3.26: NRO pairs and their products at the 1st-order saddle point of E2 reaction between OH^- and CH_3CH_2Cl. The 1st-order saddle point was optimized in ω B97XD/aug-cc-pVTZ level. The number shown below is the one-electron energy of NRO (hartree). Singular value of each NRO pair is shown below its product with the cumulative contribution percentage ($amu^{-1/2}$ $bohr^{-1}$). Product of each NRO pair indicates that electron density increases/decreases in the region colored by yellow/cyan when the nuclei displaced in the direction shown by black arrows, the normalmode with imaginary frequency.

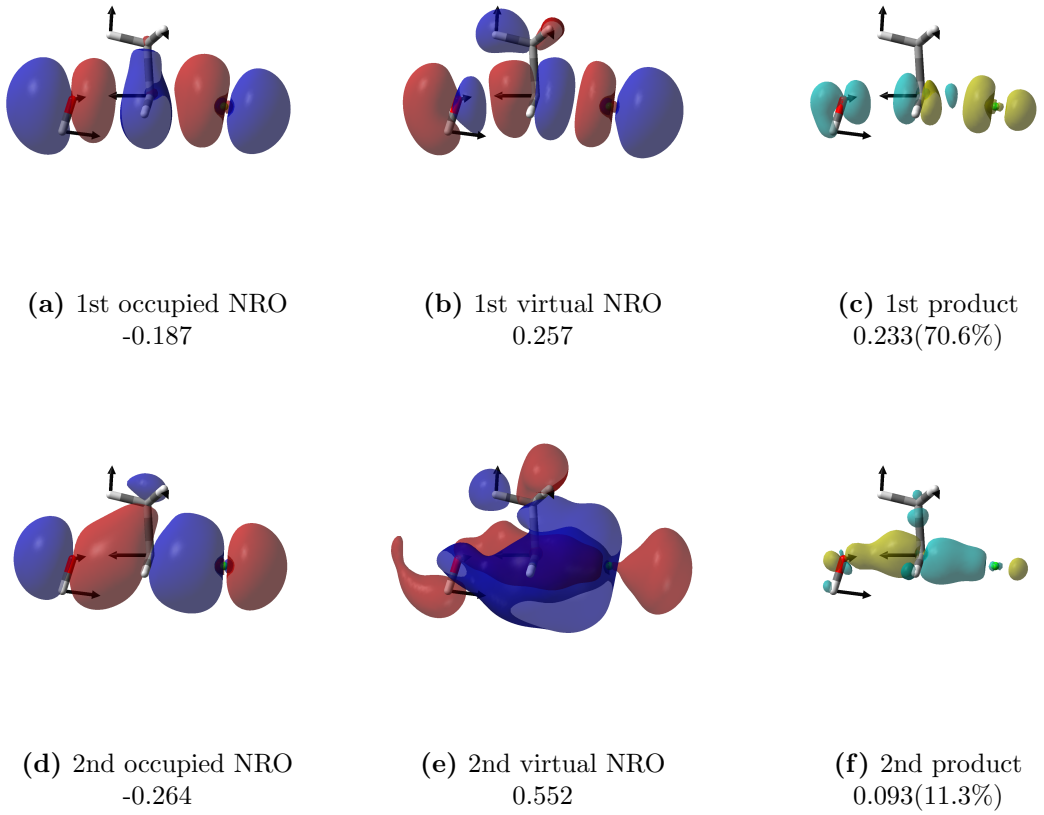

(a) 1st occupied NRO
-0.187

(b) 1st virtual NRO
0.257

(c) 1st product
0.233(70.6%)

(d) 2nd occupied NRO
-0.264

(e) 2nd virtual NRO
0.552

(f) 2nd product
0.093(11.3%)

Fig. 3.27: NRO pairs and their products at the 1st-order saddle point of S_N2 reaction between OH^- and CH_3CH_2Cl. The 1st-order saddle point was optimized in ωB97XD/aug$-$cc$-$pVTZ level. The number shown below is the one-electron energy of NRO (hartree). Singular value of each NRO pair is shown below its product with the cumulative contribution percentage (amu$^{-1/2}$ bohr^{-1}). Product of each NRO pair indicates that electron density increases/decreases in the region colored by yellow/cyan when the nuclei displaced in the direction shown by black arrows, the normalmode with imaginary frequency.

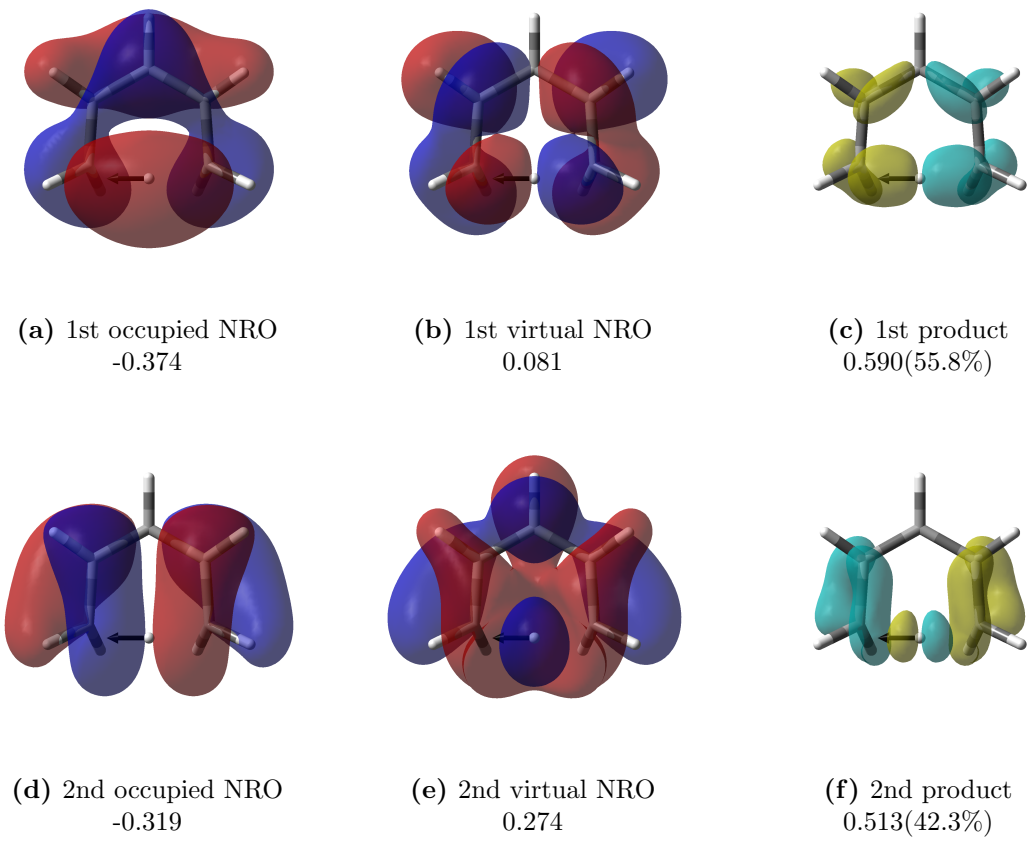

(a) 1st occupied NRO
-0.374

(b) 1st virtual NRO
0.081

(c) 1st product
0.590(55.8%)

(d) 2nd occupied NRO
-0.319

(e) 2nd virtual NRO
0.274

(f) 2nd product
0.513(42.3%)

Fig. 3.28: NRO pairs and their products at the 1st-order saddle point of [1,5]-sigmatropic rearrangement of 1,3-pentadiene. The 1st-order saddle point was optimized in ωB97XD/cc-pVTZ level. The number shown below is the one-electron energy of NRO (hartree). Singular value of each NRO pair is shown below its product with the cumulative contribution percentage (amu$^{-1/2}$ bohr^{-1}). Product of each NRO pair indicates that electron density increases/decreases in the region colored by yellow/cyan when the nuclei displaced in the direction shown by black arrows, the normalmode with imaginary frequency.

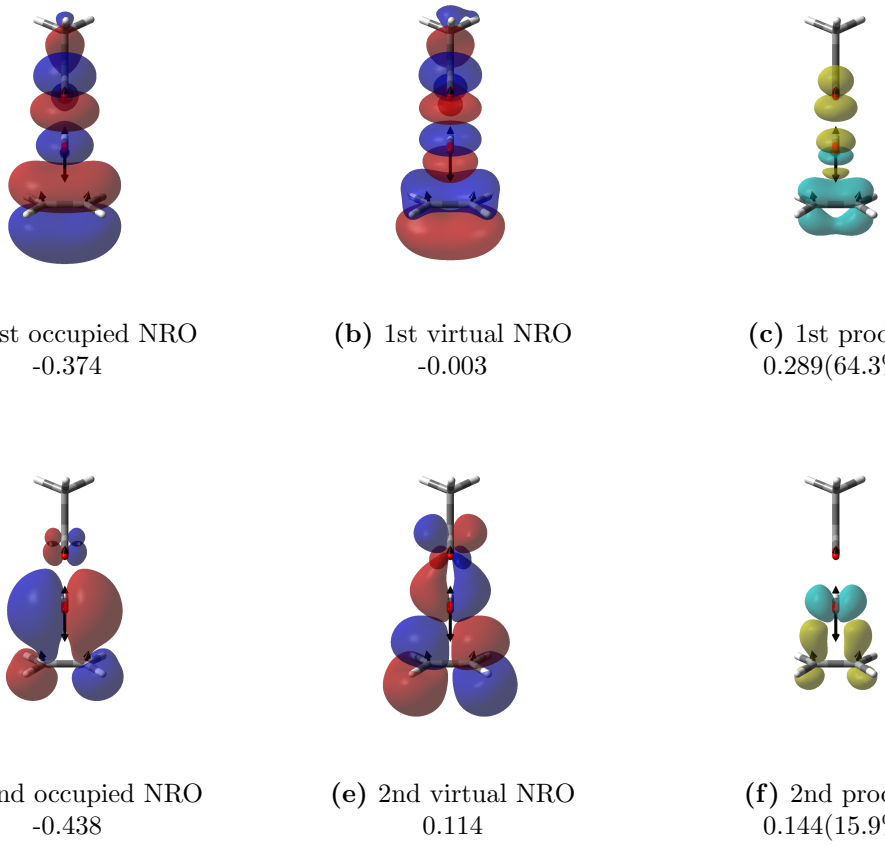

(a) 1st occupied NRO
-0.374

(b) 1st virtual NRO
-0.003

(c) 1st product
0.289(64.3%)

(d) 2nd occupied NRO
-0.438

(e) 2nd virtual NRO
0.114

(f) 2nd product
0.144(15.9%)

Fig. 3.29: NRO pairs and their products at the 1st-order saddle point of epoxidation of ethylene with peracetic acid. The 1st-order saddle point was optimized in ωB97XD/aug-cc-pVTZ level. The number shown below is the one-electron energy of NRO (hartree). Singular value of each NRO pair is shown below its product with the cumulative contribution percentage ($\mathrm{amu}^{-1/2}$ bohr^{-1}). Product of each NRO pair indicates that electron density increases/decreases in the region colored by yellow/cyan when the nuclei displaced in the direction shown by black arrows, the normalmode with imaginary frequency.

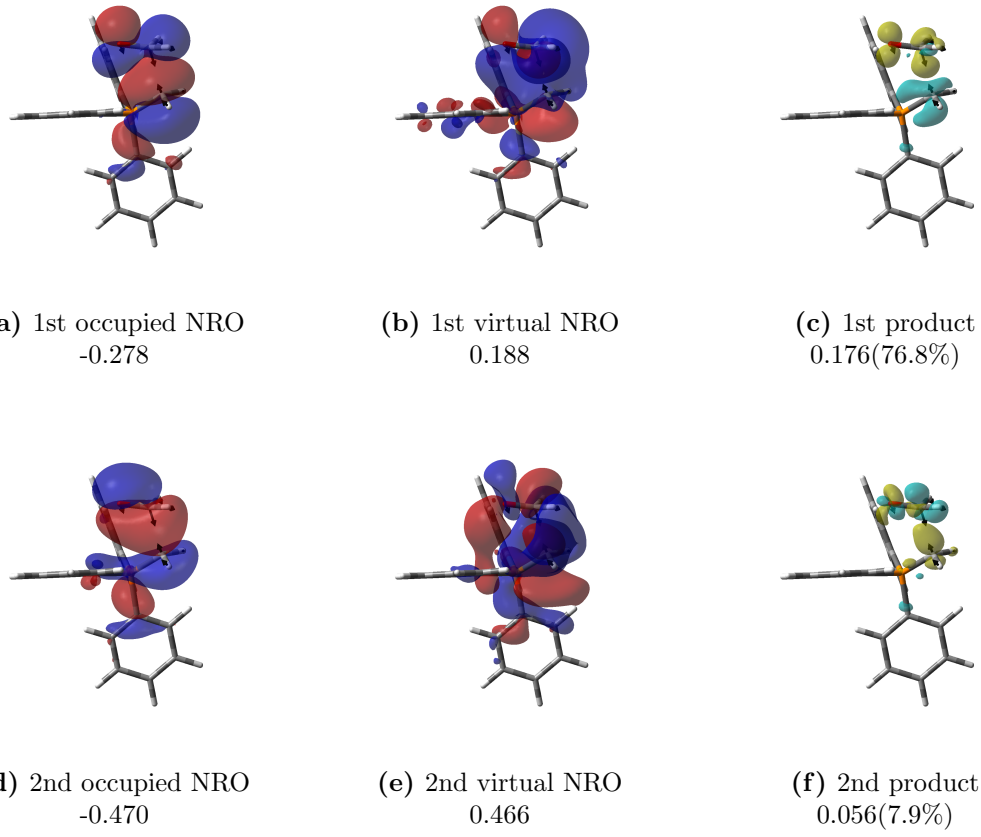

(a) 1st occupied NRO
-0.278

(b) 1st virtual NRO
0.188

(c) 1st product
0.176(76.8%)

(d) 2nd occupied NRO
-0.470

(e) 2nd virtual NRO
0.466

(f) 2nd product
0.056(7.9%)

Fig. 3.30: NRO pairs and their products at the 1st-order saddle point of Wittig reaction. The 1st-order saddle point was optimized in ωB97XD/Def2TZVPP level. The number shown below is the one-electron energy of NRO (hartree). Singular value of each NRO pair is shown below its product with the cumulative contribution percentage (amu$^{-1/2}$ bohr^{-1}). Product of each NRO pair indicates that electron density increases/decreases in the region colored by yellow/cyan when the nuclei displaced in the direction shown by black arrows, the normalmode with imaginary frequency.

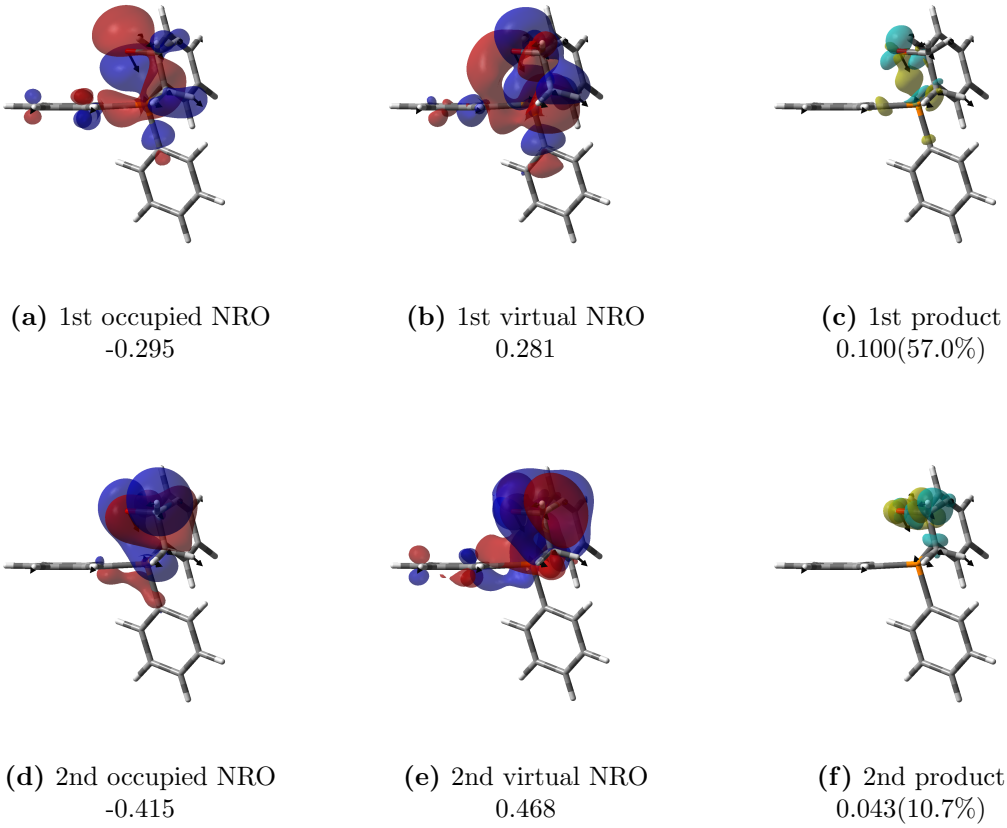

(a) 1st occupied NRO
-0.295

(b) 1st virtual NRO
0.281

(c) 1st product
0.100(57.0%)

(d) 2nd occupied NRO
-0.415

(e) 2nd virtual NRO
0.468

(f) 2nd product
0.043(10.7%)

Fig. 3.31: NRO pairs and their products at the shoulder of Wittig reaction. The 1st-order saddle point was optimized in ωB97XD/Def2QZVPP level. The number shown below is the one-electron energy of NRO (hartree). Singular value of each NRO pair is shown below its product with the cumulative contribution percentage ($\mathrm{amu}^{-1/2}$ bohr^{-1}). Product of each NRO pair indicates that electron density increases/decreases in the region colored by yellow/cyan when the nuclei displaced in the direction shown by black arrows, the normalmode with imaginary frequency.

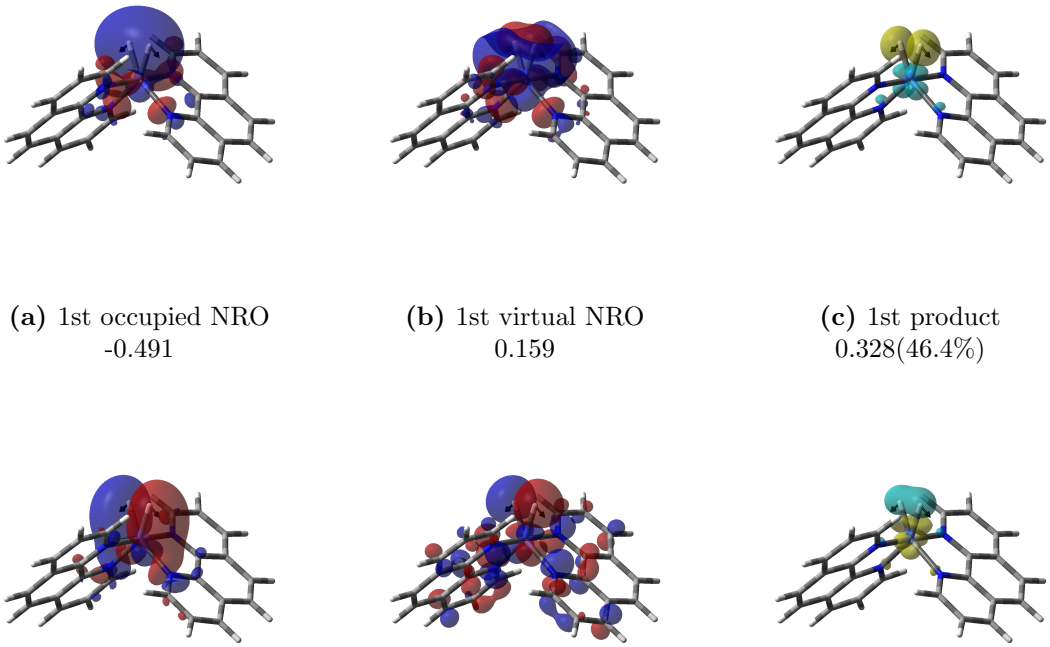

(a) 1st occupied NRO
-0.491

(b) 1st virtual NRO
0.159

(c) 1st product
0.328(46.4%)

(d) 2nd occupied NRO
-0.317

(e) 2nd virtual NRO
0.135

(f) 2nd product
0.307(40.5%)

Fig. 3.32: NRO pairs and their products at the 1st-order saddle point of oxidative addition of hydrogen to $[Co(phen)_2]^+$. The 1st-order saddle point was optimized in M06/SDD level. The number shown below is the one-electron energy of NRO (hartree). Singular value of each NRO pair is shown below its product with the cumulative contribution percentage ($amu^{-1/2}$ $bohr^{-1}$). Product of each NRO pair indicates that electron density increases/decreases in the region colored by yellow/cyan when the nuclei displaced in the direction shown by black arrows, the normalmode with imaginary frequency.

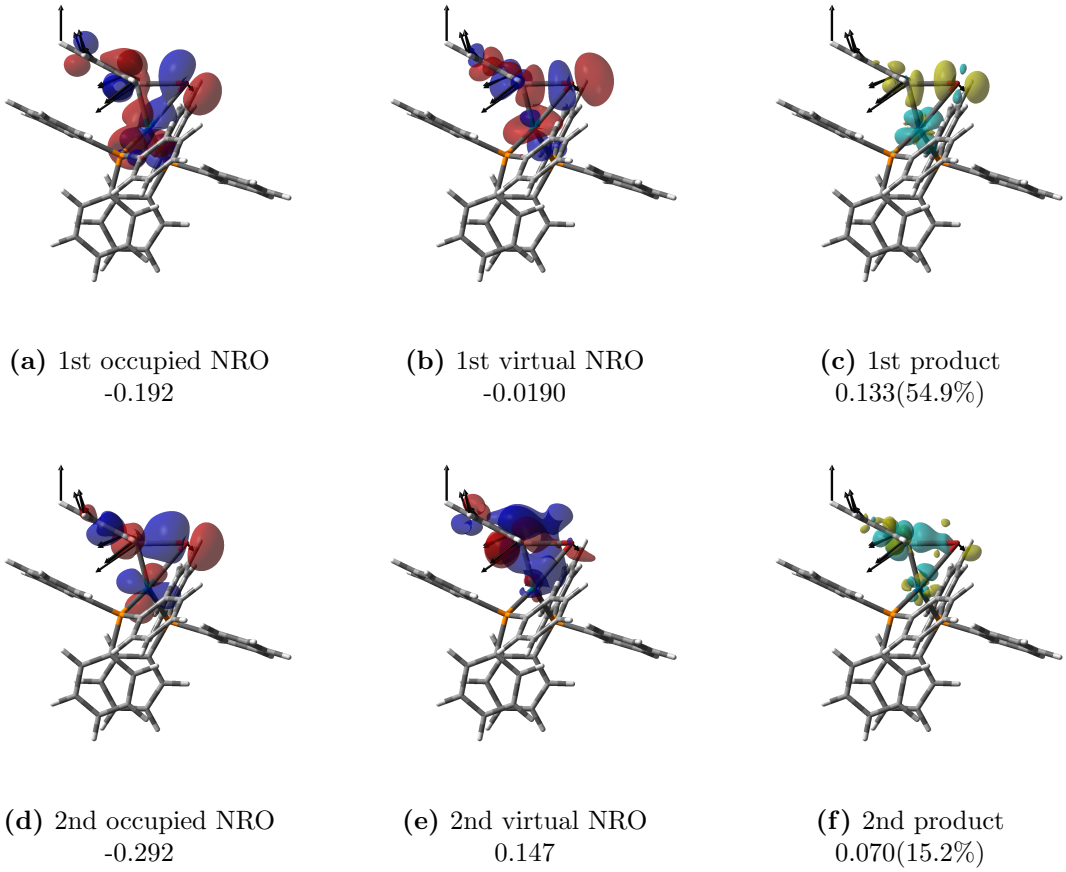

(a) 1st occupied NRO
-0.192

(b) 1st virtual NRO
-0.0190

(c) 1st product
0.133(54.9%)

(d) 2nd occupied NRO
-0.292

(e) 2nd virtual NRO
0.147

(f) 2nd product
0.070(15.2%)

Fig. 3.33: NRO pairs and their products at the 1st-order saddle point of oxidative addition step of Suzuki-Miyaura coupling. The 1st-order saddle point was optimized inM06/SDD level. The number shown below is the one-electron energy of NRO (hartree). Singular value of each NRO pair is shown below its product with the cumulative contribution percentage (amu$^{-1/2}$ bohr^{-1}). Product of each NRO pair indicates that electron density increases/decreases in the region colored by yellow/cyan when the nuclei displaced in the direction shown by black arrows, the normalmode with imaginary frequency.

Basis	1st occ. NRO	2nd occ. NRO	3rd occ. NRO	1st product
STO-3G	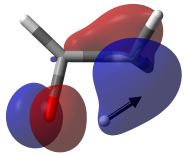	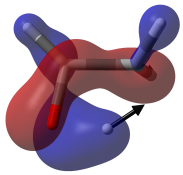	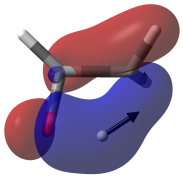	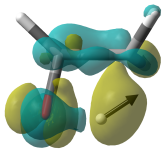
	(a) -0.258	**(b)** -0.452	**(c)** -0.580	**(d)** 1.264(87.7%)
aug-cc-pVTZ	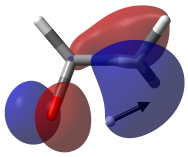	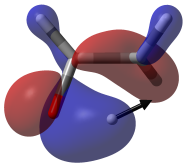	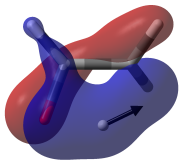	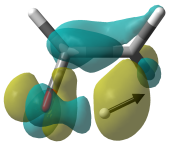
	(e) -0.328	**(f)** -0.494	**(g)** -0.555	**(h)** 0.905(88.1%)

Fig. 3.34: Occupied NROs and product of 1st NRO pair at the 1st-order saddle point of isomerization of vinyl alcohol. The 1st-order saddle point was optimized in HF/STO-3G and HF/aug-cc-pVTZ. The number shown below is the one-electron energy of NRO (hartree). Singular value of 1st NRO pair is shown below its product with the cumulative contribution percentage ($\mathrm{amu}^{-1/2}$ bohr^{-1}). Product of 1st NRO pair indicates that electron density increases/decreases in the region colored by yellow/cyan when the nuclei displaced in the direction shown by black arrows, the normalmode with imaginary frequency.

3.4 Discussion

3.4.1 S_N2-like reaction

NRO analysis is firstly applied to the S_N2-like reaction between formaldehyde radical anion CH_2O^- and methyl chrolide CH_3Cl. [32, 62, 151, 152, 160] This system is well known to have a post-transition-state bifurcation (PTSB): the reactant cluster C_R is transformed into either the C-alkylation cluster $C_{SUB(C)}$ or the dissociative electron transfer cluster C_{ET} (Fig. 3.2) through the common transition state ET-TS. A series of detailed studies were reported to clarify the unique nature of this reaction, including valence bond configuration mixing (VBCM) analysis. [32, 62, 151, 152, 160] Therefore, this system is favorable to investigate the validity of NRO analysis method.

(Fig. 3.3) shows a part of CMOs at the ET-TS. While the alpha HOMO seems to be the orbital responsible for the electron transfer, role of the highly delocalized low-lying virtual orbitals are very unclear. Unfortunately, it seems hardly possible to understand the reactivity of this S_N2-like reaction with CMO basis. On the other hand, the first alpha NRO pair shows semi-localized feature and is likely to appropriately characterize the reactivity of this S_N2-like reaction (Fig. 3.4). The direction of nuclear displacements is the imaginary frequency mode shown in Fig. 3.5. Each squared singular value of the first-order response matrix of MOs measures the degree of orbital mixing between the corresponding NRO pair. That is, NRO pairs with large singular values are mixed more strongly than those with small singular values. Considering that electron density change is induced by orbital mixing between the occupied and virtual MOs, NROs with large singular values are expected to be the essential MOs for the reactivity.. Surprisingly, more than 90% of the orbital mixing between α-spin occupied and virtual MOs at the ET-TS is described only with the first NRO pair. Also, it is shown that the contribution of β-spin MOs are negligibly small compared to that of α-spin MOs. This indicates that the electron behavior at the ET-TS may be explained enough only with the first NRO pair.

Before the detailed analysis of the reaction, the effect of basis set to NRO method is examined in Fig. 3.6. In this system, the number of basis function is given by 105 and 303 for 6-31+G(d,p) and aug-cc-pVTZ respectively. Nonetheless, there is only a slight difference between the two results. This result indicates the robustness and stability of NRO method.

The interesting relationship between NRO and density change given by (Eq. (3.2.122)) is very useful to analyze the electron transfer during chemical reaction. Fig. 3.7 shows the product of the first α-spin NRO pair which can be regarded as a component of first-order density change induce by the nuclear displacement represented by the arrows. The product of the first NRO pair clearly shows the α electron transfer from π^*_{CO}

to σ^*_{CCl} in the forward direction. it is also reasonable that the reversal electron transfer takes place given the displacements in the reverse direction.

So far, only NROs at the ET-TS was discussed. Herein, the behavior of electrons along the IRC is analyzed. Fig. 3.8 shows the energy along IRC (black curve) and the squares of Frobenius norm of the first-order response matrix of α-spin MOs and β-spin MOs along IRC (red and blue dots respectively). It is notable that there exists a very sharp peak of $\|\mathbf{\Lambda}^\alpha\|_F^2$ at the ET-TS. This means that the occupied and virtual α-spin orbitals are strongly mixed in the vicinity of ET-TS. Although $\|\mathbf{\Lambda}^\beta\|_F^2$ also has a peak at the ET-TS, it is negligibly small compared to that of $\|\mathbf{\Lambda}^\alpha\|_F^2$. It implies that the change occurring around the ET-TS will be mainly characterized as the change of α-spin orbitals. Fig. 3.8 shows another characteristic region, the shoulder of energy at $s = 4.49\mathrm{amu}^{1/2}\mathrm{bohr}$. Importantly, $\|\mathbf{\Lambda}^\alpha\|_F^2$ and $\|\mathbf{\Lambda}^\beta\|_F^2$ are almost zero except for these characteristic regions. This fact indicates that orbital mixing takes palce in a very narrow sections along IRC.

Fig. 3.9 shows the dominant NROs at the ET-TS and the shoulder ($s = 4.49\mathrm{amu}^{1/2}\mathrm{bohr}$). The result of VBCM analysis is also shown. As noted above, the electron density change at ET-TS is characterized by the first α NRO pair: α electron transfers from π^*_{CO} to σ^*_{CCl}. This is apparently consistent with the VBCM analysis. On the other hand, the contributions of α- and β-spin orbitals at the shoulder are comparable. The first α NRO pair at the shoulder brings about electron transfers from σ^*_{CCl} or C-2$\mathrm{p_z}$ to π^*_{CO}. The first β NRO pair contributes to the C-C σ bond formation through the electron migration from π_{CO} to σ_{CC} or σ^*_{CCl}. These results are also consistent with the VBCM analysis. Hence, NRO method could correctly extract the feature of this $\mathrm{S_N}2$-like reaction at the two characteristic regions.

To summarize the NRO analysis, $\mathrm{S_N}2$-like reaction between $\mathrm{CH_2O^-}$ and $\mathrm{CH_3Cl}$ consists of two asynchronous electron transfers: electron transfer π^*_{CO} to σ^*_{CCl} and the subsequent C-C σ bond formation. While the nuclear motion is hardly distinguishable from that of the usual concerted $\mathrm{S_N}2$ reaction, its electron transfer is surely different from that of $\mathrm{S_N}2$ reaction. Therefore, NRO method can provide information unavailable with only analyzing the nucler motion along IRC.

3.4.2 Claisen rearrangement

Next, NRO analysis is applied to the Claisen rearrangement of allyl vinyl ether. Fig. 3.10 shows the energy along the IRC and the square of Frobenius norm of of the first-order response matrix of molecular orbitals. There are three regions where $\|\mathbf{\Lambda}\|_F^2$ has a large value: reactant region, TS region and product region. However, the NROs at the reactant and product regions are relatively trivial for the Claisen rearrangement. Hence, NROs at the TS are discussed here. Fig. 3.11 shows the first

and second NRO pairs and the corresponding products. The first NRO pair contributes to the π bond rearrangement. On the other hand, the second NRO pair contributes to the σ_{CO} bond dissociation and the σ_{CC} bond formation. The density change clearly corresponds to the bond rearrangements in the Claisen rearrangement of allyl vinyl ether. Therefore, it is confirmed that NRO successfully extracts the MOs essential for the Claisen rearrangement.

3.4.3 Diels-Alder reaction

NRO analysis is also applied to Diels-Alder reaction of 1,3-butadiene and nitroethylene. Fig. 3.12 shows the energy along the IRC and the square of Frobenius norm of of the first-order response matrix of molecular orbitals along the IRC. There are two peaks of $\|\mathbf{\Lambda}\|_F^2$: one is at X and the other is at TS. The first and second NRO pairs at X is shown in (a) of Fig. 3.13. The nuclear motion at X is the twist mode of 1,3-butadiene. Although this conformation change is needed to reach the TS, there is apparently no bond rearrangement. The first NRO pair only shows that the electron density follows this twist motion. Hence, the small peak of $\|\mathbf{\Lambda}\|_F^2$ at X is rather trivial for the Diels-Alder reaction. On the other hand, the dominant NRO pairs at the TS clearly characterizes the bond rearrangements of the Diels-Alder reaction. Fig. 3.12 (b) shows the first and second NRO pairs contribute to the left and right C-C σ bond formation respectively. There is electron density increase between C2 and C3 of 1,3-butadiene moiety which seems to contribute to the π_{CC} bond formation. The electron density decrease in π orbitals in nitroethylene and in π_{C1C2} and π_{C3C4} correspond to the π bond cleavages taking in place in Diels-Alder reaction. Hence, the density change appropriately corresponds to the bond rearrangements in the Diels-Alder reaction. This shows NRO method suitably characterizes the reactivity of Diels-Alder reaction. Actually, the NROs of Diels-Alder reaction of 1,3-butadiene and ethylene are different from the NROs discussed above (Fig. 3.14). This difference seems to reflect the effect of substitution group, nitro group (-NO_2) and implies that NRO method may be used to analyze such effect on the reactivity.

3.4.4 Proton transfer of malonaldehyde

Next, proton transfer of malonaldehyde is analyzed with NRO method. Fig. 3.15 shows the energy and the square of Frobenius norm of of the first-order response matrix of molecular orbitals along the IRC. There is a clear peak of $\|\mathbf{\Lambda}\|_F^2$ centered at the TS. The proton transfers from left to right. The first and second NRO pairs and the corresponding products are shown in Fig. 3.16. The product of first NRO pair shows electron density decrease in the left π^*_{CO} and π_{CC}. The former contributes to the π_{CO} bond formation with weakening the anti-bonding feature. The latter directly

contributes the π_{CC} bond cleavage. The opposite behavior is shown in the right half because of the C_{2v} symmetry of the TS geometry. The product of the second NRO pair shows electron density increase/decrease in the p-type orbitals of left/right oxygen atoms. The electron density decrease in the right oxygen seems to contribute to HO bond formation with sharing its electron with the migrating proton. On the other hand, the electrons shared between the left oxygen atom and the proton are released back into the p-type orbital of the left oxygen as the proton transfer. Both of the π and σ electron density changes are consistent with the bond rearrangements of the proton transfer. Thus, NRO method can also successfully characterize the reactivity of the proton transfer of malonaldehyde.

3.4.5 1,2-alkyl shift and nitrene addition

As a relatively complicated reaction, 1,2-alkyl shift and nitrene addition are analyzed with NRO method. Interestingly, these two processes proceed as a single elementary reaction. Fig. 3.17 shows the energy and the square of Frobenius norm of of the first-order response matrix of molecular orbitals along the IRC. The energy curve has a very distinct shoulder around $s = -7.95\text{amu}^{1/2}\text{bohr}$ and $\|\mathbf{\Lambda}\|_F^2$ shows a very sharp peak in the vicinity of the shoulder. This implies the existence of some characteristic orbital mixing at the shoulder. Also, $\|\mathbf{\Lambda}\|_F^2$ has a peak around the TS. Fig. 3.18 shows the first and second NRO pairs and the corresponding products at the shoulder and TS. At glance, the nuclear motion at the shoulder seems to be a trivial rotation of nitrene moiety. However, the products of the first and second NRO pairs clearly show the dissociation of the C-N σ bond and formation of the C-C σ bond respectively. However, the contribution ratio of the second NRO pair is too small compared to the first pair. Therefore, the main event at the shoulder is the C-N σ bond dissociation and the C-C bond formation is supposed to proceed elsewhere. Indeed, the product of first NRO pair at the TS clearly shows the C-C bond formation.

3.4.6 S_N2 reaction

The first and second NRO pairs of S_N2 reaction between NH_3 and CH_3Cl are shown in Fig. 3.21. The geometry is the first-order saddle point of the reaction. The direction of nuclear displacements is in the direction of N-C bond formation. The first occupied NRO is composed of $2p_z$ of nitrogen, 2s of carbon and $3p_z$ of chlorine. On the other hand, the first virtual NRO is composed of N-$2p_z$, C-$2p_z$ and Cl-$3p_z$. The orbital mixing between the first NRO pair results in the electron density change shown in Fig. 3.21(c), electron density decreases/increases in $\sigma^*_{\text{N-C}}/\sigma_{\text{C-Cl}}$. Thus, the orbital mixing contributes to N-C σ bond formation and C-Cl σ bond dissociation. The second occupied NRO is composed of N-$2p_z$, C-$2p_z$ and Cl-$3p_z$. Although the second virtual

NRO shows a diffuse character, the density change induced by the mixing between the second NRO pair shows a tight feature (Fig. 3.21(f)). It clearly shows electron density increase/decrease in $\sigma_{\text{N-C}}/\sigma^*_{\text{C-Cl}}$ which apparently contributes to N-C σ bond formation and C-Cl σ bond dissociation. Accordingly, the density changes of the first and second NRO pairs adequately characterizes the electron transfer in the S_N2 reaction. Therefore, the corresponding NRO pairs are considered to be essential for the electron transfer in this reaction.

Fig. 3.22 shows 6 CMOs at the same geometry. HOMO and HOMO-1, Cl-3p$_x$ and Cl-3p$_y$ orthogonal to the molecular axis, seem to be unessential for this reaction. HOMO-2 seems to be rather important for the reaction with resembling the first occupied NRO. This indicates that HOMO do not necessarily play an essential role in the vicinity of the first-order saddle point. In addition, the role of LUMO is unclear. Unfortunately, LUMO+1 and LUMO+2 also show highly diffuse features and seem to be meaningless for the reaction. In this case, there is no low-lying virtual MO essential for the reactivity. Accordingly, it is found to be difficult to extract reactive MOs automatically with CMO basis used.

The situation is not necessarily improved by using NBO and NLMO because NBO and NLMO is not the technique to extract reactive MOs. Fig. 3.23 shows the highest and the second highest occupied NBOs and the lowest and the second lowest occupied NLMOs. The HONBO and HONBO-1 are almost same to HOMO and HOMO-1. Thus, HONBO is not necessarily essential for the reactivity. While LUNLMO characterizes the reactivity much better than LUMO, it seems difficult for NBO and NLMO to safely extract reactive MOs in an automated manner. However, it must be noted that this difficulty is not a drawback of NBO and NLMO because automated extraction of reactive MOs is not the original purpose of the two orbital analysis methods. They are still convenient methods for extracting Lewis structure from given multi-electron wavefunction.

The comparison of NRO, CMO and NBO presented above indicates that NRO is more effective for automation of reactive MO extraction than the other. Fig. 3.24 also confirms that dominant NROs of same type of reactions resemble each other. Fig. 3.24 shows the first NROs of S_N2 reactions between NH_3 and CH_3X (X=Cl, Br, I, MsO, CN). It clearly shows all these NROs resemble each other despite the different leaving groups. This result seems to be reasonable in chemical sense because the essence of S_N2 reaction won't be largely changed by the difference of leaving groups. Fig. 3.25 also shows similar result. Therefore, NRO provides a reasonable way to compare same type of reactions of different compounds.

Table 3.1 shows the singular values and orbital energies of the first NROs shown in Fig. 3.24. For halogen leaving groups, the orbital energy of the first occupied NRO

follows I >Br >Cl whereas the order is reversed in the first virtual NRO. The energy gap, therefore, decreases in the order Cl >Br >I. It should be noted that the order is reversed in the singular value. Conventionally, this negative correlation between energy gap and response of electrons are explained with perturbation series. That is, terms with small denominators, i.e., small energy gaps, are supposed to have larger contributions to the response. This conventional explanation seems valid for the above mentioned case of halogens whereas a problem of such explanation is pointed out [25]. Indeed, CN has larger singular value than Cl although the energy gap is larger than that of Cl. Therefore, it seems dangerous to adopt the assumption not only for the analysis of a single compound but also for the comparison of different compounds. Also, the energy gaps of the first NRO pairs and the reaction barriers shown in Table 3.3 show an interesting result. MsO shows the lowest barrier in the five leaving groups whereas its orbital energy gap of the first NRO pair is the largest. Based on the above mentioned conventional assumption, MsO is supposed to have the smallest response of electrons. Thus, the distortion or relaxation of potential energy at the TS is also supposed to be weakest and this seems to be unfavorable for the reaction. Nonetheless, the MsO shows the lowest barrier height in the five and this is qualitatively consistent with experiments. Actually, CN also shows an interesting result. The orbital energy gap of CN is between Cl and MsO. Thus, the reaction barrier is supposed to be between Cl and MsO. However, CN has by far the highest barrier in the five. This result clearly shows that the orbital energy gap at the TS is almost useless to explain the reactivity even if the orbitals appropriately characterize the reactivity. It should be noted that the orbital gaps of frontier orbitals, HOMO-LUMO gaps , at the TSs are also useless (Table 3.3). However, the reactivity of MsO and CN may be understood by orbital energies and the nodal patterns of occupied NROs. The first occupied NRO of MsO have by far the lowest orbital energy in the five (Table 3.1). Thus, the anti-bonding occupied orbital of MsO shown in Fig. 3.24 is much more stable than the other. This stabilization is apparently attributed to the MsO group because the moieties of NH_3 and CH_3 are common. Accordingly, the low reaction barrier of MsO is supposed to be caused by the stabilization of anti-bonding orbital between the leaving group and CH_3. On the other hand, the orbital energy of the second occupied NRO of CN is by far the lowest in the five. The second occupied NRO shows the bonding nature between CH_3 and CN. The strong stabilization of the bonding orbital is apparently caused by CN group since the rest part is common. Thus, the cause of the extremely high barrier of CN seems to be attributed to the strong bond between the leaving group and the CH_3. While more quantitative analysis is required to verify these two explanations, however, orbital energies of predominant NROs at the TSs seem to reflect the reactivity to some extent. It should be emphasized that frontier orbitals at the TSs cannot provide similar

explanation because they do not necessarily characterize the reactivity.

3.4.7 E2 reaction

E2 reaction between OH^- and CH_3CH_2Cl can compete with S_N2 reaction pathway. That is, the reactants of these competing pathways are identical. It is important whether NRO method can adequately characterize the different reactivities of E2 and S_N2 reaction pathways.

Fig. 3.26 shows the first and second NRO pairs and the corresponding density changes of E2 reaction pathway. The first NRO pair induces electron density increase in $\pi_{\text{C-C}}$ and $\sigma^*_{\text{C-Cl}}$ (Fig. 3.26(c)). This contributes to the C-C π bond formation and C-Cl σ bond dissociation. Also, electron density decrease in $\sigma^*_{\text{O-H}}$ is observed. This contributes to the abstraction of proton by OH^-. The second NRO pair induces electron density increase/decrease in $\sigma_{\text{O-H}}/\pi^*_{\text{C-C}}$. This also contributes to he C-C π bond formation and the abstraction of proton by OH^- (Fig. 3.26(f)).

Fig. 3.27 shows the first and second NRO pairs and the corresponding density changes of S_N2 reaction pathway. The first NRO pair induces electron density decrease/increase in $\sigma^*_{\text{O-C}}/\sigma_{\text{C-Cl}}$ (Fig. 3.27(c)). This contributes to the O-C σ bond formation and C-Cl σ bond dissociation. The second NRO pair induces electron density increase/decrease in $\sigma_{\text{O-C}}/\sigma^*_{\text{C-Cl}}$. This also contributes to the the O-C σ bond formation and C-Cl σ bond dissociation (Fig. 3.27(f)).

Comparison of Fig. 3.26 and Fig. 3.27 clearly confirms that NRO can distinguish E2 reaction and S_N2 reaction. For example, the first occupied NRO of E2 reaction has large amplitude of C2-2p_z while that of S_N2 reaction does not. Fig. 3.27(a) indicates that C1-2p_z is more essential for S_N2 reaction. Therefore, NRO method is capable of distinguishing the reactivities of different type of reactions. This may be also important for discussing reactions giving some by-products.

The barrier heights of E2 mechanism and S_N2 mechanism are 16.4 kcal/mol and 22.4 kcal/mol respectively. The difference in barrier heights may be attributed to the difference in the orbital energies of predominant NROs. The orbital energy of the first occupied NRO at the TS of E2 reaction (E2-TS) is higher than that at the TS of S_N2 reaction (S_N2-TS). Both of the two first occupied NROs show anti-bonding character between C and Cl. However, the first occupied NRO of E2-TS includes the contribution of 2p orbitals of the two carbon atoms whereas there is no contribution of C-2p in the first occupied NRO of S_N2-TS. The 2p orbitals seem to accelerate the dissociation of C-Cl bond by electronic repulsion between C and Cl. Indeed, the orbital energy is higher in E2-TS. The difference in the second NRO energies seem to be also important. The 2nd occupied NRO at E2-TS shows a distinct bonding character between O and H. On the other hand, S_N2-TS shows a bonding character between O and C. Common

bond energies of OH bond and OC bond are given by 467 kcal/mol and 358 kcal/mol. Therefore, 2nd occupied NRO at E2-TS is supposed to be more stable than that at S_N2-TS. Indeed, the orbital energy of the second occupied NRO is lower in E2-TS. This result implies that predominant NROs at the TSs may be useful for comparison of different reaction mechanisms.

3.4.8 Sigmatropic rearrangement

[1,5]-sigmatropic rearrangement of 1,3-pentadiene is recently analyzed with using correlation diagram. Therefore, the reaction is favorable to check the consistency of NRO with conventional understanding. The first and second NRO pairs and the corresponding density changes are shown in Fig. 3.28. The geometry corresponds to the first-order saddle point of [1,5]-sigmatropic rearrangement. The proton transfers from C1 (the right end) to C5 (the left end). The first NRO pair induces σ_{C5-H} bond formation and σ_{C1-H} bond dissociation (Fig. 3.28(c)). π_{C2-C3} bond cleavage and π_{C3-C4} bond formation are also observed. Electron density decrease/increase in $\pi^*_{C1-C2}/\pi^*_{C4-C5}$ seem to contribute to the π_{C1-C2} bond formation and π_{C4-C5} bond cleavage. The second NRO pair also contribute to the π_{C1-C2} bond formation and π_{C4-C5} bond cleavage.

The first and second NRO pairs clearly correspond to the MOs playing a central role in the conventional correlation diagram. This indicates that NRO method can extract the essential MOs consistent with the conventional understanding.

3.4.9 Epoxidation of alkene

Fig. 3.29 clearly illustrates the aspect of epoxidation reaction of alkene as a nucleophilic substitution. The first NRO pair induces the density change shown in Fig. 3.29(c). The density change resembles that of S_N2 reaction Fig. 3.21. This highlights that ethylene and peracetic acid may be regarded as a nucleophile and an electrophile. The second NRO pair induces the π back-donation from OH to ethylene which also contributes to the formation of three-membered ring of epoxide.

3.4.10 Wittig reaction (addition step)

NRO analysis is applied to Wittig reaction between $P(Ph)_3$ and H_2CO. Fig. 3.30 indicates that NRO method is still valid for a system of middle size. The first occupied NRO are composed of π^*_{CO} and π_{CP} of $P(Ph)_3$. Although the first virtual N RO looks complicated, it may be, approximately, regarded as what obtained by reversing the phase of π_{CP} in the first occupied NRO. The density change induced by the orbital mixing between the first NRO pair is shown in Fig. 3.30(c). It clearly shows the electron transfer from π_{CP} to π^*_{CO}. The second NRO pair contributes to the formation of $\sigma_{C\text{-}C}$ between $P(Ph)_3$ and H_2CO. However, there is no distinct density increase between the

oxygen and phosphine at the first-order saddle point. The formation of σ_{OP} proceeds in the vicinity of the shoulder of IRC. Indeed, Fig. 3.31(c) shows the σ_{OP} formation by electron transfer from the oxygen to phosphine. The second NRO pair seems trivial for the reaction. Therefore, NRO method is confirmed to be also valid for a system of middle size like Wittig reaction.

3.4.11 Oxidative additions

It is important to check the applicability of NRO method to catalytic reactions. Fig. 3.32 shows the first and second NRO pairs of oxidative addition of H_2 to $[Co(phen)_2]^+$. In spite of the large aromatic ligands, NROs show semi-localized feature. The first NRO pair contributes to π back-donation from Co to H_2 (Fig. 3.32(c)). On the other hand, the second NRO pair contribute to σ donation from H_2 to Co. This is apparently consistent with the conventional understanding of coordination chemistry.

Fig. 3.33 shows the oxidative addition of BrPh to $Pd(PPh_3)_2$. This reaction is known as one step of Suzuki-Miyaura cross coupling reaction. The first NRO pair contributes to π back-donation from Pd to BrPh. Different from the case of $[Co(phen)_2]^+$, the feature of σ donation is not clear. This seems to reflect that Pd has ten d-electrons and the ability as acceptor is not so strong as Co^+ with only eight d-electrons.

In both cases, NRO appropriately characterizes the nature of oxidative addition. It is obvious that the nature of reductive elimination can also be characterized by NRO. It is immediately confirmed only by reversing the direction of nuclear displacements in Fig. 3.32 and Fig. 3.33. Inversion of nuclear displacements just reverses the relative phase of each NRO pair and the sign of density change. Thus, reductive elimination, the reversal process of oxidative addition, can be characterized with the same NROs of oxidative addition while the relative phase needs to be reversed.

3.4.12 Comparison with paired interacting orbital

As the final demonstration, NRO method is applied to the isomerization of vinyl alcohol. Although this reaction is so simple, it is the best system to show the difference between NRO and paired interacting orbital (PIO). [47] Fig. 3.34 shows the three dominant NRO pairs for STO-3G basis and aug-cc-pVTZ basis. It is surprising that there is no significant difference between the two results. In both cases, the phases of O-2p and 2C-2p are opposite. However, the predominant PIO shows that O-2p and 2C-2p are in-phase. The difference between NRO and PIO apparently comes from the difference of definition. NRO is defined to characterize electron density change induced by nuclear displacements. Thus, the first NROs shown in Fig. 3.34 are the optimal MOs to describe the electron transfer during the isomerization. On the other hand, PIO is defined to characterize electron delocalization between two distinguished fragments.

This indicates that the most dominant PIO describes the electron delocalization from the fragment of OCH_2CH_2 to the migrating proton. However, the isomerization reaction is apparently different from a process of such delocalization. Accordingly, an important point for PIO to characterize the reactivity is obtained: it must be checked whether the delocalization between fragments corresponds to the electron transfer during the reaction. Otherwise, PIO at a single geometry does not necessarily characterize the reaction while it seems still possible to analyze the reactivity by following the change of PIOs along IRC.

3.5 Conclusion

In this chapter, a new orbital analysis method named natural reaction orbital (NRO) was introduced. NRO is defined as the SVD basis of the virtual-occupied block of the first-order response matrix of molecular orbitals, $\mathbf{U}^{(1)}_{\mathrm{VO}}$, which is obtained by solving CP-SCF equation. If the basis is complete, $\mathbf{U}^{(1)}$ is considerd as the generator of infinitesimal nuclear displacements. The SVD basis of $\mathbf{U}^{(1)}_{\mathrm{VO}}$, i.e., NRO, is the basis with which no orbital mixing between different pairs take place. Therefore, NRO can succinctly describe the orbital mixing induced by the given nuclear displacements. Also, product of each NRO pair is considered as a component of electron density change caused by the orbital mixing. Thus, NRO can also be considered as the optimal orbital basis to characterize the electron transfer induced by the nuclear perturbation.

As confirmed by the application to a variety of typical chemical reactions, NRO can automatically extract the orbitals responsible for the reactivity. NRO analysis along IRC clarified that electron transfer or orbital mixing usually takes place at some characteristic regions, first-order saddle point, shoulder of IRC, whereas an exception is observed in the carbocation rearrangement. Even in such exceptional case, the region where orbital mixing proceeds can be detected from the change of Frobenius norm of $\mathbf{U}^{(1)}_{\mathrm{VO}}$ along IRC. In every case, NRO computed at these characteristic regions successfully extracted the orbitals characterizing the electron transfer. The most important region to be analyzed at first is, however, the first-order saddle point because it determines the reaction barrier. NRO is very suited for the analysis of reactivity at the first-order saddle point since it can automatically extract the MOs essential for the reaction at a single geometry. It is a great advantage of NRO method that it does not require any trace of MOs along IRC to determine the reactive MOs. Once a saddle point is located and CP-SCF equation is solved to check the stability of the geometry, MOs responsible for the reaction can be determined locally. Thus, NRO method is highly compatible with the conventional reaction mechanism analysis along IRC. It should be also remarked that the basis set dependence of NRO is relatively low. This robustness

is very important for reliable discussion of the reactivity.

Interestingly, it is implied that the stability of predominant occupied NROs are useful for the comparison of the reactivity of different compounds in the example of S_N2 reactions. Also, comparison of different type of reactions may be possible as demonstrated by the comparison of E2 and S_N2 mechanisms. These examples imply that the extraction of MOs responsible for reactivity is effective for understanding the essence of the reaction.

Although NRO was designed to automatically extract the MOs characterizing the reactivity, it is remarkable that perturbation theory and SVD also gave the method other good features. The result seems to indicate the significance of mathematics and physics on chemical problems. For all the favorable features noted above, NRO method seems to be a very promising orbital analysis method and is expected to widely help the chemical reaction mechanism analysis from a viewpoint of orbital mixing.

Chapter 4

Extension of Natural Reaction Orbital to Multiconfigurational Theories

Abstract

In the previous chapter, natural reaction orbital (NRO) was introduced. NRO automatically extracts occupied and virtual orbital pairs that characterize electron transfer in reaction processes by using singular value decomposition (SVD) of the first-order orbital response matrix to nuclear coordinate displacements. Although NRO was found to be useful to analyze electron transfer or bond rearrangements during chemical reactions, its applicability was limited to single configuration theories such as Hartree-Fock theory and Kohn-Sham theory. In principle, it is straightforward to generalize the formalism of NRO to multiconfigurational theories, e.g., complete active space self-consistent field (CASSCF) theory, Such straightforward generalization, unfortunately, is demanding because it requires the computation of derivatives of configuration interaction (CI) coefficients. Hence, another practical formalism should be developed for multiconfigurational theories.

In this chapter, the concept of NRO is extended to multiconfigurational wavefunctions as multiconfiguration NRO (MC-NRO). MC-NRO extracts orbital pairs that characterize electron density change with respect to nuclear displacements. Not only the contribution of orbital mixing to the electron density change but also that of configuration mixing can be characterized by MC-NRO. Hence, in principle, it can be applied to wide range of chemical reactions inc luding covalent bond dissociation and those in electronically excited states. MC-NRO analysis is performed for five typical reactions in order to validate the formulation.

4.1 Introduction

In the previous chapter, natural reaction orbital (NRO) was introduced. [33] NRO is designed to optimally characterize the electron density change induced by molecular deformation. In single-configurational theories, e.g., Hartree-Fock (HF) theory, the density change is attributed to orbital mixing between occupied and virtual MOs.[1] In multiconfigurational theories, e.g., complete active space self-consistent field (CASSCF) theory, however, configuration mixing can also cause density change. Configuration mixing allows the occupation number of each MO to vary from zero to one whereas orbital mixing does not. Accordingly, the contribution of configuration mixing must be also taken into account in order for the full description of adiabatic evolution of electron density in the framework of multiconfigurational theory. As discussed in section 3.2.9, in principle, NRO can be generalized to multiconfigurational theories. The generalized formalism can also characterize the electron density change induced by configuration mixing. Unfortunately, however, the straightforward generalization is not very practical because it requires the computation of derivatives of configuration interaction coefficients with respect to the nuclear coordinates that are computationally demanding. Hence, another practical formalism must be developed to characterize adiabatic evolution of electron density in multiconfigurational theories.

4.2 Theory

In this section, the molecular orbital which characterize the electronic density change induced by nuclear displacements is introduced in the framework of multiconfigurational theory.

4.2.1 Case of Hartree-Fock limit

Before the case of finite basis set, the case of Hartree-Fock limit is discussed.

First, the matrix which characterizes the density response with respect to the nuclear displacement is introduced. In general, state ket in multiconfigurational theory is given by a linear combination of configuration state function (CSFs):

$$\big|\Psi\big\rangle = \sum_I C_I \big|\Phi_I\big\rangle. \tag{4.2.1}$$

The first-order reduced density matrix (1RDM) operator is defined by

$$\hat{\gamma}\big(\mathbf{x}', \mathbf{x}\big) \coloneqq n\big|\mathbf{x}'\big\rangle\big\langle\mathbf{x}\big|, \tag{4.2.2}$$

[1] Although the translation of atomic orbital basis also contribute to the electron density change, such contribution is regarded as an artifact. Indeed, such contribution doesn't arise in the HF limit.

where n is the number of electrons. The 1RDM is positive semi-definite. Accordingly, there exists one positive semi-definite square root of the 1RDM. [73, 98] Indeed, the operator defined by

$$\hat{\gamma}^{1/2}(\mathbf{x}', \mathbf{x}) \coloneqq n^{1/2} |\mathbf{x}'\rangle\langle\mathbf{x}|. \tag{4.2.3}$$

satisfies the following equation:

$$\langle\Psi|\hat{\gamma}(\mathbf{x}', \mathbf{x})|\Psi\rangle = \int d\mathbf{x}'' \langle\Psi|\hat{\gamma}^{1/2}(\mathbf{x}', \mathbf{x}'')|\Psi\rangle\langle\Psi|\hat{\gamma}^{1/2}(\mathbf{x}'', \mathbf{x})|\Psi\rangle. \tag{4.2.4}$$

Herein, the following quantity is considered:

$$\begin{aligned}
&\int d\mathbf{x}'' \left(\langle\Psi|\hat{\gamma}^{1/2}(\mathbf{x}', \mathbf{x}'')|\Psi\rangle\right) \partial_{\mathfrak{J}}\langle\Psi|\hat{\gamma}^{1/2}(\mathbf{x}'', \mathbf{x})|\Psi\rangle \\
=&\langle\Psi|\hat{\gamma}(\mathbf{x}', \mathbf{x})|\partial_{\mathfrak{J}}\Psi\rangle + \langle\partial_{\mathfrak{J}}\Psi \mid \Psi\rangle\langle\Psi|\hat{\gamma}(\mathbf{x}', \mathbf{x})|\Psi\rangle \\
=&\langle\Psi|\hat{\gamma}(\mathbf{x}', \mathbf{x})|\partial_{\mathfrak{J}}\Psi\rangle - \langle\Psi \mid \partial_{\mathfrak{J}}\Psi\rangle\langle\Psi|\hat{\gamma}(\mathbf{x}', \mathbf{x})|\Psi\rangle \quad (\because \partial_{\mathfrak{J}}\langle\Psi \mid \Psi\rangle = 0),
\end{aligned} \tag{4.2.5}$$

where $\partial_{\mathfrak{J}}$ is partial derivative with respect to the $\mathfrak{J}$-th mass-weighted nuclear coordinate. With using some orthonormalized spin-orbital basis set $\{\bar{\chi}_\mu\}$, the quantity in Eq. (4.2.5) can be written by

$$\begin{aligned}
&\int d\mathbf{x}'' \langle\Psi|\hat{\gamma}^{1/2}(\mathbf{x}', \mathbf{x}'')|\Psi\rangle\partial_{\mathfrak{J}}\langle\Psi|\hat{\gamma}^{1/2}(\mathbf{x}'', \mathbf{x})|\Psi\rangle \\
&= \sum_{\kappa,\lambda,\mu,\nu} \left\{\left(\delta_{\lambda\kappa}\partial_{\mathfrak{J}} + \langle\bar{\chi}_\lambda \mid \partial_{\mathfrak{J}}\bar{\chi}_\kappa\rangle\right)\gamma^{1/2}_{\mu\kappa}\right\} \gamma^{1/2}_{\lambda\nu}\bar{\chi}_\mu(\mathbf{x})\bar{\chi}^*_\nu(\mathbf{x}') + \sum_{\mu\nu}\gamma_{\mu\nu}\partial_{\mathfrak{J}}\bar{\chi}_\mu(\mathbf{x})\bar{\chi}^*_\nu(\mathbf{x}').
\end{aligned} \tag{4.2.6}$$

In HF limit, the matrix representation of rhs of Eq. (4.2.6) is given by

$$\left(\partial_{\mathfrak{J}}\boldsymbol{\gamma}^{1/2} + \mathbf{A}_{\mathfrak{J}}\boldsymbol{\gamma}^{1/2} + \boldsymbol{\gamma}^{1/2}\mathbf{A}^\dagger_{\mathfrak{J}}\right)\boldsymbol{\gamma}^{1/2} =: \mathbf{X}_{\mathfrak{J}}, \tag{4.2.7}$$

where

$$A_{\mathfrak{J}\lambda\kappa} = \langle\bar{\chi}_\lambda \mid \partial_{\mathfrak{J}}\bar{\chi}_\kappa\rangle \tag{4.2.8}$$

is gauge potential whereas it is essentially trivial. The matrix $\mathbf{X}_{\mathfrak{J}}$ introduced in Eq. (4.2.7) is the matrix to characterize the density response with respect to nuclear displacements.

Next, the optimal orbital basis to characterize the density response, multiconfigurational natural reaction orbital (MC-NRO), will be introduced. In the case of full-CI, MC-NRO can be given as the pairs of left and right singular vectors of $\mathbf{X}_{\mathfrak{J}}$. However, some additional consideration is required for more practical theories, e.g., complete active space self-consistent field (CASSCF) theory. [146] As well known, CASSCF is

orbital invariant [95,146], that is, CASSCF wavefuntion and energy are invariant to the orbital rotation in inactive, active and secondary spaces. However, CASSCF is not invariant to orbital rotation which mixes orbitals in different spaces, e.g., core and active spaces. It is unfavorable to perform any orbital rotation which violates orbital invariance with no special reason because such rotation destroys the nature of the system. Hence, MC-NRO must be defined so as not to violate orbital invariance. In the case of CASSCF, $\mathbf{X}_\mathfrak{J}$ is divided into four sub-blocks, secondary-active, secondary-core, active-active and active-core. Subsequently, SVD is performed for each of the four blocks separately. The resulting four sets of singular vectors are the MC-NRO of CASSCF theory.

In general, MC-NRO is computed as follows. Provided an electronic structure theory is invariant to any orbital rotation in m orbital spaces $\{\mathcal{S}_t\}_{t=1,2,\ldots,m}$, the matrix given by Eq. (4.2.7) is subdivided into blocks:

$$\mathbf{X}_\mathfrak{J} = \begin{bmatrix} \mathbf{X}_\mathfrak{J}^{11} & \mathbf{X}_\mathfrak{J}^{12} & \cdots & \mathbf{X}_\mathfrak{J}^{1m} \\ \mathbf{X}_\mathfrak{J}^{21} & \mathbf{X}_\mathfrak{J}^{22} & \cdots & \mathbf{X}_\mathfrak{J}^{2m} \\ \vdots & \vdots & \ddots & \vdots \\ \mathbf{X}_\mathfrak{J}^{m1} & \mathbf{X}_\mathfrak{J}^{m2} & \cdots & \mathbf{X}_\mathfrak{J}^{mm} \end{bmatrix} \tag{4.2.9}$$

the row and column spaces of $\mathbf{X}_\mathfrak{J}^{st}$ are the orbital spaces $\mathcal{S}_s$ and $\mathcal{S}_t$ respectively. The SVD of each sub-matrix is given by the form of

$$\mathbf{X}_\mathfrak{J}^{st} = \mathbf{L}\mathbf{\Lambda}\mathbf{R}^\dagger, \tag{4.2.10}$$

where $\boldsymbol{l}$ and $\mathbf{R}$, left and right singular vectors, are unitary matrices. $\mathbf{\Lambda}$ is a rectangular diagonal matrix, of which diagonal entries are singular values. MC-NRO is given by

$$\begin{cases} (\phi_1^{s\mathrm{L}}, \ldots, \phi_{N_s}^{s\mathrm{L}}) & = (\bar{\chi}_1^s, \ldots, \bar{\chi}_{N_s}^s)\mathbf{L} \quad (\bar{\chi}_1^s, \ldots, \bar{\chi}_{N_s}^s \in \mathcal{S}_s) \\ (\phi_1^{t\mathrm{R}}, \ldots, \phi_{N_t}^{t\mathrm{R}}) & = (\bar{\chi}_1^t, \ldots, \bar{\chi}_{N_t}^t)\mathbf{R} \quad (\bar{\chi}_1^t, \ldots, \bar{\chi}_{N_t}^t \in \mathcal{S}_t) \end{cases} \tag{4.2.11}$$

where N_s and N_t are the number of orbitals in the orbital spaces $\mathcal{S}_s$ and $\mathcal{S}_t$ respectively. $\phi_i^{s\mathrm{L}}$ and $\phi_i^{t\mathrm{R}}$ are the i-th left and right MC-NRO respectively. Each MC-NRO pair, the left and right MC-NRO with the same subscript, has a singular value λ_i, which is a non-negative real number. With using MC-NRO basis, the electron density leakage from $\mathcal{S}_t$ into $\mathcal{S}_s$ is written by

$$\gamma^{st(1)}(\mathbf{x}) \coloneqq \sum_{i=1}^{\min(N_s,N_t)} \lambda_i \left(\phi_i^{s\mathrm{L}}(\mathbf{x})\phi_i^{t\mathrm{R}*}(\mathbf{x}) + \phi_i^{s\mathrm{L}*}(\mathbf{x})\phi_i^{t\mathrm{R}}(\mathbf{x})\right). \tag{4.2.12}$$

This indicates that each singular value measures the degree of the electron leakage from $\mathcal{S}_t$ into $\mathcal{S}_s$ represented by the corresponding MC-NRO pair. Because of the orthonormality of the basis set $\{\bar{\chi}_\mu\}$, the following holds:

$$\int d\mathbf{x}\gamma^{st(1)}(\mathbf{x}) = 0 \quad (\mathcal{S}_s \neq \mathcal{S}_t), \tag{4.2.13}$$

For the diagonal sub-blocks, if the number of electrons in each orbital space is fixed, the integral becomes also zero:

$$\int d\mathbf{x}\gamma^{ss(1)}(\mathbf{x}) = 0. \tag{4.2.14}$$

It is ensured that the total number of electrons is preserved:

$$\sum_{s=1}^{m} \int d\mathbf{x}\gamma^{ss(1)}(\mathbf{x}) = 0. \tag{4.2.15}$$

4.2.2 Case of finite basis set

In the previous subsection, MC-NRO in the case of HF limit is introduced. In the current subsection, MC-NRO in the case of finite basis set is introduced. There are two difficulties with finite basis set: (1) the gauge potential $\mathbf{A}_\mathfrak{J}$ is not trivial though it is usually considered unphysical; (2) the derivatives of overlap matrix with respect to nuclear coordinates need to be taken into account to ensure the number to electrons to be preserved though they are usually considered unphysical. In order to handle these problems, MC-NRO in the case of finite basis set is computed as followings.

First, Eq. (4.2.7) is rewritten by

$$\left(\partial_\mathfrak{J}\mathbf{S}^{1/2}\boldsymbol{\gamma}_{\mathrm{AO}}^{1/2} + \mathbf{S}^{1/2}\partial_\mathfrak{J}\boldsymbol{\gamma}_{\mathrm{AO}}^{1/2} + \mathbf{A}_\mathfrak{J}\mathbf{S}^{1/2}\boldsymbol{\gamma}_{\mathrm{AO}}^{1/2} + \mathbf{S}^{1/2}\boldsymbol{\gamma}_{\mathrm{AO}}^{1/2}\mathbf{A}_\mathfrak{J}'^{\dagger}\right)\boldsymbol{\gamma}_{\mathrm{AO}}^{1/2}\mathbf{S}^{1/2}, \tag{4.2.16}$$

where $\boldsymbol{\gamma}_{\mathrm{AO}}^{1/2}$ is defined by

$$\boldsymbol{\gamma}_{\mathrm{AO}} = \boldsymbol{\gamma}_{\mathrm{AO}}^{1/2}\boldsymbol{\gamma}_{\mathrm{AO}}^{1/2}, \tag{4.2.17}$$

$\boldsymbol{\gamma}_{\mathrm{AO}}$ is the atomic spin-orbital basis. It should be noted that $\boldsymbol{\gamma}_{\mathrm{AO}}^{1/2}$ is not the AO representation of $\boldsymbol{\gamma}^{1/2}$. The relation between $\boldsymbol{\gamma}_{\mathrm{AO}}^{1/2}$ and $\boldsymbol{\gamma}^{1/2}$ is given by

$$\mathbf{S}^{1/2}\boldsymbol{\gamma}_{\mathrm{AO}}^{1/2}\boldsymbol{\gamma}_{\mathrm{AO}}^{1/2}\mathbf{S}^{1/2} = \boldsymbol{\gamma}^{1/2}\boldsymbol{\gamma}^{1/2} \tag{4.2.18}$$

and

$$\boldsymbol{\gamma}_{\mathrm{AO}}^{1/2}\mathbf{S}^{1/2} = \mathbf{U}\boldsymbol{\gamma}^{1/2} \tag{4.2.19}$$

where $\mathbf{U}$ is a unitary matrix. $\mathbf{A}'_{\mathfrak{J}}$ is given by

$$\mathbf{A}'_{\mathfrak{J}} \coloneqq \mathbf{A}_{\mathfrak{J}} + \mathbf{U}^{\dagger}\partial_{\mathfrak{J}}\mathbf{U} \tag{4.2.20}$$

In order to handle the first problem mentioned above, the gauge potentials $\mathbf{A}_{\mathfrak{J}}$ and $\mathbf{A}'_{\mathfrak{J}}$ are neglected:

$$\begin{aligned} &\left(\partial_{\mathfrak{J}}\mathbf{S}^{1/2}\boldsymbol{\gamma}_{\mathrm{AO}}^{1/2} + \mathbf{S}^{1/2}\partial_{\mathfrak{J}}\boldsymbol{\gamma}_{\mathrm{AO}}^{1/2} + \mathbf{A}_{\mathfrak{J}}\mathbf{S}^{1/2}\boldsymbol{\gamma}_{\mathrm{AO}}^{1/2} + \mathbf{S}^{1/2}\boldsymbol{\gamma}_{\mathrm{AO}}^{1/2}\mathbf{A}_{\mathfrak{J}}'^{\dagger}\right)\boldsymbol{\gamma}_{\mathrm{AO}}^{1/2}\mathbf{S}^{1/2} \\ \approx &\left(\partial_{\mathfrak{J}}\mathbf{S}^{1/2}\boldsymbol{\gamma}_{\mathrm{AO}}^{1/2} + \mathbf{S}^{1/2}\partial_{\mathfrak{J}}\boldsymbol{\gamma}_{\mathrm{AO}}^{1/2}\right)\boldsymbol{\gamma}_{\mathrm{AO}}^{1/2}\mathbf{S}^{1/2} \end{aligned} \tag{4.2.21}$$

The matrix is then subdivided into orbital spaces so that the electronic structure theory is invariant to any orbital rotation in each of them. Such subdivision can be carried out by using some orthonormal basis which defines the orbital spaces, e.g., natural orbitals (NOs). The subdivided matrix is written by

$$\sum_{s,t=1}^{m} \mathbf{C}_s^{\dagger}\mathbf{S}^{1/2}\left(\partial_{\mathfrak{J}}\mathbf{S}^{1/2}\boldsymbol{\gamma}_{\mathrm{AO}}^{1/2} + \mathbf{S}^{1/2}\partial_{\mathfrak{J}}\boldsymbol{\gamma}_{\mathrm{AO}}^{1/2}\right)\boldsymbol{\gamma}_{\mathrm{AO}}^{1/2}\mathbf{S}\mathbf{C}_t, \tag{4.2.22}$$

where $\mathbf{C}_s$ is the spin orbital coefficient matrix of orbital space $\mathcal{S}_s$. Here, the second problem mentioned above is handled by replacing the first term by

$$\sum_{s,t=1}^{m} \mathbf{C}_s^{\dagger}\mathbf{S}^{1/2}\partial_{\mathfrak{J}}\mathbf{S}^{1/2}\boldsymbol{\gamma}_{\mathrm{AO}}\mathbf{S}\mathbf{C}_t \to \sum_{s=1}^{m} \frac{1}{N_s}\mathrm{Tr}\left(\mathbf{C}_s^{\dagger}\mathbf{S}^{1/2}\partial_{\mathfrak{J}}\mathbf{S}^{1/2}\boldsymbol{\gamma}_{\mathrm{AO}}\mathbf{S}\mathbf{C}_s\right)\mathbf{1}_s, \tag{4.2.23}$$

where $\mathbf{1}_s$ is the unit matrix of $\mathcal{S}_s$ and N_s is the number of orbitals in $\mathcal{S}_s$. Eventually, the density response with respect to molecular deformation is evaluated with

$$\mathbf{X}_{\mathfrak{J}} \coloneqq \sum_{s=1}^{m} \frac{1}{N_s}\mathrm{Tr}\left(\mathbf{C}_s^{\dagger}\mathbf{S}^{1/2}\partial_{\mathfrak{J}}\mathbf{S}^{1/2}\boldsymbol{\gamma}_{\mathrm{AO}}\mathbf{S}\mathbf{C}_s\right)\mathbf{1}_s + \sum_{s,t=1}^{m} \mathbf{C}_s^{\dagger}\mathbf{S}\partial_{\mathfrak{J}}\boldsymbol{\gamma}_{\mathrm{AO}}^{1/2}\boldsymbol{\gamma}_{\mathrm{AO}}^{1/2}\mathbf{S}\mathbf{C}_t. \tag{4.2.24}$$

It should be noted that the matrix in Eq. (4.2.24) is not identical to that in Eq. (4.2.7) whereas the difference is trivial in HF limit. The difference comes from the treatment of gauge potential and derivatives of overlap matrix with respect to nuclear displacements. The MC-NRO for finite basis is given by replacing the matrix in Eq. (4.2.7) by that in Eq. (4.2.24). The way of subdivision and SVD is completely same. MC-NRO for finite basis also has the nature shown in Eqs. (4.2.12) to (4.2.15) though the density response is approximated one.

In practice, the derivatives of density matrix $\boldsymbol{\gamma}_{\mathrm{AO}}^{1/2}$ is evaluated numerically:

$$\partial_{\mathfrak{I}}\boldsymbol{\gamma}_{\mathrm{AO}}^{1/2} \approx \frac{1}{2\Delta\tau}\left(\boldsymbol{\gamma}_{\mathrm{AO}}^{1/2}(\boldsymbol{e}_{\mathfrak{I}}\Delta\tau) - \boldsymbol{\gamma}_{\mathrm{AO}}^{1/2}(-\boldsymbol{e}_{\mathfrak{I}}\Delta\tau)\right), \tag{4.2.25}$$

where $\Delta\tau$ is the stepsize of the numerical differentiation. $\boldsymbol{e}_{\mathfrak{I}}$ is the $\mathfrak{I}$-th direction vector. MC-NRO can be computed without solving any coupled-perturbed equation owing to the numerical approximation. It should be also noteworthy that no derivative or numerical differentiation of CI coefficients is required to compute MC-NRO because it is formulated based on density matrix. These two points are very important for reducing the computational cost of MC-NRO.

As shown above, the formulation of MC-NRO is a little complicated for some technical requirements. However, it should be emphasized that the concept of MC-NRO is quite simple and clear. MC-NRO is the orbital to characterizes the electron density change with respect to nuclear displacements. In other words, MC-NRO is designed to extract the orbitals of which occupation number drastically change.

4.3 Results and Discussion

In this section, MC-NRO analysis is applied to five typical reactions: formation of hydrogen molecule; triple bond formation of nitrogen molecule; Diels-Alder reaction of ethylene and 1,3-butadiene; [1,5]-sigmatropic rearrangement of 1,3-pentadiene; intramolecular hydrogen transfer of malonaldehyde in the S1 state. All the calculations were performed with Gaussian 16 Rev.C.01. [43]

4.3.1 Hydrogen molecule

As the simplest example, MC-NRO analysis is applied to the covalent bond formation of hydrogen molecule. It is well known that the electronic structure of the dissociated geometry (H + H) cannot be reproduced by single determinant wavefunction, e.g., Hartree-Fock wavefunction. [24,115] In the framework of MO theory, hydrogen molecule formation proceeds not by orbital mixing but by configuration mixing. Therefore, despite its simplicity, hydrogen molecule formation needs to be studied based on multiconfigurational theory. This extremely simple reaction process seems to be the best system to demonstrate that MC-NRO can extract reactive orbitals even in the reaction proceeding by configuration mixing.

The potential energy curve for the singlet ground state (black curve) of H_2 at CASSCF(2,2)/aug-cc-pVQZ [31, 87] is shown in Fig. 4.1. The sum of squares of the singular values of MC-NRO, which indicate the degree of electron density change with respect to the bond length change, are shown for two sub-blocks: active-active and

secondary-active blocks. The density changes drastically in two regions: (a) $R \approx 2.10$ Åand (b) $R < 1.20$ Å(R is the bond length of the hydrogen molecule).

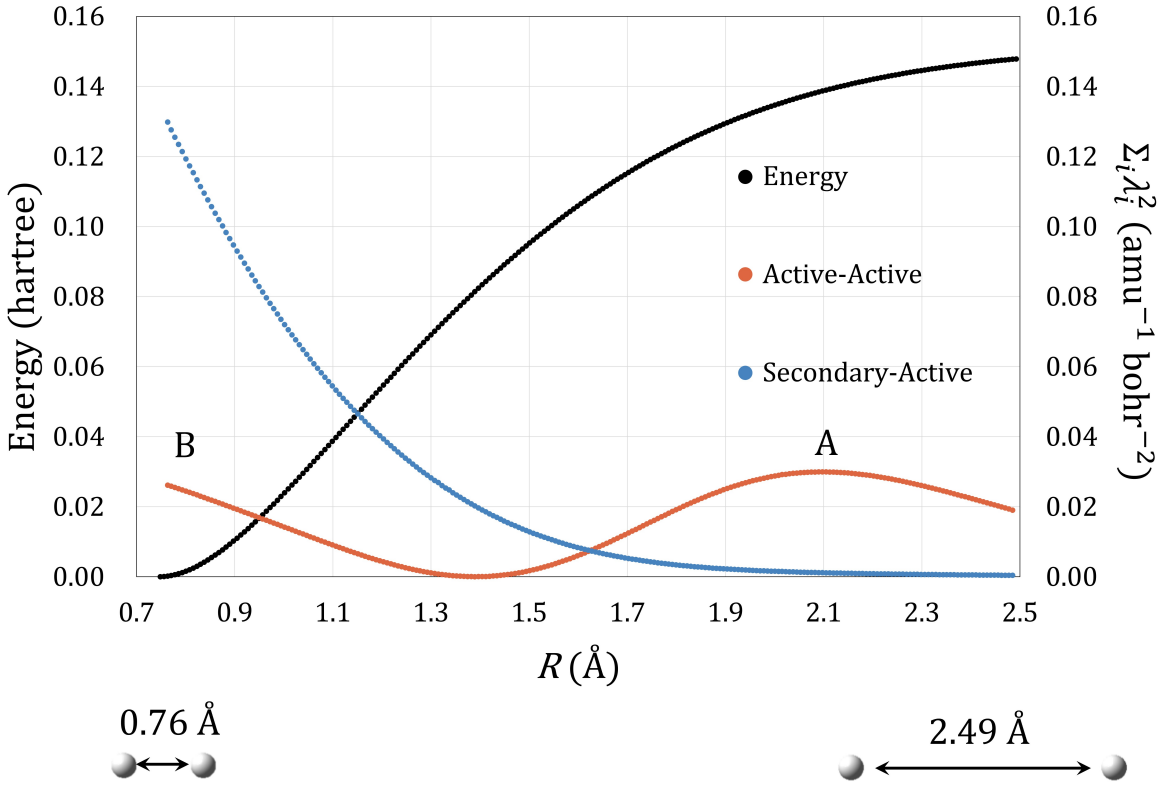

Fig. 4.1: Potential energy curve of the singlet ground state of the hydrogen molecule (black) and the sum of squares of the singular values of the MC-NROs for the two sub-blocks of active-active (red) and secondary-active (blue) (shown as $\sum_i \lambda_i^2$). The electronic structure is computed at CASSCF(2,2)/aug-cc-pVQZ level.

Fig. 4.2 shows the dominant active-active MC-NRO pairs and the corresponding electron density changes. The direction of nuclear displacements is in the direction of bond formation. The first MC-NRO pair in region (a) is anti-bonding σ_u^* orbital pair with opposite sign. The first pair shows the electron density decrease in σ_u^* as the bond formation. The second MC-NRO pair is bonding σ_g orbital pair with same sign. The second MC-NRO pair contributes to the electron density increase in σ_g. These electron density changes clearly characterize the H-H covalent bond formation, consistent with the conventional understanding. The dominant MC-NRO pair in region (b) shows an opposite density change, a decrease/increase in σ_g/σ_u^* while this behavior seems to be an artifact due to the poor active space. This point will be discussed in detail later. Fig. 4.3 shows the dominant secondary-active MC-NRO pairs in the

region (b). Since the singular value of the first pair is much larger than that of the second, the electron density change between the active and secondary space can be analyzed with only the first pair. The density change indicates that the first MC-NRO pair, σ_g orbitals composed of 1s orbitals and 2s orbitals, contributes to condense the electron density around the H-H bond axis. This density change seems to reduce the nuclear repulsion. In region (b), the orbital mixing of the first MC-NRO pair induces a significant density change, which implies that the active space is not closed in this H-H bond formation process (Fig. 4.1). Basically, active space should be large enough to be capable of describing any changes in electronic structure taking place during the chemical reaction. From this point of view, orbital mixing between the active space and inactive or secondary spaces is unfavorable. Hence, the large density change between the active and secondary spaces in region (b) indicates that the active space needs to be expanded to describe the reaction process more appropriately.

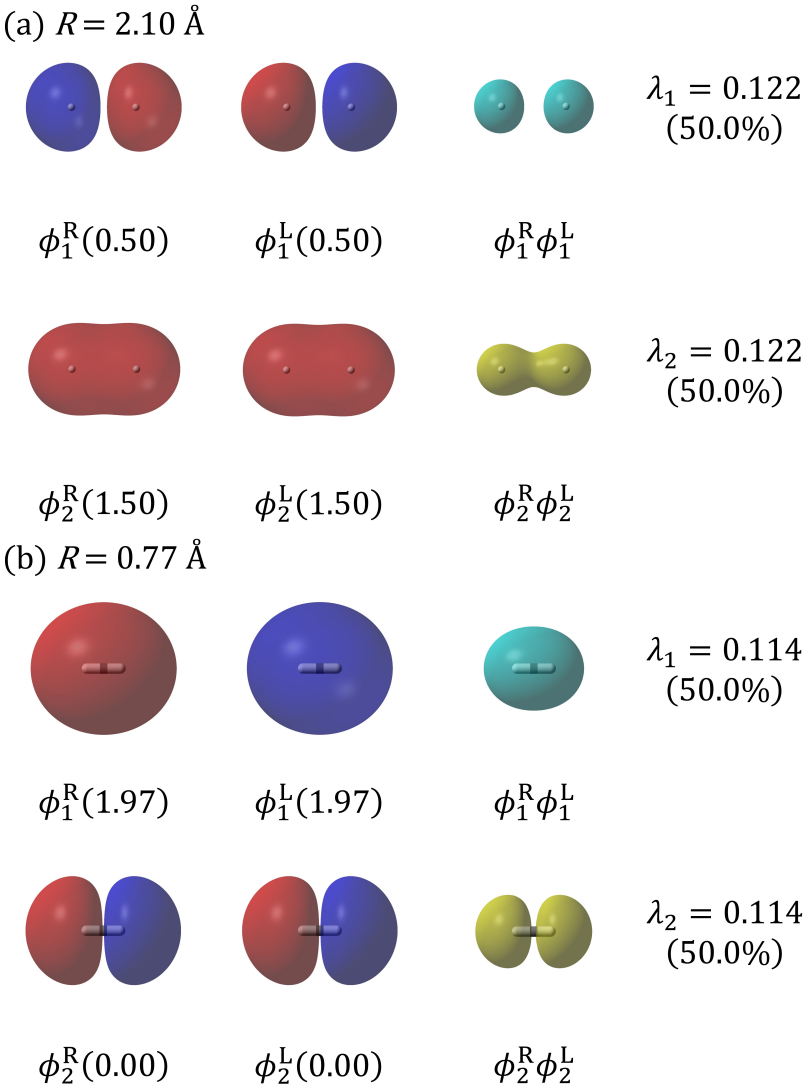

Fig. 4.2: Active-active MC-NRO pairs for H-H covalent bond formation at (a) $R = 2.10$ Åand (b) $R = 0.77$ Å. ϕ_i^{R} and ϕ_i^{L} denote the i-th right and left MC-NROs, and the number in parentheses indicate the occupation number of each MC-NRO. The product of each MC-NRO pair is also shown and electron density decreases/increases in its cyan/yellow colored regions. λ_i [amu$^{-1/2}$bohr^{-1}] indicates the singular value of the i-th MC-NRO pair. The contribution ratio of each MC-NRO pair to the density change within active-active block, defined as $100 \times \lambda_i^2 / \sum_j \lambda_j^2$, is also shown with its singular value. The isovalues of MC-NRO and density change are 0.0250 and 0.00625 respectively.

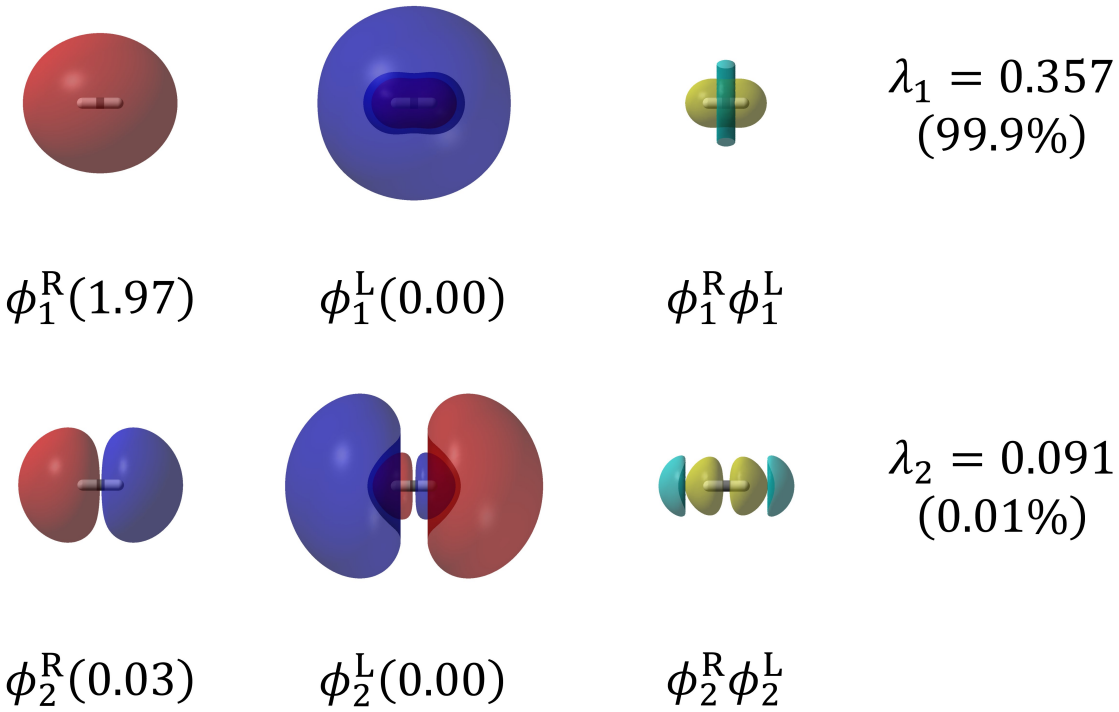

Fig. 4.3: Secondary-active MC-NRO pairs with H-H covalent bond formation at $R = 0.77$ Å. ϕ_i^{R} and ϕ_i^{L} represent the i-th right and left MC-NRO, and the number in parentheses indicates the occupation number of each MC-NRO. The product of each MC-NRO pair is also shown and electron density decreases/increases in its cyan/yellow colored regions. λ_i [amu$^{-1/2}$bohr^{-1}] represents the singular value of the i-th MC-NRO pair. Also shown below each singular value is the contribution of the MC-NRO pair to the overall density change. The isovalues of MC-NRO and density change are 0.0250 and 0.00625, respectively.

Next, the same process is computed at CASSCF(2,10)/aug-cc-pVQZ level and MC-NRO analysis is performed. The orbitals in the expanded active space are shown in Fig. 4.4. All the active orbital have σ symmetry. Fig. 4.5 shows the potential energy curve and the sum of squares of singular values of MC-NROs. Compared to Fig. 4.5, the orbital mixing between the active and secondary spaces is much suppressed. This result implies the expanded active space is large enough to describe hydrogen molecule formation.

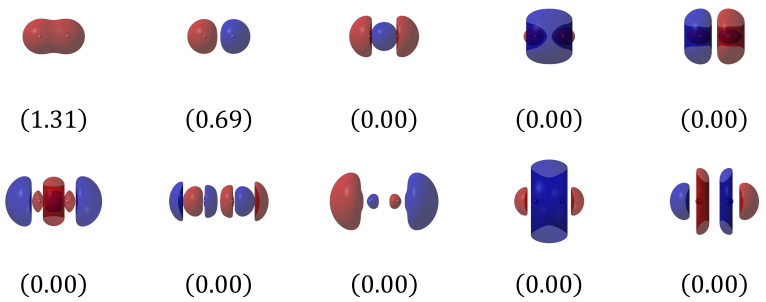

Fig. 4.4: Natural orbitals in the active space of hydrogen molecule at CASSCF(2,10)/aug-cc-pVQZ level. The internuclear distance is 2.49 Å. All the active orbitals have σ_g or σ_u^* symmetry. The occupation number of each active orbital is also shown.

Fig. 4.6 shows the dominant active-active MC-NRO pairs. The dominant MC-NRO pairs in region (a) are almost same as those shown in Fig. 4.2. In contrast, the first MC-NRO pair is different from that shown in Fig. 4.3 but rather similar to the first MC-NRO pair in Fig. 4.3. This indicates that the first left MC-NRO ϕ_1^{L} shown in Fig. 4.3 is added to the active space by expanding it. Consequently, the orbital mixing between the first MC-NRO pair in Fig. 4.3 can be described within the expanded active space. Thus, the expanded active space is considered to be more *closed* throughout the reaction process. Actually, the expansion of active space also improved the energy in region (b). Fig. 4.7 shows that the energy difference between the CASSCF(2,2) and CASSCF(2,10) results increases in the direction of bond formation. This behavior may be understood in terms of radial correlations. The significance of radial correlations for the electron affinity of carbon, oxygen, and fluorine was reported. [14] Also, the effect of radial correlation on the height of reaction barrier is studied in the reaction of X + $H_2 \rightarrow$ XH + H (X = O, F). [7, 175] In Ref. [175], orbital basis with additional radial nodes was found to be important in describing the tight-diffuse correlation of anion-like oxygen atom in the vicinity of the transition state (TS). In the present homonuclear reaction of H + H $\rightarrow$ H_2, the reactants, the two hydrogen atoms, do not have radial tight-diffuse correlations, but the product, hydrogen molecule, does. Thus, the radial

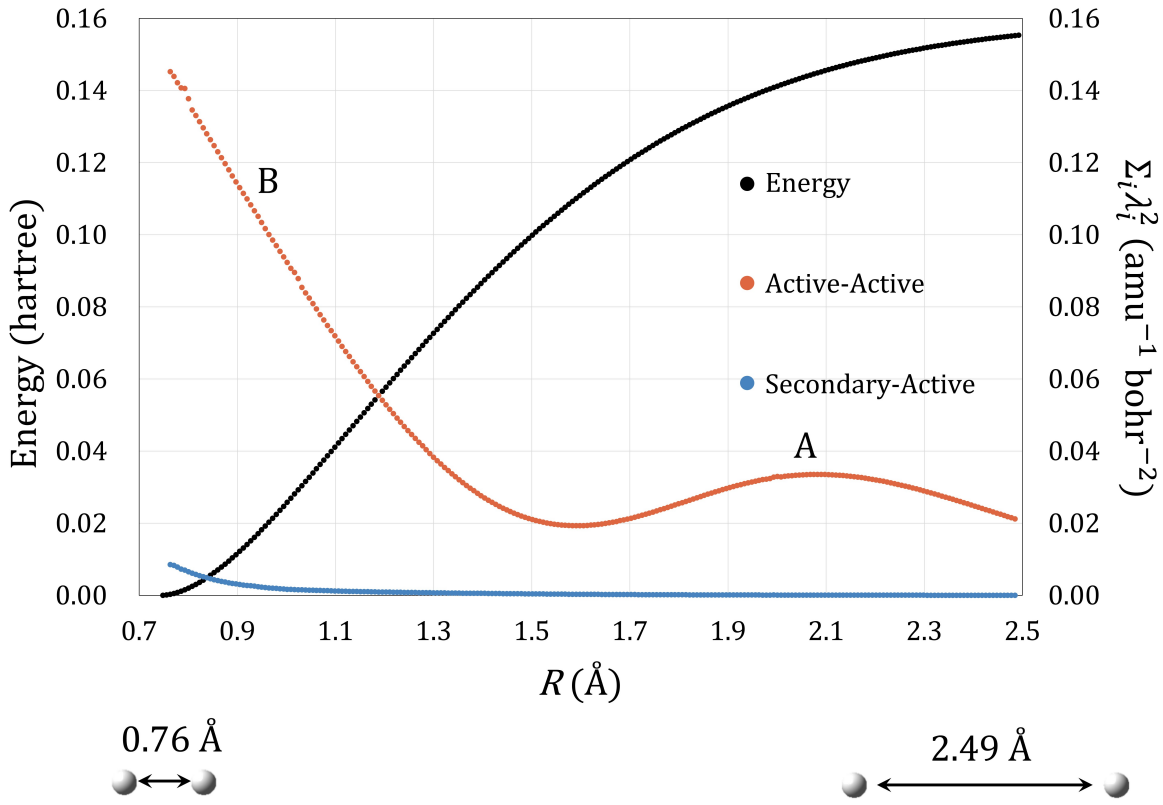

Fig. 4.5: Potential energy curve of the singlet ground state of hydrogen molecule (black curve) and the sum of squares of the singular values of MC-NROs for the two blocks of active-active (red curve) and secondary-active (blue curve) (denoted by $\sum_i \lambda_i^2$). R is the internuclear distance. The electronic structure is calculated at the CASSCF(2,10)/aug-cc-pVQZ level.

correlation should increase as the bond formation and the correlation seems to be the main cause of the energy difference in region (b). Indeed, the left MC-NRO ϕ_1^{L} shwon in Fig. 4.6(b), which has an extra radial node and non-zero occupancy, also implies the presence of tight-diffuse correlations.

Through the analysis of hydrogen molecule formation with different active spaces, it was shown that MC-NRO basis adequately characterizes the density change as the covalent bond formation. Also, it is noteworthy that the sum of squares of the singular values of MC-NRO provides a kind of criterion to validate the quality of the active space from the viewpoint of electron density change with respect to nuclear displacements. If the sum of square of singular values of active-core or secondary-active MC-NROs is larger than that of active-active MC-NROs, the size of active space seems to be insufficient for describing the chemical reaction. Since the sum of square of singular values of MC-NROs is equal to square of Frobenius norm of the matrices decomposed by SVD, validation of active space itself does not require the computation of MC-NROs. Thus, it will be sufficient for chemical reaction analysis to perform MC-NRO analysis only for the validated active space.

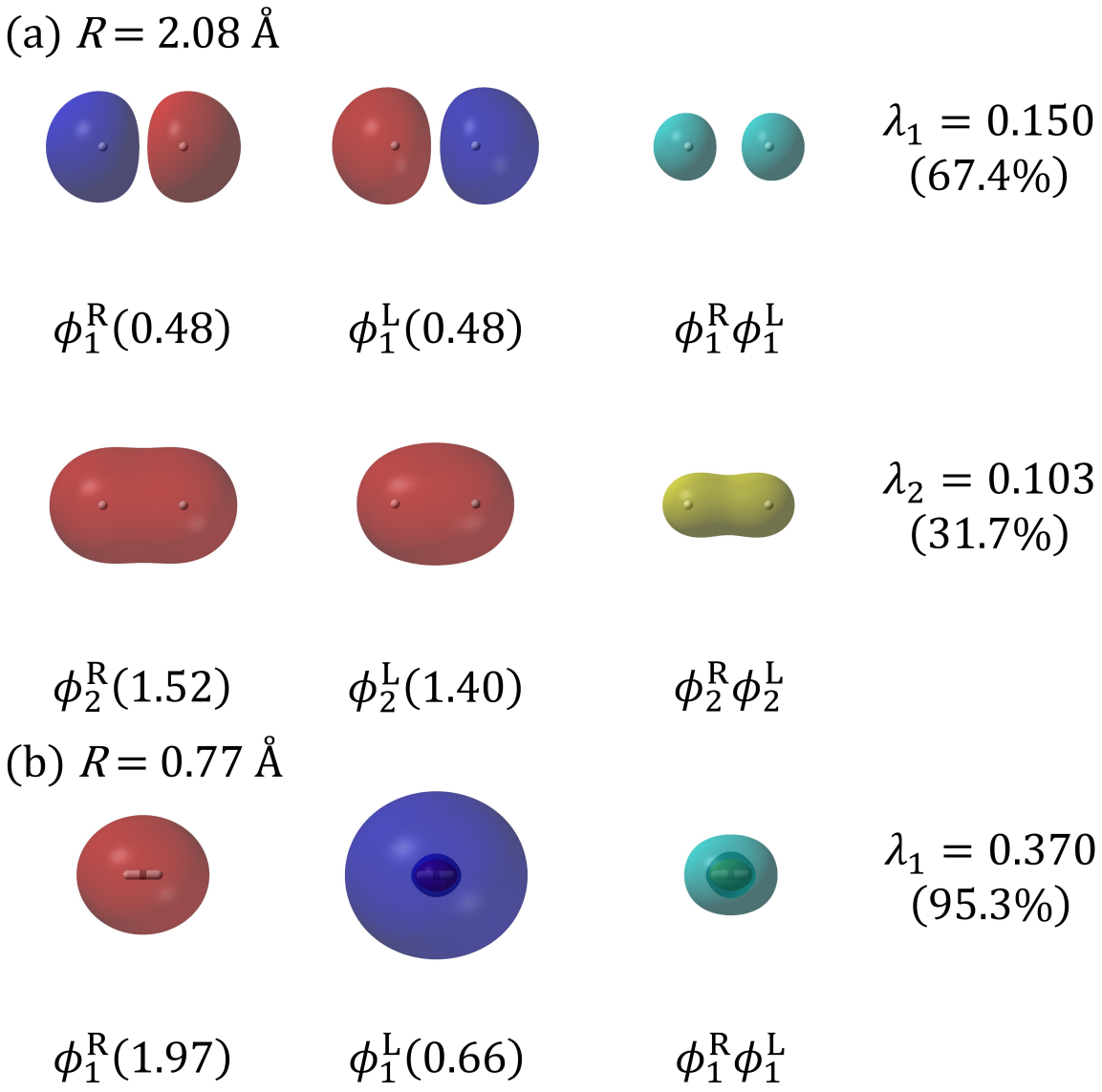

Fig. 4.6: Active-active MC-NRO pairs for H-H covalent bond formation at (a) $R = 2.08$ Åand (b) $R = 0.77$ Å. ϕ_i^{R} and ϕ_i^{L} denote the i-th right and left MC-NROs, and the number in parentheses indicates the occupation number of each MC-NRO. The product of each MC-NRO pair is also shown and electron density decreases/increases in its cyan/yellow colored regions. λ_i [amu$^{-1/2}$bohr^{-1}] indicates the singular value of the i-th MC-NRO pair. The contribution ratio of each MC-NRO pair to the density change within active-active block, defined as $100 \times \lambda_i^2 / \sum_j \lambda_j^2$, is also shown with its singular value. The isovalues of MC-NRO and density change are 0.0250 and 0.00625 respectively.

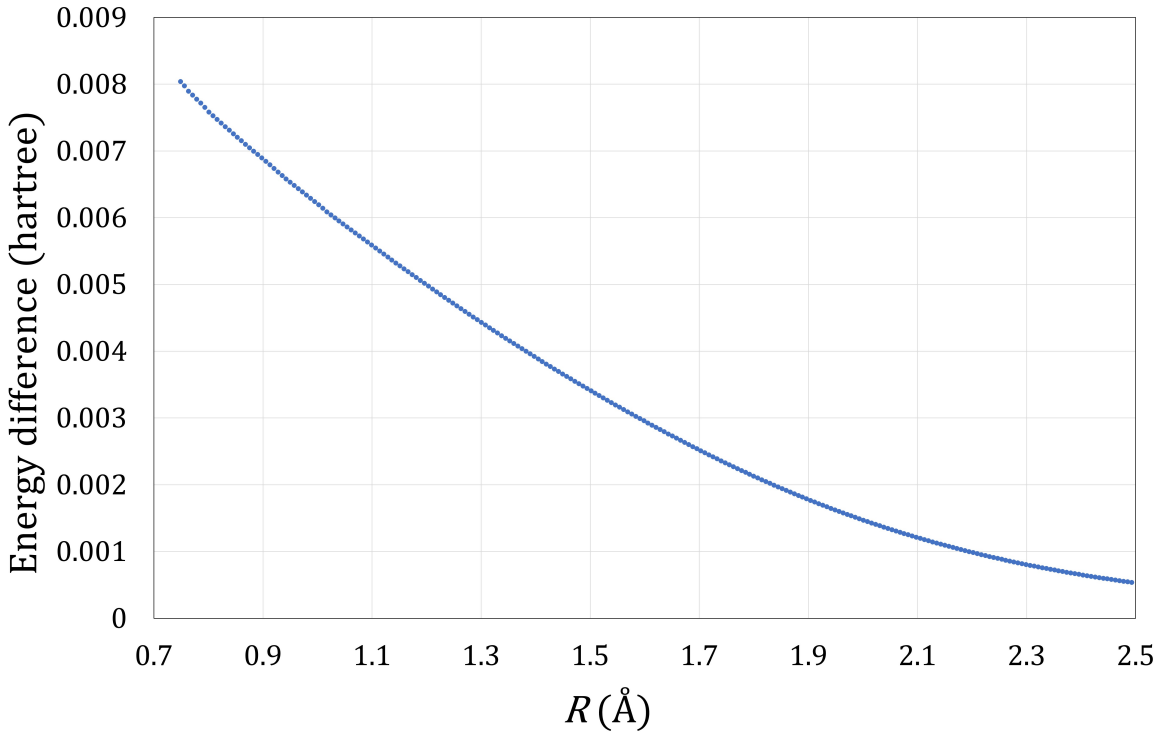

Fig. 4.7: Energy difference between CASSCF(2,2) and CASSCF(2,10) results. R is the internuclear distance.

4.3.2 Nitrogen molecule

As the second example, MC-NRO analysis was applied to the triple bond formation of N_2. N_2 molecule has two different types of chemical bonds, σ bond and π bonds. This simple reaction system is analyzed to confirm whether MC-NRO can distinguish the two types of bonds and appropriately extract the orbitals characterizing each bond formation.

Fig. 4.8 shows the potential energy curve for the singlet ground state (black curve) of N_2 at CASSCF(6,6)/cc-pVTZ [31]. The active space consists of six 2p orbitals of two nitrogen atoms. The sum of squares of the singular values, indicating the degree of electronic density change, is also shown for the four sub-blocks: active-active, secondary-active, active-inactive, and secondary-inactive sub-blocks. The active-active contribution is dominant at the early stages of bond formation. This indicates that the size of the active space is sufficiently large in the long bond-length region. Thus, the active space is large enough to investigate whether the MC-NRO can extract the orbitals characterizing each bond formation. However, the secondary-active and active-inactive contributions are non-negligible in the short bond-length region. This result indicates that the small active space consisting of only 2p orbitals is unsatisfactory near the equilibrium and the cause of this poor behavior of the active space will be discussed in the last part of this subsection.

Fig. 4.9 shows the active-active MC-NROs at $R = 2.000$ Å, which clearly characterize the formation of a σ bond, $\phi_1^{\mathrm{R}}\phi_1^{\mathrm{L}}$, and two π bonds, $\phi_{4,5}^{\mathrm{R}}\phi_{4,5}^{\mathrm{L}}$. This result indicates that MC-NRO method can distinguish the different types of chemical bonds and extract the orbitals responsible for each bond formation. This feature of MC-NRO is favorable to analyze chemical reaction because the character of chemical bond, e.g., symmetry, is crucial to understand reactivity.

Fig. 4.10 shows the secondary-active and active-inactive MC-NROs at $R = 1.120$ Å. The secondary MC-NROs with large singular values work to concentrate the electron density around the bonding region, as in the case of hydrogen molecule. This result shows that AOs with higher principal quantum number than valence AOs work to concentrate the electron density around the nucleus and mitigate internuclear repulsion in the course of covalent bond formation. Hence, ideally, AOs with one higher principal quantum number than the valence AOs relevant for bond formation also needs to be included in the active space. Inactive MC-NROs with large singular values are the σ_{u}^* and σ_{g} orbitals, which consist of 2s orbitals. The significance of these two orbitals may be understood in terms of sp hybridization. In summary, the active-inactive contribution is attributed to the use of a non-full-valence active space missing 2s AOs, and the secondary-active contribution is attributed to the lack of AOs with one higher principal quantum number than the valence AOs, which are essential for density concentration

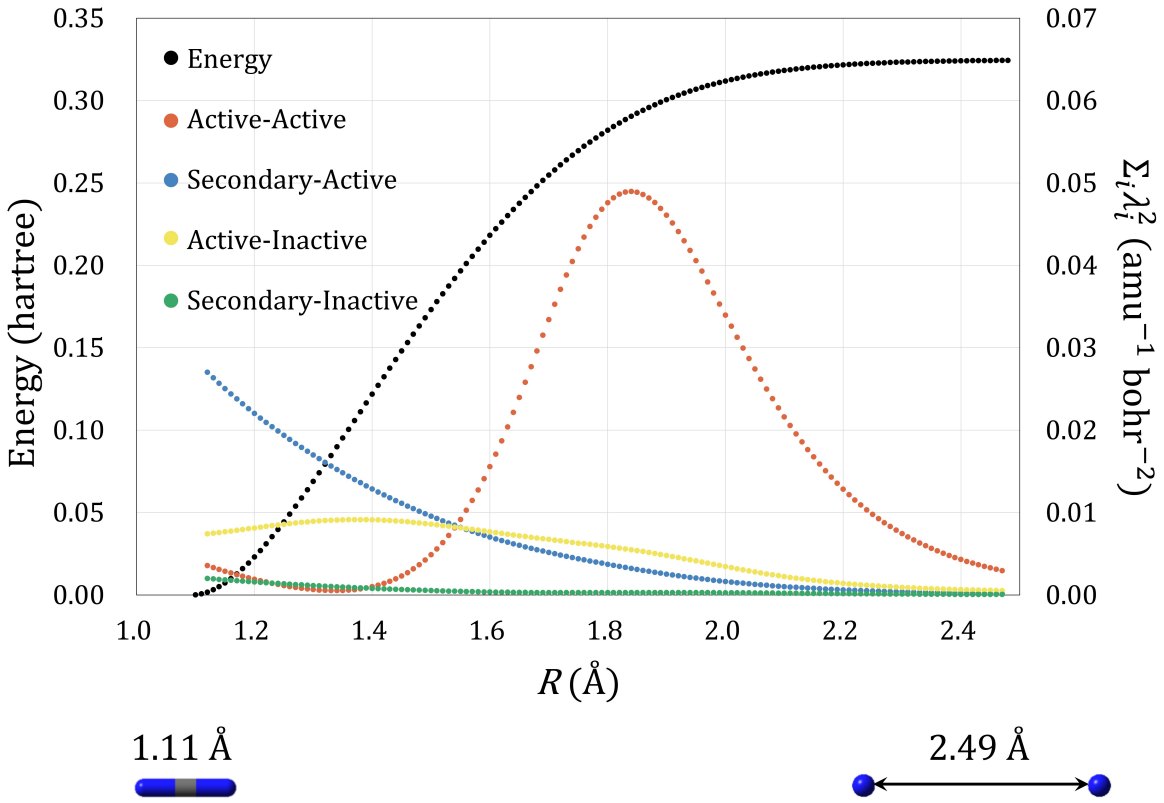

Fig. 4.8: Potential energy curve of the singlet ground state of the nitrogen molecule (black) and the sum of squares of the singular values of MC-NROs (denoted by $\sum_i \lambda_i^2$) of the four sub-blocks, active-active (red), secondary-active (blue), active-inactive (yellow), and secondary-inactive (green) sub-blocks. R is the internuclear distance. The electronic structure is calculated at CASSCF(6,6)/cc-pVTZ level.

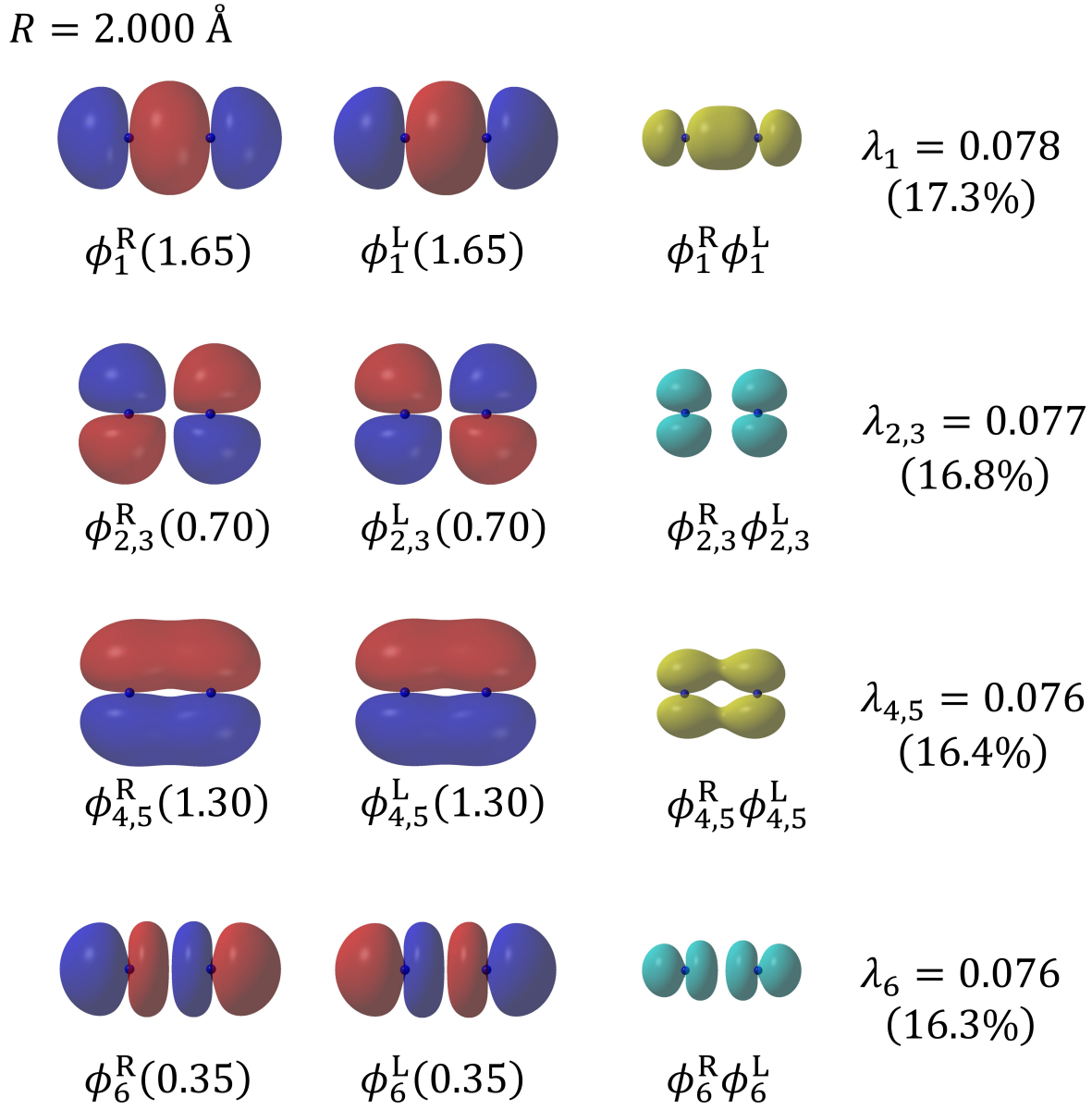

Fig. 4.9: The active-active MC-NRO pairs for the N-N triple bond formation at R = 2.000 Å. ϕ_i^{R} and ϕ_i^{L} represent the i-th right and left MC-NROs, and the number in parentheses indicate the occupation number of each MC-NRO. The product of each MC-NRO pair is also shown and electron density decreases/increases in its cyan/yellow colored regions. λ_i [amu$^{-1/2}$bohr^{-1}] indicates the singular value of the i-th MC-NRO pair. The contribution ratio of each MC-NRO pair to the density change within active-active block, defined as $100 \times \lambda_i^2 / \sum_j \lambda_j^2$, is also shown with its singular value. The isovalues of MC-NRO and density change are 0.020 and 0.004, respectively.

around nuclei. Thus, the MC-NRO method can indicate which MOs should be added to the active space from a viewpoint of density changes along the reaction path. Although it is not necessarily feasible to add all dominant MC-NROs to the active space due to computational costs, the MC-NRO method provides a suggestion for improving the quality of active space.

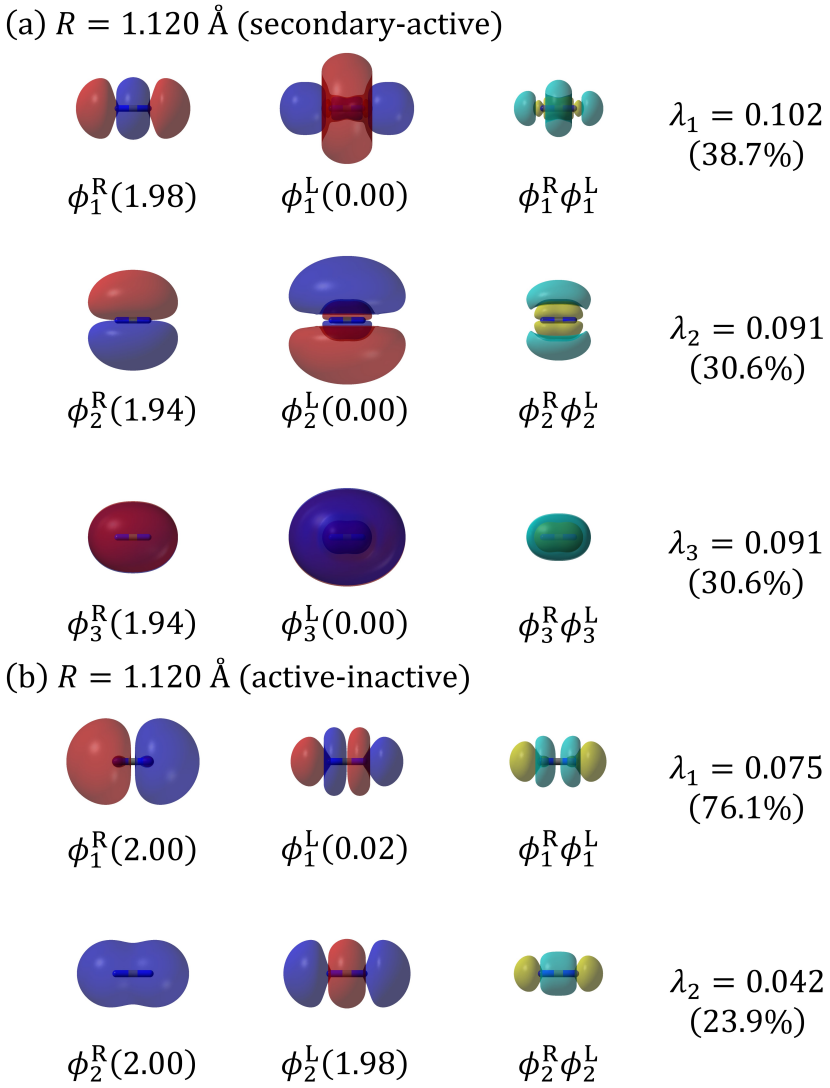

Fig. 4.10: The dominant (a) secondary-active and (b) active-inactive MC-NRO pairs for N-N triple bond formation at $R = 1.120$ Å. ϕ_i^{R} and ϕ_i^{L} represent the i-th right and left MC-NROs, and the number in parentheses indicates the occupation number of each MC-NRO. The product of each MC-NRO pair is also shown and electron density decreases/increases in its cyan/yellow colored regions. λ_i [amu$^{-1/2}$bohr^{-1}] denotes the singular value of the i-th MC-NRO pair. The contribution ratio of each MC-NRO pair to the density change within active-active block, defined as $100 \times \lambda_i^2 / \sum_j \lambda_j^2$, is also shown with its singular value. The isovalues of MC-NRO and density change are 0.020 and 0.004, respectively.

4.3.3 Diels-Alder reaction

In this subsection, Diels-Alder reaction is analyzed with MC-NRO method. Although Diels-Alder reaction can also be reproduced with single-configurational theory, it will be meaningful to confirm whether MC-NRO analysis is consistent with the conventional understanding of the well-studied reaction.

Fig. 4.11 shows energy along the intrinsic reaction coordinate (IRC) of Diels-Alder reaction of ethylene and 1,3-butadiene in the singlet ground state (black curve) calculated at CASSCF(8,7)/cc-pVTZ level. The C_s symmetry of the system is preserved along the IRC. The sum of squares of the singular values, which indicates the degree of electron density change, are also shown for the four sub-blocks: active-active, secondary-active, active-inactive, and secondary-inactive sub-blocks. It can be seen that the active-active contribution is dominant throughout the IRC. Therefore, the active space is sufficiently large to describe the density variation during the reaction. It is also shown that the electron density significantly change at the TS. The slight change in the sum of squares of the singular values around 4.6 amu$^{1/2}$ bohr in Fig. 4.11 seem to contributes to strengthening the C-C covalent bonds between ethylene and 1,3-butadiene Fig. 4.12. Indeed, $\phi_2^{\mathrm{R}}, \phi_2^{\mathrm{L}}$ and $\phi_3^{\mathrm{R}}, \phi_3^{\mathrm{L}}$ show that the electron density increases along the two covalent bond axes. The density change shown by $\phi_1^{\mathrm{R}}, \phi_1^{\mathrm{L}}$ seems to just follow the nuclear motion around the π bond.

There can be seen some discontinuity of the sum of squares of singular values of MC-NRO in Fig. 4.11, e.g., at -10.30 amu$^{1/2}$ bohr and around the TS. Such discontinuity is attributed to the discontinuous change of density matrix along the IRC. Since the sum of squares of singular values are computed with using the numerical differentiation of density matrix, the discontinuity of density matrix causes the discontinuity of singular values. However, the qualitative nature of dominant MC-NRO does not change significantly around such discontinuous points. Hence, such discontinuity seems not fatal for qualitative analysis of electron transfer during chemical reactions.

The MC-NROs at TS are shown in Fig. 4.13. The first MC-NRO pair characterizes electron transfer from the C1-C2 and C3-C4 π bonds of 1,3-butadiene to the π^* orbital of ethylene. The second MC-NRO pair characterizes electron transfer from the π bond of ethylene to the 1,3-butadiene. This result is qualitatively consistent with the previous study that analyzed the Diels-Alder reaction with NRO at the HF/6-31G(d,p) level though the order of the pair is different(Fig. 3.14). [33] This result is also consistent with the conventional understanding of the reaction mechanism based on frontier orbital theory, [54] in which the mutual electron transfer from the highest occupied MO (HOMO) of 1,3-butadiene/ethylene to the lowest unoccupied MO (LUMO) of ethylene/1,3-butadiene is considered to be the driving force of Diels-Alder reaction. Indeed, the density changes shown by MC-NRO clearly characterize the mu-

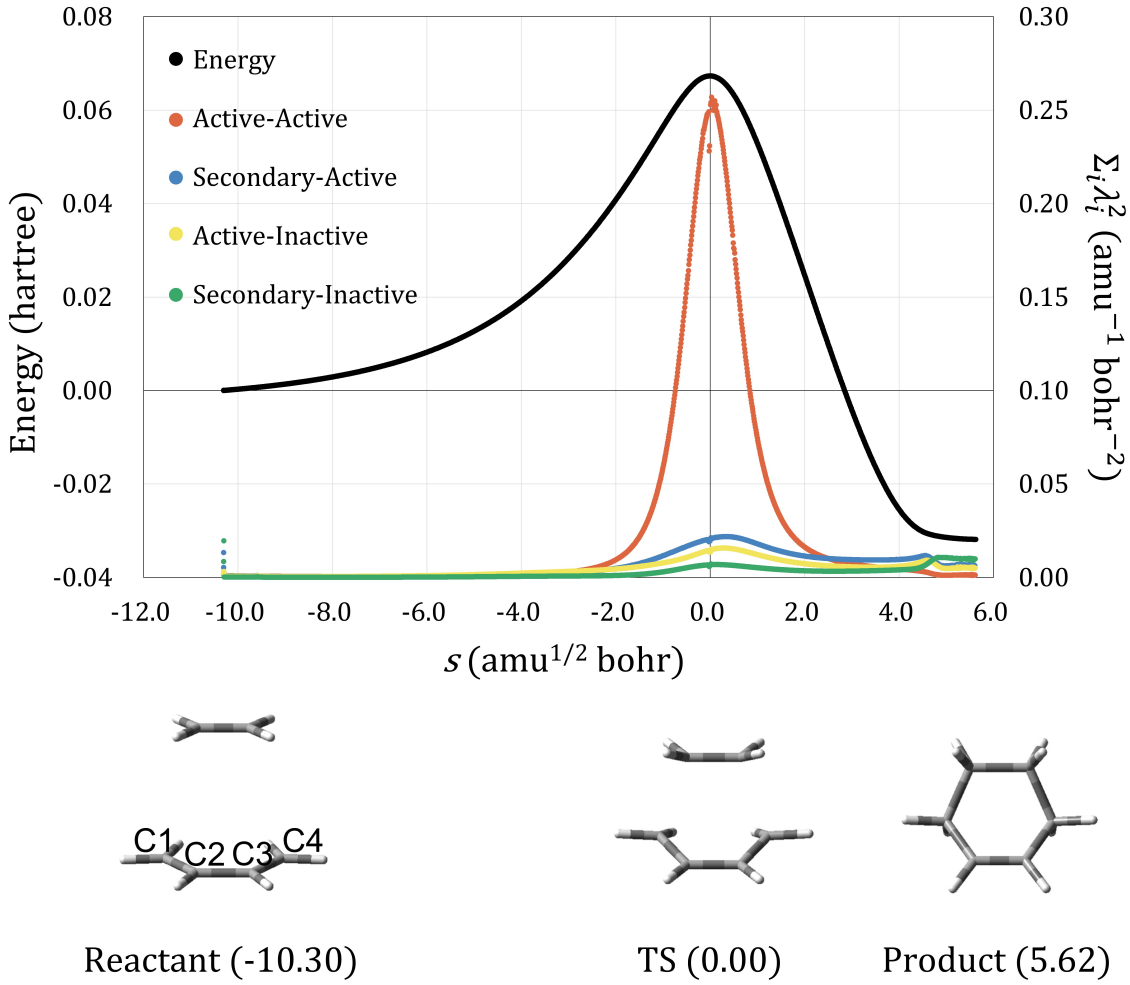

Fig. 4.11: Change of potential energy along the IRC of the Diels-Alder reaction of ethylene with 1,3-butadiene (black curve), as well as change of the sum of squares of singular values of MC-NRO for the active-active (red curve), secondary-active (blue curve), active-inactive (yellow curve), and secondary-inactive (green) blocks ($\sum_i \lambda_i^2$), at the CASSCF(8,7)/cc-pVTZ level. s is the reaction coordinate. The geometries of reactants, TS, and products are shown with the values of the reaction coordinates.

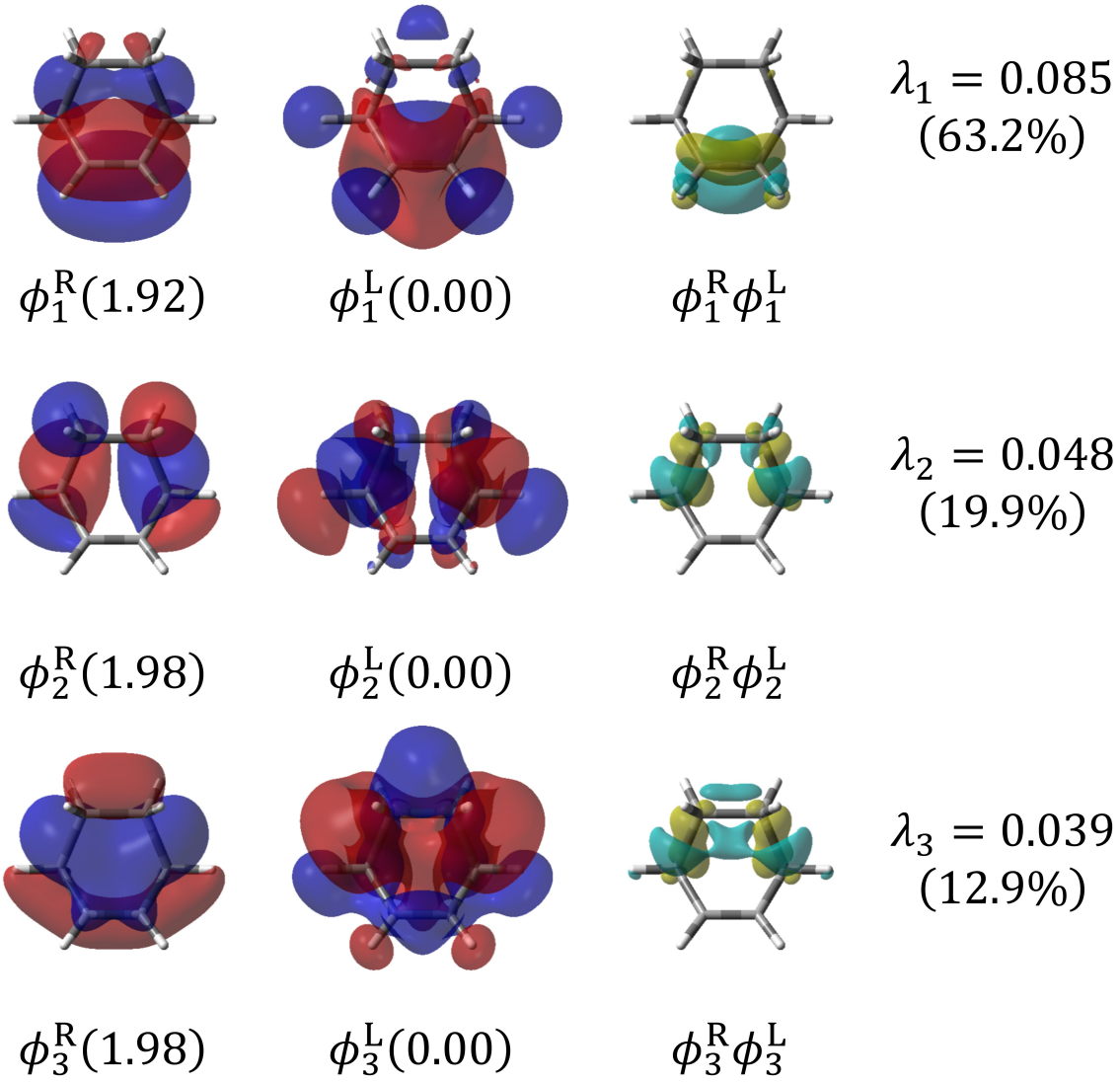

Fig. 4.12: Secondary-active MC-NRO pairs for the Diels-Alder reaction at $s = 4.59\mathrm{amu}^{1/2}\mathrm{bohr}$ in Fig. 4.11. ϕ_i^{R} and ϕ_i^{L} represent the i-th right (active) and left (secondary) MC-NROs, and the number in parentheses indicates the occupation number of each MC-NRO. The product of each MC-NRO pair is also shown and electron density decreases/increases in its cyan/yellow colored regions. λ_i [$\mathrm{amu}^{-1/2}\mathrm{bohr}^{-1}$] denotes the singular value of the i-th MC-NRO pair. The contribution ratio of each MC-NRO pair to the density change within active-active block, defined as $100 \times \lambda_i^2 / \sum_j \lambda_j^2$, is also shown with its singular value. The isovalues of MC-NRO and density change are 0.020 and 0.004, respectively.

tual electron transfer. It is also noteworthy that MC-NRO belongs to the irreducible representation of C_s symmetry, and therefore, chemical reactions can also be analyzed from the viewpoint of symmetry by using MC-NRO.

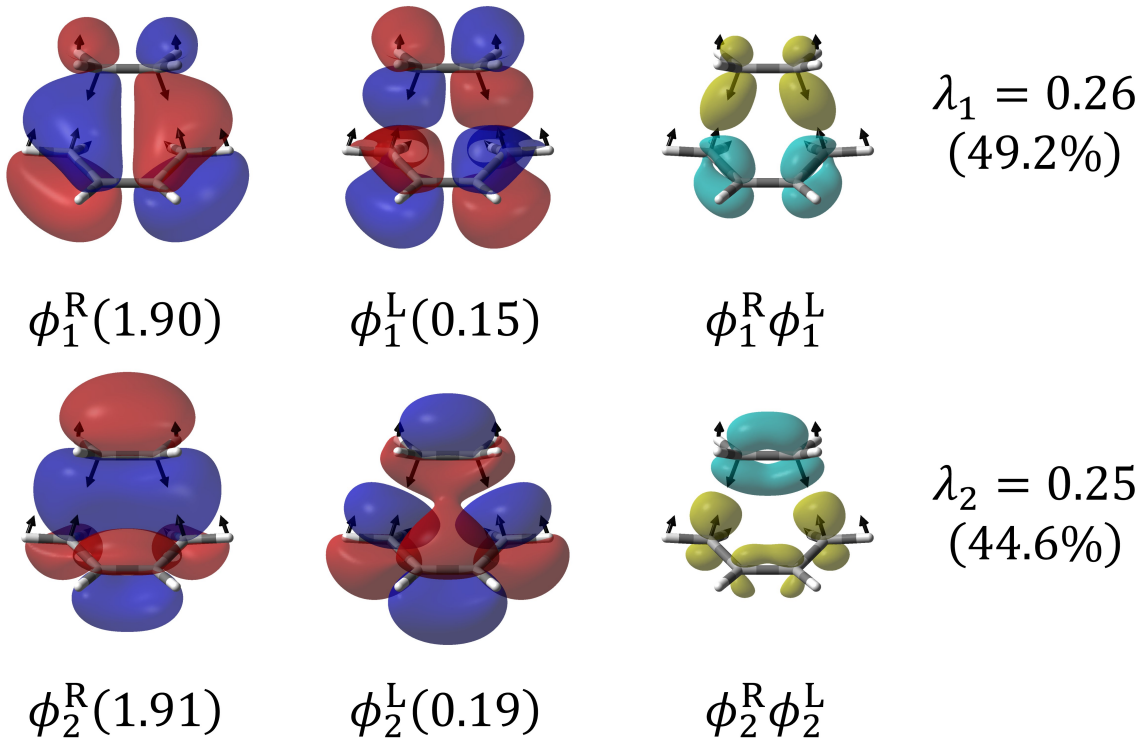

Fig. 4.13: Active-active MC-NRO pairs for the Diels-Alder reaction at TS. ϕ_i^{R} and ϕ_i^{L} represent the i-th right and left MC-NROs, and the number in parentheses indicate the occupation number of each MC-NRO. The product of each MC-NRO pair is also shown and electron density decreases/increases in its cyan/yellow colored regions. λ_i [amu$^{-1/2}$bohr^{-1}] denotes the singular value of the i-th MC-NRO pair. The contribution ratio of each MC-NRO pair to the density change within active-active block, defined as $100 \times \lambda_i^2 / \sum_j \lambda_j^2$, is also shown with its singular value. The isovalues of MC-NRO and density change are 0.020 and 0.004, respectively. The black arrows indicate the motion along the normal vibrational mode with an imaginary frequency.

4.3.4 Sigmatropic rearrangement

So far, MC-NRO analysis was applied to the reactions where symmetry is preserved along the IRCs. In this subsection, [1,5]-sigmatropic rearrangement of 1,3-pentadiene, where the nuclear motion along IRC reduces the symmetry of TS from C_s to C_1, is analyzed. IRC calculation was performed at CASSCF(6,6)/cc-pVTZ level.Fig. 4.14 shows changes of potential energy and the sum of squares of singular values which indicates the degree of electronic density change for the four sub-blocks along the IRC. It can be seen that the active space is not large enough to describe the density change because the contribution of the secondary-active and active-inactive sub-blocks is not negligible around the TS.

Based on the above result, the active space was refined by adding the first inactive and secondary MC-NROs at TS, and the TS geometry was reoptimized for the expanded active space. Fig. 4.15 shows the change in energy and sum of squares of singular values along the IRC at CASSCF(8,8)/cc-pVTZ level. It can be seen that the quality of the active space was improved by adding some dominant MC-NROs outside the original active space. This way of improvement is also important from the viewpoint of activation energy. Fig. 4.16 shows the energy difference between the CASSCF(6,6) and CASSCF(8,8) results whereas the IRC was computed separately for each active space. The energy difference is relatively large around the TS, where orbital mixing between active and non-active spaces is observed (Fig. 4.14). This result implies that the expansion of active space with using MC-NRO basis effectively improves the quality of the active space. However, it is another matter whether convergent result can be achieved with the expanded active space.

The dominant MC-NROs at TS optimized for the extended active space are displayed in Fig. 4.17. The first MC-NRO pair shows a C-H σ bond rearrangement: the electron density increases/decreases between C1/C5 and the proton. A rearrangement of the π bond from C3-C4 to C2-C3 is also observed. The second MC-NRO pair describes a π bond rearrangement from C1-C2 to C4-C5. Actually, these orbitals responsible for the sigmatropic rearrangement, automatically extracted by using MC-NRO method, are consistent with the representative orbitals shown in the conventional correlation diagram. [127] Thus, the two MC-NRO pairs appropriately characterize the concerted bond rearrangements in the [1,5]-sigmatropic rearrangement of 1,3-pentadiene. It was also confirmed that MC-NRO method works without any special problems even when there is some symmetry reduction along IRC.

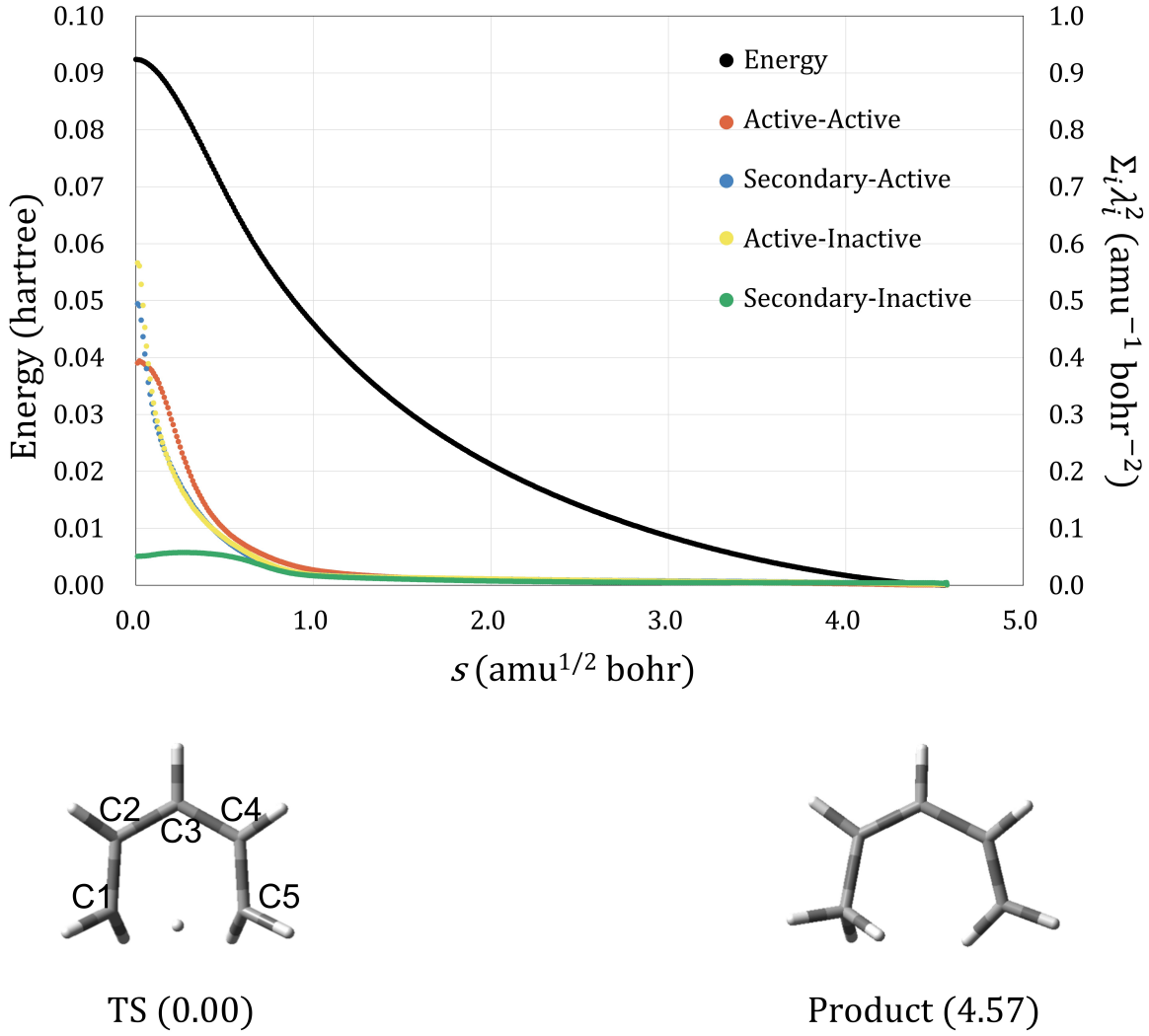

Fig. 4.14: Changes of potential energy along the IRC of the [1,5]-sigmatropic rearrangement of 1,3-pentadiene (black curve), as well as change of the sum of squares of singular values of MC-NROs, denoted by $\sum_i \lambda_i^2$, for the four blocks: active-active (red curve), secondary-active (blue curve), active-inactive (yellow curve), and secondary-inactive (green), at the CASSCF(6,6)/cc-pVTZ level. Geometries of TS and product (reactant) are shown with the reaction coordinates.

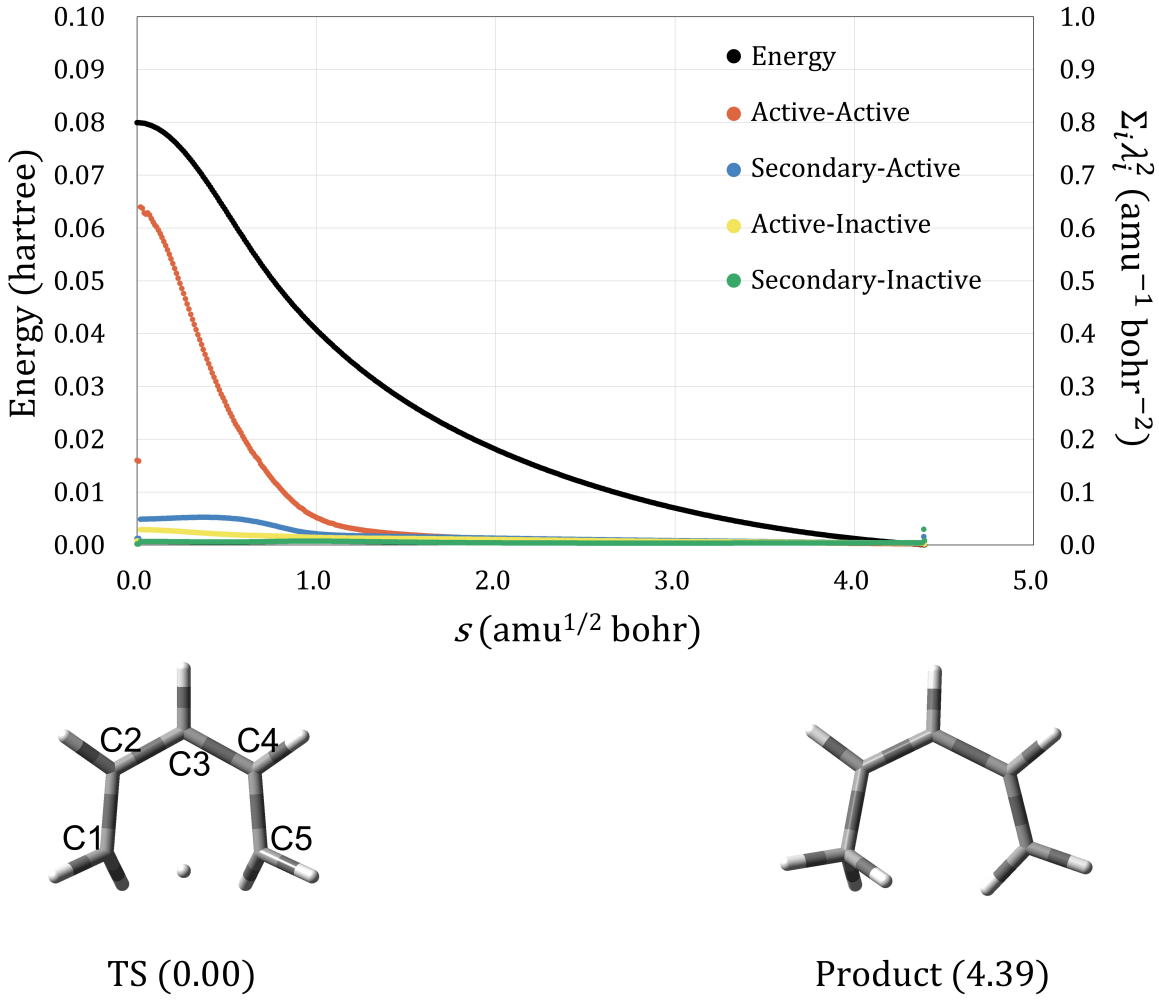

Fig. 4.15: Changes of potential energy along the IRC of the [1,5]-sigmatropic rearrangement of 1,3-pentadiene (black curve), as well as change of the sum of squares of singular values of MC-NROs, denoted by $\sum_i \lambda_i^2$ for the four sub-blocks, active-active (red curve), secondary-active (blue curve), active-inactive (yellow curve), and secondary-inactive (green), at CASSCF(8,8)/cc-pVTZ level. Geometries of TS and product (reactant) are shown with the reaction coordinates.

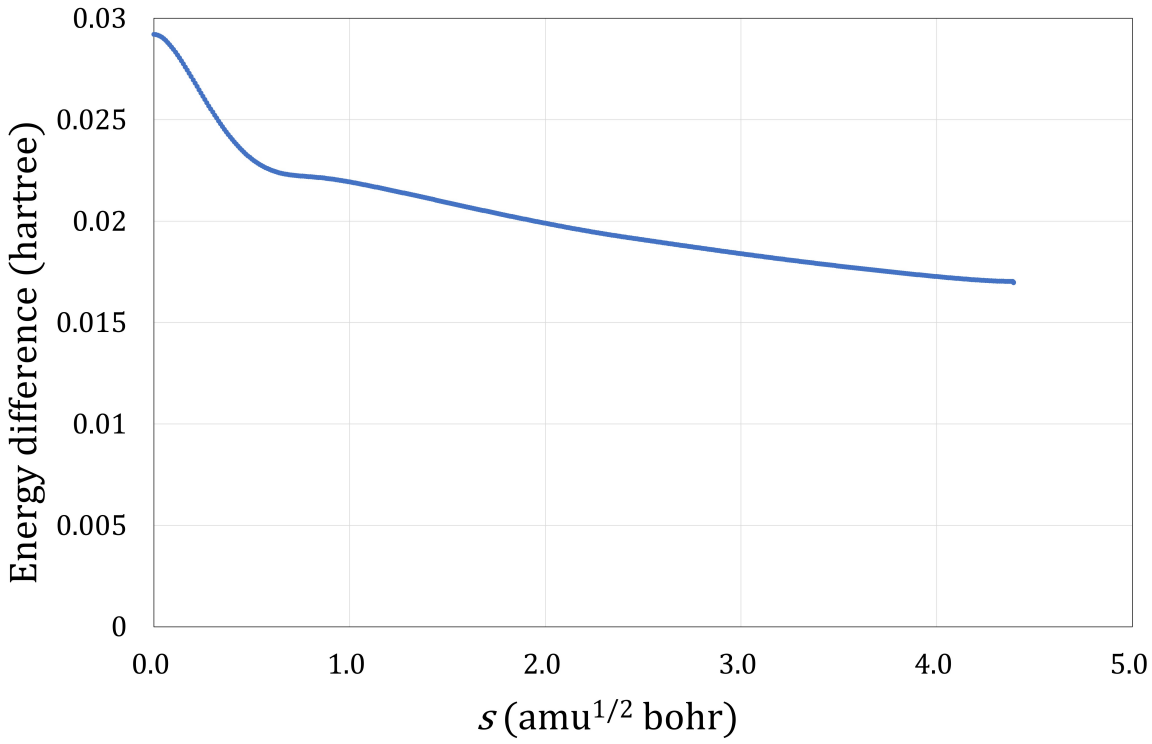

Fig. 4.16: Energy difference between CASSCF(6,6) and CASSCF(8,8) results for the [1,5]-sigmatropic rearrangement of 1,3-pentadiene along the IRC.

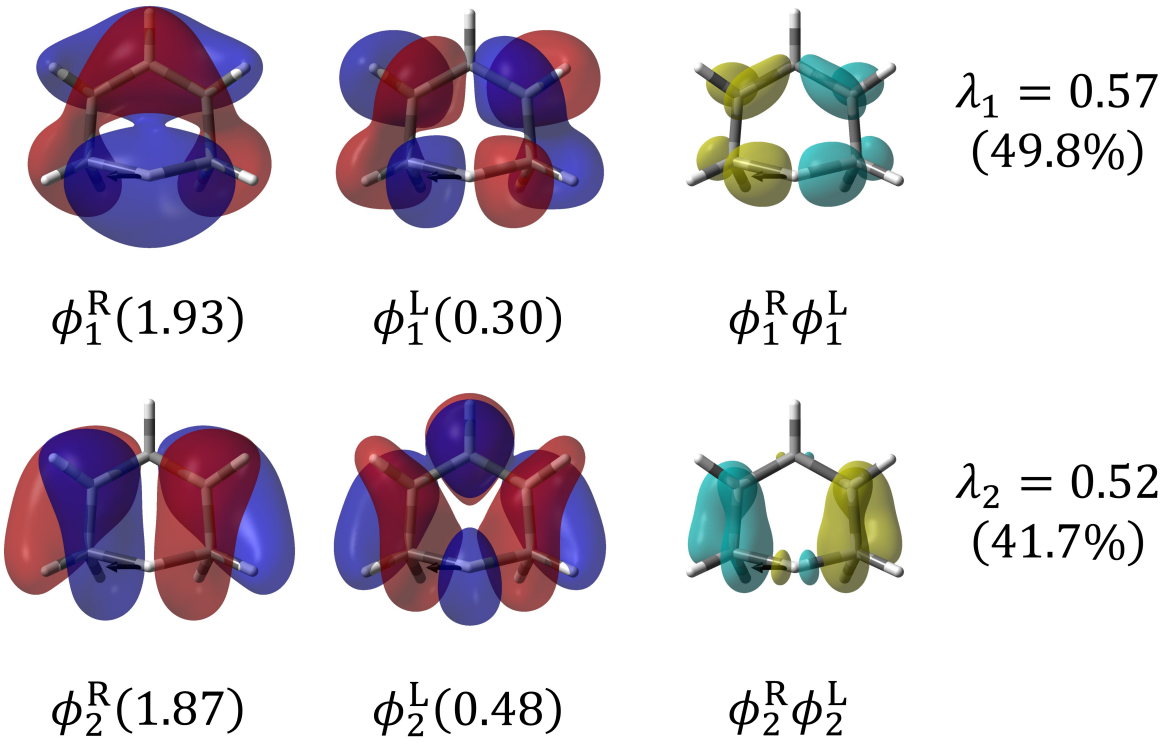

Fig. 4.17: Active-active MC-NRO pairs of the [1,5]-sigmatropic rearrangement at TS. ϕ_i^{R} and ϕ_i^{L} represent the i-th right and left MC-NROs, and the number in parentheses indicate the occupation number of each MC-NRO. The product of each MC-NRO pair is also shown and electron density decreases/increases in its cyan/yellow colored regions. λ_i [amu$^{-1/2}$bohr^{-1}] denotes the singular value of the i-th MC-NRO pair. The contribution ratio of each MC-NRO pair to the density change within active-active block, defined as $100 \times \lambda_i^2 / \sum_j \lambda_j^2$, is also shown with its singular value. The isovalues of MC-NRO and density change are 0.020 and 0.004, respectively. The black arrows indicate the motion along the normal vibrational mode with an imaginary frequency.

4.3.5 Intramolecular hydrogen transfer of malonaldehyde in the excited state

As the final example, the MC-NRO method is applied to the intramolecular hydrogen transfer of malonaldehyde in the S_1 state. [20, 85, 102, 125, 164] Chemical reactions in electronically excited states are the most important targets of MC-NRO method because multiconfigurational wavefunction is usually required to reproduce excited states. The S_1 state of malonaldehyde is characterized as a one-electron $n\pi^*$ excitation. [20,85,102,125,164] Fig. 4.18 displays the natural orbitals related to the excitation to the S_1 state, computed at the S_1-optimized geometry at CASSCF(12,9)/cc-pVTZ level. Indeed, the natural orbitals show the excitation from the in-plane lone pair of the oxygen atom (hole) to the out-of-plane π^* orbital (particle).

Fig. 4.19 shows the changes of the potential energy and the sum of squares of the singular values along the IRC in the S_1 state. The active space is large enough to describe the density variation because the active-active contribution is dominant throughout the IRC,.

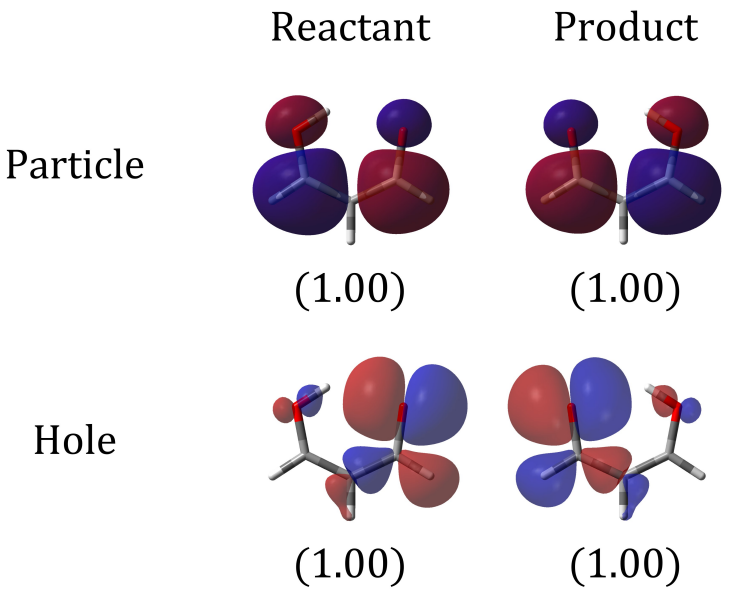

Fig. 4.18: Natural orbitals of malonaldehyde relevant to the electronic excitation from S_0 to S_1. The geometry is optimized in the S_1 state. Number in parentheses indicates the occupation number of each natural orbital.

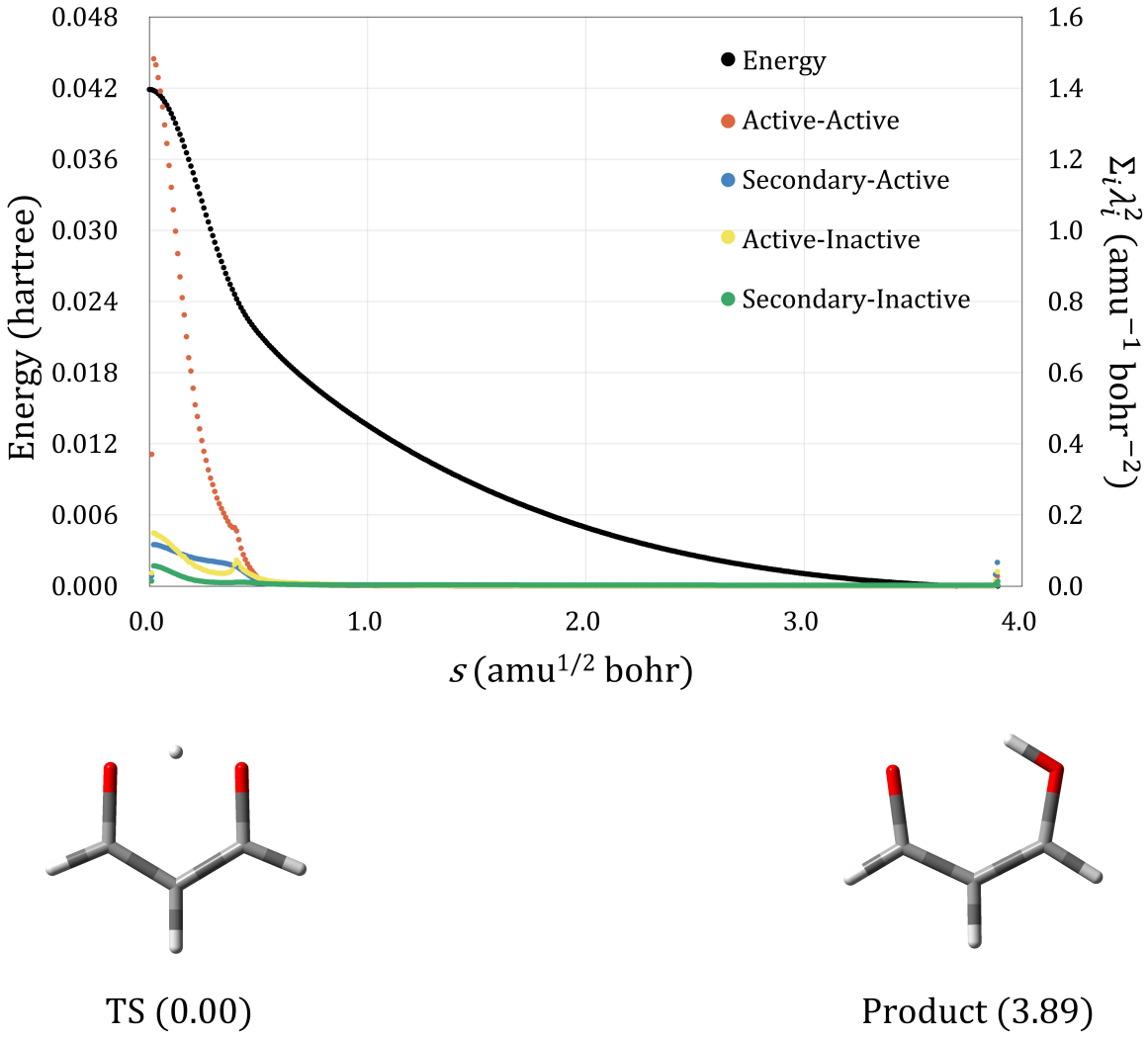

Fig. 4.19: Change of potential energy along the IRC of the hydrogen transfer reaction of malonaldehyde in the S_1 state (black curve), as well as change of the sum of squares of singular values of MC-NROs for the four blocks: active-active (red curve), secondary-active (blue curve), active-inactive (yellow curve), and secondary-inactive (green), at the CASSCF(12,9)/cc-pVTZ level. The geometry of TS and product (reactant) are shown with the values of the reaction coordinates.

Fig. 4.20 displays the MC-NROs at TS. The first and second MC-NRO pairs indicate that the electron moves in the same direction as the proton. This result is consistent with the behavior of the hole shown in Fig. 4.17. As the proton moves from the left oxygen to the right oxygen, the hole center moves from the right oxygen to the left oxygen. Therefore, electrons move in the opposite direction of the hole migration, i.e., in the same direction as the proton migration. Since the electron moves with the proton, this reaction should be characterized as hydrogen transfer rather than proton transfer. This is contrary to the ground state, where electron moves in the opposite direction of proton migration (Fig. 3.16). [33] It should be noted that the π density change shown by the fourth and fifth MC-NRO pairs is smaller than the density change induced by the first and second MC-NRO pairs. Actually, this is consistent with the behavior of the particles shown in Fig. 4.17. The particle delocalized over the molecular plane hardly changes its shape as the hydrogen transfer. Therefore, the change taking place in the π electron density is minor to that in the σ electron density. In summary, it was confirmed that MC-NRO method can systematically extract the representative orbitals for the reaction even in electronically excited state. Although there are useful orbitals to characterize the nature of excited states, such as natural transition orbitals (NTOs), [112] natural difference orbitals (NDOs), [135] and natural orbitals, the ability to systematically extract representative orbitals for reaction is a unique feature of MC-NRO.

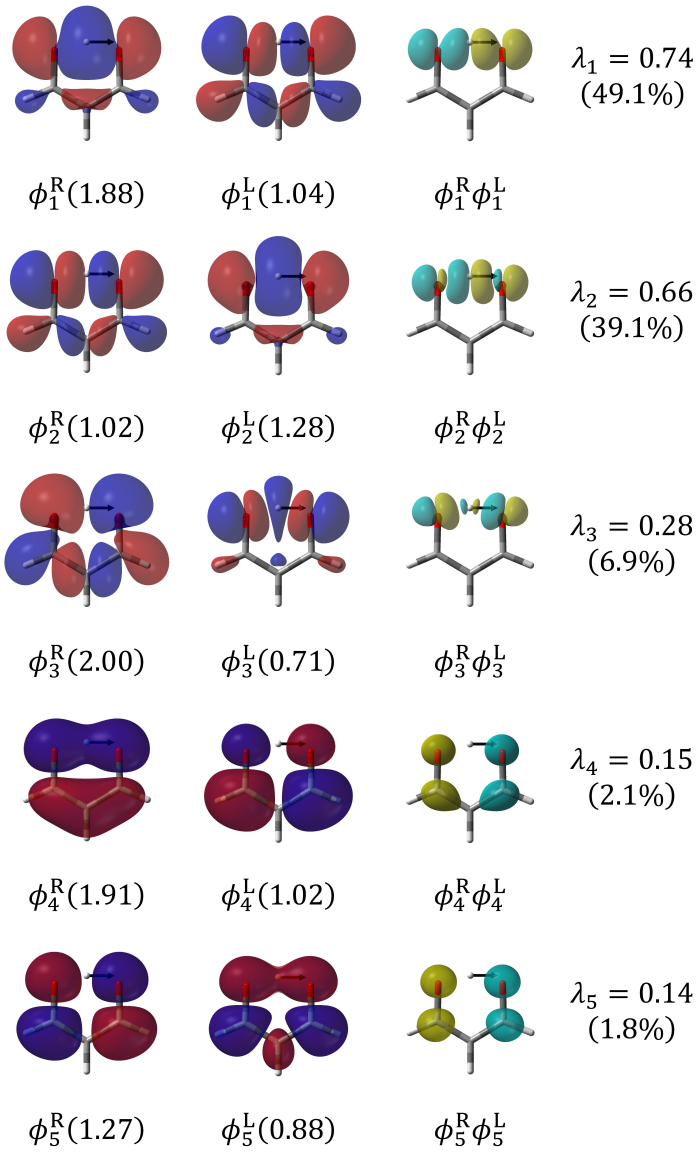

Fig. 4.20: Active-active MC-NRO pairs for hydrogen transfer of malonaldehyde at TS in the S_1 state. ϕ_i^{R} and ϕ_i^{L} denote the i-th right and left MC-NROs, and the numbers in parentheses indicate the occupation number of each MC-NRO. The product of each MC-NRO pair is also shown and electron density decreases/increases in its cyan/yellow colored regions. λ_i [amu$^{-1/2}$bohr^{-1}] denotes the singular value of the i-th MC-NRO pair. The contribution ratio of each MC-NRO pair to the density change within active-active block, defined as $100 \times \lambda_i^2 / \sum_j \lambda_j^2$, is also shown with its singular value. The isovalues of MC-NRO and density change are 0.020 and 0.004, respectively. The black arrows indicate the motion along the normal vibrational mode with an imaginary frequency.

4.4 Conclusion

In this chapter, natural reaction orbital (NRO) was extended to multiconfigurational theory and multiconfiguration natural reaction orbital (MC-NRO) was introduced, which can reveal the reaction mechanism along a reaction path from the viewpoint of electron density change. In MC-NRO method, pairs of representative orbitals with common singular values are generated by applying SVD to a matrix which characterizes the electron density change induced by nuclear displacements. The contribution of each orbital pair to the electron density change is measured by the singular value of the pair. The product of each orbital pair can show the electron density response to the molecular deformation. These features are useful to analyze the electron transfer taking place in the chemical reaction. It is also an important point that each MC-NRO belongs to an irreducible representation of the point group of the molecular structure. This allows reactions to be analyzed from the viewpoint of symmetry.

Although NRO also has the above mentioned features, MC-NRO method provides an intuitive way to analyze configuration mixing in terms of molecular orbitals. Indeed, the formation of hydrogen molecule, which proceeds by configuration mixing, was successfully characterized with using MC-NRO method. It seems to be very important that MC-NRO can automatically extract the representative orbitals characterizing the reactivity even from multiconfigurational wavefunctions considering that complex reactions proceeding by configuration mixing have also been understood on the basis of molecular orbitals. Also, MC-NRO is applicable to the reaction in electronically excited states, as demonstrated in the excited state intramolecular hydrogen transfer (ESIHT) of malonaldehyde. The nuclear motion in the ESIHT is hardly distinguishable from that in the proton transfer in the electronically ground state. What distinguishes the two process is the manner of electron transfer. Thus, it is essential to analyze electron density change along the reaction pathway to clarify what actually happens in the reaction. MC-NRO is expected to be a practical tool to study the reactivity in excited states since it can provide a way to distinguish the character of reactions in different states.

It is another interesting point of MC-NRO that can be used to improve the quality of active space. As is the case with CAS calculation, the nature of active space can change along reaction pathway. The worst case is that some of the active orbitals discontinuously change. As demonstrated in a sigmatropic rearrangement, it was found to be effective to improve the quality of active space to add some dominant MC-NROs in non-active spaces to the active space.

In summary, MC-NRO is not only important for systematic analysis of chemical reactions proceeding by configuration mixing but also useful for the construction of

active space. Thus, MC-NRO seems to be a very promising orbital analysis method which can promote theoretical studies of chemical reaction mechanisms based on multiconfigurational theory.

Chapter 5

General conclusion

In the present thesis, the following three issues were discussed.

In Chapter 2, a detailed investigation of the mathematical aspect of the ADD stationary path was presented. It was confirmed that the maximum number of the ADD stationary paths intersecting the EQ is given by $2^{f+1}-2$, where f denotes the degrees of freedom of vibration. Also, the bifurcation of the ADD stationary path was discussed. Bifurcation of ADD stationary paths takes place at the non-regular point of Hessian matrix of ADD on the hypersphere or the isosurface of harmonic potential. Typical bifurcations like saddle-node bifurcation and pitchfork bifurcation were discussed with model potentials. Although the IOE method was originally introduced to detect the ADD maximum direction on the initial hypersphere even for bifurcation, it does not always work as expected. We showed the case in which only ADD maxima of the original potential are followed and the technique fails to detect the bifurcation. However, the idea to follow not only ADD maxima but also ADD inflection points is important to reduce the risk of overlooking of the bifurcation. We demonstrated a case where following the ADD inflection points leads to finding the ADD maxima generated on the way by saddle-node bifurcation.

In Chapter 3, a new orbital analysis method specialized to reaction mechanism analysis, natural reaction orbital (NRO), was introduced. NRO is defined as the left and right singular vectors of the virtual-occupied block of the first-order response matrix of molecular orbitals, which is the solution of coupled-perturbed self-consistent field (CP-SCF) equation with respect to the perturbation of nuclear coordinates. Although this definition is only for single configurational theories, e.g., Hartree-Fock (HF) theory, the formal generalization to multiconfigurational theories was also presented in Section 3.2.9. Hence, the concept of NRO is general.

In both cases of single-configurational and multiconfigurational theories, NRO can be regarded as the optimal basis to characterize the first-order response of electron

density induced by the infinitesimal nuclear displacements. Indeed, the product of each pair of left and right singular vectors, virtual and occupied NRO pair in the case of single-configurational theories, is a component of the density change. Each singular value measures the rate of the density change with respect to the nuclear displacements. Particularly in the case of single-configurational theories, singular value can also be interpreted as the rate of orbital mixing between the occupied and virtual NRO pair with respect to the nuclear displacements. Accordingly, NRO pairs with large singular values are important for the electron transfer taking place in the chemical reaction. Provided that the reaction involves some distinct bond rearrangements or some bond formation/dissociation, the reactivity is appropriately characterized by the dominant NRO pairs. The number of dominant NRO pairs is usually small, a few or so. It indicates that the reactivity can be succinctly characterized with only a few dominant NRO pairs. In other words, the contribution to the electron transfer distributed to so many molecular orbitals can be consolidated to only a few NRO pairs. This considerable dimensionality reduction realized by singular value decomposition (SVD) seems to be very favorable for reaction mechanism analysis. Indeed, the application to a series of typical reactions showed that NRO provides a clear description of the reactivity of each reaction.

NRO has some particularly favorable features for reaction mechanism analysis. If a system has some symmetry and the direction of nuclear displacements belongs to some irreducible representation of the symmetry, NROs with nonzero singular values also belong some irreducible representations of the symmetry. The direct product of the irreducible representations of the occupied NRO, virtual NRO, and nuclear displacements is totally symmetric. This symmetry-adapted nature of NRO is highly compatible with the concept of symmetry preservation discussed by Woodward and Hoffmann. Also, basis set dependence of NRO is relatively low, that is, the qualitative nature of predominant NRO pairs is not largely affected by the choice of basis set. This robustness of NRO method seems to be very important for reliable analysis of chemical reaction mechanism with using molecular orbitals.

The observation of the square of the Frobenius norm of the virtual-occupied block of first-order response matrix, equivalent to the sum of the square of singular values, along IRC showed that electron transfer usually proceeds in some characteristic regions of IRC: the first-order saddle point and shoulder of IRC. This is reasonable considering that orbital mixing induces relaxation or downward distortion of potential energy surface. It indicates that NRO analysis needs to be performed at these characteristic regions. This is a great advantage of NRO method because trace of MOs along IRC, which is often time consuming, is not required to identify the MOs responsible for the reactivity. Although it seems interesting to trace the change of molecular orbitals along

IRC, the capability of identifying representative MOs at single geometry is so favorable in a viewpoint of practice. However, it should be remarked that there exits a case in which electron transfer proceeds without modifying the shape of potential energy curve as shown in the case of a carbocation rearrangement whereas NRO can appropriately characterize the electron transfer even in such a case. Also, there is no need to calculate NRO at all the geometry along IRC because the region where electron transfer proceeds can be detected by only tracing the change in density matrix along IRC which may evaluated numerically, of course. Thus, basically, it is enough for reaction mechanism analysis to compute NRO only at the regions where the change of density matrix is large. Omission of NRO analysis at the regions except for the first-order saddle point will be reasonable if the interest is only in the barrier height.

The comparison of NROs of different compounds at the first-order saddle point of S_N2 reaction confirmed that the predominant NROs of same type of reaction of different compounds resemble each other. The significance of this result is in that NRO provides a reasonable procedure to compare the reactivities different compounds in same type of reaction: the reactivities of different compounds can be analyzed by comparing similar NROs. Indeed, the reactivities in S_N2 reaction were clearly reflected in the orbital energies of occupied NROs. Also, the comparison of dominant NROs of competing E2 and S_N2 reactions between OH^- and CH_3Cl implied that NRO is capable of explaining the selectivity with its orbital energy. These results indicate that NRO is not only convenient for visualization but also effective to extraction of the essence of chemical reaction.

For all the features of NRO shown above, NRO seems to be a very promising orbital analysis method enabling automated extraction of representative MOs responsible for the reactivity. It is notable that the electron density changes shown by products of NRO pairs represent the patterns corresponding to the chemical bond rearrangements described by the electronic theory of organic chemistry. Although the pictures of chemical reactions provided by quantum chemistry and the electronic theory of organic chemistry are not completely identical, the consistency to a considerable extent is really surprising. This seems to imply how essential the concept of chemical bond is for describing chemical reactivity. Hopefully, NRO is expected to play an important role in bridging the gap somehow still lain between quantum chemistry and the electronic theory of organic chemistry through the concept of chemical bond.

In Chapter 4, a practical orbital analysis method for reaction mechanism analysis which is also applicable to multiconfigurational theory, MC-NRO, was introduced. Although the concept of NRO is general, the straightforward generalization presented in Section 3.2.9 is not very practical because it requires the derivatives of configuration interaction (CI) coefficients. MC-NRO, however, does not require the derivatives of CI

coefficients so far as it is computed numerically. In MC-NRO method, density chage with respective to nuclear displacements is evaluated with a matrix composed of square root of density matrix, numerical differentiation of square root of density matrix, and square root of overlap matrix. The matrix is divided into sub-blocks within which any orbital rotation does not violate the orbital invariance of the theory. MC-NRO is obtained by applying SVD to thses sub-blocks. In principle, MC-NRO method can be applied to any electronic structure theory provided density matrix is available.

As the first demonstration, MC-NRO method was applied to complete active space self-consistent field (CASSCF) theory. Application to H_2 bond formation and N_2 bond formation, which can not be reproduced by single configurational theory, confirmed that the MOs participating in the covalent bond formation are extracted appropriately. The examples of Diels-Alder reaction and [1,5]-sigmatropic rearrangements showed that MC-NRO method extracts MOs qualitatively resembling those extracted with NRO method for single configurational theory. Considering that these reactions can also be reproduced with single configurational theories, it is a reasonable result that the dominant MC-NROs and NROs resemble each other.

Also, in the application to [1,5]-sigmatropic rearrangements, it is implied that MC-NRO can provide a systematic procedure to improve the quality of active space along given reaction pathway. It should be noted that electron transfer between the inside and outside the active space induced by nuclear displacements can be used to confirm whether the active space is large enough for the description of the reactant or not. If the active space is insufficient for the description, the active space may be improved by adding dominant MC-NROs characterizing the electron transfer between the inside and outside the active space. Indeed, in the case of [1,5]-sigmatropic rearrangements, the variational energy was considerably lowered by adding dominant MC-NRO, particularly in the vicinity of the first-order saddle point. Accordingly, improvement of the active space with NC-NRO is also important in a viewpoint of energetics.

The last example of the excited-state intramolecular hydrogen transfer in the S_1 state of malonaldehyde confirmed that MC-NRO method is also applicable to the reaction in electronically excited states. Although the nuclear motion of proton in S_1 state is almost indistinguishable from that in S_0 state, the density change is definitely different from that of S_0. Thus, MC-NRO method seems to be useful to identify the reactivity of the reaction in electronically excited states.

NRO and MC-NRO, new orbital analysis methods for automated extraction of molecular orbitals responsible for the reactivity, were developed motivated by ADDF method, an automated reaction pathway searching method. Considering that orbital mixing and configuration mixing contribute to distortion of the potential energy surface, they can be regarded as an origin of ADD. Hence, the driving force of a chemical

reaction can be analyzed with NRO and MC-NRO. Also, as noted above, they are expected to bridge the gap lain between quantum chemistry and the electronic theory of organic chemistry. NRO and MC-NRO will be very promising orbital methods for understanding of chemical reactivity. Combined with the automated reaction pathway search methods, ADDF and AFIR, these automated methods to extract essential MOs for the reactivity are expected to be a very powerful tool for realization of an automated data sampling system with computational chemistry.

Bibliography

[1] A. Amos and G. Hall. Single determinant wave functions. *Proceedings of the Royal Society of London. Series A. Mathematical and Physical Sciences*, 263(1315):483–493, 1961.

[2] W. Auzinger and H. J. Stetter. An elimination algorithm for the computation of all zeros of a system of multivariate polynomial equations. In *Numerical Mathematics Singapore 1988*, pages 11–30. Springer, 1988.

[3] M. Baer. Introduction to the theory of electronic non-adiabatic coupling terms in molecular systems. *Physics Reports*, 358(2):75–142, 2002.

[4] M. Basilevsky. The topography of potential energy surfaces. *Chemical Physics*, 67(3):337–346, 1982.

[5] M. Basilevsky and A. Shamov. The local definition of the optimum ascent path on a multi-dimensional potential energy surface and its practical application for the location of saddle points. *Chemical Physics*, 60(3):347–358, 1981.

[6] C. W. J. Bauschlicher, H. F. I. Schaefer, and C. F. Bender. The least-motion insertion reaction methylene(1A1) + molecular hydrogen .fwdarw. methane. theoretical study of a process forbidden by orbital symmetry. *Journal of the American Chemical Society*, 98(7):1653–1658, 1976.

[7] C. W. Bauschlicher Jr, S. P. Walch, S. R. Langhoff, P. R. Taylor, and R. L. Jaffe. Theoretical studies of the potential surface for the F + H_2 → HF + H reaction. *The Journal of chemical physics*, 88(3):1743–1751, 1988.

[8] M. V. Berry. Quantal phase factors accompanying adiabatic changes. *Proceedings of the Royal Society of London. A. Mathematical and Physical Sciences*, 392(1802):45–57, 1984.

[9] J. M. Bofill and W. Quapp. Variational nature, integration, and properties of newton reaction path. *The Journal of chemical physics*, 134(7):074101, 2011.

[10] K. Bondensgård and F. Jensen. Gradient extremal bifurcation and turning points: an application to the H_2CO potential energy surface. *The Journal of chemical physics*, 104(20):8025–8031, 1996.

[11] M. Born. Quantenmechanik der stoßvorgänge. *Zeitschrift für Physik*, 34:803–827, 1926.

[12] M. Born and P. Jordan. Zur quantenmechanik. *Zeitschrift für Physik*, 34:858–888, 1925.

[13] M. Born and R. Oppenheimer. Zur quantentheorie der molekeln. *Annalen der Physik*, 389(20):457–484, 1927.

[14] B. H. Botch and T. H. Dunning Jr. Theoretical characterization of negative ions. calculation of the electron affinities of carbon, oxygen, and fluorine. *The Journal of Chemical Physics*, 76(12):6046–6056, 1982.

[15] U. Burkert and N. L. Allinger. Pitfalls in the use of the torsion angle driving method for the calculation of conformational interconversions. *Journal of computational chemistry*, 3(1):40–46, 1982.

[16] R. B. Campos and D. J. Tantillo. Designing reactions with post-transition-state bifurcations: Asynchronous nitrene insertions into C–C σ bonds. *Chem*, 5(1):227–236, 2019.

[17] D. Cartwright and B. Sturmfels. The number of eigenvalues of a tensor. *Linear algebra and its applications*, 438(2):942–952, 2013.

[18] T. Caves and M. Karplus. Perturbed Hartree–Fock theory. I. diagrammatic double-perturbation analysis. *The Journal of Chemical Physics*, 50(9):3649–3661, 1969.

[19] A. Chikama, H. Fueno, and H. Fujimoto. Theoretical study of the diels-alder reaction of C60. transition-state structures and reactivities of CC bonds. *The Journal of Physical Chemistry*, 99(21):8541–8549, 1995.

[20] J. D. Coe and T. J. Martínez. Ab initio molecular dynamics of excited-state intramolecular proton transfer around a three-state conical intersection in malonaldehyde. *The Journal of Physical Chemistry A*, 110(2):618–630, 2006.

[21] C. A. Coulson and H. C. Longuet-Higgins. The electronic structure of conjugated systems I. general theory. *Proceedings of the Royal Society of London. Series A. Mathematical and Physical Sciences*, 191(1024):39–60, 1947.

[22] J. G. Cramer. The transactional interpretation of quantum mechanics. *Reviews of Modern Physics*, 58(3):647, 1986.

[23] R. R. da Silva, T. C. Ramalho, J. M. Santos, and J. D. Figueroa-Villar. On the limits of highest-occupied molecular orbital driven reactions: the frontier effective-for-reaction molecular orbital concept. *The Journal of Physical Chemistry A*, 110(3):1031–1040, 2006.

[24] G. Das and A. C. Wahl. Extended Hartree–Fock wavefunctions: Optimized valence configurations for H_2 and Li_2, optimized double configurations for f2. *The Journal of Chemical Physics*, 44(1):87–96, 1966.

[25] M. J. Dewar. A critique of frontier orbital theory. *Journal of Molecular Structure: THEOCHEM*, 200:301–323, 1989.

[26] A. L. Dewyer, A. J. Argüelles, and P. M. Zimmerman. Methods for exploring reaction space in molecular systems. *Wiley Interdisciplinary Reviews: Computational Molecular Science*, 8(2):e1354, 2018.

[27] P. A. Dirac. Note on exchange phenomena in the thomas atom. In *Mathematical proceedings of the Cambridge philosophical society*, volume 26, pages 376–385. Cambridge University Press, 1930.

[28] P. A. M. Dirac and R. H. Fowler. The quantum theory of the electron. *Proceedings of the Royal Society of London. Series A, Containing Papers of a Mathematical and Physical Character*, 117(778):610–624, 1928.

[29] P. A. M. Dirac and R. H. Fowler. Quantum mechanics of many-electron systems. *Proceedings of the Royal Society of London. Series A, Containing Papers of a Mathematical and Physical Character*, 123(792):714–733, 1929.

[30] W. v. E. Doering and W. Roth. The overlap of two allyl radicals or a four-centered transition state in the cope rearrangement. *Tetrahedron*, 18(1):67–74, 1962.

[31] T. H. Dunning Jr. Gaussian basis sets for use in correlated molecular calculations. I. the atoms boron through neon and hydrogen. *The Journal of chemical physics*, 90(2):1007–1023, 1989.

[32] L. Eberson and S. S. Shaik. Electron-transfer reactions of radical anions: do they follow outer-or inner-sphere mechanisms? *Journal of the American Chemical Society*, 112(11):4484–4489, 1990.

[33] S. Ebisawa, M. Hasebe, T. Tsutsumi, T. Tsuneda, and T. Taketsugu. Natural reaction orbitals for characterizing electron transfer responsive to nuclear coordinate displacement. *Physical Chemistry Chemical Physics*, 24(6):3532–3545, 2022.

[34] S. Ebisawa, T. Tsutsumi, and T. Taketsugu. Extension of natural reaction orbital approach to multiconfigurational wavefunctions. *The Journal of Chemical Physics*, 157(8):084118, 2022.

[35] C. Edmiston and M. Krauss. Configuration-interaction calculation of H_3 and H_2. *The Journal of Chemical Physics*, 42(3):1119–1120, 1965.

[36] C. Edmiston and M. Krauss. Pseudonatural orbitals as a basis for the superposition of configurations. I. He_2^+. *The Journal of Chemical Physics*, 45(5):1833–1839, 1966.

[37] C. Edmiston and K. Ruedenberg. Localized atomic and molecular orbitals. *Reviews of Modern Physics*, 35(3):457, 1963.

[38] C. Edmiston and K. Ruedenberg. Localized atomic and molecular orbitals. II. *The Journal of Chemical Physics*, 43(10):S97–S116, 1965.

[39] V. Fock. Näherungsmethode zur lösung des quantenmechanischen mehrkörperproblems. *Zeitschrift für Physik*, 61(1):126–148, 1930.

[40] E. Frankland. XIX. on a new series of organic bodies containing metals. *Philosophical Transactions of the Royal Society of London*, (142):417–444, 1852.

[41] J. Frenkel. *Wave mechanics, advanced general theory*, volume 1. Oxford, 1934.

[42] M. Frisch, G. W. Trucks, H. B. Schlegel, G. E. Scuseria, M. A. Robb, J. R. Cheeseman, G. Scalmani, V. Barone, B. Mennucci, G. Petersson, et al. Gaussian 09, revision D. 01, 2009.

[43] M. J. Frisch, G. W. Trucks, H. B. Schlegel, G. E. Scuseria, M. A. Robb, J. R. Cheeseman, G. Scalmani, V. Barone, G. A. Petersson, H. Nakatsuji, X. Li, M. Caricato, A. V. Marenich, J. Bloino, B. G. Janesko, R. Gomperts, B. Mennucci, H. P. Hratchian, J. V. Ortiz, A. F. Izmaylov, J. L. Sonnenberg, D. Williams-Young, F. Ding, F. Lipparini, F. Egidi, J. Goings, B. Peng, A. Petrone, T. Henderson, D. Ranasinghe, V. G. Zakrzewski, J. Gao, N. Rega, G. Zheng, W. Liang, M. Hada, M. Ehara, K. Toyota, R. Fukuda, J. Hasegawa, M. Ishida, T. Nakajima, Y. Honda, O. Kitao, H. Nakai, T. Vreven, K. Throssell, J. A. Montgomery, Jr., J. E. Peralta, F. Ogliaro, M. J. Bearpark, J. J. Heyd, E. N. Brothers, K. N. Kudin,

V. N. Staroverov, T. A. Keith, R. Kobayashi, J. Normand, K. Raghavachari, A. P. Rendell, J. C. Burant, S. S. Iyengar, J. Tomasi, M. Cossi, J. M. Millam, M. Klene, C. Adamo, R. Cammi, J. W. Ochterski, R. L. Martin, K. Morokuma, O. Farkas, J. B. Foresman, and D. J. Fox. Gaussian 16 Revision C.01, 2016. Gaussian Inc. Wallingford CT.

[44] H. Fujimoto. Paired interacting orbitals: a way of looking at chemical interactions. *Accounts of Chemical Research*, 20(12):448–453, 1987.

[45] H. Fujimoto, S. Denno, and Y. Jinbu. Theoretical study of stable carbocations and their interactions with anions. *The Journal of Physical Chemistry*, 95(4):1612–1618, 1991.

[46] H. Fujimoto and R. Hoffmann. Molecular orbital study of the addition of singlet methylene to butadiene. *The Journal of Physical Chemistry*, 78(12):1167–1173, 1974.

[47] H. Fujimoto and H. Kawamura. Analysis of paired interacting orbitals for extended systems: application to the protonation of conjugated carbon chains and the chemisorption of hydrogen on nickel surfaces. *Journal of Physical Chemistry*, 91(13):3555–3559, 1987.

[48] H. Fujimoto, N. Koga, and K. Fukui. Coupled fragment molecular orbital method for interacting systems. *Journal of the American Chemical Society*, 103(25):7452–7457, 1981.

[49] H. Fujimoto, Y. Mizutani, and K. Iwase. An aspect of substituents and peripheral structures in chemical reactivities of molecules. *The Journal of Physical Chemistry*, 90(12):2768–2772, 1986.

[50] H. Fujimoto, K. Sakata, and K. Fukui. Transient bonds and chemical reactivity of molecules. *International journal of quantum chemistry*, 60(1):401–408, 1996.

[51] H. Fujimoto and S. Satoh. Orbital interactions and chemical hardness. *The Journal of Physical Chemistry*, 98(5):1436–1441, 1994.

[52] K. Fukui. Formulation of the reaction coordinate. *The Journal of Physical Chemistry*, 74(23):4161–4163, 1970.

[53] K. Fukui. The path of chemical reactions-the IRC approach. *Accounts of chemical research*, 14(12):363–368, 1981.

[54] K. Fukui. Role of frontier orbitals in chemical reactions. *science*, 218(4574):747–754, 1982.

[55] K. Fukui, S. Kato, and H. Fujimoto. Constituent analysis of the potential gradient along a reaction coordinate. method and an application to methane+ tritium reaction. *Journal of the American Chemical Society*, 97(1):1–7, 1975.

[56] K. Fukui, N. Koga, and H. Fujimoto. Interaction frontier orbitals. *Journal of the American Chemical Society*, 103(1):196–197, 1981.

[57] K. Fukui, T. Yonezawa, and H. Shingu. A molecular orbital theory of reactivity in aromatic hydrocarbons. *The Journal of Chemical Physics*, 20(4):722–725, 1952.

[58] J. M. Galbraith, S. Shaik, D. Danovich, B. Braïda, W. Wu, P. Hiberty, D. L. Cooper, P. B. Karadakov, and T. H. Dunning Jr. Valence bond and molecular orbital: Two powerful theories that nicely complement one another. *Journal of Chemical Education*, 98(12):3617–3620, 2021.

[59] P. Garcia-Fernandez, J. A. Aramburu, M. Moreno, M. Zlatar, and M. Gruden-Pavlovicć. A practical computational approach to study molecular instability using the pseudo-jahn–teller effect. *Journal of Chemical Theory and Computation*, 10(4):1824–1833, 2014.

[60] J. Gerratt and I. M. Mills. Force constants and dipole-moment derivatives of molecules from perturbed Hartree–Fock calculations. I. *The Journal of Chemical Physics*, 49(4):1719–1729, 1968.

[61] J. Handzlik, A. Shiga, and J. Kondziołka. Paired interacting orbitals (PIO) study of molybdena-alumina system active in alkene metathesis. *Journal of Molecular Catalysis A: Chemical*, 284(1-2):8–15, 2008.

[62] Y. Harabuchi and T. Taketsugu. A significant role of the totally symmetric valley-ridge inflection point in the bifurcating reaction pathway. *Theoretical Chemistry Accounts*, 130(2):305–315, 2011.

[63] D. R. Hartree. The wave mechanics of an atom with a non-Coulomb central field. part I. theory and methods. In *Mathematical Proceedings of the Cambridge Philosophical Society*, volume 24, pages 89–110. Cambridge university press, 1928.

[64] D. R. Hartree. The wave mechanics of an atom with a non-Coulomb central field. part II. some results and discussion. In *Mathematical Proceedings of the Cambridge Philosophical Society*, volume 24, pages 111–132. Cambridge University Press, 1928.

[65] I. Hataue, Y. Oishi, M. Kubota, and H. Fujimoto. Theoretical study of chemical interactions in crown ether-cation complexes. *Tetrahedron*, 47(45):9317–9328, 1991.

[66] W. Heisenberg. Über quantentheoretische umdeutung kinematischer und mechanischer beziehungen. *Zeitschrift für Physik*, 33:879–893, 1925.

[67] W. Heitler and F. London. Wechselwirkung neutraler atome und homöopolare bindung nach der quantenmechanik. *Zeitschrift für Physik*, 44(6):455–472, 1927.

[68] H. Hirao and T. Ohwada. Theoretical revisit of regioselectivities of Diels-Alder reactions: orbital-based reevaluation of multicentered reactivity in terms of reactive hybrid orbitals. *The Journal of Physical Chemistry A*, 109(5):816–824, 2005.

[69] M. Hirsch and W. Quapp. Reaction channels of the potential energy surface: application of newton trajectories. *Journal of Molecular Structure: THEOCHEM*, 683(1-3):1–13, 2004.

[70] M. Hirsch, W. Quapp, and D. Heidrich. The set of valley–ridge inflection points on the potential energy surface of water. *Physical Chemistry Chemical Physics*, 1(23):5291–5299, 1999.

[71] D. K. Hoffman, R. S. Nord, and K. Ruedenberg. Gradient extremals. *Theoretica chimica acta*, 69(4):265–279, 1986.

[72] R. Hoffmann and R. Woodward. Selection rules for concerted cycloaddition reactions. *Journal of the American Chemical Society*, 87(9):2046–2048, 1965.

[73] L. Hogben. *Handbook of linear algebra*. CRC press, 2013.

[74] P. Hohenberg and W. Kohn. Inhomogeneous electron gas. *Physical review*, 136(3B):B864, 1964.

[75] F. Hund. Zur deutung der molekelspektren. IV. *Zeitschrift für Physik*, 51(792):759–795, 1928.

[76] H. Iikura, T. Tsuneda, T. Yanai, and K. Hirao. A long-range correction scheme for generalized-gradient-approximation exchange functionals. *The Journal of Chemical Physics*, 115(8):3540–3544, 2001.

[77] S. Inagaki, H. Fujimoto, and K. Fukui. Orbital mixing rule. *Journal of the American Chemical Society*, 98(14):4054–4061, 1976.

[78] C. K. Ingold. 266. significance of tautomerism and of the reactions of aromatic compounds in the electronic theory of organic reactions. *Journal of the Chemical Society (Resumed)*, pages 1120–1127, 1933.

[79] C. K. Ingold. Principles of an electronic theory of organic reactions. *Chemical Reviews*, 15(2):225–274, 1934.

[80] C. K. Ingold and E. H. Ingold. CLXIX.—the nature of the alternating effect in carbon chains. part V. a discussion of aromatic substitution with special reference to the respective roles of polar and non-polar dissociation; and a further study of the relative directive efficiencies of oxygen and nitrogen. *Journal of the Chemical Society (Resumed)*, 129:1310–1328, 1926.

[81] C. K. Ingold and F. R. Shaw. CCCLXXXVIII.—the nature of the alternating effect in carbon chains. part xxii. an attempt further to define the probable mechanism of orientation in aromatic substitution. *Journal of the Chemical Society (Resumed)*, pages 2918–2926, 1927.

[82] K. Ishida, K. Morokuma, and A. Komornicki. The intrinsic reaction coordinate. an abinitio calculation for HNC $\rightarrow$ HCN and H^-+ $ch_4 \rightarrow ch_4$+ h^-. *The Journal of Chemical Physics*, 66(5):2153–2156, 1977.

[83] H. Jónsson, G. Mills, and K. W. Jacobsen. Nudged elastic band method for finding minimum energy paths of transitions. In *Classical and quantum dynamics in condensed phase simulations*, pages 385–404. World Scientific, 1998.

[84] P. Jørgensen, H. J. A. Jensen, and T. Helgaker. A gradient extremal walking algorithm. *Theoretica chimica acta*, 73(1):55–65, 1988.

[85] T. Kar, S. Scheiner, and M. Čuma. Comparison of methods for calculating the properties of intramolecular hydrogen bonds. excited state proton transfer. *The Journal of chemical physics*, 111(3):849–858, 1999.

[86] I. Kawata and H. Nitta. An excited state paired interacting orbital method. *The Journal of Chemical Physics*, 136(6):064109, 2012.

[87] R. A. Kendall, T. H. Dunning Jr, and R. J. Harrison. Electron affinities of the first-row atoms revisited. systematic basis sets and wave functions. *The Journal of chemical physics*, 96(9):6796–6806, 1992.

[88] W. O. Kermack and R. Robinson. LI.—an explanation of the property of induced polarity of atoms and an interpretation of the theory of partial valencies on an

electronic basis. *Journal of the Chemical Society, Transactions*, 121:427–440, 1922.

[89] V. Klema and A. Laub. The singular value decomposition: Its computation and some applications. *IEEE Transactions on automatic control*, 25(2):164–176, 1980.

[90] G. Knizia. Intrinsic atomic orbitals: An unbiased bridge between quantum theory and chemical concepts. *Journal of chemical theory and computation*, 9(11):4834–4843, 2013.

[91] G. Knizia and J. E. Klein. Electron flow in reaction mechanisms—revealed from first principles. *Angewandte Chemie International Edition*, 54(18):5518–5522, 2015.

[92] Y. Kodaya, T. Oki, H. Yamakado, H. Tokoyama, and K. Ohno. Crystal structure exploration of boron nitride polymorphs using anharmonic downward distortion following method with potential energy surface modified by the inverse of lattice volume. *Chemistry Letters*, 48(11):1288–1291, 2019.

[93] W. Kohn and L. J. Sham. Self-consistent equations including exchange and correlation effects. *Physical review*, 140(4A):A1133, 1965.

[94] A. Komornicki, K. Ishida, K. Morokuma, R. Ditchfield, and M. Conrad. Efficient determination and characterization of transition states using ab-initio methods. *Chemical Physics Letters*, 45(3):595–602, 1977.

[95] L. Kong. Orbital invariance issue in multireference methods. *International Journal of Quantum Chemistry*, 110(14):2603–2613, 2010.

[96] A. I. Krylov. From orbitals to observables and back. *The Journal of Chemical Physics*, 153(8):080901, 2020.

[97] É. Kuznetsov and K. Kholshevnikov. Estimation of the number of extrema of a spherical harmonic. *Soviet Astronomy*, 36:220, 1992.

[98] P. Lancaster and M. Tismenetsky. *The theory of matrices: with applications*. Elsevier, 1985.

[99] B. Levy and G. Berthier. Generalized Brillouin theorem for multiconfigurational SCF theories. *International Journal of Quantum Chemistry*, 2(2):307–319, 1968.

[100] G. N. Lewis. Valence and tautomerism. *Journal of the American Chemical Society*, 35(10):1448–1455, 1913.

[101] G. N. Lewis. The atom and the molecule. *Journal of the American Chemical Society*, 38(4):762–785, 1916.

[102] N. H. List, A. L. Dempwolff, A. Dreuw, P. Norman, and T. J. Martínez. Probing competing relaxation pathways in malonaldehyde with transient X-ray absorption spectroscopy. *Chemical science*, 11(16):4180–4193, 2020.

[103] P.-O. Löwdin. Quantum theory of many-particle systems. I. physical interpretations by means of density matrices, natural spin-orbitals, and convergence problems in the method of configurational interaction. *Physical Review*, 97(6):1474, 1955.

[104] S. Maeda and K. Morokuma. Communications: A systematic method for locating transition structures of A+B→X type reactions. *The Journal of chemical physics*, 132(24):241102, 2010.

[105] S. Maeda and K. Ohno. Global mapping of equilibrium and transition structures on potential energy surfaces by the scaled hypersphere search method: applications to ab initio surfaces of formaldehyde and propyne molecules. *The Journal of Physical Chemistry A*, 109(25):5742–5753, 2005.

[106] S. Maeda and K. Ohno. A new global reaction route map on the potential energy surface of H_2CO with unrestricted level. *Chemical Physics Letters*, 460(1-3):55–58, 2008.

[107] S. Maeda, K. Ohno, and K. Morokuma. An automated and systematic transition structure explorer in large flexible molecular systems based on combined global reaction route mapping and microiteration methods. *Journal of Chemical Theory and Computation*, 5(10):2734–2743, 2009.

[108] S. Maeda, K. Ohno, and K. Morokuma. Automated global mapping of minimal energy points on seams of crossing by the anharmonic downward distortion following method: a case study of h2co. *The Journal of Physical Chemistry A*, 113(9):1704–1710, 2009.

[109] S. Maeda, K. Ohno, and K. Morokuma. Systematic exploration of the mechanism of chemical reactions: the global reaction route mapping (GRRM) strategy using the ADDF and AFIR methods. *Physical Chemistry Chemical Physics*, 15(11):3683–3701, 2013.

[110] S. Maeda, Y. Osada, T. Taketsugu, K. Morokuma, and K. Ohno. Anharmonic downward distortion following for automated exploration of quantum chemical

potential energy surfaces. *Bulletin of the Chemical Society of Japan*, 87(12):1315–1334, 2014.

[111] S. Maeda, T. Taketsugu, K. Morokuma, and K. Ohno. GRRM14, 2014.

[112] R. L. Martin. Natural transition orbitals. *The Journal of chemical physics*, 118(11):4775–4777, 2003.

[113] E. Martínez-Núñez. An automated transition state search using classical trajectories initialized at multiple minima. *Physical Chemistry Chemical Physics*, 17(22):14912–14921, 2015.

[114] J. W. McIver Jr and A. Komornicki. Structure of transition states in organic reactions. general theory and an application to the cyclobutene-butadiene isomerization using a semiempirical molecular orbital method. *Journal of the American Chemical Society*, 94(8):2625–2633, 1972.

[115] A. McLean, A. Weiss, and M. Yoshimine. Configuration interaction in the hydrogen molecule–the ground state. *Reviews of Modern Physics*, 32(2):211, 1960.

[116] C. Melania Oana and A. I. Krylov. Dyson orbitals for ionization from the ground and electronically excited states within equation-of-motion coupled-cluster formalism: Theory, implementation, and examples. *The Journal of chemical physics*, 127(23):234106, 2007.

[117] W. Meyer. Ionization energies of water from PNO-CI calculations. *International Journal of Quantum Chemistry*, 5(S5):341–348, 1971.

[118] Y. Mitsuta, J. Kästner, S. Yamanaka, T. Kawakami, and M. Okumura. Free energy reaction root mapping of alanine tripeptide in water. *Molecular Physics*, 117(17):2284–2292, 2019.

[119] Y. Mitsuta and Y. Shigeta. Analytical method using a scaled hypersphere search for high-dimensional metadynamics simulations. *Journal of Chemical Theory and Computation*, 16(6):3869–3878, 2020.

[120] G. Montavon, M. Rupp, V. Gobre, A. Vazquez-Mayagoitia, K. Hansen, A. Tkatchenko, K.-R. Müller, and O. A. Von Lilienfeld. Machine learning of molecular electronic properties in chemical compound space. *New Journal of Physics*, 15(9):095003, 2013.

[121] A. Morita and S. Kato. Ab initio molecular orbital theory on intramolecular charge polarization: effect of hydrogen abstraction on the charge sensitivity of aromatic and nonaromatic species. *Journal of the American Chemical Society*, 119(17):4021–4032, 1997.

[122] K. Müller. Reaction paths on multidimensional energy hypersurfaces. *Angewandte Chemie International Edition in English*, 19(1):1–13, 1980.

[123] R. S. Mulliken. The assignment of quantum numbers for electrons in molecules. II. correlation of molecular and atomic electron states. *Physical review*, 32(5):761, 1928.

[124] S. Nakamura, H. Hirao, and T. Ohwada. Rationale for the acidity of Meldrum's acid. consistent relation of C-H acidities to the properties of localized reactive orbital. *The Journal of Organic Chemistry*, 69(13):4309–4316, 2004.

[125] K. Nandipati, A. K. Kanakati, H. Singh, and S. Mahapatra. Controlled intramolecular H-transfer in malonaldehyde in the electronic ground state mediated through the conical intersection of ^{1}nπ^* and $^1\pi\pi^*$ excited electronic states. *Physical Chemistry Chemical Physics*, 21(36):20018–20030, 2019.

[126] G. Ni, L. Qi, F. Wang, and Y. Wang. The degree of the E-characteristic polynomial of an even order tensor. *Journal of Mathematical Analysis and Applications*, 329(2):1218–1229, 2007.

[127] H. Nohira and T. Nohira. Dynamic correlation diagrams for sigmatropic reactions based on orbital phase conservation theory. *Journal of Theoretical and Computational Chemistry*, 16(06):1750055, 2017.

[128] D. H. Nouri and D. J. Tantillo. Hiscotropic rearrangements: hybrids of electrocyclic and sigmatropic reactions. *The Journal of Organic Chemistry*, 71(10):3686–3695, 2006.

[129] A. Ogawa, M. Tachibana, M. Kondo, K. Yoshizawa, H. Fujimoto, and R. Hoffmann. Orbital interactions between a C60 molecule and Cu (111) surface. *The Journal of Physical Chemistry B*, 107(46):12672–12679, 2003.

[130] K. Ohno and S. Maeda. A scaled hypersphere search method for the topography of reaction pathways on the potential energy surface. *Chemical physics letters*, 384(4-6):277–282, 2004.

[131] T. Ohwada, H. Hirao, and A. Ogawa. Theoretical analysis of Lewis basicity based on local electron-donating ability. origin of basic strength of cyclic amines. *The Journal of Organic Chemistry*, 69(22):7486–7494, 2004.

[132] K. Omoto and H. Fujimoto. Theoretical study of activation of oxirane by bidentate acids. *The Journal of Organic Chemistry*, 65(8):2464–2471, 2000.

[133] J. Pancíř. Calculation of the least energy path on the energy hypersurface. *Collection of Czechoslovak Chemical Communications*, 40(4):1112–1118, 1975.

[134] L. Pauling. The shared-electron chemical bond. *Proceedings of the national academy of sciences*, 14(4):359–362, 1928.

[135] F. Plasser, M. Wormit, and A. Dreuw. New tools for the systematic analysis and visualization of electronic excitations. I. formalism. *The Journal of chemical physics*, 141(2):024106, 2014.

[136] J. Pople, R. Krishnan, H. Schlegel, and J. S. Binkley. Derivative studies in Hartree-Fock and Møller-Plesset theories. *International Journal of Quantum Chemistry*, 16(S13):225–241, 1979.

[137] W. Quapp. Gradient extremals and valley floor bifurcations on potential energy surfaces. *Theoretica chimica acta*, 75(6):447–460, 1989.

[138] W. QUAPP. Reduced gradient methods and their relation to reaction paths. *Journal of Theoretical and Computational Chemistry*, 2(03):385–417, 2003.

[139] W. Quapp. Newton trajectories in the curvilinear metric of internal coordinates. *Journal of mathematical chemistry*, 36(4):365–379, 2004.

[140] W. Quapp, J. M. Bofill, and M. Caballero. Search for conical intersection points (CI) by newton trajectories. *Chemical Physics Letters*, 541:122–127, 2012.

[141] W. Quapp, M. Hirsch, and D. Heidrich. Bifurcation of reaction pathways: the set of valley ridge inflection points of a simple three-dimensional potential energy surface. *Theoretical Chemistry Accounts*, 100(5):285–299, 1998.

[142] W. Quapp, M. Hirsch, and D. Heidrich. An approach to reaction path branching using valley–ridge inflection points of potential-energy surfaces. *Theoretical Chemistry Accounts*, 112(1):40–51, 2004.

[143] W. Quapp, M. Hirsch, O. Imig, and D. Heidrich. Searching for saddle points of potential energy surfaces by following a reduced gradient. *Journal of computational chemistry*, 19(9):1087–1100, 1998.

[144] A. E. Reed and F. Weinhold. Natural bond orbital analysis of near-Hartree–Fock water dimer. *The Journal of chemical physics*, 78(6):4066–4073, 1983.

[145] A. E. Reed and F. Weinhold. Natural localized molecular orbitals. *The Journal of chemical physics*, 83(4):1736–1740, 1985.

[146] B. O. Roos, P. R. Taylor, and P. E. Sigbahn. A complete active space SCF method (CASSCF) using a density matrix formulated super-CI approach. *Chemical Physics*, 48(2):157–173, 1980.

[147] C. C. J. Roothaan. New developments in molecular orbital theory. *Reviews of modern physics*, 23(2):69, 1951.

[148] M. J. Rothman and L. L. Lohr Jr. Analysis of an energy minimization method for locating transition states on potential energy hypersurfaces. *Chemical Physics Letters*, 70(2):405–409, 1980.

[149] D. Rowe and A. Ryman. Valleys and fall lines on a riemannian manifold. *Journal of Mathematical Physics*, 23(5):732–735, 1982.

[150] L. Salem. Conditions for favorable unimolecular reaction paths. *Chemical Physics Letters*, 3(2):99–101, 1969.

[151] G. N. Sastry and S. Shaik. Stereochemistry and regiochemistry in model electron transfer and substitution reactions of a radical anion with an alkyl halide. *Journal of the American Chemical Society*, 117(11):3290–3291, 1995.

[152] G. N. Sastry and S. Shaik. Structured electron transfer transition state. valence bond configuration mixing analysis and ab initio calculations of the reactions of formaldehyde radical anion with methyl chloride. *The Journal of Physical Chemistry*, 100(30):12241–12252, 1996.

[153] S. Satoh, H. Fujimoto, and H. Kobayashi. Theoretical study of NH_3 adsorption on Fe (110) and Fe (111) surfaces. *The Journal of Physical Chemistry B*, 110(10):4846–4852, 2006.

[154] P. Scharfenberg. Theoretical analysis of constrained minimum energy paths. *Chemical Physics Letters*, 79(1):115–117, 1981.

[155] H. B. Schlegel. Following gradient extremal paths. *Theoretica chimica acta*, 83(1):15–20, 1992.

[156] H. B. Schlegel. Exploring potential energy surfaces for chemical reactions: an overview of some practical methods. *Journal of computational chemistry*, 24(12):1514–1527, 2003.

[157] H. B. Schlegel. Geometry optimization. *Wiley Interdisciplinary Reviews: Computational Molecular Science*, 1(5):790–809, 2011.

[158] M. W. Schmidt, E. A. Hull, and T. L. Windus. Valence virtual orbitals: An unambiguous ab initio quantification of the LUMO concept. *The Journal of Physical Chemistry A*, 119(41):10408–10427, 2015.

[159] E. Schrödinger. An undulatory theory of the mechanics of atoms and molecules. *Phys. Rev.*, 28:1049–1070, Dec 1926.

[160] S. Shaik, D. Danovich, G. N. Sastry, P. Y. Ayala, and H. B. Schlegel. Dissociative electron transfer, substitution, and borderline mechanisms in reactions of ketyl radical anions. differences and difficulties in their reaction paths. *Journal of the American Chemical Society*, 119(39):9237–9245, 1997.

[161] N. Shida, J. E. Almlöf, and P. F. Barbara. Molecular vibrations in a gradient extremal path. *Theoretica chimica acta*, 76(1):7–31, 1989.

[162] J. Slater. Molecular orbital and Heitler–London methods. *The Journal of Chemical Physics*, 43(10):S11–S17, 1965.

[163] J. C. Slater. Note on Hartree's method. *Physical Review*, 35(2):210, 1930.

[164] A. L. Sobolewski and W. Domcke. Ab initio potential-energy functions for excited state intramolecular proton transfer: a comparative study of o-hydroxybenzaldehyde, salicylic acid and 7-hydroxy-1-indanone. *Physical Chemistry Chemical Physics*, 1(13):3065–3072, 1999.

[165] S. H. Strogatz. *Nonlinear dynamics and chaos: with applications to physics, biology, chemistry, and engineering*. CRC press, 2018.

[166] J.-Q. Sun and K. Ruedenberg. Gradient extremals and steepest descent lines on potential energy surfaces. *The Journal of chemical physics*, 98(12):9707–9714, 1993.

[167] T. Suzuki and H. Fujimoto. Theoretical study of the mechanisms of palladation of methylenecyclopropane and [3+ 2] cycloadditions. *Inorganic Chemistry*, 39(6):1113–1119, 2000.

[168] A. Szabo and N. S. Ostlund. *Modern quantum chemistry: introduction to advanced electronic structure theory*. Courier Corporation, 2012.

[169] M. Tachibana, K. Yoshizawa, A. Ogawa, H. Fujimoto, and R. Hoffmann. Sulfur-gold orbital interactions which determine the structure of alkanethiolate/Au (111) self-assembled monolayer systems. *The Journal of Physical Chemistry B*, 106(49):12727–12736, 2002.

[170] K. Takatsuka and Y. Arasaki. Energy natural orbitals. *The Journal of Chemical Physics*, 154(9):094103, 2021.

[171] D. J. Tantillo. Recent excursions to the borderlands between the realms of concerted and stepwise: carbocation cascades in natural products biosynthesis. *Journal of Physical Organic Chemistry*, 21(7-8):561–570, 2008.

[172] M. Tsuyuki, S. Furudate, Y. Kugaya, and S. Yabushita. Graphical transition moment decomposition and conceptual density functional theory approaches to study the fundamental and lower-level overtone absorption intensities of some oh stretching vibrations. *The Journal of Physical Chemistry A*, 125(10):2101–2113, 2021.

[173] O. A. von Lilienfeld, K.-R. Müller, and A. Tkatchenko. Exploring chemical compound space with quantum-based machine learning. *Nature Reviews Chemistry*, 4(7):347–358, 2020.

[174] J. von Neumann. *Mathematical Foundations of Quantum Mechanics*. Springer Verlag, 1932.

[175] S. P. Walch and R. L. Jaffe. Calculated potential surfaces for the reactions: O + N_2→ NO + N and N+ O_2→ NO+ O. *The Journal of chemical physics*, 86(12):6946–6956, 1987.

[176] C. Weatherburn. Introduction to tensor calculus and Riemannian geometry, 1938.

[177] I. H. Williams and G. M. Maggiora. Use and abuse of the distinguished-coordinate method for transition-state structure searching. *Journal of Molecular Structure: THEOCHEM*, 89(3-4):365–378, 1982.

[178] R. B. Woodward and R. Hoffmann. Selection rules for sigmatropic reactions. *Journal of the American Chemical Society*, 87(11):2511–2513, 1965.

[179] R. B. Woodward and R. Hoffmann. Stereochemistry of electrocyclic reactions. *Journal of the American Chemical Society*, 87(2):395–397, 1965.

[180] R. B. Woodward and R. Hoffmann. The conservation of orbital symmetry. *Angewandte Chemie International Edition in English*, 8(11):781–853, 1969.

[181] D. R. Yarkony. On the consequences of nonremovable derivative couplings. I. the geometric phase and quasidiabatic states: A numerical study. *The Journal of chemical physics*, 105(23):10456–10461, 1996.

[182] J.-X. Zhang, F. K. Sheong, and Z. Lin. Unravelling chemical interactions with principal interacting orbital analysis. *Chemistry–A European Journal*, 24(38):9639–9650, 2018.

List of publications

(1) S. Ebisawa, T. Tsutsumi and T. Taketsugu. Geometric analysis of anharmonic downward distortion following paths. *Journal of Computational Chemistry*, 42(1):27-39, 2021.

(2) S. Ebisawa, M. Hasebe, T. Tsutsumi, T. Tsuneda and T. Taketsugu. Natural reaction orbitals for characterizing electron transfer responsive to nuclear coordinate displacement. *Physical Chemistry Chemical Physics*, 24(6):3532-3545, 2022.

(3) S. Ebisawa, T. Tsutsumi and T. Taketsugu. Extension of natural reaction orbital approach to multiconfigurational wavefunctions. *The Journal of Chemical Physics*, 157(8):084118, 2022.

Acknowledgement

I would like to express my sincere thanks to my supervisor Prof. Tetsuya Taketsugu for all the gentle and patient instruction. Whenever the study encountered some difficulty, Prof. Taketsugu always encouraged me and provided instructive advice on the study from the viewpoint an experienced researcher. Even when I had a misunderstanding, he never rebuked me sharply but leaded me to the right way with his in-depth knowledge. All the achievements in this thesis owe much to his direct and indirect support. Here I would like to sincerely appreciate all of his kind instruction and support again.

Now I wish to thank all the staff of Taketsugu group, Visiting Prof. Takao Tsuneda, Associate Prof. Masato Kobayashi, Associate Prof. Andrey Lyalin, Assistant Prof. Tomoko Akama, Assistant Prof. Takeshi Iwasa, Assistant Prof. Yuriko Ono, Assistant Prof. Kenichiro Saita, Assistant Prof. Takuro Tsutumi, Dr. Sonu Kumar and Dr. Ben Wang. I am also grateful to the former staff, Prof. Satoshi Maeda, Associate Prof. Takahiro Doi, Associate Prof. Kimichi Suzuki, Associate Prof. Ryo Wakeshima, Assistant Prof. Min Gao, Assistant Prof. Yu Harabuchi, Dr. Tomoya Ichino and Dr. Kaoru Yamazaki. All the staff always provided me various advice on my study. Particularly, I am grateful to Visiting Prof. Tsuneda and Assistant Prof. Tsutumi for invaluable discussion about the studies.

I would like to thank Masatoshi Hasebe and Hiroki Sumitomo for invaluable discussion about the studies. Particularly, Hasebe studied actively and provided a large number of meaningful data. The data shown by him was very important for the study.

Also, I express my sincere thanks to the chief advisor Prof. Satoshi Maeda, and the deputy advisors, Prof. Tetsuya Taketsugu, Prof. Jun-ya Hasegawa, Prof. Tamiki Komatsuzaki, Associate Prof. Shin-ichiro Satoh despite their so busy schedule.

Finally, I would like to express my sincere thanks to Prof. Koichi Ohno, the chief director of institute for quantum chemical exploration (IQCE). Prof. Ohno administered a scholarship program for young students exploring unknown chemistry based on quantum chemistry. All the studies of this thesis were supported by the scholarship program. Furthermore, I could not continue my study without the scholarship. I owe

much to his strong avidity for chemistry and education. As one student, I sincerely thank him again.